

NANOPOROUS LAYERED GRAPHENE HYDROGEL
FOR CONTROLLED DRUG DELIVERY

Meisam Valizadeh Kiamahalleh

A thesis submitted for the degree of

Doctor of Philosophy

School of Chemical Engineering

The University of Adelaide

Australia

September 2015

Declaration

I certify that this work contains no material which has been accepted for the award of any other degree or diploma in my name in any university or other tertiary institution and, to the best of my knowledge and belief, contains no material previously published or written by another person, except where due reference has been made in the text. In addition, I certify that no part of this work will, in the future, be used in a submission in my name for any other degree or diploma in any university or other tertiary institution without the prior approval of the University of Adelaide and where applicable, any partner institution responsible for the joint award of this degree.

I give consent to this copy of my thesis when deposited in the University Library, being made available for loan and photocopying, subject to the provisions of the Copyright Act 1968.

The author acknowledges that copyright of published works contained within this thesis resides with the copyright holder(s) of those works.

I also give permission for the digital version of my thesis to be made available on the web, via the University's digital research repository, the Library Search and also through web search engines, unless permission has been granted by the University to restrict access for a period of time.

Meisam Valizadeh Kiamahalleh Date: 15/09/2015

Abstract

Graphene-related materials with tuneable pore sizes in the nanoscale range offer the potential to address significant challenges in biomolecule separation, controlled delivery of drugs, selective biosensor, rechargeable batteries, supercapacitors and solar cells. Layered assemblies of graphene-related sheets with physical and chemical cross-linkers between the sheets have been recognized as one possible strategy for making such nanoporous materials. However, current approaches give very limited control over the pore size distribution, particularly with regards control of the mean pore size and the degree of spread around it.

This work particularly outlined the design, synthesis and characterization of a nanoporous layered graphene hydrogel produced via peptide-mediated self-assembly of reduced graphene oxide (rGO). The peptides have been designed using molecular dynamics (MD) simulation to self-assemble the rGO sheets with a desired inter-sheet spacing (pore size). The hydrogel material was synthesized and characterized using a range of methods to demonstrate the desired pore size is achieved.

In the second body of this work, the rGO binding peptide hydrogel, denoted rGOPH, showed to be a promising candidate for the controlled delivery of an anti-cancer drug. In particular, it was shown that the rGOPH has a high doxorubicin (DOX) loading capacity achieved through physical adsorption within its nanoporous structure. Design of experiments (DoE) and statistical analysis on different preparation parameters revealed that pore size and drug loading capacity are tuneable.

In the final part of the work, a desirable pH-dependant drug release properties was shown by rGOPH nominating such hydrogels as promising candidates for cancer therapy. In addition, the hydrogel materials exhibited a high biocompatibility to the healthy cells for their attachments and proliferation. The cytotoxicity of the hydrogel materials demonstrated to be low.

The work reported in this thesis has provided new computational and experimental understanding for fabrication of graphene based nano-constructs with tuneable pore size as

well as new methodologies and approaches. Although the focus was only on one designed peptide, the design and methodologies developed here are quite potent and, therefore, lay the foundations for fabrication of nanoporous graphene based materials of virtually any pore size to suit the needs of users in broader applications (such as nanomedicines, nanobiotechnology, nanoelectronics, biosensors and biomolecular and nanoparticle separations).

Achievements

Two patents were achieved from this work:

- 1) Compositions comprising self-assembled carbon based structures and related methods. A. P. Patent. **AU2014/900273**.
- 2) Self-assembled carbon based structures and related methods. **PCT/AU2015/000034**.

This work was presented in conferences with the following titles:

- 1) “Nanoporous Layered Graphene Hydrogels with Controlled Pore Sizes: Design, Synthesis, Characterization and Applications” Pacific Conference on Energy and Environmental Materials (APCEEM) 9th–11th February 2014 Gold Coast, Australia.
- 2) “Graphene binding peptide hydrogel in controlled drug delivery; loading, release and cytotoxicity effect of doxorubicin” OzCarbon(2014), Adelaide, Australia.
- 3) “Molecular Modelling of Protein Adsorption: From Fundamentals to Design.” FOA11 (the 11th International Conference on the Fundamentals of Adsorption), (2013) Baltimore, Maryland, USA.
- 4) “Molecular modelling of protein adsorption on graphite & graphene: From fundamentals to design” Annual World Conference on Carbon - Carbon 2013 (Carbon 2013) Rio de Janeiro, Brazil
- 5) “Peptide-mediated assembly of nanoporous graphene films with dialable pore sizes” OzCarbon(2013), Melbourne, Australia.

Acknowledgements

I would like to express my sincere gratitude to those who gave me the possibility to complete this dissertation.

First and foremost, I would like to thank my dear supervisors, Prof. Mark J. Biggs and Dr. Sheng Dai from the University of Adelaide and my previous supervisor, Prof. Habibah A Wahab, from Universiti Sains Malaysia, for their ongoing advice, encouragement and support during the entire course of my PhD study. This thesis could not have been completed without your constant encouragement, support and guidance. My special thanks also go to our team members Dr. Milan Mijajlovic and Dr. Matthew J. Penna for their support as well as comments on my work. I feel privileged to have been able to work with all members (former and current)

Australian Postgraduate Award (APA) and International Postgraduate Research Scholarship (IPRS) from the University of Adelaide are gratefully acknowledged for providing me scholarship for my study in Australia. The support of the Australian Research Council Discovery Program (DP20111888) is also gratefully acknowledged. The supercomputing resources for this work were provided by eResearchSA, the NCI National Facility at the Australian National University and the iVEC Facility at Murdoch University under the National Merit Allocation Scheme.

I would also like to thank Dr. Wenrong Yang, Dr. Da Li, Motilal Mathesh Shanmugam, Zhen Liu and Mahesh Vaka of Deakin University for their support and assistance with AFM related work. I am also very thankful to Prof. Skinner for his support and assistance with XPS experiments. Special thanks to Mr. Jason Peak, Mr. Michael Jung and Mr. Jeffrey Hiorns, for their help and assistance with many laboratory setups. I am also grateful to my dear friends Amir, Hadi, Saeid, Shervin, Tushar and Tariq for their helps, comments and suggestions on my experimental works.

I would like to express my deepest appreciation to Julie for her encouragements and helps in corrections and proofreading of this thesis. For the friends (Moein, Hamideh, Sanaz, Benyamin, Masoumeh, Mahya, Mehdi, Munkhbayar, Priyantha Indrajith, Alireza,

Masi, Hosna, Rasta, Bita, Saeed, Nima, Amir Ebrahimi, Aida, Hassan, Claudia, MohammadReza, Ms. Jacqueline and Samantha Cookes) I made here in Adelaide, thanks a lot for your accompany and encouragements.

Last but not least, with tears in my eyes, I would like to thank my parents and family members (Motahhareh, Mehdi, Muahmmad and Fereshteh) for their infinite and never ending love. Without their support, I would never achieve what I have today.

List of Figures

Figure 1-1. Self-assembly of graphene hydrogel construct with tuneable pore size (<i>h</i>).....	4
Figure 2-1. Single layer graphene presented as a material from which other structures such as fullerenes, carbon nanotube (CNT) and graphite can be built.[55]	7
Figure 2-2. Schematic illustration of the main graphene production techniques including exfoliation and growth on substrate. [56]	8
Figure 2-3. Proposed mechanisms for the reduction of epoxide groups with hydrazine via four different routes [83].....	14
Figure 2-4. SEM images of (a) rGO film and (b) CNTs network (Scale bars = 1 μm). Phase-contrast images of PC12 cells grown on (c) rGO film and (d) CNTs network for 5 days (Scale bars = 100 μm) [192].	24
Figure 2-5. Micrographs showing human adenocarcinoma HT-29 cell attachment and growth on glass slides (a) without or (b) with GO film.[195].	25
Figure 2-6. Released drug concentration over time (gathered from ref [202, 205, 207]. The lines that indicate the toxic and minimum effective levels of the drug are coloured red and green respectively. The desirable-controlled drug release is shown in blue solid line. Two cases of problematic drug release (either conventional or sustained release) indicate the drug release ending too soon or, occasionally, being below the minimum effective level or higher than the toxic level and these are shown in grey dash lines.....	29
Figure 2-7. (a) Schematic of the formation of graphene-based 3D porous macroforms with different drying process and the SEM images of the resultant PGM and HPGM and (b) PSD plots of HPGM before and after annealing process. [269, 284].	42
Figure 2-8. Schematic representation of (a) LBL assembly of rGO multilayer with rGO-COO ⁻ and rGO-NH ₃ ⁺ , and (b) the resulting LBL film of rGO [286].	44
Figure 2-9. Schematic illustration of the multilayered graphene (a1) before (a2) after carbon black (CB) intercalation, [35] (b) the preparation procedure for the RGO-CMK-5 composite, [37] (c) graphene/CNTs composite preparation process, [293] and (d) CNTs based pillared graphene oxide construct [38].....	46
Figure 2-10. (a) Schematic diagram of a 3D pillared VACNT-graphene nanostructure. (b) Schematic representation of the procedure for the preparation of the 3D pillared VACNT-graphene architectures. Optical images of (c) original highly ordered pyrolytic graphite (HOPG) with a thickness of 80 μm and (d) the thermally expanded graphene layers intercalated with VACNTs. [298].....	48
Figure 2-11. (a) Schematic model of a sheet of GO showing oxygen-containing functionalities. (b) Chemical structure of polyallylamine [291].....	50
Figure 2-12. Schematic Illustration of the Formation Process of GOPPy Composite [301].	51
Figure 2-13. (a) Schematic of a transparent and flexible molecular monolayer junction between the two graphene electrodes, (b) Molecular tunneling barriers (with h_1 and h_2	

being the vertical distance between the two graphene electrodes) corresponding to conformational changes in aryl azobenzene molecules with light irradiation [302].52

Figure 2-14. (a) Schematic illustration of the proposed incorporation of TPA within the rGO-layered structure, (b and c) Cross-sectional scanning electron microscopy (SEM) images of pristine rGO (on the left) and TPA-treated rGO papers (on the right). The scale bars indicate 2 μm [306].54

Figure 2-15. Schematic diagram for the conversion of GO to GPPD [307].55

Figure 2-16. Models of the M-modified graphene oxide papers: (a) schematic model of the reaction between graphene oxide paper and MCl_2 ($\text{M} = \text{Mg}$ and Ca); (b) proposed model for the enhanced mechanical properties of graphene oxide paper observed after metal modification [93].56

Figure 2-17. The LBL preparation of ruthenium oxide (RuO_2)/graphene sheet composites by combining a sol-gel method [41].57

Figure 2-18. Schematic of the two-step procedure in fabrication of layer-by-layer assembled Au-graphene films; (a) AuNPs formation on graphene film (b) Layer-by-Layer assembly of graphene and AuNPs [42].58

Figure 2-19. Schematic presentation of the green synthesis and potential formation mechanism of rGO/AuNP film.59

Figure 2-20. The procedure of preparing GO/DNA self-assembled hydrogel and the proposed gelation mechanism [47].59

Figure 2-21. Probable interaction between amino acids and GO. (a) DL-aspartic acid with GO, (b) L-glycine with GO, and (c) L-arginine with GO [292].61

Figure 2-22. The design of the hybrid hydrogel. (a) The peptide sequence. (b) The hierarchical construction scheme for the hydrogel [49].62

Figure 2-23. (a) Schematic diagram of EAK16-II structure [356] (b) Side view of the snapshots of the peptide-graphite surface system at adsorbed state (the three residues alanine, glutamic acid, and lysine are colored in gray, red, and blue, respectively) [328]. ..68

Figure 4-1. Self-assembly of graphene hydrogel construct with tuneable pore size (h)82

Figure 4-2. The equilibrated structure of the peptide in physiological solution after 10ns of MD simulation.83

Figure 4-3. Contour plot for distribution of tilting angle between the normal of PHE rings and graphene surface correlating with the ring-surface distance for (a) PHE1, (b) PHE2, (c) PHE13 and (d) PHE14. (Derived from all 45 MD simulations.)88

Figure 4-4. Variation with normal distance above the solid surface of: (a) relative density of the oxygen (solid line) and hydrogen (broken line) in the water and (b) water net charge density (c) GLU residues' side-chain distribution.91

Figure 4-5. TEM images of (a) single rGO sheet and (a) GRP-UA2.92

Figure 4-6. AFM 2D and 3D images and height profile of the X cross-sections indicated in black for rGO sheets (left) and GRP-UA2 (right).93

Figure 4-7. Side view snapshots of the representative UA2 adsorption on graphene surface. The snapshots of the designed UA2 in the side view are displayed by the new cartoon model, and the graphene is displayed by a VDW model.	95
Figure 4-8. Trajectory of the exemplar MD simulation from initiation of the lockdown phase to the complete peptide adsorption: Correlation of the fraction of UA2 adsorbed atoms with interaction energy. Snapshots three different event where the peptide undergoes major changes in structure from: (i) initial states at bulk water to (ii) lockdown state of one end and (iii) lockdown of the other end (complete adsorption).....	98
Figure 4-9. The fraction of 45 simulations in which the indicated terminal/residue side-chain groups initiated adsorbed (lockdown state) and their first and second follower.	100
Figure 4-10. The probability of a residue following the adsorption initiator into the adsorbed (lockdown) state as a function of its distance from the initiator in number of residues. The exponential fit to the data is characterized by a coefficient of determination of $R^2 = 0.9372$	101
Figure 4-11. Time-averaged fraction of initial α -helix of each residue over the 100 ns for 45 MD runs	102
Supplementary Figure 4-1. GO (left) and rGO (right) dispersions.	105
Supplementary Figure 4-2. Variation of α -helicity (black) and RMSD (red) of the solvated UA2 over a sample simulation.....	106
Supplementary Figure 4-3. Simulation representative snapshots for the UA2 peptide with different initial orientations interacting with graphene surface. Water molecules are not displayed for clarity.....	107
Supplementary Figure 4-4. The normal distance of GLU side-chain to the graphene surface.	108
Supplementary Figure 4-5. Interaction energy between UA2 residues ((a) PHE, (b) GLY and (c) GLU) and graphene surface.	109
Supplementary Figure 4-6. Variation of α -helicity (black) and RMSD (red) of the adsorbed UA2 over 100ns of MD simulation.	110
Figure 5-1. (a) Self-assembly of graphene related hydrogel with tuneable pore size and (b) the components of the peptide design used to self-assemble the graphene-based nanoporous hydrogel with a specific pore size.	115
Figure 5-2. Photographs of (a) thick and (b) transparent hydrogel films (c) Cross-section view SEM image of rGOPH (d) TEM image of multi-layered rGOPH from the top view (red arrows correspond to individual layering of graphene sheets covered by peptide), (e) Tapping-mode AFM image (blue and red lines are random sections for pore measurements) and (f) height profile of rGOPH which illustrates an inter-layer spacing of ~ 2.6 nm comparable with that of in rGOH,	117
Figure 5-3. (a) Nitrogen adsorption isotherms, and (b) Pore size distribution derived from nitrogen adsorption isotherm on dried rGOPH film based on the Quenched Solid Density Functional Theory (QSDFT) method [407]. Pores are classified as Category0: non-	

detectable pores, Category1: Stack mediated pores, Category2: Peptide mediated pores and Category3: inter-particles void.	119
Figure 5-4. (a) Time evolution of the FITC-labeled dextrans concentration change in hydrogels (adsorption profile) and (b) the representative colors of the dye solutions before and after the dye adsorption.....	121
Supplementary Figure 5-1. The snapshots for the graphene nanosheets self-assembly using the peptide molecule: (a) the initial and (b) final configurations.....	125
Supplementary Figure 5-2. (a) Time evolution of graphene interlayer distance ¹³ and the interaction energy between UA2 peptide and below (blue) and top (red) graphene sheets, (b) Variation of α -helicity (blue) and RMSD (red) of rGOPH over a sample simulation. Insets are snapshots for the peptide initial, 24th ns and final configuration in MD simulation.	128
Supplementary Figure 5-3. Graphite to graphene oxide.....	129
Supplementary Figure 5-4. (a) GO and (b) rGO dispersions.....	130
Supplementary Figure 5-5. Filtering apparatus (left) filtrate cake or hydrogel.....	130
Supplementary Figure 5-6. Optical images of (a) vice clamp holding the graphene film between two glass substrate (b) transparent film of rGOH and rGOPH.	131
Supplementary Figure 5-7. (a) The absorption peak of the GO and rGO dispersions (Inset images are Milli-Q water droplets on GOH and rGOH films), (b) FT-IR spectra of GOH and rGOH, (c) Deconvoluted XPS C1s spectra of (c) GOH and (d) rGOH.	133
Supplementary Figure 5-8. (a) Photographs of rGOH film in both transparent and thick form, (b) SEM image of rGOH obtained from the cross section view, (c) Tapping-mode AFM image, and (d) TEM image of multi-layered rGOH from the top view, (e) Height profile of rGOH which illustrates a graphene interlayer spacing of about $\sim 7\text{\AA}$, and (f) side view snapshots of the representative rGOH from MD simulation.	135
Supplementary Figure 5-9. WXR patterns of graphite (black), GOH (brown), rGOH (blue) and rGOPH (red).	136
Supplementary Figure 5-10. Raman spectra of graphite (black), GOH (brown), rGOH (blue) and rGOPH (red).	137
Supplementary Figure 5-11. Time evolution of graphene interlayer distance (green) and the interaction energy between two graphene nanosheets (black). (Insets are the evolutionary snapshots of two graphene nanosheets self-assembly and the interlayer water relative density.)	139
Figure 6-1. Schematic drawing of the real time monitoring of DOX loading on hydrogels placed inside a cuvette.	148
Figure 6-2. The loading capacity of DOX in rGOPH (prepared at optimized conditions) at different pH values adjusted by PBS buffer.	152
Figure 6-3. The experimental DOX loading capacity plotted against the predicted values calculated from the DOE-RSM model.	155

Figure 6-4. Response surfaces for DOX loading capacity against A:reduction temperature and B:amount of hydrazine depicted as contour (a) and three-dimensional (b) plots. The variable C was kept at its zero (centerpoint) level.	156
Figure 6-5. Tapping-mode 2D AFM images of (a) rGOPH-HR and (c) rGOPH-SR; Height profile of (b) rGOPH-HR and (d) rGOPH-SR.	158
Figure 6-6. (a) The wide-scan X-ray photoelectron spectra (XPS) of various hydrogels. (b) the content of each hydrogel, The XPS spectra of the N1s for (c) rGOH, (d) rGOPH-SR, (e) rGOPH-HR and (f) rGOPH-OR.	160
Figure 6-7. Time evolution of interactions in (a) graphene-graphene and (b) graphene-peptide MD simulation systems.	161
Figure 6-8. Response surfaces for DOX loading capacity against A:reduction temperature and C:peptide concentration depicted as contour (a) and three-dimensional (b) plots. The variable B was kept at its zero (centerpoint) level.	163
Figure 6-9. Response surfaces for DOX loading capacity against B: amount of hydrazine and C:peptide concentration depicted as contour (a) and three-dimensional (b) plots. The variable A was kept at its zero (center-point) level.....	164
Figure 6-10. (a) Tapping-mode 2D AFM image and (b) height profile of the rGOPH with 0.04 μM of peptide concentration. (X cross-sections labeled from A to B)	165
Figure 6-11. (a and c) Tapping-mode 2D AFM images of the rGOPH-OR with of peptide concentration of 0.08 and 0.10 μM , respectively. (b and c) height profile of the rGOPH-OR with of peptide concentration of 0.08 and 0.10 μM , respectively. (Cross-sections labeled from A to B and from C to D).....	165
Figure 6-12. (a) Nitrogen adsorption isotherm and (b) PSD analysis of hydrogels; rGOH (without the peptide), rGOPH-0.08 μM (with optimum peptide concentration), and rGOPH-0.10 μM (with the highest peptide concentration).....	167
Figure 6-13. The time evolution of the DOX adsorption into the graphene hydrogel with pore size of ~ 1.0 nm. Insets are different views simulation representative snapshots for before and after DOX adsorption. (Water molecules are not displayed for clarity). The inserted photographs of cuvettes show the DOX solutions before and after treating with hydrogel.....	169
Figure 6-14. The time evolution of the DOX adsorption into the graphene hydrogel with pore size of ~ 2.6 nm. Insets are different views simulation representative snapshots for before and after DOX adsorption. (Water molecules are not displayed for clarity). The inserted photographs of cuvettes show the DOX solutions before and after treating with hydrogel.....	170
Figure 6-15. (a) Real time monitoring of DOX adsorption by hydrogels, DOX adsorption kinetics of (b) pseudo-first-order, (c) pseudo-second-order, (d) intra-particle diffusion models.	173
Supplementary Figure 6-1. UV absorbance versus concentration of DOX. The fit (red curve) was used for calculation of the amount of DOX that was loaded on the hydrogels.	181

Supplementary Figure 6-2. Water contact angle: (a) rGO treated with 25 μL (1), 54 μL (b) and 75 μL (3) of hydrazine at a constant temperature of 89 $^{\circ}\text{C}$ and (b) rGO treated at 85 $^{\circ}\text{C}$ (1), 89 $^{\circ}\text{C}$ (2) and 95 $^{\circ}\text{C}$ (3) with using a constant amount of hydrazine; 54 μL **182**

Supplementary Figure 6-3. (a) GO and rGO dispersions (5 $\text{mg}\cdot\text{mL}^{-1}$) prepared (a) with different amount of hydrazine at constant temperature of 89 $^{\circ}\text{C}$ and (b) at different temperature with constant volume of hydrazine (54 μL). Their corresponding zeta potential graphs are given below the photograph. **183**

Supplementary Figure 6-4. FT-IR spectra of GO and rGO-SR, rGO-OR and rGO-HR **184**

Supplementary Figure 6-5. Interaction energies between plain graphene sheets (blue line), between graphene sheets and PHE residues of the (a) two and (b) three peptides located at the interlayer space (red line). Insets are snapshots from the initial, stacking and final states of the MD simulation..... **185**

Supplementary Figure 6-6. Real time monitoring of DOX adsorption by hydrogels; rGOH (without the peptide), rGOPH-0.08 μM (with optimum peptide concentration), and rGOPH-0.10 μM (with the highest peptide concentration) **186**

Figure 7-1. Schematic drawing of the real time monitoring of DOX release from hydrogels..... **192**

Figure 7-2. UV calibration curve of DOX concentration in PBS buffer at the wavelength of 490 nm. **192**

Figure 7-3. The cumulative release of DOX from rGOPH at different pH values. **196**

Figure 7-4. The effect of rGOPH (0, 5, 10, 15, 20 and 25 mg) on cell viability of MSCs for 24 hrs. The results represent the means of three separate experiments, and error bars represent the standard error of the mean. Treated groups did not show any statistically significant differences from the control group by Student’s t-test ($P < 0.05$). **197**

Figure 7-5. The effect of rGOPH, DOX, and rGOPH/DOX on cell viability of MSCs for 24 hrs. The results represent the means of three separate experiments, and error bars represent the standard error of the mean. Treated groups showed statistically significant differences from the control group by Student’s t-test ($P < 0.05$). **198**

Figure 7-6. Confocal laser scanning microscopy images (live, dead and mix of live/dead images) of MSCs treated with rGOPH(25 mg) at day1 and 10. **199**

List of Tables

Table 2-1. Bonded and non-Bonded terms of empirical forcefield.....	71
Table 3-1. Materials and chemicals used in this study.....	73
Supplementary Table 5-1. Mean pore size measurements from different AFM height profile images of rGOPH.	140
Supplementary Table 5-2. Possible pores in wet-state hydrogels.	141
Table 6-1. Coded and actual values of variables of the design for graphene oxide reduction and rGOPH preparation.....	150
Table 6-2. Groups form hydrogen bonds in rGOPH and DOX at different pH values.	153
Table 6-3. Experimental design and the actual response of the DOX loading on rGOPH samples.....	154
Table 6-4. Kinetic parameters for Pseudo-first-order, Pseudo-second-order and Intra-particle diffusivity.	175
Supplementary Table 6-1. Experimental matrix for central composite design (CCD) for rGOPH preparation.	177
Supplementary Table 6-2. Analysis of variance ^[444] for the response-surface quadratic model of the DOX loading capacity.....	179
Supplementary Table 6-3. Statistical parameters as obtained from ANOVA for the response(DOX loading)-surface fitted model.	180
Table 7-1. Groups form hydrogen bonds in rGOPH and DOX in different pH values.....	195

Abbreviations

ANOVA	Analysis of variance
AFM	Atomic force microscopy
BJH	Barrett-Joyner-Halenda
CPT	Camptothecin
CB	carbon black
CNT	Carbon nanotube
CCD	Central composite design
CCFD	Central composite face centered design
CTAB	Cetyltrimethylammonium bromide
CVD	Chemical vapor deposition
CCG	Chemically converted graphene
CF	Ciprofloxacin
CV	Coefficient of variation
DOE	Design of experiments
DMSO	Dimethyl sulfoxide
DTAB	Dodecyltrimethylammonium bromide

ds-DNA	Double stranded
DOX	Doxorubicin
DDS	Drug delivery systems
EthD-1	Ethidium homodimer-1
FD4,10 and20	Fluorescein isothiocyanate–dextran (4, 10 and 20 KD)
FTIR	Fourier transform infrared
Glu	Glutamic acid
Gly	Glycine
AuNP	Gold nanoparticle
g-C ₃ N ₄	Graphene based carbon nitride
GO	Graphene oxide or graphite oxide
GS	Graphene sheet
HOPG	Highly ordered pyrolytic graphite
hFOB	Human fetal osteoblast
HOG	Human oligodendroglia
LBL	Layer by layer

LCST	Lower critical solution temperature
M-LBL	Manual layer-by-layer
MSCs	Mesenchymal stem cells
MD	Molecular dynamics
MM	Molecular mechanics
MC	Monte Carlo
DMF	N,N-dimethylformamide
NG	Nitrogen doped graphene
NMP	N-methyl-2-pyrrolidone
Phe	Phenylalanine
PMAA	Poly (methacrylic acid)
P(AA-co-AM)	Poly(acrylic acid-co-acrylamide)
PMVE	Poly(methylvinylether)
DEAM	Poly(N,N'-diethylacrylamide)
PAcrNPP	Poly(N-acryloyl-N'-Propylpiperazine)
PNIPAAm	Poly(N-isopropylacrylamide)

PVA	Poly(vinyl alcohol)
PAA	Polyallylamine
PANI	Polyaniline
PDMS	Polydimethylsiloxane
PEG	Polyethylene glycol
PEI	Polyethyleneimine
PET	Polyethyleneterephthalate
PPy	polypyrrole
PSD	Pore size distribution
PPD	p-phenylenediamine
QM	Quantum mechanics
QSDFT	Quenched Solid Density Functional Theory
ROS	Reactive oxygen species
rGO	Reduced graphene oxide
rGOH	Reduced graphene oxide hydrogel
RSM	Response surface method

rGOPH	rGO binding peptide hydrogel
SEM	scanning electron microscopy
SA	Self-assembly
SiC	Silicon carbid
ss-DNA	Single stranded DNA
SWCNTs	Single wall carbon nanotubes
SD	Standard deviation
SA	Succinic acid
TPA	Terephthalic acid
THF	Tetrahydrofuran
TEM	Transmission electron microscopy
3D	Tri-dimensional
Trp	Tryptophan
2D	Two-dimensional
Tyr	Tyrosine
UHV	Ultra high vacuum

UV-vis	Ultraviolet-visible
UCST	Upper critical solution temperature
VACNTs	vertically aligned CNTs
VMD	Visual molecular dynamics
VPTT	Volume phase transition temperature
WAXRD	Wide Angle X-ray Diffraction
XPS	X-ray Photoelectron Spectroscopy

Nomenclatures

M_{∞}	Final amount of molecule released after an infinite time
M_t	Cumulative amount of drug released at time t
D	Drug diffusion coefficient
L	Thickness of the drug-releasing implant
pK_a	Acid dissociation constant,
$\Delta\omega$	Raman shift (in cm^{-1}), is the, and
λ_0	Excitation wavelength
λ_1	Raman spectrum wavelength
P/P_0	Relative pressure (-)
d_{002}	Interlayer spacing of (002) face (nm)
λ	Wavelength (nm)
E_b	Electron binding energy
d_{hkl}	Interplanar spacing of planes (between the layers of atoms)
θ	Bragg angle between the incident x-ray beam and the surface of crystal
A	Measured absorbance

I_{in}	Intensity of the incident radiation
I_{out}	Transmitted intensity
L	Path length of light travels through the cuvette
ϵ	Molar extinction coefficient
c	Sample concentration
$W_{initial\ DOX}$	Weight of DOX initially added
$W_{final\ DOX}$	Weight of DOX left in the cuvette after 24 hrs
$W_{hydrogel}$	Weight of rGOH and rGOPH samples
Y_i	Predicted response (dependent variable)
X_i	Independent variables
X_iX_j	Variables interactions
β_0	Constant coefficient
β_i	Coefficients for the linear effects
β_{ii}	Coefficients for the quadratic effects
β_{ij}	Coefficients for the interaction effects
ϵ	Standard error

k	Number of independent variables
$p(F)$	Probability of Fisher's F-test
k_1	Lagergren rate constant of adsorption (min^{-1})
q_e	Ultimate adsorption capacity
q_t	Adsorption capacity at time t
k_2	Pseudo second-order rate constant of adsorption ($\text{g mg}^{-1} \text{min}$)
k_{ipd}	Rate constants of intra-particle diffusion ($\text{mg g}^{-1} \text{min}^{-0.5}$)

Table of contents

Declaration	i
Abstract	ii
Achievements	iv
Acknowledgements	v
List of Figures	vii
List of Tables	xiii
Abbreviations	xiv
Nomenclatures	xx
Chapter 1: Introduction	1
1.1 Introduction	1
1.2 Aim and Objectives of thesis:	4
1.3 Organization of thesis:.....	5
Chapter 2: Literature Review	7
2.1 Brief overview of graphene, GO and rGO	7
2.1.1 Graphene synthesis methods.....	8
2.1.1.1 Growth on Substrate.....	8
2.1.1.2 Exfoliation method.....	10
2.1.2 Properties and applications of graphene	15
2.2 Graphene toxicity and biocompatibility	18
2.2.1 Bacterial Toxicity	19
2.2.2 In Vitro Cell Toxicity	20
2.2.3 In Vivo Toxicity.....	25
2.3 Controlled release in drug delivery technology.....	27
2.3.1 Overview of drug delivery options and why controlled release is desirable?	27
2.3.1.1 Drug loading into hydrogels.....	29
2.3.1.2 Drug delivery mechanisms for hydrogel formulations	30
2.3.2 Overview of drug delivery technology for DOX.....	36
2.3.3 pH responsive graphene-based materials in drug delivery	37
2.4 Graphene based materials with controlled structure.....	39
2.4.1 LBL assembly of graphene hydrogels without spacer	40

2.4.1.1 Hydrothermal method.....	41
2.4.1.2 Vacuum filtration method.....	43
2.4.1.3 Spin-coating method.....	44
2.4.2 LBL assembly of graphene hydrogels with spacer	45
2.4.2.1 Carbon materials as spacer	45
2.4.2.2 Polymers as spacer.....	49
2.4.2.3 Organic molecules as spacer.....	51
2.4.2.4 Metal ions/oxides/nanoparticles as spacer.....	55
2.4.2.5 Biomolecules as spacer.....	59
2.5 Experimental of protein/peptide adsorption on graphitic surfaces	63
2.6 Molecular modelling of protein/peptide adsorption on graphitic surfaces	66
2.6.1 The use of MD in peptide/graphene interactions	66
2.6.2 Simulation	69
2.6.2.1 Potentials and molecular simulation methods	69
2.6.2.2 Empirical Force field	70
Chapter 3: Methodology.....	72
3.1 MD simulations.....	72
3.2 Experiments	72
3.2.1 Material and Chemicals.....	72
3.2.2 Preparation.....	73
3.2.2.1 Preparation of graphene oxide (GO).....	73
3.2.2.2 Preparation of reduced graphene oxide (rGO).....	74
3.2.2.3 Preparation of reduced graphene oxide hydrogel (rGOH) thick films	74
3.2.2.4 Preparation of peptide solution.....	75
3.2.2.5 Preparation of rGO binding peptide hydrogel (rGOPH) thick film.....	75
3.2.2.6 Freeze drying	75
3.2.3 Instrumentation.....	75
3.2.3.1 Zeta Potentials	75
3.2.3.2 Contact Angle	76
3.2.3.3 Raman Spectroscopy	76
3.2.3.4 Scanning Electron Microscopy (SEM).....	77
3.2.3.5 Transmission Electron Microscopy (TEM)	77

3.2.3.6 Fourier Transform Infrared Spectroscopy (FTIR)	77
3.2.3.7 X-ray Photoelectron Spectroscopy (XPS).....	78
3.2.3.8 Wide Angle X-ray Diffraction (WAXRD)	78
3.2.3.9 Ultraviolet-visible (UV-vis) Spectroscopy	79
3.2.3.10 Atomic Force Microscopy (AFM)	80
Chapter 4: Molecular Dynamics and Experimental Study of the Adsorption of a Designed Peptide on Graphene	81
4.1 Introduction	82
4.2 Methods	83
4.2.1 Molecular Modelling	83
4.2.2 Microscopy	85
4.2.2.1 Materials.....	85
4.2.2.2 Transmission Electron Microscopy (TEM)	85
4.2.2.3 Atomic Force Microscopy (AFM)	85
4.3 Results and Discussions	86
4.3.1 Peptide structure in the solution phase	86
4.3.2 Adsorbed peptide structure	86
4.3.2.1 Modelling	86
4.3.2.2 Experiment	92
4.3.3 Adsorption Mechanism.....	93
4.3.3.1 Exemplar trajectory	93
4.3.3.2 Statistical analysis of ensemble of simulations	99
4.4 Conclusions	103
Chapter 5: Peptide-mediated Self-assembly of Graphene and Related Materials to form Nanoporous Hydrogel with Tuneable Pore Size	111
5.1 Introduction	111
5.2 Results and discussions	113
5.2.1 Peptide design	113
5.2.2 Hydrogel synthesis.....	115
5.2.3 Hydrogel characterisation	116
5.2.4 Dry-state characterization of porosity (nitrogen adsorption).....	118
5.2.5 Demonstration of size-exclusion and kinetic separation	120

5.3 Conclusions.....	121
5.4 Methods.....	122
5.4.1 MD simulation.....	122
5.4.1.1 Preparation of rGOH thick films	122
5.4.1.2 Preparation of peptide solution.....	123
5.4.1.3 Preparation of rGOPH thick film.....	123
5.4.2 Characterizations	123
5.4.2.1 Hydrogel pore size confirmation in the dry-state via nitrogen adsorption .	124
5.4.2.2 Hydrogel pore size confirmation in the wet-state via real time UV-vis	124
Chapter 6: Peptide Mediated Self-Assembly of Graphene based Hydrogels:	
Preparation, Optimization and Drug Delivery Application	142
6.1 Introduction.....	142
6.2 Experimental Details.....	145
6.2.1 Materials.....	145
6.2.2 Methods.....	145
6.2.3 Characterization.....	146
6.2.3.1 GO and rGO surface charge measurements.....	146
6.2.3.2 Contact angle measurements	146
6.2.3.3 Fourier transform infrared (FTIR) spectroscopy analyses.....	146
6.2.3.4 Atomic force microscopy (AFM) investigations.....	146
6.2.3.5 X-ray photoelectron spectroscopy (XPS) analyses.....	146
6.2.4 Loading of DOX in hydrogels.....	147
6.2.5 Statistical analyses on the effecting parameters for DOX loading.....	148
6.2.6 MD simulations	151
6.3 Results and discussion	151
6.3.1 DOX loading capacities under different pH values.....	151
6.3.2 Model equation development and DOE statistical analysis	153
6.3.2.1 Effect of the temperature and Hydrazine amount on DOX loading capacity	
.....	156
6.3.2.2 Effect of reduction degree and peptide concentration on DOX loading	
capacity.....	162
6.3.3 Pore size effects on DOX loading capacity; MD simulation perspective	167

6.3.4 Kinetics of adsorption.....	170
6.4 Conclusions	175
Chapter 7: A Peptide Mediated Self-Assembled Graphene Hydrogels: Controlled Drug Release and Cytotoxicity Tests.....	188
7.1 Introduction	188
7.2 Experimental Details	191
7.2.1 Materials	191
7.2.2 Methods	191
7.2.2.1 Release of DOX from rGOPH hydrogels.....	191
7.2.2.2 Cell culture	192
7.2.2.3 Cytotoxicity: Analysis of cell viability	193
7.2.2.4 Biocompatibility studies of rGOPH.....	193
7.3 Results and discussion.....	194
7.3.1 DOX release.....	194
7.3.2 Effects of hydrogels weight on cell viability	196
7.3.3 Effects of DOX and GO/DOX on cell viability.....	197
7.3.4 Biocompatibility studies	198
7.4 Conclusions	199
Chapter 8: Conclusions	201
References.....	205
Appendix A:Patent Specification (PCT/AU2015/000034)	233
Appendix B: Patent Figures	274

Chapter 1: Introduction

1.1 Introduction

Hydrogels are highly cross-linked materials possessing a tri-dimensional (3D) and flexible structure with hydrophilic and polymeric networks able to hydrate and swell when they are immersed in aqueous solutions [1]. In fact, each individual building block of hydrogel might be soluble in aqueous, but their chemical or physical cross-linking avoids their solubilization. However, water and biological fluids can penetrate through the hydrogel networks without breaking the strong interactions of polymeric binding structure. Due to their peculiar features and changes in properties in response to external stimuli (e.g. solvents, temperature, pH, ionic force, etc.) hydrogels have become the focus of considerable research interest in pharmaceutical and biological fields. Some examples of hydrogel usage are contact lenses, membranes for biosensors, reconstruction of cartilages, artificial tendons, skin, and organs, gene and drug delivery systems [2-9]. A detailed state of the art on hydrogels, and in particular graphene based hydrogel is presented in Chapter 2 of this thesis. Hydrogels in pharmaceutical applications can be categorized as stable and degradable ones, with the latter having hydrolytically or enzymatically labile bonding structure. For drug delivery purposes in particular, breaking these bonds will add more complexity to the system for which complicated mathematical modeling is required to interpret the delivery mechanism of the drugs. Thus, hydrogels with stable structures are the focus of this study.

It is widely known that the traditional hydrogels have been extensively used in biomedical fields due to their excellent properties. These include biocompatibility, rubber elasticity, equilibrium swelling, network structure characteristics and environmental sensitivity. However, traditional hydrogels and aerogels have drawbacks, such as poor mechanical properties and limited functional properties. Graphene as a planar monolayer of sp^2 hybridized carbon atoms, arranged into a two-dimensional (2D) honeycomb lattice, has attracted immense research interest to improve traditional hydrogels (reference for graphene hydrogels) due to its outstanding thermal conductivity and mechanical stiffness ($\sim 3,000 \text{ W m}^{-1} \text{ K}^{-1}$ and 1,060 GPa, respectively) [10, 11]. In addition to the stability, the

surface area and porous structure of the hydrogels [12-14] play key roles in different applications. Three-dimensional (3D) graphene macrostructures, such as hydrogels [15-18] and aerogels,[17, 19-21] not only possess the large accessible surface areas from the graphene nanosheets, but also have highly porous structures with pore sizes ranging from nanometers to several micrometers, which makes them suitable candidates for drug delivery to tissue engineering applications.

Three dimensional graphene macrostructures can also be materialized in composite hydrogels which are stimuli-responsive for example in pH sensitive, electro-responsive, thermo-sensitive hydrogels. Since Bai et al. [22] reported a pH-sensitive GO/poly(vinyl alcohol) (PVA) composite hydrogel prepared by a direct mixing method for drug delivery, some other graphene-based hydrogel materials began to emerge, such as electro-responsive graphene/poly (methacrylic acid) (PMAA) composite hydrogels [13] and temperature-sensitive GO/Poly(N-isopropylacrylamide) (PNIPAAm) nanocomposite hydrogels that all use graphene derivatives and copolymer cross-linkers. However, graphene hydrogels can be formed using solely graphene or GO dispersions, but nanosheets are particularly prone to self-assemble and aggregate. They restack due to strong π - π stacking interactions between graphene sheet and hydrogen bonding between oxygen functionalities, consequently, deducing its accessible surface area to uptake biomolecules such as drug molecules.

In order to solve this problem, layer by layer (LBL) assembly of graphene and graphene oxide (GO) sheets “with” and “without” the presence of spacer has attracted considerable attention from researchers [23], aiming to create out-of-plane pores (or inter-sheet distance) which result in the enhancement of their adsorption characteristics. The advantage of graphene LBL assembly is a high level of control over layering and the thickness of the obtained construct which arises due to the linear growth of the films with the number of bilayers [24] The out-of-plane pores will benefit different applications and devices, for instance, proposed for water treatment where the pore size and water flow rate matter [25], in gas and energy storages where the accessibility to the active surface areas is the key issue [26, 27] and in drug delivery where the poor solubility of the drug, yield of drug uptake as well as the release rate are the main concerns [28, 29].

In the field of fabricating porous media, it is extremely important to construct them with an ordered microstructure and uniform pore size, [14, 30, 31] particularly for the drug delivery application, as the uniform spatial structure and pore distribution will ensure that the drugs are homogeneously loaded and distributed. Similar to other porous media, tuning the pore size in graphene based hydrogels is vital in the sense that the loading and release of the drug may be conducted in a more controllable, reproducible and predictable manner.

The graphene based hydrogel fabricated without presence of inter-sheet spacers exhibited the inter-sheet distances varying from 0.39 nm for rGO [32, 33] to ~1.2 nm for GO [34]. This range is not suitable for taking up biomolecules as their sizes are about the same size or larger than inter-sheet distance. Therefore, the attentions of researchers went toward using spacers. Different types of spacers including carbon materials, (such as carbon black [35, 36], CMK [37] and CNTs [38, 39]), metallic particles (iron oxide nanorods [40], ruthenium dioxide nanoparticles [41], gold nanoparticles [42-44] and tin oxide nanoparticles [45]), polymers (such as polyaniline (PANI) [36] and polypyrrole (PPy) [46]) and biomolecules (such as DNA [47], Amino Acids [48] and peptides [49]) were used between graphene sheets, to effectively prevent the self-restacking of the graphene sheets and to increase the size of out of plane pore. None of the above approaches had a satisfactory degree of control over the pore size anything beyond 1 nm and well into the mesopore size range as defined by IUPAC. Such a control of pore size remained as main gap in the field of fabricating graphene based hydrogel.

In addition, many of the mentioned approaches involve layer-by-layer manufacturing where the macroscopic material is built up by putting down on a substrate successive layer of graphene or graphene-related material and spacer in an alternating fashion. This process leads to only a small fraction of the graphene or graphene-related material being separated by the spacers, with the remainder being essentially multi-layer graphene or graphene-related material or even more disordered than this. It also has the disadvantage that it is a cyclic process requiring significantly more than one cycle to be undertaken to achieve the final product.

In this study, one step self-assembly of graphene hydrogel using peptide as spacer was proposed. Amongst mentioned spacers, peptides are of particular interest, due to high

biocompatibility and degree of control over their sizes and interactions with graphene sheets through adjustment in their amino acid sequences. Thus, the formation of graphene hydrogels with uniform and desirable pore sizes (h) was expected via a simple peptide-mediated self-assembly of graphene sheets as schematically shown in Figure 1-1. Only a small fraction of the prior art involves a self-assembly process in the manufacture and, even then, they do not lead to structures akin to those proposed here in any way, nor provide the degree of control over the pore size proposed here.

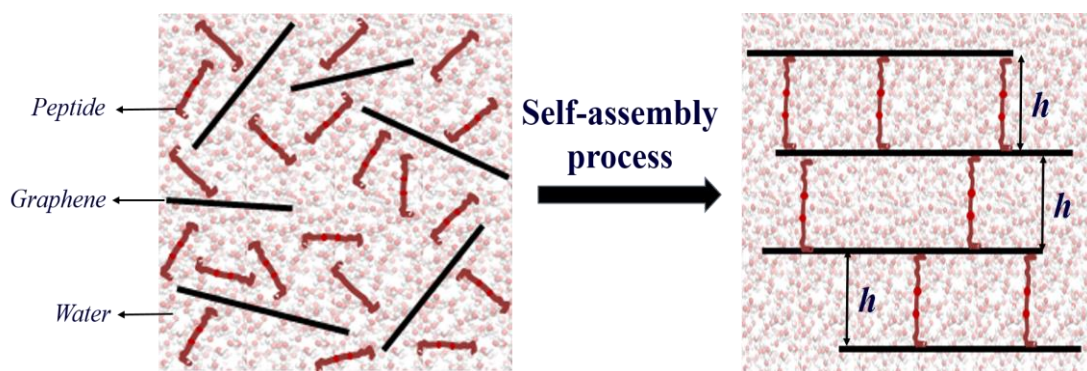


Figure 1-1. Self-assembly of graphene hydrogel construct with tuneable pore size (h)

1.2 Aim and Objectives of thesis:

The main aim of this thesis was two-fold: Develop a graphene based layered hydrogel material with tuneable pore sizes in the nm-range, and demonstrate its application for controlled drug delivery systems (DDS). This aim was achieved by meeting the following objectives:

- (1) Using molecular dynamics (MD) simulation to design a peptide that induces the self-assembly of graphene for forming nanoporous graphene hydrogel constructs.
- (2) Experimental implementation of the peptides designed in Obj. 1 and validation the self-assembled graphene nano-constructs.
- (3) Assessing the self-assembled nanoporous graphene hydrogel in the controlled drug delivery application.

1.3 Organization of thesis:

The thesis is divided into seven chapters covering the major objective of the present work; that is, to develop a design approach suitable for the peptide-mediated self-assembly of layered graphene hydrogels and their application for drug delivery systems. However, before the synthesis and applying these hydrogel materials for the drug delivery purpose, it is prudent to understand the graphene binding peptide self-assembly mechanisms, the process of hydrogel preparation as well the different mechanisms of controlled DDS.

In Chapter 2, we review and explain various types of available DDS and their mechanism for particular use of hydrogels. We also review recent contributions made to find suitable spacers, and how they might help with the self-assembly of the graphene sheets preparation of layered graphene hydrogel constructs. Later, the potential drugs that could be effectively loaded and delivered using such hydrogel materials are reviewed.

Chapter 3, summarizes the general strategies utilized in the whole PhD project, including MD simulation, materials, synthetic methods for graphene based hydrogels, their applications and the techniques for material characterizations and biological evaluations. However the detailed experimental procedures for different characterizations and applications of prepared hydrogels will be explained in their relevant chapters.

Chapter 4 describes a novel systematic design approach based on the nature of the peptide and graphene sheets in order to realize the feasibility of peptide binding to the single graphene surface through both simulations and experiments. The spatial structuring of interfacial solvent as a key determinant in peptide adsorption mechanism, peptide structure on the graphene surface and the stability of the system are also discussed here through statistical analysis of the extensive simulation results.

Chapter 5 discusses the results of MD simulations for the peptide mediated self-assembled graphene to form a nanoporous hydrogel construct of tuneable pore size (interlayer spacing). In this chapter, the designed systems are experimentally implemented in order to synthesis the layered graphene hydrogels. The hydrogels underwent the

validation process to determine whether the desirable pore size is achieved. The hydrogel structural stability both in the wet- and dry-states are also widely discussed.

Chapter 6 deals with drug (DOX) loading on the prepared hydrogel materials with the focus on the effective parameters on pore size and the yield of drug uptake. Design of experiments (DOE) is employed as a systematic method to statistically analyze the data, and determine the relationship between the effective parameters and their optimizations in order to reduce costs, and more importantly the time of conducting experiments. In addition, the influences of the hydrogel pore size on drug adsorption mechanism are studied from both simulation and experiment perspectives.

In Chapter 7, the drug releases of the drug loaded hydrogel (from chapter 6) in three environments of acidic, basic and neutral are discussed. This is to elucidate whether the hydrogel material are pH sensitive for the release of the loaded drug, and also to find out whether it is suitable for cancer therapy. The cytotoxicity tests on the hydrogels with and without loading of the drug are conducted to measure the cell viability after their treatment with the prepared graphene hydrogels.

Chapter 8 summarizes the general conclusions of the present work and the potential of the graphene layered hydrogel materials for future research.

Chapter 2: Literature Review

2.1 Brief overview of graphene, GO and rGO

Graphene, a single-layer carbon sheet with a two-dimensional (2D) hexagonal packed lattice structure of carbon atoms has remarkable electronic, mechanical, thermal and optical properties. It has many unique properties, including high carrier mobility at room temperature ($\sim 10,000 \text{ cm}^2 \text{ V}^{-1} \text{ S}^{-1}$) [50], large specific surface area ($2630 \text{ m}^2 \text{ g}^{-1}$) [51], good optical transparency ($\sim 97.7\%$) in the UV-Visible range [52], high Young's modulus ($\sim 1 \text{ TPa}$) [53] and excellent conductivity ($3000\text{--}5000 \text{ Wm}^{-1} \text{ K}^{-1}$) [54]. Single layer of graphene sheet can be obtained by ripping off graphite flakes. The single sheet of graphene is flexible, and hence, can be “wrapped up into fullerene and rolled into nanotube or even stacked and back to original graphite” (as is shown in) [55].

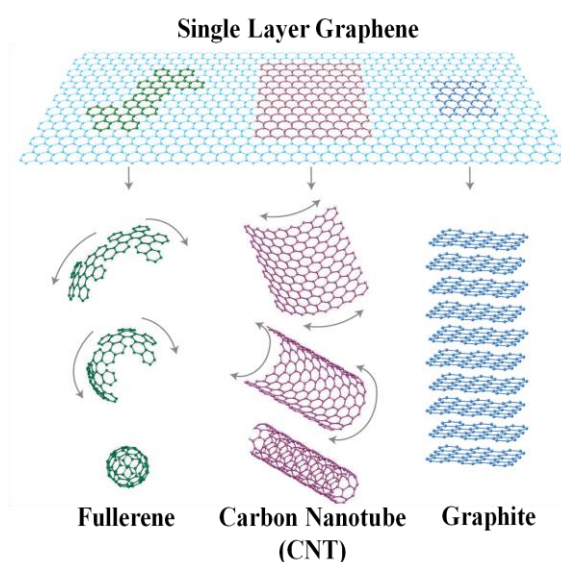


Figure 2-1. Single layer graphene presented as a material from which other structures such as fullerenes, carbon nanotube (CNT) and graphite can be built.[55]

Real life applications of this outstanding material have been retarded due to the need of developing challenging and costly processes to synthesize it purely and on a large scale. It is worth noting that depending on the applications, different amounts, sizes and qualities of graphene sheets need to be produced. Accordingly, there has been considerable effort directed towards synthesizing graphene with required properties.

2.1.1 Graphene synthesis methods

In general, graphene can be produced in two manners (schematically shown in Figure 2-2): (1) growth on substrate; growing a single graphene layer directly on a substrate surface, and (2) exfoliation; detaching graphene from an already existing graphite crystal. The former, due to high level of control in size and geometry of produced graphene, has received attention for limited applications, whereas the latter, because of producing a large amount of graphene with reasonable quality, has recently received considerable research interest. Each of these methods is reviewed in details as follows;

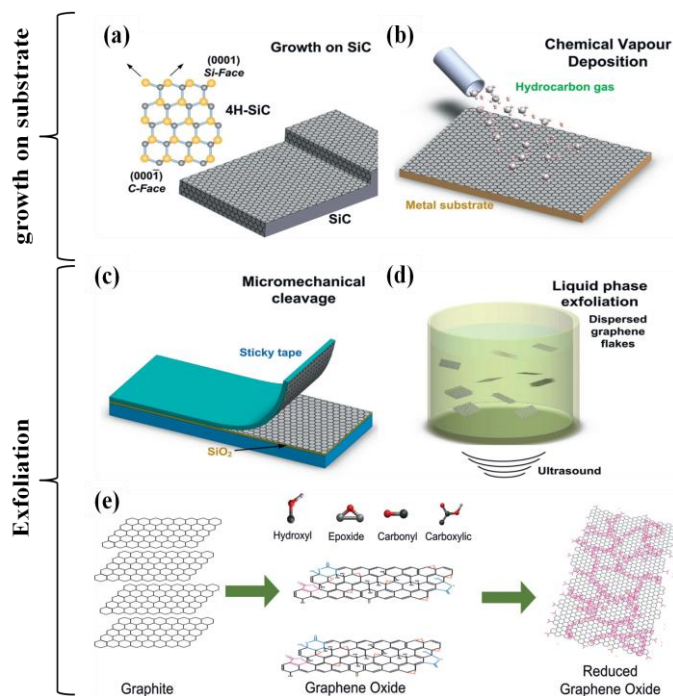


Figure 2-2. Schematic illustration of the main graphene production techniques including exfoliation and growth on substrate. [56]

2.1.1.1 Growth on Substrate

Epitaxial Method

As early as 1975, van Bommel et al. [57] discovered that carbon layers ordered into a graphene structure by heating a silicon carbide (SiC) at ultra-high vacuum condition. This vaporized the silicon face and left behind a carbon-rich surface as a source for graphene production (shown in Figure 2-2a). Generally, a single-, bi-layer, or few-layer graphene can be formed on the SiC crystal simply by heating and cooling down the substrate. This

idea has been welcomed in the last decade by researchers, who reported a noncatalytic and catalytic production of graphene sheets on SiC [58, 59] and NiC [60, 61] substrates. In both systems the carbon face of the substrate acted as the solid carbon source for graphene production. In the instance of NiC, Weatherup et al. [61] found that the thick layer of Ni(111) substrates not only act as a catalyst, but also played the role of diffusion barrier which further widened the window of synthesis to result in a more stabilized monolayer of graphene. However, in the instance of SiC, sputtering carbon films on the Si- and C-faces formed a diffusion barrier suppressing the growth of CNT and mainly forming the stable graphene sheets. Besides the role of diffusion barrier, it is also worth noting that the epitaxial method is highly dependent on the parameter control, such as temperature, heating rate, or pressure. For instance, nanotube instead of graphene was synthesized when the reaction temperatures and pressure were set too high [59]. Thus, a sophisticated setup with high controllability is required to produce the desired graphene sheets.

Chemical vapor deposition (CVD) method

CVD is a popular and widely used process in which a substrate is exposed to gaseous compounds, particularly carbon precursors for production of graphene, CNT or fullerene. The type of carbon source is highly dictated by the availability, the desired amount and quality of the product, and more importantly, the cost effectiveness for specific application [56]. Depending on all these factors, different types of CVD process; for example thermal, plasma enhanced, cold wall, hot wall, reactive, and many others have been introduced. Thermal CVD on metal surfaces in the presence of carbonaceous precursor led to the formation of thin graphite film [62], and few layer [63] and single layer [64] graphenes (shown in Figure 2-2b). Since then, the CVD based production of graphene has consistently received interest, particularly for electronic and semiconductors applications. Li et al. [65] reported for the first time, the uniform large area of graphene ($\sim\text{cm}^2$) on copper foils using CVD technique. Although large size graphene sheet was attained, such a technique was self-limiting as the graphene growth ceased as two or three layers of graphene fully covered the metal surface [65, 66]. As the graphene size and shape matter when it comes to the use of this material in device applications, Kim and co-workers grew a large scale graphene (with various sizes and shapes of graphene film) by decomposing

methane as carbon source on an arbitrary substrate of Ni at the temperature about 1000 °C [67]. In this CVD process of using methane, the hydrogen evaporates, the carbon diffuses into the Ni followed by nucleation and then nuclei grow into large domain. Consequently, the graphene layer can grow on the surface right after cooling down to room temperature. Similar to epitaxial method, temperature, heating rate and experimental pressure are the key parameters in CVD to optimize the formation and quality of graphene. Although there are some controls on the size and the amount of graphene produced by epitaxial and CVD method, they both require a complex and costly setup and careful control of synthesis parameters in order to grow graphene of reasonable quality.

2.1.1.2 Exfoliation method

Exfoliation of graphene film from graphite flakes can be performed in dry or liquid phase. In the dry phase, the splitting of layered materials into atomically thin sheets of graphene occurs via mechanical, electrostatic, or electromagnetic forces, whereas in the liquid phase the graphite flakes are dispersed in liquid environments followed by exploiting ultrasound to extract individual graphene layers [56].

The “Scotch tape method”

One common technique in micromechanical exfoliation (or micromechanical cleavage) of graphene is known as the “Scotch tape method,” in which a piece of adhesive tape is used to peel multilayer graphene flakes off from a chunk of graphite. This was first demonstrated by Novoselov et al. [68], who achieved micrometer-sized graphene using a scotch tape, as shown in Figure 2-2c. In 1999 and before the discovery of scotch tape method, Lu et al. [69], reported a controlled method of cleaving graphite to achieve multiple or even single atomic layers of graphite plates simply by rubbing graphite surface against other flat surfaces. However, the product was mixture of sheets with different numbers of layers where it was difficult to search for individual single sheet among multilayers. Later, the scotch tape method helped with detaching transparent monolayer graphene from graphite. In this method, first the multilayer of graphene is peeled off from graphite crystal by the adhesive tape attached to SiO₂ or Si substrate [68, 70, 71]. The glue needs to be solved in solvent, for example by acetone, in order to detach the tape, then the

peeling of the multilayer with the tape is repeated until it becomes thinner and thinner and no thick flakes are visible on the substrate. Finally, the last peeling leads to graphene sheets where the sizes vary between nanometers to several micrometers for a graphene monolayer, depending on the preparation method of the used substrate. The graphene monolayer is visible on the SiO₂/Si substrate because it adds up sufficiently to impact on the optical path of reflected light. Nevertheless, it is possible to see graphene monolayer under a light microscope, due to interference color effects with respect to the one of an empty substrate (phase contrast) [68, 72].

The advantages of scotch tape method include the production of high quality graphene with almost no defects, and the low complexity of this technique. Nevertheless finding and separating the individual graphene sheets from the substrate surface at the end might be challenging. However, the major disadvantages of this technique are the difficulty in obtaining large amount of graphene by this method, and the lack of controllability of this method.

Graphite dispersion

Graphene can also be prepared from the dispersion of graphite crystals in liquid-phase (shown in Figure 2-2d). The easiest method to obtain large amount of graphene is to disperse graphite in an organic solvent with similar surface energy as graphite [73]. Ideal solvents are those that can minimize the interfacial tension between the liquid and graphene flakes [74]. If the interfacial tension between the immersed solid and liquid is high, there is poor dispersibility of the solids in liquid [74-76]. This has been demonstrated for the graphitic flakes in a liquid with a high interfacial tension and as a result the flakes due to high cohesion between them tend to adhere to each other. Solvents with surface tension (γ) of about ~ 40 mN/m, [77] are the "best" candidates for the dispersion of graphene and graphitic flakes since the interfacial tension between them and graphene is minimum. When the interfacial tension is minimized, the energy barrier to detach a graphene layer from the crystal is also reduced. In addition to solvent, other external forces like ultrasonication or voltage need to be applied, possibly for several hundred hours to help the formation of dispersion [78-81]. The dispersion then needs to be centrifuged in order to dispose the thicker un-dispersed flakes [82]. Similar to micromechanical

exfoliation, the quality of the obtained graphene flakes is high and does not need a complicated setup. This method allows preparing large amount of graphene, however, the size of graphene sheets obtained here is small, due to lack of control over the process.

Graphite oxide exfoliation followed by reduction

Liquid phase exfoliation of graphite is known as a versatile technique, exploited not only for the exfoliation of pristine graphite, but also for the exfoliation of graphite oxide and graphite intercalated compounds which have different structures and properties with respect to pure graphite [56]. Graphite oxide and graphene oxide (GO) do not differ from each other in chemical composition. Although they are only structurally different in terms of the number of stacked graphene layers [83], they can both be addressed as GO. The oxidation of graphite generates several functional groups such as epoxide, hydroxyl and carboxyl, which results in the graphene surface dispersing in water when followed by sonication or stirring.

The earliest examples of graphite oxide preparation were reported in the presence of nitric acid (HNO_3) [84] or sulphuric acid (H_2SO_4) [85]. Each of these was mixed with potassium chlorate (KClO_3). Because this approach was time consuming and produced explosive gas chlorine dioxide (ClO_2), researchers investigated a safer and quicker method with no explosive byproducts. In 1958, Hummers and Offeman [86] modified the oxidation process using a mixture of sodium nitrate (NaNO_3), sulphuric acid (H_2SO_4) and potassium permanganate (KMnO_4) which is widely known as “Hummers method”. Later, many researchers replaced the sodium nitrate with less corrosive phosphoric acid (H_3PO_4) as an “improved hummers method” in order to prepare improved GO with fewer defects in the basal plane as compared to the GO prepared by the original method [87-90]. In such aggressive chemical methods (all Hummers based methods), the sp^2 -bonding structure of graphene surface is partially disrupted and introduces oxygen containing groups. For instance, hydroxyl or epoxide groups on the basal plane [91-93] with carbonyl and carboxylic groups attached to the edges [93-96] of graphene sheets (shown in Figure 2-2e). These functional groups endow high negative charge and electrostatic repulsion to each individual graphene sheet, making them highly hydrophilic, and consequently inhibiting their recombination and aggregation in water [97, 98] or polar organic solvents [99-102],

such as acetone, methanol, ethanol, ethylene glycol, [103] propanol, dimethyl sulfoxide (DMSO), N,N-dimethylformamide (DMF), N-methyl-2-pyrrolidone (NMP), and tetrahydrofuran (THF) [102, 103]. The graphite oxidation method is almost similar to liquid based exfoliation of pristine graphite. The main difference is to use several chemicals to oxidize graphite, and the obtained graphite oxide possesses the layered structure with lighter color (brownish) than dark graphite due to partially loss of conjugation during oxidation where the hybridization of planar sp^2 carbon changes to tetrahedral sp^3 .

If the goal is to produce exfoliated graphene, the GO dispersion needs to be chemically [99, 104-108] or hydrothermally [15, 40, 109-112] reduced, resulting in a suspension of nanosheets which closely resemble to the structure of graphene [83, 113-115]. Nevertheless, eliminating all oxygen containing groups on GO is impossible. The graphene nanosheets produced chemically are generally called chemically-reduced graphene oxide [104, 105, 116], chemically-modified graphene [106, 107, 117] or chemically converted graphene (CCG) sheets [99, 108, 118]. This distinguishes them from the more pristine graphene layers isolated via micromechanical exfoliation [56, 119] techniques. One of the earliest reports of graphite oxide chemical reduction occurred in 1963 when Brauer, in his “Handbook of Preparative Inorganic Chemistry”, noted a number of reducing agents such as hydrazine, hydroxylamine, hydroiodic acid, iron(II) and tin(II) ions [120]. Numerous other methods of chemical reduction of graphite/graphene oxide involving different reducing agents with either ‘well-supported’ or ‘proposed’ mechanisms were extensively reviewed by Chua and Pumera [83]. The most widely used reducing agent, albeit toxic and dangerous, is hydrazine (N_2H_4) [98, 121], typically known to form hydrazone with carbonyl groups of GO. It is a powerful and efficient reducing agent that can inactivate free radicals and as a result can break down into nitrogen and water. The reaction is known as the Wolff–Kishner reduction and Figure 2-3 outlines four different proposed routes of epoxide reduction).

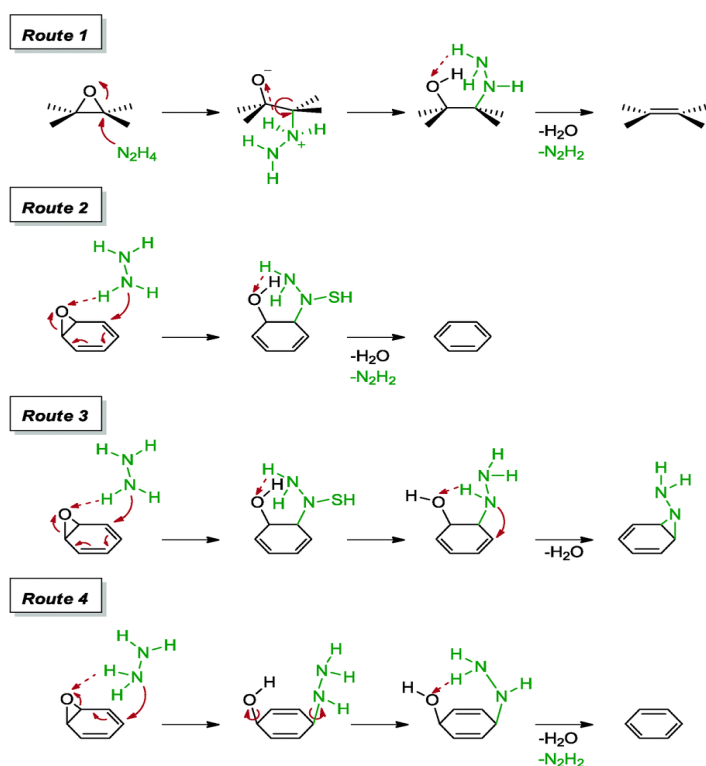


Figure 2-3. Proposed mechanisms for the reduction of epoxide groups with hydrazine via four different routes [83].

In order to avoid the generation of toxic chemicals and produce graphene sheets with less defects, hydrothermal reduction (hydrothermal dehydration) was proposed, which provides a simple, clean way to deoxygenate the GO [112]. In the hydrothermal method, a sub- or supercritical water is produced varying the pressure and temperature [122]. Due to behaving like a water-like fluid with strong electrolytic solvent power, high diffusion coefficient and dielectric constant, the supercritical water plays the role of reducing agent. A plausible mechanism for deoxygenation of GO under hydrothermal conditions was proposed where the hydrogen ion initiates the dehydration (where water acts as a source of H^+) by reducing of epoxide, hydroxyl and carboxyl groups, thereby promoting the recovery of π -network conjugations [112, 122, 123]. The experiment of hydrothermal treatment contains autoclaving GO dispersion under supercritical conditions and then cooling it down to room temperature. Usually, the hydrothermally treated GO possesses minimum level of defects and nearly perfect π -network conjugates. It aggregates quickly, and precipitates at the bottom of the autoclave container as a black powder. However, it can be re-dispersed in water via ultrasonification and adjustment of the pH to basic condition

(where most of functional groups exist in deprotonated states), although the dispersibility is not comparable to what is achieved in chemically reduced GO.

In addition to the chemical and hydrothermal reduction for GO dispersion, there is another popular reduction technique called “thermal reduction” which unlike the other two is in the dry-state. That is a high-temperature treatment ($\sim >1000\text{ }^{\circ}\text{C}$), resulting in so-called “annealing”, from the dry GO film which gradually pyrolyzes and eliminates the oxygen containing groups from the GO sheets, reducing them into the more conductive and temperature-stable graphene [91, 124-127].

All three methods mentioned above for reducing GO result in graphene of varying properties and performances in terms of electronic, structural, physical and surface morphological properties. Depending on the applications, one would choose more suitable method(s). Although the chemistry of graphene oxides reduced using different techniques is not unique, they are all generally known as reduced graphene oxides (rGO). Compared with the pristine graphene, the produced rGO is of very poor quality, because they contain structural defects and broken bonds, nevertheless GO could be the desired product.

2.1.2 Properties and applications of graphene

Physicochemical properties

The graphene with one atom thickness and a honeycomb lattice structure contains two equivalent sub-lattices joined together by σ bonds with aromatic ring carbon atoms having free π electrons contributing towards a delocalized electron network [128]. The free π electrons in planar structure endow graphene with participation in a number of reactions like click reactions, cyclo-additions and carbene insertion reactions, transformation from the sp^2 to the sp^3 arrangements. This leads to generation of topological defects (pentagon, heptagon, their combinations), vacancies, cracks, edges, and impurities [129]. The geometrically strained areas and zigzag edges of graphene exhibit better chemical reactivity compared to the unstrained areas or arm-chair edges because of the ease of electron displacement from upper plane of the aromatic ring. Therefore, geometric strains or defects are deliberately formed on graphene for the applications requiring high chemical reactivity [128, 129].

Pure and perfect graphene sheet is hydrophobic (poorly dispersible in water) in nature with the water contact angle in the range of 95–100°[130]. Hence, surfactants or other stabilizing agents are required to prevent their agglomeration to achieve better suspension in biological fluids. The oxidized form of graphene sheet (GO), on the other hand is hydrophilic with the water contact angle of about 30.7° [131] which can form hydrogen bonds with water molecules due to the polar oxygen functionalities [128]. Reduced form of GO which contains less of oxygen containing group with basal vacancy defects that occurred during oxygen removal endows the graphene sheet with amphiphilic properties and with less basal reactivity than GO [132, 133]. Physicochemical properties like unique planar 2D structure, high specific surface area and availability of free π electrons strengthen the physicochemical properties and hence, make it a promising candidate for its interaction with organic molecules, in particular drug molecules.

Thermal and electrical properties

Graphene sheet due to its unique conjugated structure and its strong carbon bonding exhibits an excellent thermal and electrical conductivity [128]. The single layer and defect-free graphene sheet possesses about ~ 4500 to 5200 W/mK of thermal conductivity significantly higher than that of GO sheet (~ 2000 W/mK). It also exhibits the electrical conductivity as high as 10^4 S/cm at room temperature which is yet larger than that of GO with the value of 10^{-1} S/cm [115]. The heat and electrons over the graphene sheet reduces when chemical modification and defects are introduced thereby reducing the conductivity [134-136]. Electronic devices [137] in particular biomedical devices can benefit from the exceptional thermal and electrical conductivity of the graphene sheet specially for measuring cell potential and as a substrate for conductive cell culture devices and biosensors [138-141].

Optical properties

To date immense interest was gained by graphene based materials for their excellent electric charge transport and optical properties. A graphene sheet exhibits light transmittance of about 97.7% of the total incident light over a wide range of wavelengths [52]. However with increasing the number of graphene layers the light absorption and the

optical image contrast will also increase [142]. The use of such properties in optoelectronic devices including tunable IR detectors, modulators and emitters by electrical gating and charge injection [143]. By cutting graphene sheets into nanoribbons and quantum dots, one can make luminescent material with a suitable band gap. Their connectivity of the π electron network can also be declined by physicochemical treatment using different gases [144-146]. Photoluminescence is another properties of graphene sheets which comprise of luminescence properties and electron-hole pairs [128]. Large photoluminescence, high light transmittance and high charge mobility of the graphene based materials made them a great candidate for biomedical imaging applications [147, 148].

Biological properties

Graphene based materials with their different physicochemical properties exhibit unique interactions with biomolecules, cells and tissues. It is also vital to understand the impacts of such graphene interactions from two different perspectives; their biomedical applications and their toxicity or biocompatibility [128]. Sanchez et al. [149] and Bianco [150] provided a comprehensive discussion on biological properties of graphene based nanomaterials and their toxicity. The biomolecule-graphene and cell-graphene interactions were briefly overviewed by Goenka's group [128]. Such unique interaction between graphene-based materials and biomolecules like DNA and RNA, can be utilized for DNA or RNA sensing and delivery. Hydrophilic GO exhibits preferential adsorption of single stranded (ss) DNA rather than double stranded (ds) DNA and hence, protects the adsorbed nucleotides from attacking by nuclease enzymes opening up a broad range of application [47, 151, 152]. At very low pH, the GO sheets can interact with the negative charges on DNA and further enhances the adsorption of small oligomers in high ionic strength solution [153].

In contrast to the graphene -DNA (or RNA) interactions, other larger biomolecules such as proteins and lipids lack of detailed information about their interactions with graphene base materials. Therefore, Titov et al. [154] used coarse grained MD simulations demonstrated the formation of stable and functional hybrid structures through graphene interacting with lipids. Although experimental data is necessary support the MD simulation

results. Such investigations will be crucial in order to understand the interactions of graphene with lipid bilayer on cell membrane.

Graphene similar to other carbon-based materials shown to be non-biodegradable leading to potential lung toxicity and environmental hazards [155, 156]. However, they are removable if their robust films are used in the forms of implants in body. Single wall carbon nanotubes (SWCNTs) show no biological degradation; however carboxylated SWCNTs can undergo degradation on exposure to hydrogen peroxide and horseradish peroxidase, or hypochlorite and the mammalian myeloperoxidase [157-159]. Following this data, the experiments conducted by Kotchey et al. [160] showed that the presence of oxygen containing groups on graphene sheets can participate oxidative attack using hydrogen peroxide and horseradish peroxidase leading to a susceptible to biodegradable. Such studies may lead to a potential design of graphene based materials for their safer biodegradable properties with minimum environmental and health hazards.

Most of the recent reports on the use of graphene based materials (either in the form of dispersion or film) have demonstrated the superior biocompatibility of these materials which provide a favourable environment for the effective proliferation of human and mammalian cells. Such outstanding characteristics seem to indicate that graphene based materials could be promising agents to be used in tissue engineering, tissue implants, wound therapy, gene and drug delivery applications. Nevertheless, it is worthwhile to underline that before using graphene based materials in such biomedical applications, understanding its cytotoxicity and biocompatibility is crucial.

2.2 Graphene toxicity and biocompatibility

The toxicity of graphene based materials has been a hot topic in research in the delivery of genes, pharmaceutical compounds, and in tissue engineering, as it concerns the potential short-and long-term health issue of patients. Since the history of serious research on graphene biomedical applications has not reached to even a decade, the general concern of the public is related to the use of such new nanomaterials and their nanotoxicology, and the verification of their acute and chronic toxicity.

There are three ways of introducing nanomaterials into the body; (1) inhaling into the lungs (biocompatibility test of graphene platelets in the mouse lung from biomedical/therapeutic point of view [161, 162]) (2) injection intravenously for drug or gene delivery [163, 164] or (3) using them as an implant for drug delivery and tissue engineering [165-167]. Sanchez and co-workers [149] reviewed research on the putative toxicity of graphene family. They reported that biological interactions of target cells can vary across the graphene family depending on layer number, lateral size, stiffness, hydrophobicity, surface functionalization, and dosage. However, the short- and long-term toxicities of graphene based materials are yet to be clearly defined and discussed. In contrast to other carbon nanomaterials such as activated carbon, carbon black and carbon nanotubes, there is inadequate information confirming the interactions of graphene based materials with different types of target cells and their potential toxicity.

2.2.1 Bacterial Toxicity

Since the highly purified CNTs confirmed its antibacterial activity after inactivating *E. coli*. [168, 169], a number of researchers have reported the effects of graphene based materials on bacterial toxicity, and their findings have opened up pathways for future applications in antimicrobial products. For instance, Akhavan and Ghaderi investigated the antibacterial activities of both GO and rGO against Gram-negative, *E. coli*, and Gram-positive, *S. aureus* bacteria. Both graphene based materials were shown to be effective agents for killing these bacteria, with rGO exhibiting the higher antibacterial effectiveness [170, 171]. Their results showed that GO can be reduced to rGO due to exposure to the bacteria and through the metabolic activity of the surviving bacteria via their glycolysis process. Similarly, Hu and co-workers [172] showed a reduction of *E. coli* cell metabolic activity to almost 70% and 13% in the presence of GO at the concentrations of 20 and 85 $\mu\text{g.mL}^{-1}$. However, only 10% of the bacteria survived when they used rGO with concentration of 85 $\mu\text{g.mL}^{-1}$. Such a significant difference in microbial cytotoxicity was attributed to different surface charges and oxygen containing groups on the surfaces of GO and rGO. The lesser the oxygen group, the lesser the metabolic activity and the greater the fatality of the bacteria. The authors confirmed these results using transmission electron microscopy, which revealed the loss of integrity and damage on bacterial cells membrane upon contacting with GO and rGO nanosheets. Nevertheless, the fundamental toxicity

mechanism and its relationship to structural properties of graphene based material remains to be elucidated.

Contrary to these findings, Wang et al. [173] found that the *Shewanella* family of bacteria containing iron in their chemical structures (in decaheme c-type cytochromes) are capable of metal reduction and to reduce GO in suspension cultures without any inhibition of bacterial growth in an aerobic condition. Salas et al. [174] also reported the rGO production by *Shewanella* cells as electron donor under strictly anaerobic conditions, where the GO sheets served as the sole electron acceptor. Such microbial reduction of GO provides a unique, environmentally friendly and nonhazardous approach for the synthesis of graphene sheets.

2.2.2 In Vitro Cell Toxicity

Several efforts to date have been devoted to explore the *in vitro* cytotoxic effects of graphene based materials [175-178]. The CVD prepared graphene layers used by Zhang and co-workers [178] induced a larger metabolic activity and lower cytotoxicity of neuronal PC12 cells than that of CNTs. This was due to an increase in the activation of caspase 3 (apoptosis marker; known as an effector for death signal), and hence, the release of lactate dehydrogenase, and consequently the generation of reactive oxygen species (ROS) in neural PC12 cells. The GO cytotoxicity effect against human fibroblast cells was demonstrated by Wang et al. [175]. They found dose- and time-dependency for the cytotoxicity; where GO at a concentration less than 20 $\mu\text{g.mL}^{-1}$ did not exhibit significant toxicity to human fibroblast cells, whereas the concentration above 50 $\mu\text{g.mL}^{-1}$ resulted in the largest fatalities. In this instance, excessive water-soluble GO can enter into the cytoplasm and nucleus, decreasing cell adhesion, inducing cell floating and apoptosis and consequently killing majority of the cells. Their transmission electron microscopy (TEM) images showed that as the culture time increased, the amount of GO inside human fibroblast cells increased accordingly. This was evident in the presence of many black dots (GO) scattered in the cell cytoplasm around cell nuclei and several located inside nucleus. When the dose of GO in the medium reached 100 $\mu\text{g.mL}^{-1}$, the cell could not survive for 24 hrs, however, the cells cultured with 5 $\mu\text{g.mL}^{-1}$ GO stayed alive and showed normal cell morphology for more than 100 hrs.

The cellular uptake and cytotoxicity of the GO dispersion against a mammalian lung cell line, A549 was evaluated by Hu and co-workers [172]. They also demonstrated that the cell metabolic activity with GO dispersion is concentration and time dependant. GO with a concentration of $20 \mu\text{g.mL}^{-1}$ was found to have low cytotoxicity to A549 within the first 2 hrs of incubation, but the cell viability decreased slightly (~20%) after incubation for 24 hrs. In addition, the higher concentration of GO ($85 \mu\text{g.mL}^{-1}$) led to a significant and unacceptable cytotoxicity (~50%) within 24 hrs of incubation. Later, Chang and co-workers [179] added the parameter of GO sheet size to the dosage dependency cytotoxicity of A549 cell line. They found that the large-GO ($780 \pm 410 \text{ nm}$) and medium-GO ($430 \pm 300 \text{ nm}$) resulted in no significant loss on the viability of A549 cells because they could not penetrate into the cell membrane. The highest GO concentration of $200 \mu\text{g.mL}^{-1}$ for large- and medium- size sheets exhibited more than 80% cell viability. However, small-GO sheets induced the viability loss more than large-GO and medium-GO with the cell viability of 67% at GO concentration of $200 \mu\text{g.mL}^{-1}$.

In contrast to the high antibacterial properties of rGO, Hu et al. [172] observed a remarkable cytotoxicity to the same cell line (A549) after treating them with by hydrazine reduced-GO (cytotoxicity of ~47% and ~15% with rGO dispersion of 20 and $85 \mu\text{g.mL}^{-1}$). Again, this could be attributed to the difference in surface charges and functional groups of GO and rGO [180, 181]. Unwanted $-\text{NH}_2$ functionalities on hydrazine treated rGO (see in Figure 2-3, route 3) probably initiates oxidative stress in cells that is followed by their aggregation and subsequent damage to the cells. Similar effects were seen from $-\text{NH}_2$ functionalities on fullerene when *S. oneidensis* MR-1 and *E. coli* W3110 were treated [180], however, this endowed great antibacterial properties to the functionalized fullerene. Another possibility was raised by Akhavan and Ghaderi [170], who attributed the higher toxicity of hydrazine-reduced GO compared with GO, to the sharp edges of graphene sheets after losing oxygen containing groups in the reduction process. They believed that the sharpened edges of rGO led to stronger interaction with cell membrane and consequently a better charge transfer between bacteria and the edge of rGO. In contrast, Liao and co-workers [182] found a lower hemolytic activity (cell membrane disruption) of red blood cells (skin fibroblasts) when they were treated with rGO than with dispersed GO sheets that possess higher surface oxygen content. The membrane disruption

of the red blood cells was attributed to the strong electrostatic interactions between negatively charged oxygen functional groups on GO surface and positively charged phosphatidylcholine lipids presented on the outer surface of membrane. In another report, Sasidharan et al. [183] examined the cytotoxicity effect of graphene sheets toward monkey renal cells before and after functionalizing the graphene surface with carboxyl groups. The pristine graphene, with its strong hydrophobic interaction with the cells membrane accumulated on the cell and deformed the membrane. This eventually resulted in high oxidative stress and led to apoptosis of the cells, whereas carboxyl modified hydrophilic graphene was welcomed and internalized the cells without causing any significant cytotoxicity.

Most of the cell fatalities reported in literature were due to induced cell apoptosis, hemolysis, and oxidative stress [179, 180, 182, 184]. One possibility for inducing the oxidative stress and toxicity is that graphene can adsorb the nutrients in culture medium, resulting in the depletion of nutrients for the cell growth. The solution to overcome this would be incubating graphene based materials in cell culture medium one night before treating cell with them, thus, they are saturated of the medium and therefore no further need to adsorb nutrients. The other factor which induces the oxidative stress is the strong interactions between the cell membrane and graphene based materials and/or charge transfer between them [170, 171, 185]. Hence, regardless of using GO or rGO, the graphene surface functionalities (charge groups) and the nature of cell membrane play an important role in controlling the interactions and minimizing the oxidative stress and mortality.

In order to find a solution for apoptosis and hemolysis, chemical modification of graphene surface with biocompatible groups was suggested. For instance, PEGylation [164, 186] and chitosan coating [182] of the GO sheets improved the biocompatibility of GO. As Liao and co-workers [182] reported, coupling of biocompatible polymers to the GO surface either serves as a protective layer, hampering the electrostatic interactions between the cell membrane and oxygen containing groups of the GO, or aggregates the graphene based particles to minimize the cell-contactable surface area and consequently minimize the level of toxicity. Another example is biocompatible PEGylation of the GO

surface with the which exhibited neglectable *in vitro* toxicity to many cell lines, including lymphoblastoid cells; Raji [187], colon cancer cell lines; HCT-116 [186] human ovarian carcinoma cell line; the OVCAR-3, a glioblastoma cell line; U87MG [188], MDA-MB-435 [189], mammalian lung cell line; A549 and breast cancer cells; MCF-7 [190], even at high concentrations. However, the chemical bonds coupling GO with modified polymer is a crucial issue that needs to be carefully considered as their breakage in *in vivo* systems can induce *in vivo* toxicity [191].

In comparison with the *in vitro* studies reviewed above for cytotoxicity of graphene based material in dispersion form, some results have shown such materials in the form of film, and paper or slabs can exhibit excellent biocompatibility with no viability inhibition of the treated cells. Agarwal and co-workers [192], examined the cytotoxicity effects of the rGO in the form of a film treating three types of cells, such as rat pheochromocytoma (PC12) cells, human oligodendroglia (HOG) cells, and human fetal osteoblast (hFOB) cells. In agreement to their observations of cell proliferations, they found biocompatibility of rGO being with all these cell types. Their comparative studies of rGO film and CNTs network revealed that topographic features in nanoscale (shown in Figure 2-4 a and b) results in a profound influence on cell functionalities (inhibitory effects such as; cell proliferation, viability, and neuritegenesis). Such influences of nanotopographic features on the cell functions have been extensively reported elsewhere [193, 194]. Agarwal and co-workers [192] believe that 10–20 nm bundles of CNTs may induce deformation of the thin cell membrane (5 nm thick) and hinder cell proliferation (shown in Figure 2-4 c and d) by inflicting negative impacts to the cell functions such as fluidity of the lipid membrane, mobility, and reorganization of membrane proteins. However, different cell types respond differently and show distinct sensitivities to the nanotopographic features of carbonaceous nanomaterials, however the underlying molecular mechanisms are yet to be discovered.

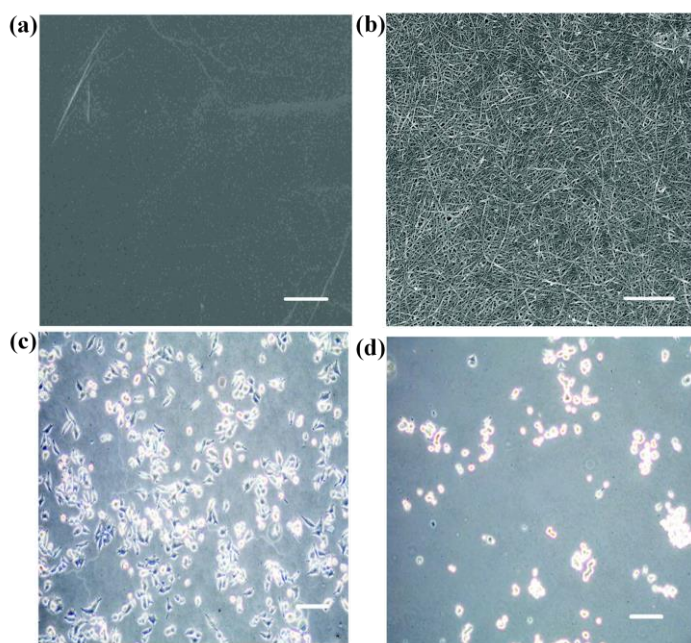


Figure 2-4. SEM images of (a) rGO film and (b) CNTs network (Scale bars = 1 μm). Phase-contrast images of PC12 cells grown on (c) rGO film and (d) CNTs network for 5 days (Scale bars = 100 μm) [192].

Later, in 2011, Ruiz et al. [195] investigated the role of GO film (10 μg of GO coated on the glass slide) on the mammalian colorectal adenocarcinoma HT-29 cells. They examined the cell functions of attachment and proliferation using optical microscopy for the glass substrates with and without GO coating (shown in Figure 2-5). Their results indicated that HT-29 cells were attached more efficiently to the GO films without damage to the cells morphology and without any enlargement. The GO film surface was demonstrated to be non-toxic and biocompatible to the HT-29 cells as it promoted the cell proliferation immediately after their attachment to GO up to 5 days. In contrast to previous reports on the antibacterial properties of the GO film, Ruiz and co-workers [195] found GO was a friendly material to the *E. coli* bacterial cells. Controversially, they believed that the residual contamination retained from the GO preparation might be responsible for some of bacteria mortalities which were observed in previous reports.

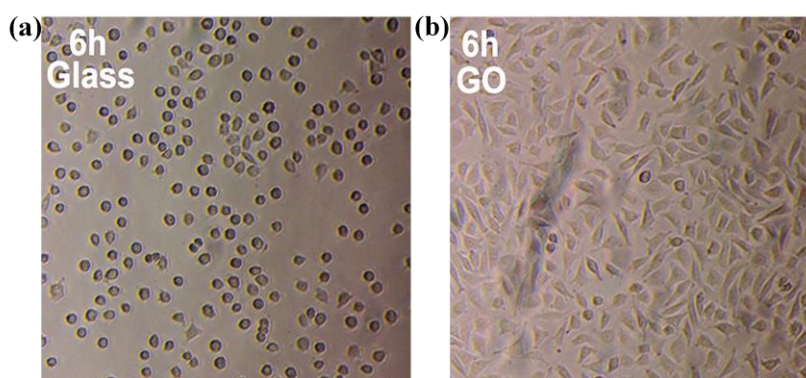


Figure 2-5. Micrographs showing human adenocarcinoma HT-29 cell attachment and growth on glass slides (a) without or (b) with GO film.[195].

2.2.3 *In Vivo* Toxicity

After confirming the high biocompatibility of graphene based materials toward the cultured cells (*in vitro*), several other groups continued investigating the potential *in vivo* toxicity of graphene in animals.

In two different studies, the as-prepared GO showed dosage dependent behaviours and a severe toxicity when it was overdosed. Zhang and co-workers [163] showed that as-prepared GO predominantly accumulated in lungs and had a long retention time after being intravenously injected into rats or mice. This induced dosage-dependent pulmonary toxicity and significant pathological changes, and toxicity was clear when it reached to a dose of 10 mg/kg body weight of the mice. Similarly, Wang et al. [175] injected GO dispersion intravenously with three different dosages of 0.1, 0.25, and 0.4 mg corresponding to mild, medium and high, doses respectively. GO nanosheets of mild (0.1 mg) and medium dosages (0.25 mg) did not exhibit obvious toxicity to mice, however, increasing the dosage to 0.4 mg resulted in severe chronic toxicity. The side effect was death of 4/9 mice, and there were pathological effects on the lung, liver, spleen, and kidney because they had the highest accumulation of GO. The possible mechanism of GO inducing these side effect in mice suggested by Zhang et al. [163] is as follows: when GO is intravenously injected into blood circulation system, it should be recognized and tracked by immune cells as a foreign body agent. With the exception of the brain, which has blood barrier, GO rapidly distributes into other organ like lung, liver, spleen, and kidney. GO nanosheets are captured and wrapped by immune cells as soon as they enter into lung, and this results in lung granuloma formation. Due to their flake-shapes, GO nanosheets cannot

be fully removed by liver, spleen, and kidney, and remain as long-term causes of inflammation. When the GO dose is low, there are not significant side effects and the organs maintain their normal function, but with a high dosage of GO, there is damage to homeostasis. This severely influences the function of these organs and results in organ failure and the fatality of mice.

Although the as prepared-GO nanosheets were used for biomedical applications such as cell imaging and drug delivery [187, 196, 197], because of its long-term side effects and toxicity to organs such as lung, liver and kidney, it is not a good candidate to be used in human body applications. However, further functionalization of the GO surface is likely to improve water dispersion. Moreover, better stability of GO will prevent its non-specific binding with proteins and decrease its electrostatic interactions with cell membrane [186]. These factors may increase its mobility and reduce the extent to which it remains in organs.

One of the earliest examples of exploring the *in vivo* behaviours, applications, and potential toxicology of modified graphene in animal models was reported by Yang et al. [198] who injected PEGylated graphene sheets for photothermal therapy of tumour using intravenous administration. This *in vivo* study did not show any obvious sign of toxicity or side effects in the treated mice at the dosage of 20 mg.kg^{-1} body weight within 40 days. Neither the injection of modified graphene nor the laser irradiation could cause in any side effects (such as body weight loss or death). After one year they studied the pharmacokinetics and biodistribution of graphene using ^{125}I radionuclide labelled PEGylated graphene sheets and also carried out more systemic toxicology examination of such modified graphene material in mice [199]. Their examination on blood biochemistry, hematological analysis, and cell histology analysis did not show any appreciable toxicity to the treated mice even over the period of 3 months. The biodistribution revealed that the presence of PEGylated graphene were minor in any organs of the mouse, except in the liver and spleen. In recent comparative studies, Yang's group also characterized the fate of PEGylated GO from two different ways of administration; oral feeding and intraperitoneal injection into healthy mice [200]. Their investigations showed no uptake of PEGylated GO nanosheets via oral administration, demonstrating limited intestinal absorption of the

nanosheets, with approximately complete excretion. In contrast, injection spread the PEGylated GO widely in mouse organs, with some accumulation in the liver and spleen.

Zhang et al. [201] functionalized GO with dextran to improve its stability, biocompatibility, pharmacokinetics, and thus biomedical functions of carbonaceous materials. Dextran exhibits a spherical shape and is fully degradable in living biological systems. The GO conjugated dextran with enhanced stability demonstrated an obvious excretion from mouse body after intravenous injection. This was without causing any noticeable toxicity to the treated mice over the course of a week.

Duch et al. [161] in agreement with other previous reports, found that oxygen containing functional groups of GO mainly contribute to the pulmonary cytotoxicity in mouse alveolar macrophages (MHS) and epithelial cells (MLE 12) after being injected directly into the lungs of six C57BL mice. The toxicity of GO raised by generating the reactive oxygen species, activating inflammatory and apoptotic pathways and led to severe lung injury. In order to minimize the oxidation process, they administered the solutions of unoxidized (pristine) graphene and Pluronic (copolymer) dispersed graphene. These two species due to lack of oxygen containing groups did not generate any obvious intracellular reactive oxygen and resulted in minimal histologic evidence of lung inflammation.

In summary, the in vivo cytotoxicity of graphene based materials depends on dosage, administration approach, and surface oxidation degree and polymer functionalization.

2.3 Controlled release in drug delivery technology

2.3.1 Overview of drug delivery options and why controlled release is desirable?

The term “drug delivery system (DDS)” refers to the technology utilized to present a pharmaceutical compound (drug) to the desired body sites to achieve therapeutic effect in humans or animals [202]. There are three major types of drug release; (1) conventional (traditional) release, (2) first order sustained release and (3) zero order controlled release. The conventional DDS has been denoted by immediate release and repeated dosing of drug, which might lead to the risk of dose fluctuation and side effects. The major drawbacks of the conventional DDS are poor patient compliance for frequent necessary

administration and the unavoidable fluctuation of drug concentration which may lead to under or over medication. In order to resolve these issues, the formulation of a release system that points towards the increased time of drug delivery at a slow and a near constant rate is required. This often translates into better patient compliance, and enhances clinical efficacy of the drug for its proposed use. The sustained and controlled release formulations could be the solutions to the above problem because they might both achieve immediate therapeutic response and maintaining desired drug concentrations. Although sustained and controlled release systems perform similar functions, the latter is more preferred for the following reasons;

(1).**Loading:** Drugs are coated with resinous plastic materials in sustained drug delivery [203] whereas in controlled drug delivery the drug is delivered through a semi-permeable membrane [204]. The hydration occurs in membrane core, therefore, there will be a stationary concentration gradient across the membrane and release will proceed at constant rate.

(2).**Release kinetics:** Both Sustained and controlled deliveries offer prolonged drug release, however, controlled release systems offer release at a specific controllable or predetermined rate. The kinetics in controlled drug delivery is zero order and the release take place at constant rate independent of initial drug concentration [205], whereas the sustained drug delivery tries to achieve zero order kinetics but follows first order kinetics [206].

(3).**Therapeutic effect:** Controlled drug delivery has the largest contribution to the therapeutic range, whereas the other methods meet either the toxic or minimum effective level (as shown in Figure 2-6). Note that it is desirable, after an initial period of time, that the released drug concentration is constant and between the toxic and the minimum effective level [202].

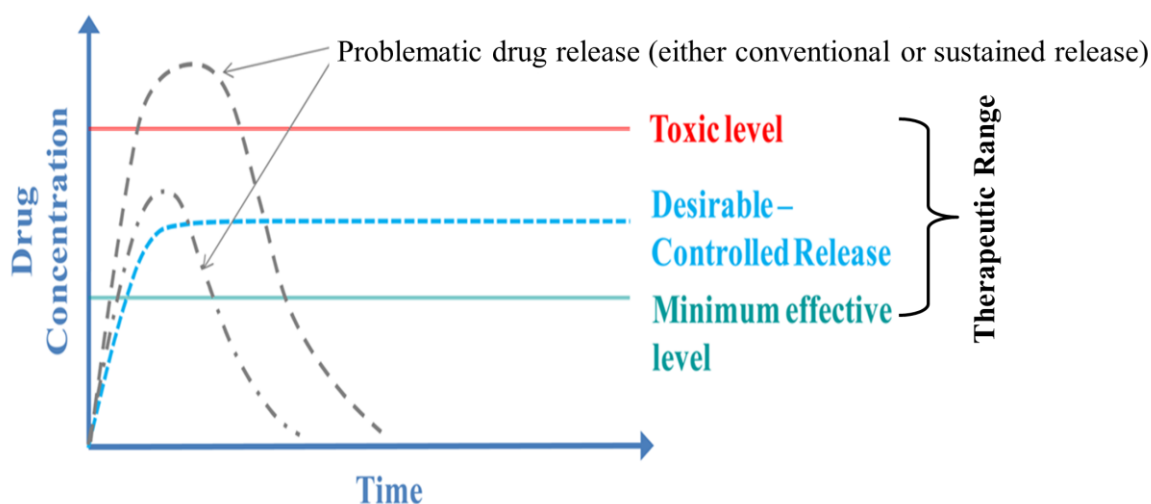


Figure 2-6. Released drug concentration over time (gathered from ref [202, 205, 207]). The lines that indicate the **toxic** and **minimum effective** levels of the drug are coloured **red** and **green** respectively. The **desirable-controlled drug release** is shown in **blue** solid line. Two cases of **problematic drug release** (either conventional or sustained release) indicate the drug release ending too soon or, occasionally, being below the minimum effective level or higher than the toxic level and these are shown in **grey** dash lines.

2.3.1.1 Drug loading into hydrogels

Depending on hydrogel preparation methods, drug can be incorporated into hydrogel matrices via the following ways [208, 209]: (1) **post-loading**. In this method, the hydrogel matrix is formed prior to the drug incorporation into the matrix. When an inert hydrogel system is used, the major force for taking up drug is diffusion, whereas in the instance of drug-binding hydrogels the drug/hydrogel interactions will be added to the diffusion as driving forces for both loading and releasing. (2) **in-situ loading**. In this case, a hydrogel precursor binds with drugs or drug-polymer conjugates through a mixing process. The hydrogel network construction and drug incorporation are accomplished simultaneously. In such an instance, the drug loading and release are dominated by diffusion, hydrogel swelling, reversible drug hydrogel interactions or the degradation of labile covalent bonds. In practice, the post-loading is preferred over the in-situ loading due to its simplicity of the operation, significant drug encapsulation, and more accurate traceability on drug loading and release dosage. Furthermore, the rates of drug loading/release and encapsulation efficiency can be easily modulated in post-loading [209], whereas modeling drug release from in-situ forming hydrogels is very challenging for several reasons [208]. Firstly, there are difficulties in quantifying the extent of drug/hydrogel interactions because they are

dependent on hydrogel and drug chemistries together with the method of hydrogel fabrication. Secondly, there is no control over the shape of in-situ formed hydrogels, which increases the model complexity. Thirdly, it contributes to non-uniform drug distribution within the hydrogels. This further increases the difficulties in accurately representing the real system in a mathematical construct and experimental measurements, and also involves excessive risk when it comes to clinical applications.

2.3.1.2 Drug delivery mechanisms for hydrogel formulations

The first step for the prediction of release profile from hydrogels, in particular the drug release, is to better understand the release mechanisms. The next step is to identify the key factors which govern the drug release from hydrogels.

2.3.1.2.1 Diffusion-controlled delivery systems

Diffusion is of the most vital mechanism employed to control the drug release from pharmaceutical devices and the resulting release kinetics depend on the size and shape of the drug carriers [210]. By adjusting the geometry and the structure of hydrogels, one can achieve the desired release profiles. For hydrogels, when the pore sizes are much larger than drug molecules, the diffusion coefficient can be directly related to the porosity and tortuosity of the hydrogels [211]. Typically the pore sizes of hydrogels are larger than most small-molecule drugs, hence, the diffusion of drug molecules are not significantly retarded in hydrogel matrices [208]. However, for the hydrogels with the pore sizes comparable to or smaller than the drug molecular size, drug diffusion coefficients are decreased because of the steric hindrance introduced by the hydrogel matrices [1, 208, 211]. In such systems, the average accessible pore volume per available drug molecule is decreased and the hydrodynamic drag experienced by the drug is increased, thereby deducing the permeability [212, 213]. As stated earlier, hydrogel networks usually possess high water permeability and water-soluble compounds can uniformly disperse but tend to diffuse out fast during releasing [214], which is not favorable for sustained drug delivery applications. To reach to an optimization between the pore size of hydrogel matrices and the drug molecules dimension for a desired delivery process, most research efforts have focused on

understanding diffusion-controlled release and diffusion coefficient of encapsulated drugs in relation with the geometry of 3D hydrogel matrices.

Several efforts have undertaken to empirically determine diffusion coefficients for diffusion-controlled drug delivery from hydrogels. The drug release ratio up to any time t (M_t) to the final amount of molecule release (M_∞) can be expressed by best fitting curves according to (2-1 below [208, 215, 216]:

$$\frac{M_t}{M_\infty} = 1 - \sum_{n=0}^{\infty} \frac{8}{(2n+1)^2 \pi^2} \cdot \exp\left[\frac{-(2n+1)^2 \pi^2 D}{L^2} t\right] \quad (2-1)$$

where M_t represents the cumulative amount of drug released at time t ; M_∞ cumulative drug amount after an infinite time; D the drug diffusion coefficient within the hydrogel network and L the thickness of the drug-releasing implant. Although this equation is used for several diffusion-controlled drug release systems, the model complexity will increase if hydrogel–drug interactions are involved, and when non-spherical drugs molecules are used. It is also noted that the equation above is only valid for slab (film) shape hydrogel, however, models for other geometries (e.g. spherical and cylindrical) have been extensively reviewed elsewhere [216].

2.3.1.2.2 Stimuli-sensitive swelling-controlled release systems

The swelling-controlled delivery is another mechanism for drug delivery in which the hydrogels may undergo a swelling-driven phase transition. The transition results in entrapped immobile drug molecules rapidly diffuse into medium. The swelling process takes place in three different steps: (a) diffusion of water molecules through hydrogel matrix, (b) relaxation of hydrogel via hydration, and (c) expansion of hydrogel network upon relaxation.

In such delivery systems, the rate of drug molecule release depends on the rate of hydrogel swelling. Environmentally-sensitive hydrogels are able to exhibit dramatic changes in their swelling behavior in response to the changes in external environments such as the pH, (ionic strength) or temperature [217]. Due to their outstanding swelling nature, hydrogel materials can be employed in broad variety of applications, such as

separation membranes, biosensors, artificial muscles, chemical valves and drug delivery devices [217].

pH-sensitive hydrogels

The hydrogels showing pH-dependent swelling behavior can be swollen using the ionic networks containing either acidic (anionic) or basic (cationic) groups [218-220]. The swelling occurs as a result of the electrostatic repulsion when functional groups are ionized in aqueous media of appropriate pH associated with hydrogel expansion, hence, the uptake of solvent into the hydrogel matrix increases [221, 222]. Ionic hydrogels containing anionic groups such as carboxylic acid exhibit sudden or gradual changes in their dynamic and equilibrium swelling behavior when the pH of the environment goes above the pKa of the ionizable species [218, 221, 222]. In contrast, cationic materials contain functional groups such as amines ionize in the media at a pH below the pKa of the ionizable groups [218, 221, 222]. Consequently, as the degree of ionization increases, the charge density increases, causing increased electrostatic repulsions between individual chains. Hence, the hydrogel becomes hydrophilic with a great swelling ratio.

In the case of graphene hydrogels, the same phenomenon applies when the presence of coion and counter-ion impacts on swelling and deswelling. For instance, Huang et al. [223] found that the presence of (Na⁺) counter-ion could induce a significant decline of electrostatic repulsion between the charge groups of -COO⁻ in poly(acrylic acid-co-acrylamide) bound GO hydrogel (GO/P(AA-co-AM)) and lead to a decrease of the osmotic pressure and swelling of hydrogel networks. Conversely, they observed a dramatic swelling capacity when they increased the pH value from 3 to 7, as a large number of COOH groups were ionized and converted into COO⁻. Consequently many hydrogen bonds were broken and the electrostatic repulsion of anionic groups results in the swelling of GO hydrogel networks. The effect of oxygen containing functional group on graphene sheets on swelling behavior was later investigated by Tai and co-workers [224]. They prepared polyacrylic acid [225] hydrogels with and without presence of GO and then compared the swelling curves of these two hydrogels. A higher swelling capability from the GO/PAA composite hydrogel than that of the PAA hydrogel (~1.4 times higher) was achieved. The increase of the swelling capability was attributed to both structure and

chemistry change of the hydrogel upon adding GO. The hydrogel turned into a fluffy structure and introduced several other oxygen containing groups after adding GO, thereby catching some additive water and resulting in the increase of the swelling ratio. Similarly, Jiang et al. [226] investigated the swelling behavior of a composite hydrogel prepared by cross-linking GO and PAA through whole pH ranges from 1 to 14. Their measurements indicated that regardless of GO concentration, the swelling gradually increased until pH 11, because most of the oxygen containing groups were ionized and generated the highest electrostatic repulsion that interrupted the hydrophobic interaction and hydrogen bonding inside the hydrogel. Further increase of pH by adding sodium hydroxide resulted in a sharp decrease of the swelling ratio because the reaction between GO and sodium hydroxide led to strong interaction between GO and then outflowing of water from the hydrogel networks [226]. They also realized that at any constant pH, increasing the GO concentration would decrease the swelling ratio of the hydrogel because the higher the concentration of GO the higher hydrophobic interaction occurs.

Temperature-sensitive hydrogels

Temperature sensitive/responsive hydrogels are the most studied class of stimuli sensitive hydrogel systems in the biological field, particularly in drug delivery research. This is because it is easy to change and to control the temperature of hydrogel surrounding fluids, hence, making it widely applicable for both *in vitro* and *in vivo* studies.

To be more specific, the temperature responsive hydrogels are materials that exhibit significant changes in volume and solvation state at certain temperature (volume phase transition temperature (VPTT)) which is accompanied by coil-to-globule shape transition of hydrogels. Altering the temperature across VPTT may result in contraction or expansion of the hydrogel structure as a consequence of the optimization of the hydrophobic and hydrophilic interaction between hydrogen and aqueous solution. Thus, such hydrogels can be categorized as positive or negative temperature-sensitive systems. The positive temperature-sensitive hydrogel has an upper critical solution temperature (UCST). These hydrogels deswell when the temperature goes below the UCST and swell at higher than given temperature. Conversely, the negative temperature-sensitive hydrogels possess a

lower critical solution temperature (LCST) meaning that they deswell upon heating above the LCST and swell upon cooling below the LCST [1].

Tanaka and co-workers as one of the pioneers in the field temperature-sensitive hydrogels introduced PNIPAAm as the best example of negative temperature-sensitive hydrogels [227, 228]. There are numbers of polymers in the thermo-sensitive hydrogel family possessing hydrophobic groups of methyl, ethyl and propyl, such as poly(N,N'-diethylacrylamide) (DEAM) [229-231], poly(N-acryloyl-N'-propylpiperazine) (PAcrNPP) [232, 233], and poly(methylvinylether) (PMVE) [234-236]. However, PNIPAAm due to the LCST of 32 °C close to body temperature received extensive attention for biological applications. After the introduction of PNIPAAm, Hitotsu et al. [228] conducted research on cross-linked PNIPAAm and found the LCST of their PNIPAAm gels is ~34.3 °C. They also found that the LCST could be increased through adjusting ionic interactions by adding small amounts of ionic copolymers into the hydrogels. A similar result was attained by Beltran and co-workers [237] by adding ionic comonomers into PNIPAAm hydrogels.

In order to enhance the stimuli responsive properties of PNIPAAm hydrogels, Ma et al. [238] introduced in-situ polymerization with GO to prepare a composite hydrogel material with enhanced swelling capability and mechanical properties. Combination of GO and PNIPAAm offers both electro- and thermo-sensitivity to the composite hydrogels. They achieved the equilibrium swelling ratio for GO/ PNIPAAm is almost two times larger than that of pristine PNIPAAm, and the final water retention of the composite hydrogels was also slightly higher than that of pure PNIPAAm hydrogel. Thermo-sensitivity of PNIPAAm in conjunction with hydrophilic groups on GO sheets cause more water molecules to hold in the composite hydrogels, thus leading to the increase of the equilibrium swelling ratio.

Peptides and polypeptides [239] due to their amphiphilicity (via charge interactions, hydrogen bonding, and hydrophobic interactions, π - π stacking), they can self-assemble to form thermo-sensitive hydrogel networks in the form of either nanofibril [240] or scaffold shapes [241, 242]. They possess excellent biocompatibility and structural controllability making them suitable candidates for therapeutic applications. Pollock et al. [243] revealed that introducing the hydrophilic moieties such as poly(ethylene glycol) (PEG), hydrophilic

polypeptide, and methacrylate into PNIPAAm bestowed thermogelling properties to the polymer aqueous solution. Elastin-like polypeptides or their copolymers with other thermo-sensitive polymers, like PNIPAAm, have been used *in vitro* and *in vivo* for cancer treatment. An example of thermo-sensitive polypeptide used for cancer therapy was reported by Dreher et al., [244], who conjugated a common anticancer drug doxorubicin (DOX), to polypeptide hydrogels (made by incorporation of Val, Ala and Gly residues with different ratios) resulting in a broader transition than the parent polypeptide above the LCST. Interestingly, both the polypeptide/DOX hydrogel and the free DOX exhibited near equivalent *in vitro* cytotoxicity because almost all the drug was released at the LCST, indicating outstanding thermal responsive properties of the hydrogel.

In summary, from the drug delivery perspective, the design and usage of polypeptide and PNIPAAm either as polymer or copolymer in hydrogels are vital because they should uptake drugs at the temperature below their LCST and release entrapped drugs in response to the LCST transition. This transition is thermodynamically reversible. The drug release occurs when hydration surrounding the hydrogel networks is mostly released upon reaching to LCST point through the hydrophobic collapse of the hydrogel, leading to hydrogel aggregation and separation from the aqueous phase. Although the LCST behavior of polypeptide and PNIPAAm hydrogels are thermodynamically similar, each hydrogel needs to be carefully considered due to its distinct advantages and disadvantages as a carrier for therapeutics.

Chemically-controlled delivery systems

In addition to diffusion and swelling, there is a third type drug release mechanism in DDS called, chemically-controlled delivery. The chemically-controlled system can be further classified into two systems of erodible and pendent chains [1]. In erodible systems, the drug release rate is controlled by degradation or dissolution of the polymer carrier and depends on whether diffusion or erosion is the rate-controlling step. When erosion of the hydrogel matrix is much slower than the diffusion of the drug through the hydrogel, then the drug release is diffusion controlled. The other possibility is that the drug remains incorporated in the hydrogel matrix due to the low rate of diffusion, and therefore, drug release is erosion-controlled. On the other hand, for pendent chain systems, there is a

different scenario in which the drug is attached to the hydrogel via a hydrolytically or enzymatically labile bond. In such a case the drug release is based on reaction-diffusion which is controlled by the rate of degradation of the bond [208].

2.3.2 Overview of drug delivery technology for DOX

The exploration of graphene derivatives based drug delivery derives from anticancer drugs to other drugs for non-cancer diseases treatment. Comparing to covalently bonded drugs, the physical binding of drugs onto graphene sheets would maximally preserve the biological activity, owing to the lack of chemical reactions between them [245]. Hence, the focus of most research was on choosing drug molecules which non-covalently incorporate with graphene (through either π - π stacking and/or hydrogen bonding).

Cancer treatment

Chemical drugs such DOX [28, 196, 197, 246-249] and camptothecin (CPT) [196, 245, 249-253] have a high density of π -electron clouds and more than two aromatic rings have been used broadly as anticancer agents. camptothecin (CPT) has one aromatic ring containing molecule [254-256] and is also considered as common anticancer drug used in the treatment of solid tumors [257]. Although it can have both π - π stacking and hydrogen bonding interaction with graphene derivatives, the interactions are not comparable to that of DOX and CPT as they contain more aromatic rings.

Non-cancer treatment

Rana and co-workers [258] reported the delivery of Ibuprofen as an anti-inflammatory drug via using a chitosan-grafted GO with a drug loading rate of 9.7%. They demonstrated that controlled drug release can be achieved by the adjustment of pH. Another example pH dependent delivery is the release of antibacterial ciprofloxacin (CF) loaded on the polyethyleneimine (PEI) cross-linked GO film [259]. The loading and release of drug molecule is based on different electrostatic interactions between the drug and the carrier at different pHs.

Among all chemotherapeutic agents, particularly for cancer treatment, DOX has been shown to be exceptionally active in a large variety of cancers including hematopoietic

malignancies, carcinomas of the breast, lung, ovary, stomach and thyroid, as well as sarcomas of bone and soft tissue origin [244]. However, there are several side-effects such as cardiotoxicity, alopecia, vomiting, leucopenia, and stomatitis which have hindered the successful use of DOX. In order to diminish the undesired effects without reducing drug potency, DOX has to be encapsulated into drug delivery agents. These agents should be able to efficiently take up the drug, protect it, and selectively release it in specific sites without having adverse effects to surrounding tissues [260]. Moreover, it is difficult to incorporate drugs with low water solubility into the sustained and controlled release mechanism where a constant rate of release is required. Hence, graphene derivatives offering both π - π stacking and hydrogen bonding interactions can help most insoluble drugs, in particular, DOX to load and release in a controlled way by tuning the hydrophobicity/hydrophilicity degree of graphene sheets. Yang et al. [248] found that the loading ratio of DOX to GO as carrier could reach 200%, much larger than that of other nanocarriers which usually have a loading ratio lower than 100%. They demonstrated that graphene derivatives can be employed as efficient nanocarriers for the loading and delivery of water-insoluble aromatic drugs.

2.3.3 pH responsive graphene-based materials in drug delivery

One of the smartest properties of graphene derivatives is controlled drug delivery based on drug-graphene interactions (e.g., hydrogen bonding, hydrophobic, π - π stacking and electrostatic interactions) that respond to the stimuli release by adjusting pH, temperature, ultraviolet or visible lights, chemical substances or electric fields [258, 261, 262]. Moreover, graphene sheets as drug carriers are interesting because both sides of single graphene sheet could be accessible for drug binding [263, 264]. Graphene with extremely large surface area of about $\sim 2,630 \text{ m}^2/\text{g}$, allows for ultra-high drug loading efficiency on the sheets as compared to CNT surface with the surface area of almost half that of graphene[265].

Recently, the functionalization chemistry has rationally focused on endowing graphene with more aqueous solubility [261] and biocompatibility [160]. The oxygenated functional groups on GO surfaces also enabled it to serve as a physical cross-linker in the formation of a hydrogel. Bai and co-workers [22] reported a pH-sensitive GO-poly(vinyl

alcohol) composite hydrogel by a direct mixing method for drug delivery, which exhibited a storage modulus of ~ 200 Pa and was able to release 84% of the loaded vb12 molecules into a neutral solution after 42 hrs as opposed to 51% into an acidic solution. The basic functionalization of graphene that have been reported to date mainly concerns introducing chemically reactive oxygen-containing groups, including carboxylic acid groups which situate at the edges of the sheets as well as epoxy and hydroxyl groups on the basal planes [106, 129].

In the instance of graphene based material in the dispersion phase, the gradual release of drug into blood circulation after injection is necessary whereas the rapid release rate of drug in endosomes and lysosome is favorable. This issue has been address by the investigations of [266] pH-responsive drug delivery. [28] demonstrated the reactive oxygen species (ROS) generation and anticancer effect of graphene based carbon nitride (g-C₃N₄) nanosheets under low intensity light irradiation with low cytotoxicity and excellent biocompatibility. These nanosheets exhibited the pH-responsive behavior for the delivery of the anticancer drug, DOX. Nanosheets had a significant release of DOX of about $\sim 41.4\%$ under acidic condition (pH=5.0) whereas the DOX release in neutral (pH=7.0) and basic (pH=9.0) mediums were as low as 6.1% and 2.8%, respectively. This mainly attributed to increased protonation and enhanced solubility of DOX under acidic environment.

Similar pH dependent release of DOX was also reported by Wu et al. [246] who observed the highest release in the acidic pH=3.4 where the electrostatic repulsion interactions between positively charged DOX and GO was the main reason of such large release. In contrast, in basic pH, negatively charged GO formed strong electrostatic interactions with the positively charged DOX, hence remaining most of the drug on the GO sheets.

Similar phenomenon of release applies for the graphene based materials in the form of films. Huang et al. [259] reported a pH dependent in vitro drug delivery of ciprofloxacin CF using the polyethyleneimine (PEI) cross-linked GO porous film. They found that accelerated CF release in acidic pH compared to that neutral and basic medium, due to weakened electrostatic interactions between CF and PEI modified GO porous film. In

acidic environment, the PEI chain undergoes electrostatic repulsions via the ionization of amine groups which results in the chain stretch, decreased diffusion resistance and consequently enhanced drug release. The CF loaded porous film also exhibited significant antibacterial properties compared to that of plain film demonstrating the successful release of antibacterial agent of CF.

2.4 Graphene based materials with controlled structure

In the field of fabricating porous media, it is extremely important to construct the media with an ordered microstructure and uniform pore size, [14, 30, 31] particularly for drug delivery applications, as the uniform spatial structure and pore distribution will ensure that drugs are homogeneously loaded and distributed. The use of mesoporous, microporous and nanoporous graphene based hydrogels as carriers in drug delivery systems is a part of a growing body of research [18, 263, 267, 268]. Similar to other porous media, tuning the pore size in graphene based hydrogels is vital in the sense that the loading and release of the drug may be conducted in a more controllable, reproducible and predictable manner. LBL assembly of graphene, GO sheets has attracted considerable attention from researchers [23] to create out-of-plane pores which results in the enhancement of their adsorption characteristic. This out-of-plane pore benefits different applications and devices, for instance, in water treatment where the pore size and water flow rate matter [25], in gas and energy storages where the accessibility to the active surface areas is the key issue [26, 27] and in drug delivery where the poor solubility of the drug, yield of drug uptake as well as the release rate are the main concerns [28, 29]. The advantage of graphene LBL assembly is a high level of control over layering and the thickness of the obtained construct, which arises due to the linear growth of the films with the number of bilayers [24]. As in the construction of self-assembled materials, the control of the periodic structures and physiochemical properties of the hybrid graphene materials over a large scale is crucial. Particularly, when it comes to applications because the integration of the properties of disparate materials is beneficial. With LBL 3D assembly of the graphene sheets with desired pore size; one can tune the physiochemical properties and consequently address all the issues mentioned above. The best strategies are to materialize graphene constructs in a manner that avoids re-stacking and agglomerate formation, and contributes

to the material's active surface. This would benefit many different applications. Currently used protocols for the synthesis of this sort of graphene constructs can be classified into two types of “with” and “without” spacers, which are explained in detail below.

2.4.1 LBL assembly of graphene hydrogels without spacer

Recent researches on the facile self-assembly of layered graphene materials report the success in manipulating the assembly of graphene using the principles of colloidal chemistry and without using additional matter. [32, 269, 270] The principle is serving soft matter, “water” acting as an effective “spacer” to prevent the restacking of graphene sheets. Without a spacer, the self-assembly driving force is the strong van der Waals interaction between graphene sheets. The pore size can be altered via differing reaction parameters in graphene preparations [26] and also the applied pressure on layering graphene sheets [269, 271]. In most of these experiments, the graphene sheets orient in nearly parallel manner, nevertheless, the precise controlling of the interlayer spacing (pore size) is difficult. From natural graphite, Kovtyukhova et al. [24] prepared monolayer and grew multilayer of thin GO films on cationic surfaces via electrostatic self-assembly. They are one of the pioneers in the field of LBL assembly, and interestingly, they achieved unilamellar GO sheets by alternate adsorption of anionic GO sheets and cationic poly(allylamine hydrochloride) (PAH). With only GO sheets, the monolayer GO films showed the thickness in the range from 10 to 14 Å with GO out of plane (*c*-axis) spacing of 6.91 Å, which falls within the range of 6.3–7.7 Å reported in the literature.[272-275]. However, sequential adsorption of GO sheets and polycations via electrostatic interactions invariably resulted in a thickness change, which was 2–3 times by average larger than the GO monolayer thickness. The graphene interlayer distance for graphite oxide can be varied within the range of 6.87 to 8.72 Å depending on the extent of oxygen content and dehydration. Nakajima et al. [273] discovered that when the dried graphite oxide (ID=6.87 Å) was exposed to air, the interlayer distance increased to 7.75 Å, within 10min, and to 8.72 Å after 16 hrs. The moisture adsorption is very fast. Thus, a number of preparation parameters including pH, level of functionalities, and applied pressure need to be carefully considered for controlling the LBL assembly of graphene constructs. Also, a number of approaches including hydrothermal reduction [15, 111, 269], vacuum filtration, [32, 276, 277] spin-coating [125, 278], dip-coating [279-281], Langmuir–Blodgett assembly [95,

282], and direct chemical vapor deposition [39, 67, 283] have been employed to assemble GO and rGO nanosheets constructing thin films with tailorable properties. Here, we focus on reviewing the first three methods, as they are simple and economical methods that have been widely used to prepare 3D graphene.

2.4.1.1 Hydrothermal method

Without using any spacer, Tao et al. [269] prepared different types of layered graphene films to investigate the effect of pressure and different drying process on the pore size distribution (PSD) of these layered materials and their electrical conductivity (shown in Figure 2-7a). Parent samples in the form of hydrogels were first prepared using hydrothermal reduction of GO sheets and their self-assembly through van der Waals interactions. Hydrothermal treatment is one convenient method used to convert GO to rGO [269, 284] and involves minimum defects on carbon graphitic structure and the facile self-assembly of graphene sheets. Each sample was cut from the parent cylindrical hydrogel and treated in different ways. The first sample was freeze-dried hydrogel followed by annealing at 800°C, called PGM-800. The second and third samples were the room temperature vacuum dried hydrogels with and without following annealing, called HPGM and HPGM-800, respectively. In the upper part of Figure 2-7a the SEM image clearly shows how freeze drying effectively aided fixing the 3D network constructed of interlinked nanosheets, but in a random and spongy assembly which resulted in a mainly macroporous structure with some mesoporosity. This demonstrates how freeze-drying can retain the morphology of the parent hydrogel without shrinkage. For HPGM, the vacuum drying also leads to the formation of porous structure in a disordered, but highly compact way (shown in lower part of Figure 2-7a). The proof of highly dense and interlinked layered morphology beside scanning electron microscopy (SEM) is the PSD analysis from nitrogen adsorption, in which the HPGM showed predominant mesoporosity (smaller than 2 and centered at 1.1) and microporosity with a very small size (slightly larger than 2 nm). Compared with HPGM, HPGM-800 showed a slightly smaller pore size (shown in Figure 2-7b) in the micropore range possibly due to thermal shrinkage, and the appearance of pores from 1.3 to 3.7 nm could be attributed to the evolution of pores resulting from the removal of trapped water and bound oxygen during the annealing process. In summary,

freeze-drying can retain the original structure of layered graphene materials. Vacuum drying and annealing, respectively, due to increasing the interlinking of graphene nanosheets and removal of oxygen containing groups, substantially contribute to enhancing electrical conductivity and the charge transfer of these materials. Although the graphene interlayer spacing in this spacer-free approach is more controllable than previous spacer aided graphene constructs, it mostly generates microporosity of about 1 nm which is only able to uptake sub-nanometer size molecules, and this limits its applications.

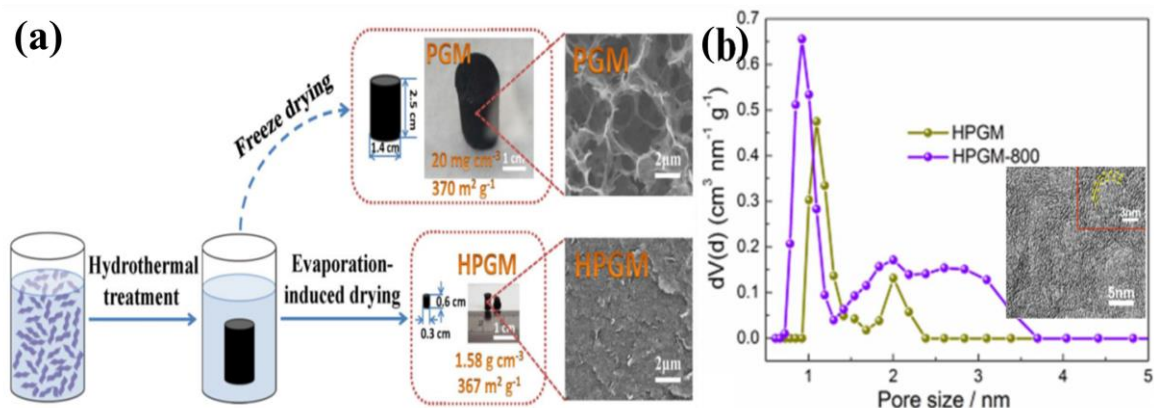


Figure 2-7. (a) Schematic of the formation of graphene-based 3D porous macroforms with different drying process and the SEM images of the resultant PGM and HPGM and (b) PSD plots of HPGM before and after annealing process. [269, 284].

Shi et al. [111] employed a facile hydrothermal reduction of hydrochloric acid-treated GO solution to prepare self-assembled 3D construct of H-rGO to be used as supercapacitor electrode material. They believe that the existing hydroxyl and carboxylic groups in GO solution cause the GO colloid particles to be highly negatively charged and repulse each other. Adding hydrochloric acid or positively charged ions lead to an ionization equilibrium and fair distribution of electrostatic repulsion among GO sheets in dispersion. As reported, the assembly of H-rGO resulted in a much more ordered structure compared to typical disordered 3D cross-linking network usually made by the normal hydrothermal reduction method, but this was not as parallel as is evident in vacuum filtered graphene films. The advantages of ordered over disordered 3D graphene networks is that they possess large, open, and smooth interlayer spaces instead of randomly distributed pores and fractures. The large average pore-size of approximately 3.8 nm with minimum level of graphene restacking in H-rGO led to smooth ion diffusion, satisfactory

electrical conductivity, and consequently exhibited higher capacitance compared to that of rGO.

rGO layered materials with more uniform layering but smaller pore size were synthesized in the form of fiber by Yu et al. [285] through a hydrothermal process followed by drying. Capillary forces during the drying process lead to densely stacked rGO sheets that were highly aligned along its main axis. Similar to other dense stacking graphene films reported elsewhere, this rGO nanofiber also suffered from low accessible surface areas for electrolyte penetration into in plane pores, low ion interaction with electroactive surface, and hence low capacitive behaviors were observed. The solution to this matter is increasing the on-plane (cross-plane) pore size which could be achieved either with or without using spacer.

2.4.1.2 Vacuum filtration method

The vacuum filtration technique was used by Li and co-workers [32] to self-assemble space-free macroscopic layered graphene materials. Using the hydration force and remaining oxygen moieties on rGO, they increased the graphene interlayer spacing in freeze dried sample to 0.39 nm compared to that of 0.34 nm in graphite. This experiment was followed by annealing which caused a drastic restacking and shrinkage in the volume of self-assembled material. The increase in interlayer spacing enhanced the capacitive properties of the supercapacitor electrode fabricated by this material, but then after annealing almost no capacitance was observed. This could be ascribed to the formation of a highly open, continuous pore structure, which facilitates the electrolyte diffusion across the entire freeze-dried sample, whereas the annealed sample has no accessible pore for electrolyte diffusion across the sample. The main preventing factors for graphene restacking are intersheet electrostatic repulsions caused by the negatively charged groups (oxygen moieties) in conjunction with adsorbed water on rGO, which induce repulsive hydration forces between sheets and their interlayer spacing. Moreover, rGO due to loss of most of oxygen functionalities possesses an enhanced intersheet π - π stacking interaction results in their adhesion. To attain layered graphene materials with the desired pore size one has to reach the balance between these repulsive interactions and the intersheet π - π stacking, and this is a complex task. Furthermore, the applied pressure via vacuum

filtration also plays a key role in the dynamics and layering of graphene sheets, which makes the system more complicated in order to achieve a construct with unique pore size.

2.4.1.3 Spin-coating method

The spin-coating method has several advantages over dip-coating and spray-coating methods, in terms of the level of control on transmittance, thickness, and time for fabrication of thin films - particularly for LBL assembly of graphene. Lee et al. [286] constructed LBL assembled graphene multilayer in a controlled way with a fairly good transmittance and reasonable electrical resistance without using a spacer and by employing only the electrostatic interactions between oppositely charged exfoliated graphene nanosheets (schematically shown in Figure 2-8a). The GO dispersion with its native negative charge (GO-COO^-) simply mixed with positively charged GO dispersion (GO-NH_3^+ : GO treated with N-ethyl-N-(3-dimethyl aminopropyl) carbodiimide methiodide (EDC) followed by chemical reduction, can produce bilayers of oppositely charge (schematically shown in Figure 2-8b). Controlling the degree of GO reduction and the number of bilayers aided in tuning the thickness of graphene monolayer and multilayer, with consequent impacts on the transparency and electrical conductivity. We believe that this work could be further extended by manipulating the electrostatic interactions through varying the amount charged group graphene surface to potentially tune the interlayer spacing of graphene nanosheets. As it is well understood, differing the internal porous structures between graphene nanosheets may induce different properties and open up pathways for broader real life applications for layered graphene materials.

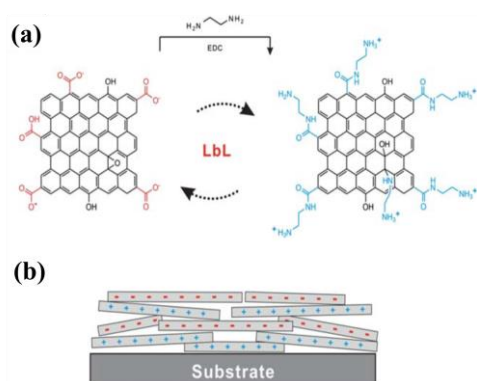


Figure 2-8. Schematic representation of (a) LBL assembly of rGO multilayer with rGO-COO^- and rGO-NH_3^+ , and (b) the resulting LBL film of rGO [286].

2.4.2 LBL assembly of graphene hydrogels with spacer

GO, due to its thermally instability and high chemical activity can easily undergo an exothermic disproportionation reaction under mild heating conditions or be reduced by some reducing reagents to convert to rGO [287-290]. However, because of the restoration of sp^2 carbon network and introducing the strong π - π interaction the re-stacking of graphene sheets is an issue that needs to be considered during the reduction process. This is an unfavorable event in the self-assembly of 3D graphene layered materials for many applications, such as adsorption, ionic transportation, and catalysis where a large surface area and controlled pore size of the material are required. Therefore, as a solution, weakening the π - π stacking interactions by introducing other materials as the spacers between graphene sheets has recently attracted substantial research attention [27, 35, 37-39, 291, 292]. The main role of spacers is to enlarge the interlayer spacing between graphene sheets and weaken the inter-planar interactions, and hence prevent the re-stacking of the graphene sheets during reduction process. However, in some electrochemical applications, spacers have additional roles such as conductive pillars in between graphene sheets to enhance the electrical conductivity of graphene films in vertical axes. The spacer based graphene assembly can be eventually replicated into 3D multilayered macroscopic materials resulting in graphene-based materials after reduction.

2.4.2.1 Carbon materials as spacer

Carbon materials such as carbon black, [35, 36] CMK [37] and CNTs [38] have been used as spacers between graphene sheets, and effectively prevent the self-restacking of the graphene sheets. The resulting materials (Schematically shown in Figure 2-9) are promising candidates for supercapacitor electrode materials due to rapid electron transport capability. By enlarging the inter-layer spacing between the graphene sheets, the electrolyte ions are allowed to easily diffuse through the graphene constructs. This efficiently improves electrolyte-electrode accessibility, charge transport capability in graphene 3D geometry, and enhances the electrode conductivity [36]. In addition, adding carbon based materials as spacers dramatically reduces the internal resistance of pillared graphene constructs acting as a conductive bridge connecting neighboring graphene sheets, and consequently assists in effective charge transport in both lateral (along graphene

sheets) and vertical directions [35]. According to Lei et al. [37] mesoporous CMK-5 as a spacer has advantages over solid carbon spheres due to its straight mesoporous channels which serve as a highway, allowing the fast transport of electrolyte ions in the composite when used as an electrode. Although this benefits the electrode electrochemical behaviors, the non-similarity in CMK-5 particles size (~500 nm) do not fully control the interlayer spacing of multi-layered graphene constructs to make uniform parallel structure for other applications.

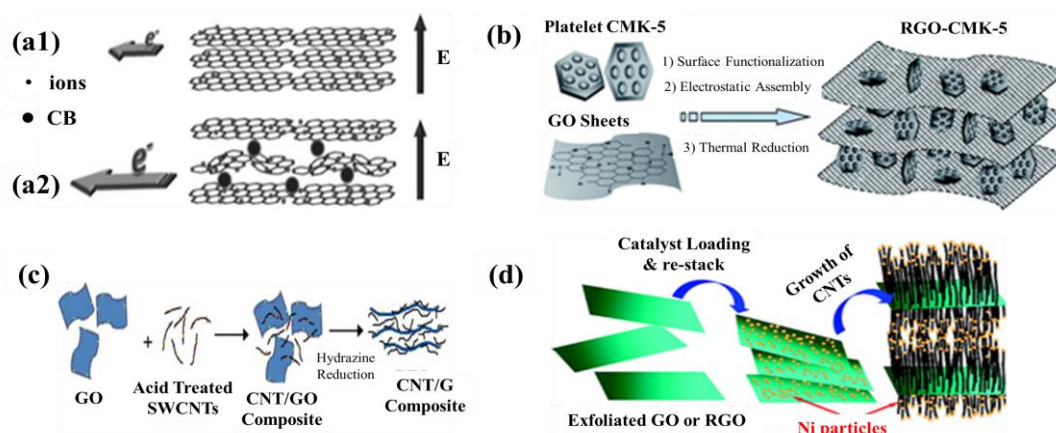


Figure 2-9. Schematic illustration of the multilayered graphene (a1) before (a2) after carbon black (CB) intercalation, [35] (b) the preparation procedure for the RGO-CMK-5 composite, [37] (c) graphene/CNTs composite preparation process, [293] and (d) CNTs based pillared graphene oxide construct [38].

CNTs assisted pillared graphene constructs have been made in two different ways so that the CNTs sit randomly [293, 294] or perpendicularly [38] in between graphene sheets. With random decoration of CNTs between graphene layers, a broad range of pore size is achieved. For instance, Cheng and co-workers [295] prepared a graphene/CNT composite with the CNTs of 1-2 nm in diameter, but because there was no means to precisely control the graphene-CNT interactions the pore size achieved in composite film varied between 1.3 to 32.7 nm with an average value of 6.1 nm. Although in this case the CNTs act as a smart spacer to increase the graphene interlayer pore size and contribute to better electrolyte accessibility, the precise control on pore size using CNT was a major challenge. A similar story is evident in the experiments carried out by Wimalasiri and Zou,[293] who randomly mixed different amounts of CNTs with graphene to prevent from their restacking. Using N₂ adsorption, they showed that the mean pore diameter of graphene film could be enhanced from 4.38 to 5.00 nm (with a broad range) after intercalating the

CNTs with graphene sheets. Yu et al. [285] using BJH analysis obtained the PSD ranges from ~1.5 to 18 nm with a peak at ~5 nm from their microfibrinous construct made of an interconnected network of CNTs with interposed nitrogen-doped rGO sheets. Although the random composition of graphene with CNTs helped with the enhancement of graphene interlayer spacing and provided a large accessible surface for fast ion transport, the graphene-CNTs binding occurred randomly throughout the whole dispersion without any control on parallel morphology for either CNTs or graphene layers. Researchers continue working on the graphene-CNTs binding constructs, manipulating different parameters such as the degree of GO reduction and CNTs content [270], nitrogen-doped and boron-doped CNTs intercalation [296], and generating cross-plane pore on top in-plane pore [297]. These efforts all aim to produce graphene layered materials with uniform morphology and enhanced interlayer spacing that ultimately possess high surface area and diffusivity rates into their porous structures. The uniformity of morphology in macroscopic scale was attained, but uniformity of the pores, particularly the in-plane pore is a major challenge.

In contrast, almost perpendicularly pillaring of CNTs on graphene surface was carried out by Zhao's group [38, 39] in which the nickel ion particles as catalyst for CNT nucleation were decorated with different concentration on graphene and GO surfaces (shown in Figure 2-9d). The CVD method with acetonitrile as the carbon source was used for CNTs nucleation and growth on the nickel intercalated graphene platelets. They believe that both the amount and length of the CNTs can be tuned by controlling the amount of catalyst and reaction time. They also reported preliminary porosity characteristics data including surface area and total pore volume measured for such pillared layered graphene constructs. SEM images for their samples showed the growth of carbon nanotubes with random lengths and in different directions that might result in improper pore size control. Unfortunately, the surface area and pore volume are not enough for estimating the pore size. The missing element here, the PSD, was not investigated, and how well the pore size is controlled is questionable. Another thing that may be worthwhile investigating is the stability of such 3D layered structure in vertical axis. As CNTs from one end bonded strongly with the two adjacent graphene planes and entangled in each other from the other loose end, this might have impacted on the stability of structure, particularly during shrinking and swelling in different applications.

Another example of CNTs intercalated graphene 3D layered construct is from Roy and co-workers [298] who deposited iron catalyst particles on thermally expanded graphene layers and then grew the vertically aligned CNTs (VACNTs) between the graphitic layers (schematically shown in Figure 2-10). Like other CNTs pillared graphene constructs, they attained an efficient charge transport by VACNT/graphene conductive network for energy generation and storage applications. Synthesizing such an inherently porous structure significantly facilitated electrolyte diffusion into the pores and, hence, enhanced ionic conductivity. By assuming the geometry of pore to be cylindrical, they estimated the PSD from the corresponding pore volume in the range 1 to 12 nm which is a wide range for micro-mesoporous materials. There could be some more microporosities in expanded stacks of graphene (hundreds of layers) which have not been detected via their method of PSD analysis.

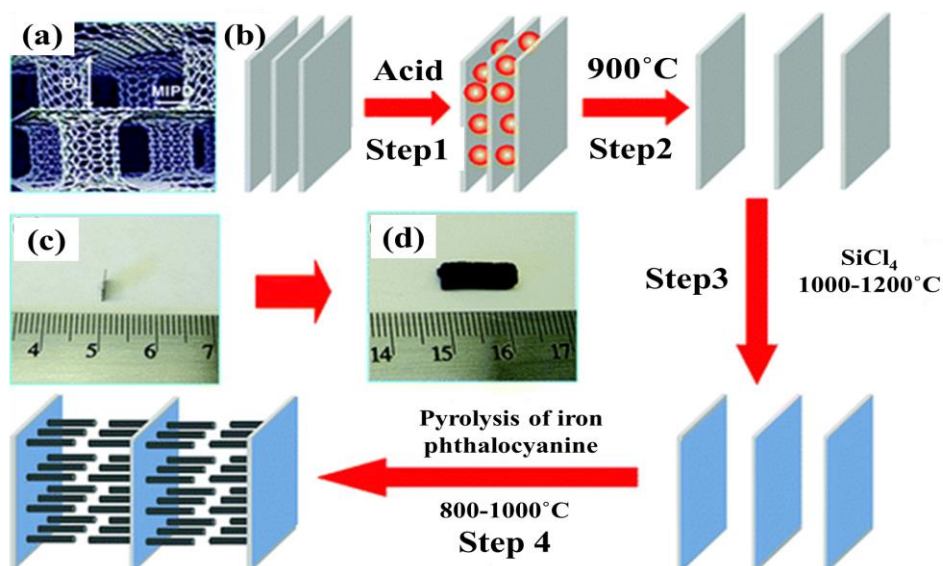


Figure 2-10. (a) Schematic diagram of a 3D pillared VACNT–graphene nanostructure. (b) Schematic representation of the procedure for the preparation of the 3D pillared VACNT–graphene architectures. Optical images of (c) original highly ordered pyrolytic graphite (HOPG) with a thickness of 80 μm and (d) the thermally expanded graphene layers intercalated with VACNTs. [298]

The main issues with most out of plane CNTs intercalated graphene constructs [38, 298, 299] are PSD (which depends on regularity in pore shape) and physiochemical disruption to the planar graphene surface. Firstly, the pores reported in such layered constructs are defined as the spacing between CNTs, but not the graphene interlayer spacing. Although the CNTs in their microscale look aligned, they have some curvatures in

their nanoscale which affect the shape of the pores. Secondly, covalent bonding of dense CNTs forests on graphene planar surfaces disturbs the planar graphitic lattice structure and occupies most of its accessible surface. This might decay or even fade away the outstanding physiochemical properties of graphene. Hence, tuneability of the pore size together with retaining the physiochemical properties of graphene are the major issues that need to be carefully considered.

2.4.2.2 Polymers as spacer

The graphene-polymer based films were also prepared and used for electrochemical application due to the enhancement of graphene conductivity and electroactivity via grafting with conducting polymers. Polymers such as PANI[36], polypyrrole (PPy)[46] due to their high conductivity and fast redox activity were used in layered graphene constructs to make promising electrode materials. Wu et al. [300] prepared a nanocomposites by mixing graphene and polyaniline nanofiber dispersions made uniformly sandwiched nanofibers between graphene layers. The interspaces between the graphene layers were non-controllable in a broad range of 10 to 200 nm as it is difficult to control the dimensions (thickness and the length) during polymer synthesis as well as its coating on the graphene surface. Although parallel sandwiching of polymers between graphene sheets forms a porous structure and endows with additional specific surface area compared to that of the compact graphene films, but it is not yet comparable to that of nano- and meso-porous graphene constructs formed by using other smaller spacers.

Rouf and co-workers, [291] similar to their divalent metal ion bonded GO method, introduced a polymer cross-linked GO sheets, in which polyallylamine (PAA) chemically bonded with reactive oxygen groups on graphene surface. The PAA modified GO sheets showed higher stiffness compared to that of metal ion bonded GO and unmodified GO sheets in linear region. According their hypothesis (shown in Figure 2-11), the PAA via its long alkyl chain with a number of reactive amine groups strongly cross-link to GO sheets by reacting with the epoxide ring across GO surface as well as some carboxylic groups on the edge of GO. That cross-linking played a major role in the mechanics of this highly stiff material.

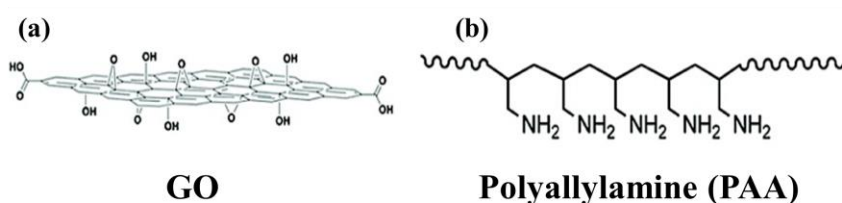


Figure 2-11. (a) Schematic model of a sheet of GO showing oxygen-containing functionalities. (b) Chemical structure of polyallylamine [291].

Zhao and co-workers who have recently focused on pillared graphene constructs [38], also synthesized layered GO constructs pillared by PPy as a conducting polymer (schematically shown in Figure 2-12) in which the polymerization occurred with the aid of different surfactants; cetyltrimethylammonium bromide (CTAB) or dodecyltrimethylammonium bromide (DTAB) [301]. They believe that with using different surfactants, they are able to control PPy polymerization in the sense of controlling the shape and morphology of PPy. Spherical and fibrous shapes PPy were synthesized and sandwiched between GO layers using DTAB and CTAB, respectively. Ion transport resistance was investigated to compare two different morphologies and their influences in electrochemical performance of supercapacitors fabricated using such multilayered graphene materials. Synthesizing random shaped fibrous PPy led to generate highest ion accessible areas between GO layers resulting in a lower ion diffusion resistance and better capacitive performance over spherical PPy-GO composites and plain GO constructs. The advantage of such pillared graphene composite materials over using each individual component is the strong support of graphene matrix that provide enough surface for the deposition of the pillars on both surfaces of the graphene sheets. Furthermore, the strong binding between the graphene matrix and pillars further enhances the mechanical strength and long-term stability of such multilayered constructs. Although graphene-polymer composite constructs are of recent research interests, particularly in electronics, but the rapid degradation due to swelling and shrinkage of the polymers [46] might lead to a poor stability, thereby limiting their applications.

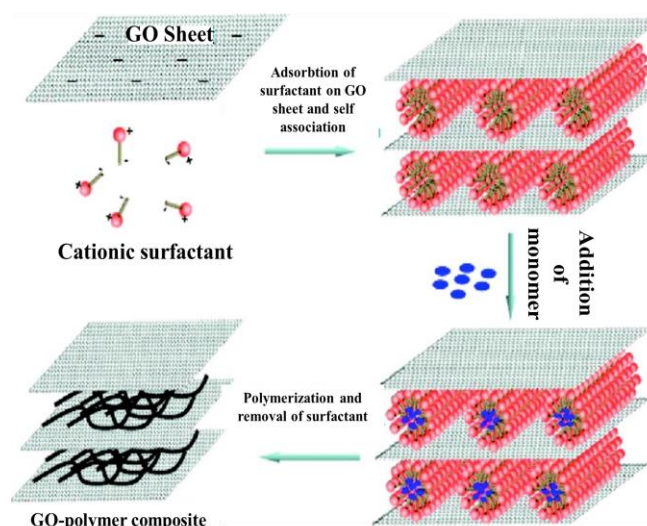


Figure 2-12. Schematic Illustration of the Formation Process of GOPPy Composite [301].

2.4.2.3 Organic molecules as spacer

Recruiting both physical and chemical bindings, Lee and co-workers [302] reported molecular monolayer self-assembly of photo-switchable aryl diazonium compounds onto a graphene sheet, and then placed it between two graphene electrodes to fabricate a chemically stable, optically transparent, mechanically flexible and molecularly compatible junction. The conformational structure-dependent photo-switching between the *cis* and *trans* isomers of aryl azobenzene molecules (shown in Figure 2-13a) were tested under light irradiation generated ultraviolet-visible kit. The switching between the *cis* and *trans* isomers effectively influenced the vertical distance between two graphene electrodes (shown in Figure 2-13b), and changes in tunneling barrier, consequently impacting on the electrodes current density. Large-area single layer graphene, carefully transferred onto the polydimethylsiloxane/polyethyleneterephthalate (PDMS/PET) substrates was used as a bottom electrode. Aryl diazonium compounds were then self-assembled onto the graphene/PDMS/PET substrate using an immersion method in such a way that covalent C-C sp^3 bonds formed between the aryl radicals of aryl diazonium compound and C=C sp^2 carbon atoms of the graphene sheet. The graphene top electrode was transferred onto and physically contacted with the aryl molecular monolayer/graphene/PDMS/PET substrate. The physical contact was to test the bending and twisting flexibilities of the device made out of such layered graphene circuit. This is a limited technique as it forms a construct of

only two layers graphene and one layer spacer between them. Hence, it is unable to fabricate macroscopic multi-layer porous constructs.

According to Cui et al., the conductance of junctions depended on whether the molecules were chemisorbed or physisorbed to the contacts. Junctions with two “chemicontacts” were orders of magnitude less resistive than junctions with only one chemisorbed contact [303]. Although the chemical contacts in molecular electronics applications exhibit a higher junction conductance than the physical contacts [304, 305], Lee and co-workers [302] in their photo-switching devices found nearly symmetric current-voltage characteristics from molecular junctions of both one- or two-sided chemically bound contacts with the same electrode material. It is worth mentioning that the design of aryl diazonium compound could be used in a totally different way, for example by mixing it with exfoliated graphene sheet dispersion to promote the LBL self-assembly of graphene sheet. Multilayered graphene construct with photo-switching properties and tuneable pore sizes could offer additional applications in which the swelling and shrinking of the construct play a major role.

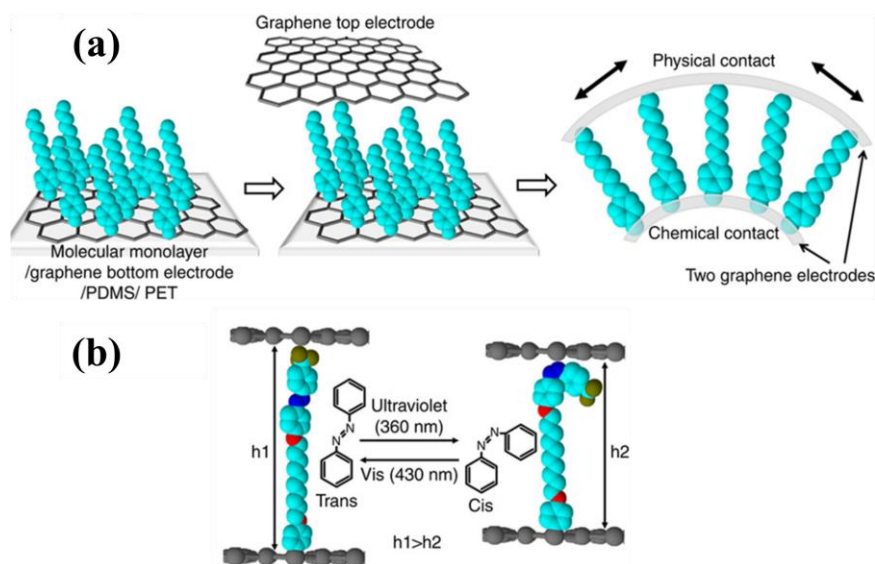


Figure 2-13. (a) Schematic of a transparent and flexible molecular monolayer junction between the two graphene electrodes, (b) Molecular tunneling barriers (with h_1 and h_2 being the vertical distance between the two graphene electrodes) corresponding to conformational changes in aryl azobenzene molecules with light irradiation [302].

Non-covalent functionalization of rGO with terephthalic acid (TPA) and succinic acid (SA) was utilized by Chow and co-workers [306] to prepare LBL graphene based paper (shown in Figure 2-14) with enhanced mechanical properties. SA due to its middle hydrophobic alkyl chain had a much stronger interaction with rGO sheets than the TPA, hence, caused immediate rGO destabilization and precipitation. The role of the functional molecule, TPA, was to prevent re-stacking of rGO sheets and to increase the interlayer spacing of the graphene sheets in TPA/rGO by $\sim 2.2 \text{ \AA}$ (according to their XRD results) although the end-to-end length of the molecule is $\sim 8 \text{ \AA}$. This indicates that the TPA molecule lies flat along the basal plane of the rGO surface through π - π interaction via its middle aromatic ring. A post-yielding linear elastic behavior named “slip-and-stick” was observed in TPA/rGO compared to the pristine rGO, meaning that despite the increasing the interlayer spacing of graphene sheets, TPA did not altered the bonding structure of graphene. Such post-yielding behavior arose from the repulsive interactions between carboxylic acid functional groups of the TPA and carboxylic sites at the edges rGO sheets, whereas pristine rGO paper quickly had a catastrophic fracture because of the inherent stiffness that resulted from interactions between rGO flakes. As mentioned above in other literature, oxygen removal from GO and intercalating graphene sheets with spacers favor ion diffusion and electric charge transfer, however, Chow and co-workers [306] realized that increases in interlayer spacing increases the resistance (reducing the conductivity) associated with electron-hopping across the sheet-to-sheet interfaces. The intercalation of rGO with TPA did not significantly increase the inter-sheet spacing; the LBL graphene material possesses micro-porous structure, hence limiting its application because few of the ions and molecules could penetrate through such small pore. Hence, the two issues raised above further emphasize the importance of finding an optimum condition for each influencing parameter on the LBL of graphene based materials; that is degree of GO reduction and designing sorts of molecules with tuneability in their sizes and interactions with graphene sheets.

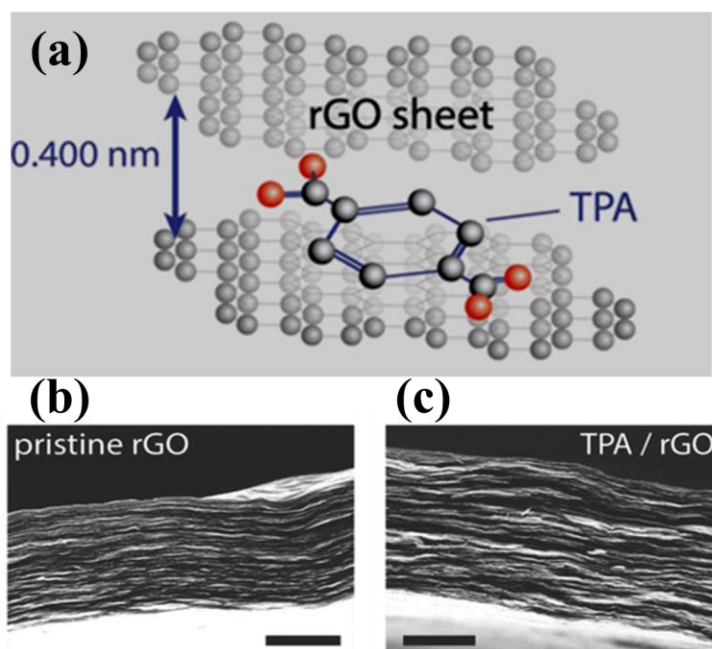


Figure 2-14. (a) Schematic illustration of the proposed incorporation of TPA within the rGO-layered structure, (b and c) Cross-sectional scanning electron microscopy (SEM) images of pristine rGO (on the left) and TPA-treated rGO papers (on the right). The scale bars indicate 2 μm [306].

Sk and Yu [307] reported a LBL assembly of graphene sheets via covalent functionalization of GO with *p*-phenylenediamine (PPD) (forming GPPD) mostly through bonding between the PPD amine and the epoxy groups on graphene basal plane, and some insignificant amide bonding ($-\text{NHCO}-$) between the PPD amine the $-\text{COOH}$ groups on graphene (shown in Figure 2-15). Their approach for preventing the restacking graphene sheet, not only induced the specific surface area, but also enhanced the ion transport, specific capacitance, and cyclic stability of the LBL graphene construct during the electrochemical process. Although their Barrett-Joyner-Halenda (BJH) analysis of PSD showed the existence of wide range for GPPD film, there were two major peaks demonstrating that many pores with pore sizes of 4.21 and 6.02 nm. The BJH method can be the evidence for the development of a mesoporous structure, but it fails for mesoporous structure [308] and is unable to predict the restacking event of graphene sheet which might occur during LBL assembly. Moreover, the major issue with pore sizes of 4.21 and 6.02 nm is that they are far larger than the size of single PPD molecule. This could be an indication of PPD particles with different sizes in between sheets, and probably of their aggregation due to their intermolecular interactions.

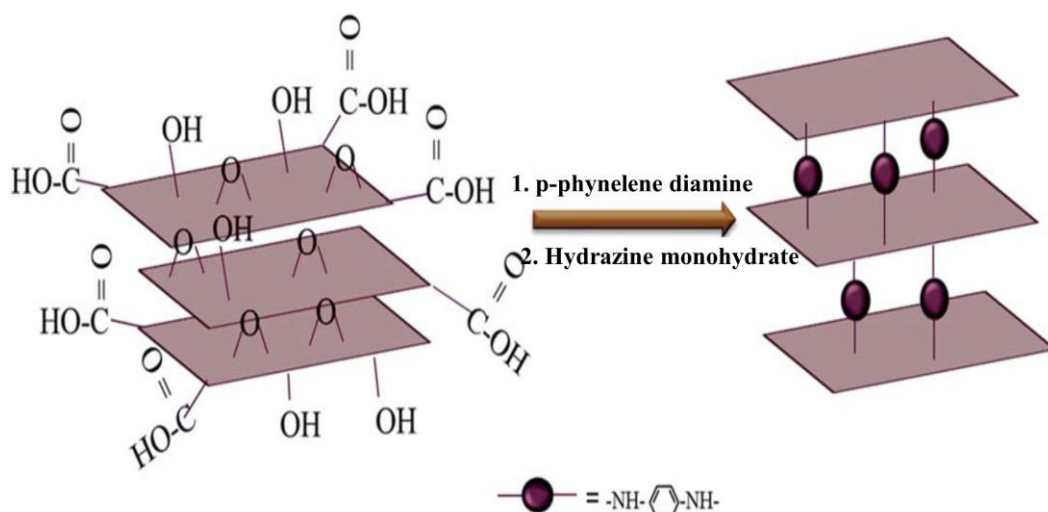


Figure 2-15. Schematic diagram for the conversion of GO to GPPD [307].

2.4.2.4 Metal ions/oxides/nanoparticles as spacer

Ruoff and co-workers [93] investigated the positive and negative impacts of chemically cross-linked multilayer graphene constructs and the contribution of the size of spacer in the mechanical properties of GO papers. Using divalent metals ions (M^{2+}) of different sizes; Ca^{2+} with the ionic radius of 1.06 Å vs. 0.78 Å for Mg^{2+} , they hypothesized that M^{2+} can tightly bond with the carboxylic acid groups on GO edge and weakly bond with epoxy group on the planar surface of GO (as shown in Figure 2-16a). The positive side of such cross-linking is the strong edge-to-edge binding, resulting in some cross-linking of neighboring sheets and also improvements in the mechanical stiffness and strength of the un-modified GO macroscopic construct in linear region (as shown in Figure 2-16b). Binding the M^{2+} to the graphene planar surface and increasing the graphene sheets interlayer spacing (d-spacing) are the negative contributions of this cross-linking process to the mechanical properties in cross-sectional region. The axial interactions between the metal ions and the graphene oxide sheets, which are called intercalations, are much weaker than those of metal ions between sheets on the sample plane. These intercalations can increase the d-spacing and the cross-sectional area of the sample which are excellent points, but lead to an overall reduction of stress (force/cross-sectional area) which is a negative contribution to stiffness of M^{2+} -modified GO constructs. Although these weak intercalations can be removed by rinsing with water, the problem is that the d-

spacing will decrease back to that of GO constructs, thereby reducing the accessible surface area of macroscopic constructs.

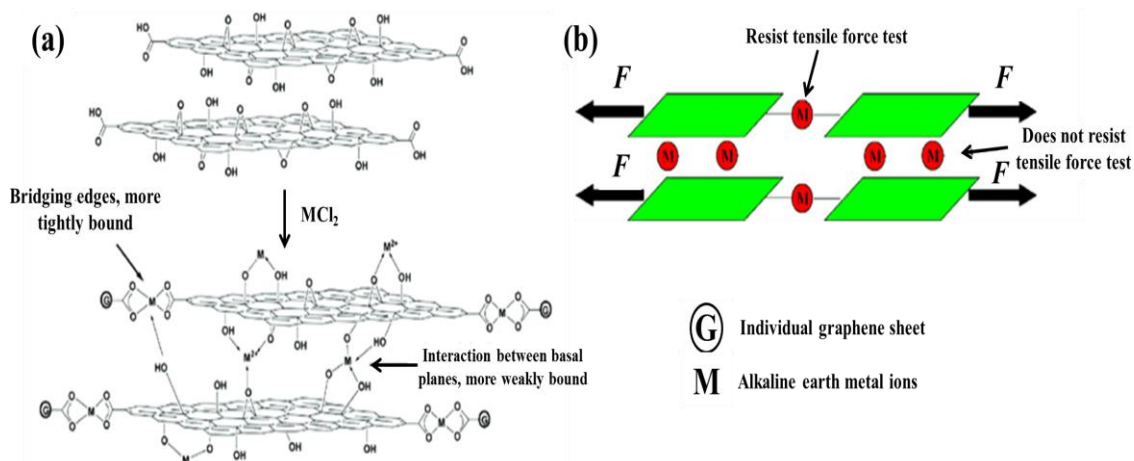


Figure 2-16. Models of the M-modified graphene oxide papers: (a) schematic model of the reaction between graphene oxide paper and MCl_2 ($M = Mg$ and Ca); (b) proposed model for the enhanced mechanical properties of graphene oxide paper observed after metal modification [93].

Ruthenium oxide (RuO_2) anchoring on graphene sheets was another approach to construct multilayer graphene electrode materials for hybrid supercapacitors with enhanced energy-storage capabilities and lower costs [41]. Similar to other spacers, the role of RuO_2 particles was to avoid or decrease the possibility of serious agglomeration and restacking of graphene sheet (GS) ensembles (schematically shown in Figure 2-17), and consequently provide a higher available electrochemically active surface area for increasing supercapacitor energy storage. It has also been emphasized that the presence of some oxygen-containing groups helps the dispersibility and uniform decoration of RuO_2 nanoparticles on graphene nanosheets. Both XRD and electrochemical testing results from the research carried out by Wu et al. [41] were the confirmation of the separation of neighboring graphene sheets, and consequently results in rich porous texture and a larger available surface area for enhancing the energy storage of supercapacitor. However, the role of RuO_2 nanoparticles in the controlling of the graphene interlayer spacing and interlayer spacing effects on the electrochemical behavior of multilayered graphene construct were not investigated.

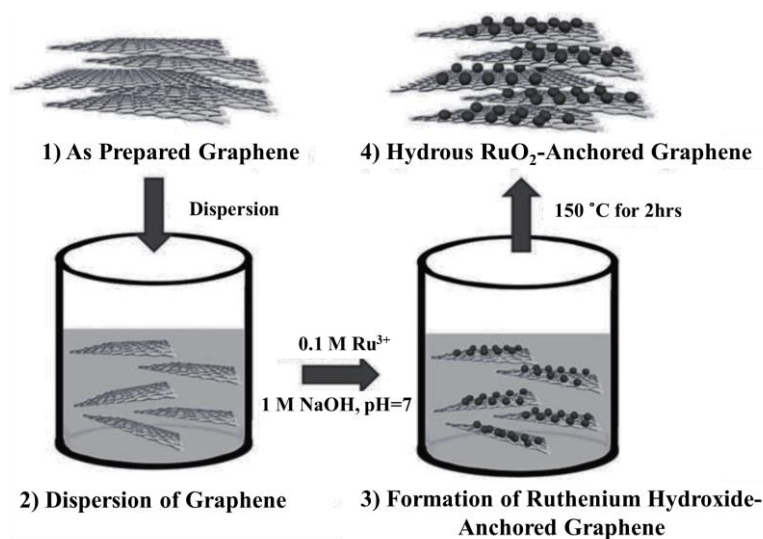


Figure 2-17. The LBL preparation of ruthenium oxide (RuO_2)/graphene sheet composites by combining a sol-gel method [41].

Among the most popular metal nanoparticle, gold nanoparticle (AuNP) due its outstanding chemical, electrical, and catalytical stability, is commonly used to functionalize graphene or its derivatives [43]. The graphene-AuNP hybrid materials present fascinating aspects including multiple types, size-related electronic, magnetic, and optical properties, and have attracted immense attention in electrical and electronics applications such as fast data accesses and improved data retention in flash memory [309], and as biosensors [43].

One of those earlier interesting works in the preparation of graphene-AuNP hybrid materials was reported by Kong et al. [42] who obtained LBL graphene films comprised of alternating graphene and AuNP layers (schematically shown in Figure 2-18). LBL graphene-AuNP hybrid films were formed by using the sequential vacuum filtration of graphene dispersion and spontaneous reduction of gold ions on the surface of top layers of graphene in a repetitive manner. Spherically shaped AuNPs, with sizes ranging from subnanometer to ~ 200 nm were formed on the rGO sheets. Although a uniform AuNPs intercalated graphene film was prepared, the uniformity is in macroscale. There are two issues which could be considered to improve the periodic structure of the film in nanoscale. Firstly, the broad range in AuNP size results in a broad PSD in and it would be worthwhile to develop a controlled method for the formation of AuNP with unique particle size on graphene surface. Secondly, the graphene bilayers provide a strong support to

AuNP formed by stacking of graphene sheet which results in producing subnanometer pores and this makes a large amount of graphene surface area inaccessible for uptaking larger molecules.

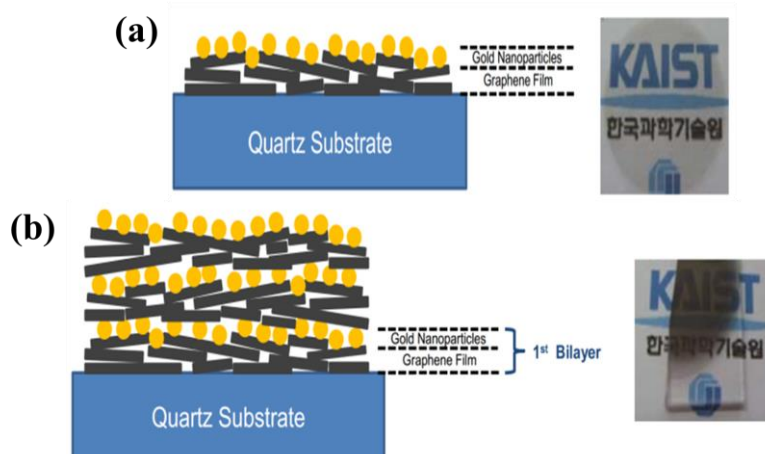


Figure 2-18. Schematic of the two-step procedure in fabrication of layer-by-layer assembled Au-graphene films; (a) AuNPs formation on graphene film (b) Layer-by-Layer assembly of graphene and AuNPs [42].

Later, other researchers developed a new and simple method by mixing Au ion precursors with the dispersion of exfoliated graphene sheets for preparing the graphene-AuNP hybrid films [43, 310, 311]. Using well-dispersed graphene sheets, these researchers addressed the graphene restacking issue as they could benefit the most from the exposible surface of graphene sheets, decorating both sides with synthesized AuNPs. However, they could reduce the size of AuNPs to tens of nanometers, and control the interactions AuNPs and graphene sheets, but the issue of the uniform growth of AuNPs to tune the graphene interlayer spacing remained unresolved. For instance, Zhang et al. [43] reported possibilities of chemical and physical attachment of AuNPs at the graphene surface through existing functional groups on both sides of rGO. They suggested that AuNPs physically attach residual oxygen-containing groups of rGO sheets under the Brownian motion and electrostatic interactions whereas these particles tend to chemically bond with N-containing groups (N–Au) on the GO sheets (schematically shown in Figure 2-19). Eventually, with the continuous evaporation of the mixed solution, there are more opportunities for AuNPs and graphene sheets to interact with each other and promote self-assembly. Although the layered graphene materials prepared here may not have uniform nanostructure along the vertical axis due to different size and shape of AuNPs, it showed

long-term strong stability because of strong interactions between AuNPs and graphene sheets.

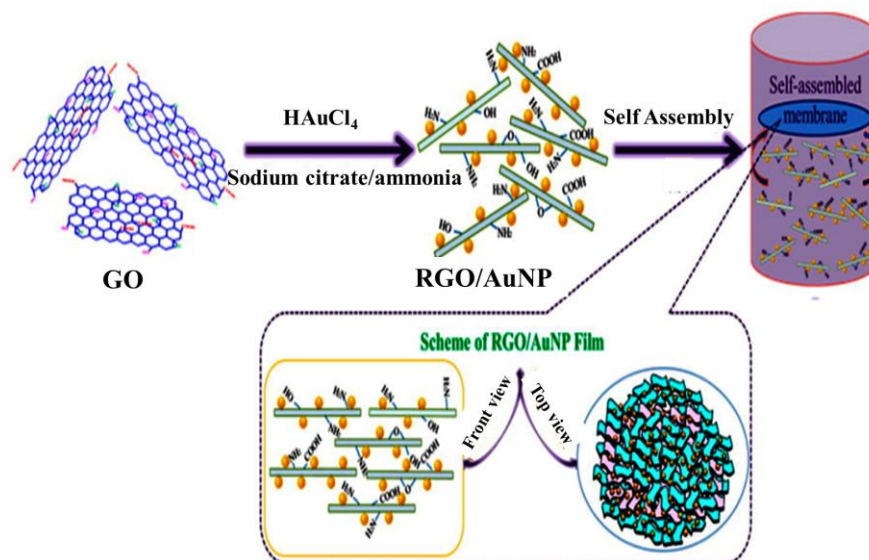


Figure 2-19. Schematic presentation of the green synthesis and potential formation mechanism of rGO/AuNP film.

2.4.2.5 Biomolecules as spacer

Xu et al. [47] used a convenient hydrothermal method for an impressive 3D self-assembly of GO sheets and *in situ* formed single strand DNA (ssDNA) chains into multifunctional hydrogels (Schematically shown in Figure 2-20). They believe there is strong binding of DNA chains to GO sheets via multiple noncovalent interactions, including the π - π stacking and hydrophobic interactions.

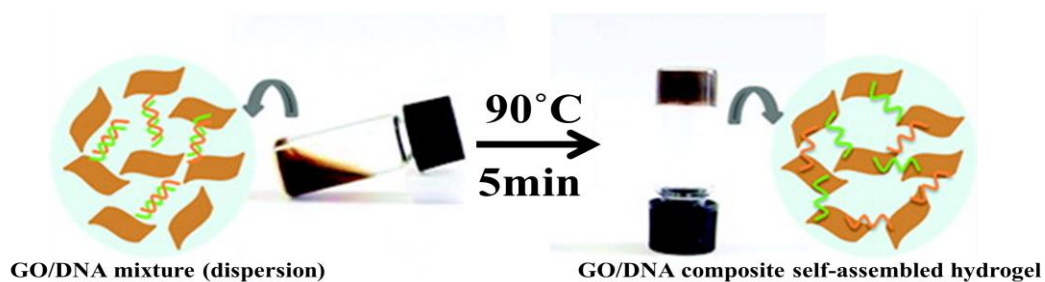


Figure 2-20. The procedure of preparing GO/DNA self-assembled hydrogel and the proposed gelation mechanism [47].

Controlling crystal structure or chemical doping of graphene with guest atoms has attracted considerable attention over the last few years to tune the electronic properties of graphene. Guest atoms such as nitrogen, sulfur, phosphorus and boron are the most

commonly used dopants for the doping of carbon materials, which have effectively extended their end use applications. Nitrogen, in particular, seemed to be the ideal dopant for carbon materials such as carbon nanotubes [312, 313] graphene [48, 314] and their composites [315, 316] because of its comparable atomic size to carbon and its high electronegativity [292].

Wang et al. [48] synthesized nitrogen doped graphene (NG) using ranges of amino acids as nitrogen source via hydrothermal method which was accompanied by the reduction of GO as the oxygen containing groups were reduced. Their extensive analysis on NGasp, NGarg and NGgly compared with rGO reduced the same method in the absence of amino acids. Their nitrogen adsorption results showed that NGasp had the largest surface area and total pore volume and that the NGarg exhibited significantly lower surface area and volumes than other samples. This could be due to different interactions of negatively charged aspartic acid, positively charged arginine and glycine with the negatively charged GO sheets. As shown schematically in Figure 2-21, the negatively charged GO sheets, attract similarly with the $-NH_3^+$ group of all amino acids through electrostatic attraction, which endows with their binding with GO surface. The negatively charged groups (COO^-) can repel the negatively charged GO sheets, which can enhance the repulsive force between the GO layers. In contrast, the counter-ions of positively charged arginine and glycine were attracted by negatively charged GO which weakened the electrostatic repulsion of GO sheets. The former enhanced repulsive force allows consecutive expansion of the graphene interlayer spacing, but the latter narrowed the interlayer distance and ultimately leads to aggregation of graphene sheets. The graphene layer expansion combined with the effect of nitrogen doping in NGasp not only led to the largest accessible surface area, but also exhibited the highest electrochemical performance compared with other samples. Their XRD investigating the d002 peaks as a support to surface area and pore volume measurements implied that the interlayer spacing of NGgly and NGarg are smaller than that of NGasp, but all are less than 1 nm (in microporous range). However, their SEM images together with the BJH method of the PSD analysis revealed the presence of even bigger pore size in mesoporous (~ 2.6 nm for NGasp) and macroporous (~ 1 μm) structure in each sample, indicating that hydrothermal method may

not be the suitable method for LBL assembly of graphene sheets in terms of controlling the pore size and 3D structure of graphene constructs.

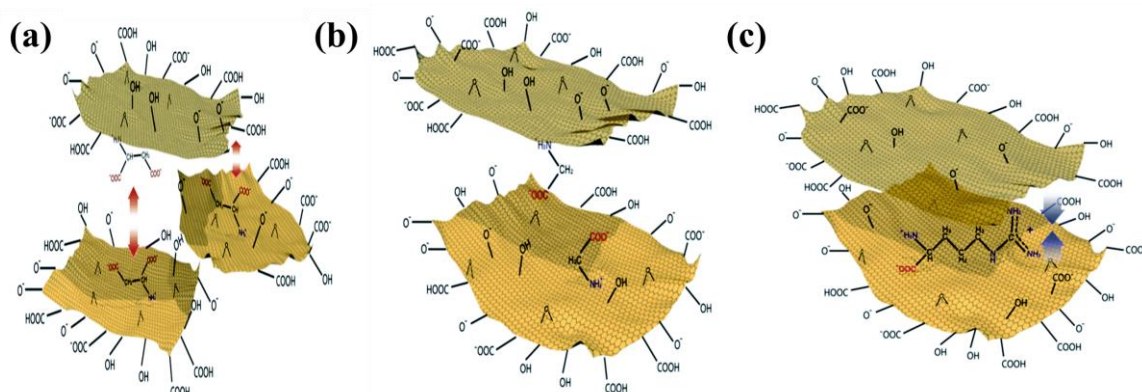


Figure 2-21. Probable interaction between amino acids and GO. (a) DL-aspartic acid with GO, (b) L-glycine with GO, and (c) L-arginine with GO [292].

Peptide as a short chain of amino acids was used in GO hybrid hydrogel for anticancer drug delivery purpose with near-infrared (NIR) light triggered release functionalities. The reason that Wu et al. [49] hybridized pyrene ending peptide (PyGAGAGY) with GO sheets (GOS) was the gelation problem of the peptide as the highly hydrophilic bit, GAGAGY, does not allow to form gel. Their design of peptide was smart in that it could bind with graphene sheets from either end; graphene binding motif (pyrene) from one end and tyrosine from the other end, bound physically and chemically with GO surface (the process schematically shown in Figure 2-22). Owing to strong π - π stacking between pyrene and graphene and covalent photo-crosslinking of tyrosine to the GO surface, a stable hydrogel with reasonable flexibility was prepared. In addition, the repeat sequence of GA in the middle of peptide subsequently leads to the formation of β -sheets between adjacent peptides [317], that facilitated the inter-sheet crosslinking, consequently strengthening the hydrogels. This hydrogel was then used for controlled drug release application, where NIR irradiation played a central role in triggered release on demand. Using different powers or different irradiation time, they could adjust the local temperature of the hydrogel. As soon as the temperature reached to ~ 47 °C, the β -sheet structure of PyGAGAGY melts, starts unfolding, and also disrupts the π - π stacking between pyrene and GOS, and together these events facilitated the release of drugs. NIR irritation acted as a promising stimulus for controlled drug release, because upon laser irradiation each time, the drug exhibited a burst release and the release was terminated

once the laser was turned off. Although the hybrid hydrogel carried excellent drug loading and release properties, that could be further enhanced by controlling the morphology of hydrogel. Their SEM and TEM images showed that the inter-crosslinking between peptides did not occur in a controlled way and this resulted in random size of interweaved fibrous peptide and ultimately non-uniform assembly of graphene sheet. Other characterizations may also be required to qualify the peptide decoration in between GO sheets, and more importantly to ensure whether only a monolayer of designed peptide or their aggregate performs the LBL assembly of graphene sheet.

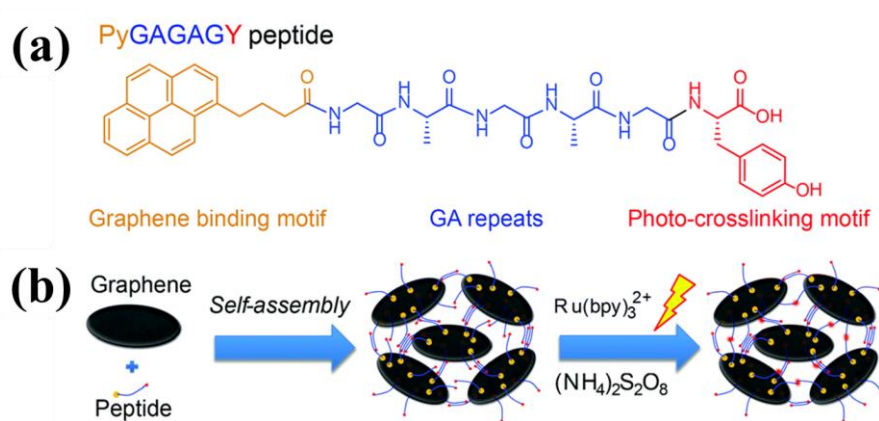


Figure 2-22. The design of the hybrid hydrogel. (a) The peptide sequence. (b) The hierarchical construction scheme for the hydrogel [49].

Organic molecules of different sizes and binding groups [47-49, 302, 306, 307] were intercalated between graphene sheets and this successfully increased their interlayer spacing. However, the uniformity of pore size distribution in their macroscopic structure and their stabilities were not well-understood. Recent research have demonstrated that regardless of their sizes, small and large biomolecules (such as peptide, or protein and enzymes) assemble either to the edge or planar surface of graphene, GO, or rGO via simple physisorption or through electrostatic, hydrogen bonds, hydrophobic or π - π stacking interactions [318-323]. However, the design of biomolecules might have greater impact than just adsorbing on surface when applied to the engineering of controllable defined assemblies. They can be engineered to help the graphene sheets LBL assembly and to aid in controlling their interlayer spacing. The impacts of their design along with their surface interaction will be extensively discussed in the next sections.

2.5 Experimental of protein/peptide adsorption on graphitic surfaces

Proteins/solid surfaces interactions have been an active area of study, which is of great interest to different fields of physic, biology, and engineering as it plays a key role in interfacial engineering, tissue engineering, materials science, nanotechnology, and biomedicine. [324-327]. For instance, in drug delivery system where the biocompatibility is of critical issues, a good understanding of the protein–surface interaction will aid to designing more effective delivery agents for cellular targeting and membrane penetration with minimum toxicity level [267, 328]. The initial event for a material when contacts with blood stream is the adsorption of proteins. It is been emphasized that the nature of adsorbed protein and its amount directly impact on the compatibility of the material [329].

Proteins are chemically engineered to interact and bind with specific surfaces, such as inorganic materials [330], biomaterials [331], CNTs [332, 333], and graphene [320, 334] to form ordered self-assembled nanostructures with controlled surface chemistry. Among these surfaces, graphene sheet, an individual layer of graphite, acts as an ideal planar platform for biomolecule adsorptions via enhancing the effective area of interaction without any significant perturbation to the biomolecules. It also does not involve in chemical reactions under standard conditions [335, 336]. Biomolecules have received interest because they can be designed in a controlled way to conjugate non-covalently with different surfaces with less disruption to either the surface or themselves. These attachments also enhance the surface biocompatibility [337] and minimize the toxicity risk [338] in biological applications. For some biomolecules from small DNA [339, 340] to large proteins [341, 342], it is critical for them to retain their biological activities on the surface as a small change in their conformation may result in undesirable biological consequences. Therefore, predicting their adsorbed conformation and controlling their physico-chemical properties at the graphene-biomolecule interface is pivotal to realizing their full potentials in biological applications.

Among different sizes and conformations of proteins, peptides have been the concern of many studies due to the flexibility in the selection, design, and tailoring of this versatile

biomolecule as a molecular building block [337]. Peptides are short from polymers of amino acid monomers linked by peptide bonds (covalent bond formed between two monomers when the carboxyl group of one monomer reacts with the amino group of the other monomer). They are easily distinguished from proteins based on the size, which contain fewer than 50 monomers [343]. Engineered artificial peptides and their interactions with solid surfaces have been suggested as a means whereby the self-assembly of nanoscale entities may form nanostructured materials [344]. The flexibility in design leads to control of the solid-peptide intermolecular interaction and also of the materials formation in order to produce the highly efficient self-assembled nano-constructs [345, 346].

The binding of peptides to graphitic surfaces concern the adsorption and/or desorption of peptides on these surfaces [347]. Few experiments with varied methods have been performed to qualitatively and quantitatively study the adsorption and structure of the peptides bound to graphitic surfaces. For instance, by using the phage display technique, atomic force microscopy (AFM), and Raman and fourier transform infrared (FTIR) spectroscopy, Katoch et al. [320] identified peptides with a selective affinity for graphene. Their results elucidated that a helical conformation peptide via its hydrophobic side-chain can non-covalently bind with the graphene surface and functionalize it without any chemical perturbation to the graphene structure. It has also been shown that the morphology of the peptide does not change significantly even after incorporating reduced graphene oxide sheets. Adhikari and Banerjee [348] carried out transmission electron microscopic (TEM) and AFM experiments to show the high morphological stability peptide whilst bound with graphene via its phenyl and fluorene aromatic rings. Aromatic containing biomolecules are capable to strongly interact with graphene's polarizable, hydrophobic surface. It has been shown both experimentally [349] and via molecular simulations [350-352] that aromatic groups adsorbed strongly to graphitic carbon surfaces. Using AFM imaging for graphite-binding peptide, So et al. [349] revealed that there is a strong correlation between the amino acid composition (their sequence) and the result of peptide self-assembly on the surface. They also found that the mutations of the peptide aromatic residues significantly influence the binding characteristics. Their results showed that by replacing Tyrosine (Y) residue (with aromatic side-chain) with alanine (A) (without

aromatic side-chain) the ability for the peptide to bind to graphite surface was eliminated, whilst replacing tyrosine with tryptophan (W) or phenylalanine (F), respectively, tunes the peptide's affinity to graphite from strong to weak or moderate binding. In other reports, ssDNA has exhibited relatively strong binding to graphene basal plane via the aromatic groups of the nucleobases through π - π stacking interaction [339, 340, 353, 354]. More interestingly the ssDNA retains its activity to hybridize with a complementary strand, even in the adsorbed state on graphene.

Depending on the surface characteristics (whether polar or non-polar), different interactions govern the peptide adsorption and assembly. Chen and co-workers [355] implemented their computational aided designed peptide (EAK16-II) in experiments to grow nanofiber out of peptide assembly on the negatively charged surface of Mica. This was to investigate the importance of peptide-peptide and peptide-surface electrostatic interactions in the affinity of peptide and its self-assembly on surface. An in situ atomic force microscopy and dynamic light scattering (DLS) and ζ -potential experiments were conducted for real time observing peptide adsorption on surface and measuring the nanofiber growth rate along with the peptide charge under various pH conditions. They introduced a controllable peptide assembly by controlling the peptide-surface and peptide-peptide interactions. The Strongest affinity of the peptide to the negative mica surface was seen when highly concentrated HCl (10 mM, pH=2.2) was used relative to that observed in pure water and 1 mM HCl solution, while the highest peptide adsorption rate was in pure water. Although the acidic environment makes the EAK16-II molecules positively charged and facilitating its interaction with negatively charged surface of Mica, these positive charges are enough to inhibit peptide-peptide and peptide-nanofiber assembly after a short nanofibers assembled on surface. This is due to the large repulsion between positively charged (protonated) residues of peptide in acidic environment, when the pH of solution is lower than the pK_a of the glutamic acid (E, pK_a of 4.05) and lysine (K, pK_a of 10.54). In the case pure water, the rate of peptide self-assembly and nanofiber growth was the highest as the pH is between the two pK_a of positively and negatively charged residues, leading to fairly distribute the opposite charges in the solution and enhancing the inter-peptide interaction. In contrast to the neutral and acidic condition, with using 1 mM NaOH, the pH increased to 9.9 very close to the pK_a (10.54) of lysine residues, hence, they became

slightly deprotonated and negatively charged which led to smaller adsorption rate than that in pure water and HCl. However, with further increasing in pH (to 11.5) and the concentration of the basic solvent (to 10mM), lysine became highly negative and no assembly of peptide was observed on mica substrate.

In another work, Chen and co-workers [356] investigated the adsorption of ionic peptide of EAK16-II on the HOPG and its comparative affinity and stability studies with the negatively charged surface of Mica. The EAK16-II nanofibers made by the peptide assembly on mica remain stable in acidic solution but not in alkaline solution, while they exhibited a high stability on HOPG surface regardless of solution pH. The lower stability EAK16-II modified Mica in basic pH was due to the weakening of peptide-surface interaction as a result of changing the charge to negative and enhancement in peptide-surface repulsion. When hydrophobic interaction governs the peptide-surface affinities, for instance, in EAK16-II modified HOPG, the interaction would be strong enough for not being affected by varying pH. Their AFM images evidenced to a highly ordered deposition of EAK16-II nanofibers on the HOPG (either parallel or aligned 60° or 120° to each other), whereas they formed a randomly oriented nanofiber networks on the surface of Mica. The highly ordered structure of EAK16-II on HOPG resembles the crystallographic structure of the graphite surface.

2.6 Molecular modelling of protein/peptide adsorption on graphitic surfaces

2.6.1 *The use of MD in peptide/graphene interactions*

Although experimental studies have substantially improved the understanding of both the impacts of the surface and the peptide on their binding conformations, the detailed mechanism of adsorption and structural dynamics at surfaces are not yet well understood. However, force-field based atomistic simulations (molecular mechanics, or MM) and molecular dynamics (MD) [348] can play valuable roles in providing detailed information on graphene-peptide surface interactions and any conformational changes in peptide. These adsorption processes can be modelled with tens of thousands of atoms at a given temperature and in a reasonable computational time. Computational studies

complementary to experimental studies have therefore been emerging about the protein adsorption on different surfaces in recent years.

MD simulation based research to date have clearly revealed that peptide adsorption on graphitic surface can comprise of direct surface [321, 328, 352, 357] and solvate mediated interactions [335, 351]. Direct graphene-peptide interactions may consist of hydrophobic [341, 352, 358, 359] and π - π stacking [321, 341, 360] interactions if the surface is non-polar and it could be electrostatic interaction when the surface is polar [341, 358]. Apart from graphene-peptide specific interactions, the interfacial water profile on graphene surface are also considered in the peptide adsorption process. It has been shown that water behaves in an unusual way at graphene and graphite surfaces as they form ordered layers of opposite charges [361, 362] that could potentially impact biomolecule dynamics [335, 351], particularly for peptides containing polar residues. These studies have focused on water layering and peptide conformational changes cover fix graphene sheets. However, to the best of our knowledge the peptide penetration into interfacial water of the flexible graphene sheet and its adsorption mechanism on the surface has not been well studied. It is worth to understand whether the ordering of water molecules is a surface flexibility dependent and if such layering has different behavior than that of the fixed graphene sheet. It is also vital to know if the oscillation of the flexible graphene has a serious impact on the peptide conformation. By elucidating the peptide behavior in interfacial water and on flexible graphene surface, MD simulation can aid in developing new peptide designs that demonstrate controllable and predictable binding interactions and structures. The choice of flexible graphene here further illuminate the graphene-binding peptide structure as the graphene sheets in reality exists flexible in aqueous phase.

In this review, the adsorption of peptides on different graphitic surfaces is investigated as they make similar interactions with peptides due to the similarities in carbon-carbon bonding and aromatic structures. However, among these surfaces, graphene sheet, an individual layer of graphite, acts as an ideal planar platform for biomolecule adsorptions via enhancing the effective area of interaction between the surface and biomolecules without any significant perturbation to the biomolecules. It also does not involve in chemical reactions in aqueous solution under standard conditions [335, 336].

Using MD simulations, Kim et al. [321] revealed that the designed peptides are able to bind to either the planar or the edge of graphene sheets through π - π stacking or electrostatic interactions, respectively. Chen and co-workers [328] using accurate all-atomic MD simulation and via the CHARMM22 empirical force field demonstrated the adsorption and initial assembly events of an ionic peptide, EAK16- II, on the extremely hydrophobic surface of HOPG. An accurate all-atomic MD simulation of EAK16-II adsorption on HOPG was performed using the CHARMM22 empirical force field. They used two peptide molecules with the same chain of AEAEAKAKAEAEAKAK (where A corresponds to alanine, E glutamic acid, and K lysine) mixing of neutral, positively and negatively charged residues (shown in Figure 2-23a). They believed that deposition of first peptide was governed mainly by the hydrophobic interactions between Alanine residues and the graphitic surface, while the second peptide approached the surface via both electrostatic and hydrophobic interactions. Unlike Alanine which bound tightly to the surface, the charged residues stayed deeper into the solvent led to electrostatic interactions between opposite charged residue of two peptides (shown in Figure 2-23b). Although the hydrogen bonding had a non-significant impact during peptide adsorption, it aided with inter-peptides interactions and succeeding peptide assembly process on the surface. The peptide chains could self-assemble both in solution and on the surface; thus, indicating that peptides intermolecular interactions during their adsorption and initial folding/assembly stage is also of vital cases to be studied besides the peptide adsorptions on the surface.

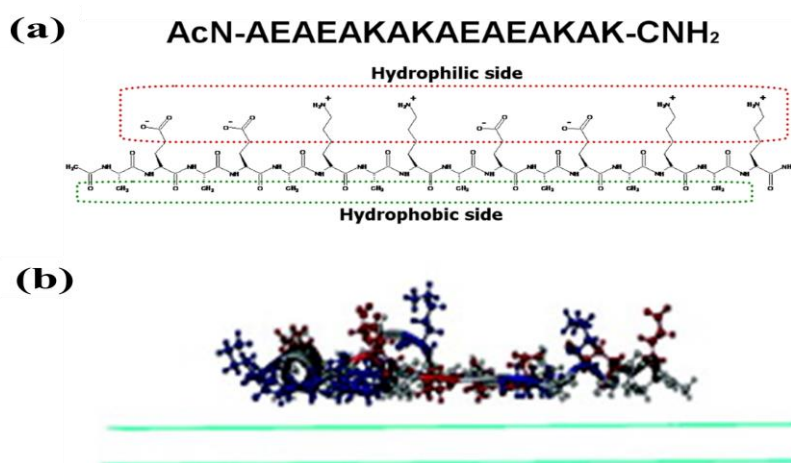


Figure 2-23. (a) Schematic diagram of EAK16-II structure [356] (b) Side view of the snapshots of the peptide-graphite surface system at adsorbed state (the three residues alanine, glutamic acid, and lysine are colored in gray, red, and blue, respectively) [328].

Recently, numbers of interesting computational studies have been carried out on peptides adsorption, and their interactions with fixed graphitic surfaces, for instance single graphene sheet [320] or graphite [328, 359, 363]. Their observations showed that the peptides have undergone some conformation changes, due to their strong interaction with the graphene surface. Their findings can be helpful to better understand the intermolecular interactions in peptide-graphene system, but it is still far to match with what is really occurring in the experiment. In the experiment, both peptide and graphene sheet are flexible and there are more than one graphene sheet which interact with both of peptide and other graphene sheet at the same time. To the best of our knowledge, the adsorption behavior in such complex system either computationally or experimentally has not been reported elsewhere. The effects of charged groups (oxygen functionalities) on graphene and peptides concentration to build a framework of graphene nano-construct still remained unclear. In general, molecular simulation methods hold promise to provide an excellent complement to experimental studies [364] and it is this which motivated to work computationally and experimentally in this project. However, before conducting simulation, very well understanding of different methods of simulation together with the applied empirical forcefields are necessary.

2.6.2 Simulation

2.6.2.1 Potentials and molecular simulation methods

Molecular simulation methods can basically be separated into two distinct categories; (1) quantum mechanics (QM) methods which treat electrons as the basic elements of the system and apply Schrödinger's equation to calculate the molecules behavior, and (2) classical mechanics (CM) methods which treat individual or groups of atoms as the basic units of the system by applying empirical force fields to calculate the molecular behavior [364, 365]. However, QM is very accurate, but it is generally restricted to small set of atoms and unsuitable for the simulation of protein (or peptide)-surface interactions.

CM simulation methods can be further subdivided into three basic types: (1) molecular mechanics (MM), (2) Monte Carlo (MC), and (3) molecular dynamics (MD) methods [365]. MM methods are used to calculate the potential energy of a molecular structure based on the coordinates and bonded state of the atoms. It includes 'energy

minimization’ or ‘geometry optimization’ and almost always used at the front end of an MC or MD simulation. MC and MD methods are similar to MM methods in using the same empirical force field for the calculations; however, the MC and MD methods incorporate temperature for calculation of thermodynamic properties of the system, especially changes in free energy. The difference between MC and MD are in time dependency. MC can calculate thermodynamic properties (e.g., changes in free energy) of a system, but do not provide direct information regarding the rate, or the kinetics of molecular processes. Unlike MC, MD is time dependent and is suitable to predict both the thermodynamic and kinetic behavior of the system by using Newton’s equations of motion. MD methods are much more commonly used to simulate the behavior of large biomolecular systems since MC is drastically limited for any large change in the position of the atoms of the protein for instance when the simulation is conducted in explicit water.

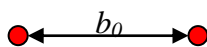
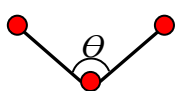

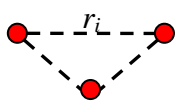
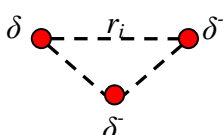
2.6.2.2 Empirical Force field

In addition to Newton’s equations of motion, there are some other equations based on molecular thermodynamics and statistical mechanic which are useful to control and determine the system temperature and pressure. The empirical force field given in equation below (for which the terms are displayed in **Table 2-1**) that is used in an MM, MC, or MD simulation to calculate the potential energy (E) of the biomolecular system (e.g., proteins, carbohydrates, phospholipids, RNA, and DNA).

$$E = \sum_{bonds} K_b (b - b_0)^2 + \sum_{angle} K_\theta (\theta - \theta_0)^2 + \sum_{dihedrals} K_\phi [1 + (n\phi - \delta)] + \sum_{vdW} 4\epsilon_{ij} \left[\left(\frac{\sigma_{ij}}{r_{ij}} \right)^{12} - \left(\frac{\sigma_{ij}}{r_{ij}} \right)^6 \right] + \sum_{Coulomb} \frac{q_i q_j}{4\pi\epsilon_0\epsilon_r r_{ij}} \quad (2-2)$$

where the first three terms on the right-hand side of the equation represent the potential energy of the covalently bonded atoms in the system generated by covalent bond stretching, bond bending, and dihedral bond rotation, respectively. The last two terms of this equation represent the contributions of the non-bonded interactions (Lennard-Jones (L-J) 12-6 interactions and electrostatic interactions) to the potential energy of the system [364].

Table 2-1. Bonded and non-Boned terms of empirical forcefield.

Force field equation		Terms	
$E = \sum_{bonds} K_b(b - b_0)^2$ $+ \sum_{angle} K_\theta(\theta - \theta_0)^2$ $+ \sum_{dihedrals} K_\phi[1 + (n\phi - \delta)]$	Bond stretching		Bonded terms
	Angle bending		
	Dihedral rotation		
$+ \sum_{vdW} 4\epsilon_{ij} \left[\left(\frac{\sigma_{ij}}{r_{ij}} \right)^{12} - \left(\frac{\sigma_{ij}}{r_{ij}} \right)^6 \right]$ $+ \sum_{Coulomb} \frac{q_i q_j}{4\pi\epsilon_0\epsilon_r r_{ij}}$	12-6 L-J interactions		Nonbonded terms
	Electrostatic interactions		

The values of empirical parameters for both bonded and non-bonded terms are extremely important. For a system with properly parameterization, an empirical force field can provide an accurate representation; however, for the system which is not parameterized properly, the predicted behavior of the system would be far from reality [364].

Chapter 3: Methodology

3.1 MD simulations

In this study, three series of MD simulations were carried out before conducting experiments. First was a system containing single graphene sheet with a MD designed peptide molecule (UA2) in the bulk water phase at about 15 Å above graphene sheet, in order to investigate the feasibility and the mechanism of peptide binding to graphene surface. Second was the system with two graphene sheets with different numbers of peptide to promote the self-assembly of graphene sheets and constructing hydrogels with layered structure. After accomplishing the second set and validation the self-assembled graphene nano-constructs, the third set of MD simulations dealt with assessing the nano-constructs in the application for drug (DOX) taking-up. In all simulations, the graphene and UA2 peptide (with the sequence of FFGGEEEEEEGGFF) were, respectively generated using the graphene and protein builder in the VMD package.[366] In keeping the neutral pH, zwitterionic form of the UA2 molecule with negatively charged side-chains of the glutamic acid residues was modelled. DOX molecule and its force field parameters were generated by SwissParam Technology[367], where the NH_3^+ group of DOX deprotonated to NH_2 in neutral pH condition. The intra-graphene and peptide-graphene interactions in nano-constructs together with the DOX interaction with nano-construct were all modelled by the CHARMM27 all-atom forcefield [368] and water molecules treated using the TIP3P model. The MD simulations were performed using the NAMD [369] free software, (see details of each MD simulation procedure in its relevant chapters of thesis).

3.2 Experiments

3.2.1 *Material and Chemicals*

The details of materials and chemicals used in this study are given in Table 3-1:

Table 3-1. Materials and chemicals used in this study.

No	Materials and chemicals	Formula	Supplier
1	Natural graphite, (325 mesh, 99.8%)	C	Alfa Aesar
2	Sulfuric Acid	H ₂ SO ₄	Sigma Aldrich
3	Phosphoric Acid (85wt. % in H ₂ O)	H ₃ PO ₄	Sigma Aldrich
4	Potassium Permanganate	KMnO ₄	Sigma Aldrich
5	Hydrogen peroxide (30 wt% in H ₂ O)	H ₂ O ₂	Sigma Aldrich
6	Hydrochloric acid (32wt% in H ₂ O)	HCl	Sigma Aldrich
7	Hydrazine	N ₂ H ₄	Sigma Aldrich
8	Ammonia	NH ₃	Sigma Aldrich
9	Fluorescein isothiocyanate–dextran (FITC)-(4kD, 10kD and 20kD)	C ₂₁ H ₁₁ NO ₅ S	Sigma Aldrich
10	Doxorubicin hydrochloride	C ₂₇ H ₂₉ NO ₁₁ ·HCl	Sigma Aldrich
11	Sodium chloride	NaCl	Sigma Aldrich
12	UA2 Peptide	FFGGEEEEEGGFF	Synthesized in Laboratory

3.2.2 Preparation

Below are the information in regard to step by step production of rGO from natural graphite and fabrication of related hydrogels in both wet and freeze-dried forms. Detailed experimental procedures for different characterizations and applications of prepared hydrogels will be explained in their relevant chapters.

3.2.2.1 Preparation of graphene oxide (GO)

Graphite oxide or Graphene oxide was prepared by the oxidation of natural graphite according to the improved Hummer's method [88]. Briefly, a 9:1 mixture of concentrated sulphuric acid and phosphoric acid (120:13 mL) was cooled overnight to 4 °C. The already cooled acid mixture was slowly added to graphite powder (1 g) and potassium

permanganate (6 g) under stirring at room temperature. Then, the mixture was heated to 50 °C for about 12 hrs to form a thick paste. After the reaction, the paste was cooled down to room temperature and quickly poured onto ice cubes (150 mL) with 30% hydrogen peroxide (1 mL) for an hour. The mixture was washed and filtered with distilled water and hydrochloric acid (32%) followed by repeated washing with ethanol and eventually with Milli-Q water. For each successive wash, the obtained brown dispersion was centrifuged at 4400 rpm for 2 hrs to remove residual salts and any un-exfoliated graphite oxide. The obtained GO was vacuum dried overnight at room temperature.

3.2.2.2 Preparation of reduced graphene oxide (rGO)

In a typical procedure for chemically reducing GO to prepare rGO, the GO from previous step was used to prepare homogeneous dispersion (0.5 mg.mL^{-1}) in a 25 mL flask. Different reduction experiments were conducted by varying hydrazine amount and the reduction temperature. Hydrazine solution (35wt% in water) of different amounts (varied between 25 and 75 μl) and constant volume (75 μl) of ammonia solution (28 wt% in water) were added into the flask and mixed with the GO dispersion. The dispersions with different amounts of hydrazine were shaken vigorously and stirred for a few minutes, then placed in an oil bath (with the temperature varied between 85 and 95 °C) for 1hr. In all reduction experiments, the brownish dispersion of GO turned to black rGO. The rGO dispersions prepared were used for further characterization and hydrogel fabrication.

3.2.2.3 Preparation of reduced graphene oxide hydrogel (rGOH) thick films

To prepare the rGOH film, a 25 mL of rGO dispersion (0.5 mg.mL^{-1}) was filtered through a Millipore mixed cellulose esters filter membrane (47mm in diameter, 0.45 μm pore size,) by vacuum filtration. The vacuum was disconnected once no free rGO dispersion was left on the filtrate cake. The resultant rGOH film was then immediately transferred to a Petri dish and immersed in Milli-Q water overnight to remove remaining ammonia and unreacted hydrazine. A relatively thick film was carefully peeled from the filter membrane using tweezers. The obtained rGOH film was stored in Milli-Q water prior to any characterization to prevent the water evaporation. The thickness of the rGOH films can be controlled by adjusting the concentration and/or volume of feed rGO dispersion.

3.2.2.4 Preparation of peptide solution

The UA2 peptide was synthesised using a solid phase standard Fmoc chemistry procedure with a rotary sintered glass funnel [370, 371]. The UA2 stock solution of 25 μM was prepared by dissolving 4 mg of peptide into 150mM sodium chloride solution made in 100 mL Milli-Q water. The salt was used for enhancing the solubility of peptides. It is known that using high concentrations of NaCl perturbs peptide conformations and promotes peptides to form beta-sheets by reducing electrostatic repulsion [372-374]. Our simulation results have shown that the UA2 is stable in NaCl solution even at concentration as high as 0.3M.

3.2.2.5 Preparation of rGO binding peptide hydrogel (rGOPH) thick film

Non-covalent adsorption of UA2 onto the rGO sheets occurred by adding 25 mL rGO dispersions (0.5 mg.mL^{-1}) to 25 mL of UA2 (with different concentrations varied between 0.04 and 0.10 μM). The mixtures of rGO and UA2 were stirred for about 30 min and filtered through a mixed cellulose esters filter membrane (47mm in diameter, 0.45 μm pore size, Millipore) by vacuum filtration. The resultant rGOPH film was then washed three times and immediately transferred to a Petri dish and immersed in Milli-Q water overnight to remove the remaining unbound peptides.

3.2.2.6 Freeze drying

The wet hydrogel films were freeze-dried prior to their characterizations. The wet-state rGOH and rGOPH films were transferred into cylindrical containers and immersed into liquid nitrogen to freeze the hydrogels. A lab-scale freeze-drying device ALPHA 1-2LD plus (CHRIST, Germany) was used to dry the frozen films at the temperature of 188K and under the pressure of 10^{-2}Pa for 24 hrs.

3.2.3 Instrumentation

3.2.3.1 Zeta Potentials

In fact, there is no direct way of measuring the surface charge density and the zeta potential of particles. However, zeta potential can be calculated through the particles

mobility which is determined via electrophoresis phenomena. The particle mobility is measured by laser Doppler velocimetry and Smoluchowski model can be used to convert the mobility to particle zeta potentials. As a quantitative method, the zeta potential was utilized in this study to confirm the functional groups of aqueous GO/rGO dispersions after reducing GO at varying different parameters. The electromobility was monitored by a Malvern Zetasizer Nano-ZS particle analyzer.

3.2.3.2 Contact Angle

Contact angle in air measurements were taken using an Attension Theta optical tensiometer to establish the correlation between the GO reduction process and material hydrophobicity/hydrophilicity characteristics. The freeze-dried films of GOH and rGOH (with different reduction degree) were attached on a glass slide and water droplets (1~2 μL) were then dropped carefully on the surfaces of films. Wetting behaviors of each film was recorded and imaged using a camera installed on the tensiometer.

3.2.3.3 Raman Spectroscopy

Raman Spectroscopy was used to characterize the quality and graphitic structure of graphite powders, GOH, rGOH and rGOPH films. Raman relies on the Raman scattering of monochromatic light and records the shift of energy known as the Raman Shift calculated by the following equation:

$$\Delta\omega = \frac{1}{\lambda_0} - \frac{1}{\lambda_1} \quad (3-1)$$

where $\Delta\omega$ is the Raman shift (in cm^{-1}), λ_0 is the excitation wavelength, and λ_1 is the Raman spectrum wavelength. The Raman experiments were conducted using a HORIBA Scientific Raman system with the excitation wavelength of 537 nm. The freeze-dried hydrogel films were scanned while placing on a glass substrate. The Raman band of substrate at 520 cm^{-1} was used as a reference to calibrate the spectrometer. LabSpec Raman spectroscopy software was used to analyze of the spectra.

3.2.3.4 Scanning Electron Microscopy (SEM)

SEM is a nondestructive surface microscopy technique using a beam of electrons and the backscattered electrons to generate two dimensional images of the sample surfaces. The SEM experiment can be carried out either under vacuum or the environmental condition and the sample surface must be conductive. In the instance of non-conductive samples, sputter coating with other conductive elements (e.g. carbon, platinum and gold) is necessary before SEM imaging. A FEG Environmental (QUANTA_450) scanning electron microscope was used at various magnifications. Samples were adhered by conductive carbon tape to the side walls of nut mounted in metallic pegs. The sample films were oriented in a way that films cross sections were pointing to the microscope camera in order to better visualize the graphene parallel layering structure.

3.2.3.5 Transmission Electron Microscopy (TEM)

TEM is a powerful technique whereby a beam of electrons are transmitted through an ultra-thin sample under vacuum. Owing to the small de Broglie wavelength of electrons, TEM can resolve down to the nano-scale. Graphene sheets of single layer and multilayer rGOH and rGOPH were imaged under TEM using a Philips CM200 with a charge coupled device (CCD) camera, Gatan at the power of 80 eV. Sample preparation was done by crushing, ultrasonating and dispersing the graphene-related hydrogels in Milli-Q water. A small droplet of each dispersion was placed on a mesh carbon coated copper grid. After drying, the grid was placed in the TEM chamber for imaging.

3.2.3.6 Fourier Transform Infrared Spectroscopy (FTIR)

FTIR is a nondestructive technique where infrared (IR) radiation is passed through a sample in which some IR radiation is absorbed and some transmitted. Molecules absorb radiation, moving them to a higher energy state that causes molecules to stretch, bend, or rotate. The absorption spectrum is a physical property of the molecule; a molecular “fingerprint” identification. The term FTIR originates from the fact that a Fourier transform algorithm is required to convert time domain raw data into a frequency domain actual spectrum with either transmission or absorption percentage against wavenumber (cm^{-1}). The Nicolet 6700 Thermo Fisher FTIR Infrared Spectrometer was used to identify

the functional groups of freeze-dried hydrogels, particularly existence/removal of the oxygen containing groups on/from graphene sheet whilst oxidation and reduction process. The FTIR was attached with an ATR enabling the use of solid samples directly without any further preparation. The FTIR resolution was set to $.1\text{ cm}^{-1}$ at 64 scan rate and from 4000 to 600 cm^{-1} range. In order to collect the background before scanning the hydrogel samples, a spectrum was run without sample on the sample holder stage. The background spectrum was subtracted from the sample spectrum in order to avoid contributions of the ambient air. All measurements were conducted at room temperature.

3.2.3.7 X-ray Photoelectron Spectroscopy (XPS)

XPS is a technique for the surface elemental analysis which utilizes monochromatic x-rays in order to eject inner shell electrons of the sample surface along with their energy measurements. Unlike XRD, ultra high vacuum (UHV) is needed for the detector to record incoming photoelectrons. The identification of presented elements on the sample surface is carried out through the electron binding energy (E_b) that depends on the energy of the electronic orbit and the element from which the electron is emitted. Chemical shifts which are in effects of E_b are used to detect compounds of different electro-negativity and valance number in the sample. The XPS spectra are plotted as photoelectron intensity against binding energy providing with the information about the elements and their electronic states in the samples. A Kratos (UK) Axis-Ultra spectrometer with a monochromatic Al $K\alpha$ source (1487 eV) operating at 15 kV and 14 mA was used to estimate degree of oxidation, reduction, and chemical functional groups at the surface of GOH and rGOH. In the instance of the rGOPH samples, the XPS aided to measure the peptide concentration bound to the graphene surface with different degrees of reduction. The analysis of the photoelectron spectra (peak identification and curve fitting) was conducted using CasaXPS (V2.3.5) software. All hydrogel samples were freeze-dried and the XPS measurments were conducted at room temperature.

3.2.3.8 Wide Angle X-ray Diffraction (WAXRD)

WAXRD or generally known as XRD is another non-destructive technique used for the analysis of physical (crystalline or semi-crystalline) structures of solid materials at room

temperature. It is suitable to obtain information about the crystalline structures of the materials and amorphous materials exhibit poor feature whilst undergoing XRD experiments. By the use of electromagnetic radiation wave properties that interact with the atoms or molecules in the unit cell of a crystal, XRD is able to record the interference patterns in the form of peaks. These peaks at certain incident angle represent planes aiding to measure the interplanar spacing using the Bragg Relation as follows:

$$n\lambda = 2d_{hkl} \sin \theta \quad (3-2)$$

where n is the order of diffraction of parallel planes with indices (hkl), λ is the wavelength of x-ray, d_{hkl} is the interplanar spacing of planes (between the layers of atoms), and θ is the Bragg angle between the incident x-ray beam and the surface of crystal. Cu K α wavelength at 1.54 angstroms was used in X-ray instruments which is appropriate for most crystals. The XRD plots the sum of diffracted x-rays from the sample surface as a function of 2θ . In the context of layered graphene-related hydrogels; the XRD aids to infer the graphene interlayer spacing at different instance of with and without spacers in between sheets. All samples in the form of powder (graphite) or film (freeze-dried hydrogels) were placed on a glass substrate prior to XRD measurement.

3.2.3.9 Ultraviolet-visible (UV-vis) Spectroscopy

UV-vis as a non-destructive technique using ultraviolet-visible spectral region to irradiate liquid samples, excites their electrons, and measures their absorbance. The molecular structure of the liquid samples can be determined by knowing absorbance wavelengths and the electronic transition rules. These transitions then can be plotted as absorbance vs. wavelength. The major use of UV-vis in this study is to determine and monitor the solute concentration in a solution during adsorption and release into and from different media. According to the Beer-Lambert Law:

$$A = \log_{10} \frac{I_{in}}{I_{out}} = \varepsilon c L \quad (3-3)$$

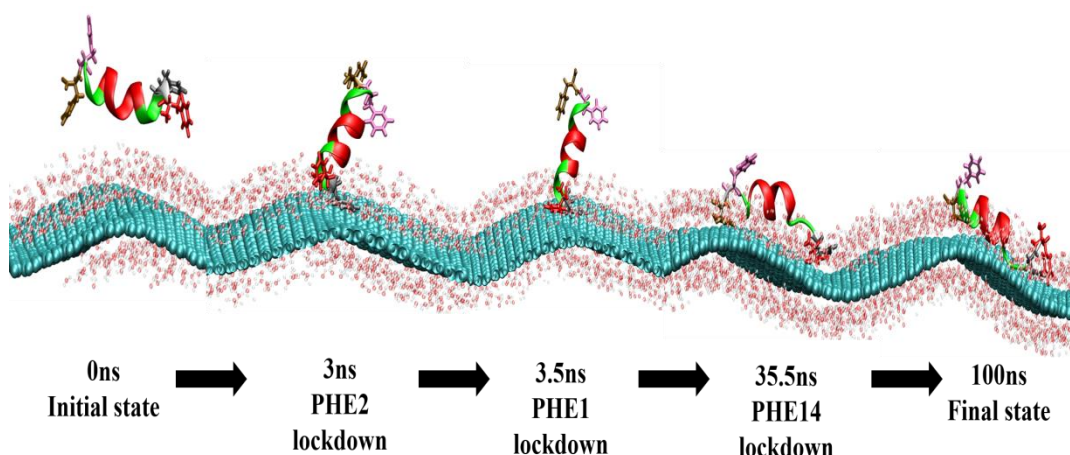
where A is measured absorbance, I_{in} is intensity of the incident radiation, I_{out} is the transmitted intensity, L is the path length of light travels through the cuvette, ε is the molar

extinction coefficient, and c is the sample concentration. In this study a UV-vis spectrometer (USB4000-UV-VIS - Ocean Optics) was used to confirm the reduction of GO to rGO, real time monitoring the solute concentration change in dye adsorption, drug loading and drug release. Quartz cuvette was used and Milli-Q water was used for baseline measurements. All UV-vis spectra were taken at room temperature. Ocean optics spectrasuite software was used for analysis of the spectra.

3.2.3.10 Atomic Force Microscopy (AFM)

AFM is a nondestructive surface analysis technique with a subnanometer level resolution. The operational basic principle of AFM is a Si tip of known dimensions mounted on a cantilever brought into near contact with the surface of the sample through a computer based control. The Si tip experiences forces from the surface of the sample (electrostatic, van der Waals interactions) which result in a deflection in the cantilever in accordance to Hooke's Law. The cantilever contains a piezoelectric element which transmits these forces into signals and ultimately converts them into a 2D and 3D images of the sample surface. The advantage of the AFM over other imaging techniques is the precise height measurement that can aid in measuring the graphene inter-sheet spacing (pore size) in graphene-related layered materials. The AFM samples in this study were prepared by drop-casting a diluted suspension of each sample onto a fresh-cleaved Mica substrate. Surface topography and height profile of the samples were examined by a MultiMode® 8 (Bruker) AFM and NT-MDT Ntegra Solaris AFM. A Nanoscope software was used to image the surfaces and height profile analyses of single layer and LbL films of graphene. All experiments were conducted on tapping mode at room temperature.

Chapter 4: Molecular Dynamics and Experimental Study of the Adsorption of a Designed Peptide on Graphene



Abstract

Non-covalent binding of peptide with a graphene surface is a promising method for their self-assembly and for producing graphene based nano-constructs. A newly designed amphiphilic surfactant peptide (with amino acid sequence of FFGGEEEEEEGGFF), named UA2, succeeded in interacting favorably with flexible graphene surfaces in an aqueous solution by hydrophobic to hydrophobic non-covalent interactions. The computer aided molecular dynamics (MD) simulations demonstrated that adsorption mechanism of a single UA2 peptide at a flexible graphene water interface is two-fold: (1) direct adsorption and (2) water-mediated adsorption. The phenylalanine (PHE) residues as hydrophobic face of UA2 are the dominant adsorption factor for the direct adsorption of the peptide as they prefer to lie flat against the graphene sheet with only a slight unfolding of the α -helical peptide backbone. This occurs through π - π stacking interactions and the regions between stacked PHE residues and the graphene sheet are devoid of water molecules. In the instance of water-mediated adsorption, the enhanced layering of interfacial water prevents the peptide from completely flattening and unfolding on graphene surface. This also allows the water molecules moving between the glutamic acid residue (GLU) and the graphene surface which endow wettability to the GRP-UA2 construct. The atomic force microscope

(AFM) and transmission electron microscope (TEM) images in agreement with MD simulation result demonstrated the UA2 affinity and its stable adsorbed structure toward the graphene surface. These results provide some structural information about the interactions of the amphiphilic peptide with a hydrophobic surface and their stability at the solid-water interface. We anticipate that the fundamental finding in this paper can be extended to design the self-assembly process of complex graphene binding peptide nano-constructs.

4.1 Introduction

The authors have recently developed a peptide that mediates the self-assembly of graphene oxide (GO) and reduced GO (rGO) to form a layered hydrogel with desired pore size as illustrated in Figure 4-1. The peptide is composed of three basic components: the ‘anchor’ that prefers to engage with the GO/rGO rather than water, the ‘bridge’ that prefers to remain in water, and the ‘neck’ between the bridge and anchor that is sufficiently flexible to allow the latter to fully engage with the graphene whilst leaving the former within the solution phase. By having an anchor at either end of a bridge of a particular size, graphene sheets are drawn together to form the layered structure with a corresponding pore size.

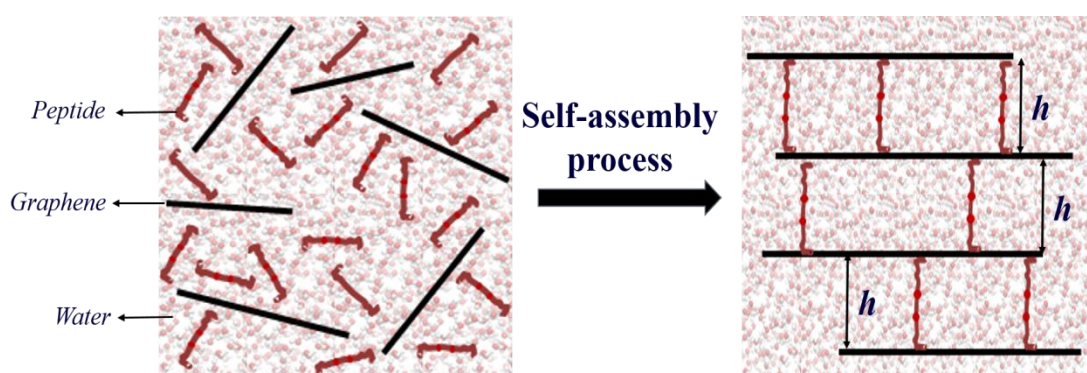


Figure 4-1. Self-assembly of graphene hydrogel construct with tuneable pore size (h)

There are a variety of possible candidates for the three components of the peptide used to create the material illustrated in Figure 4-1. The one of particular interest here, which has been shown through experiment to yield the layered structure with a pore size of around 2.6 nm [375, 376], is $F_2G_2E_6G_2F_2$, henceforth termed UA2. As shown in Figure 4-

2, this sequence yields a bridge that is α -helical in nature, as suggested by the work of [377, 378]. Selection of the anchor groups was informed by our prior work [363, 379], which suggests that the aromatic rings in phenylalanine (and other aromatic-containing residues) may well engage with the graphene through what are presumably π - π stacking interactions. As part of our efforts to test this hypothesis, we have used molecular dynamics (MD) simulation to understand the adsorbed state of the peptide shown in Figure 4-2 and the mechanism by which it is formed from the bulk phase. In as far as is possible, the predicted peptide adsorbed state was validated by use of atomic force microscopy (AFM). This combined modelling and experimental study is reported here. The modelling and experimental methodologies are first detailed along with the materials used. The modelling results are then presented and compared with prior work focused on peptide/protein adsorption on graphite and graphene. The AFM-based validation is then presented and discussed before conclusions are drawn.

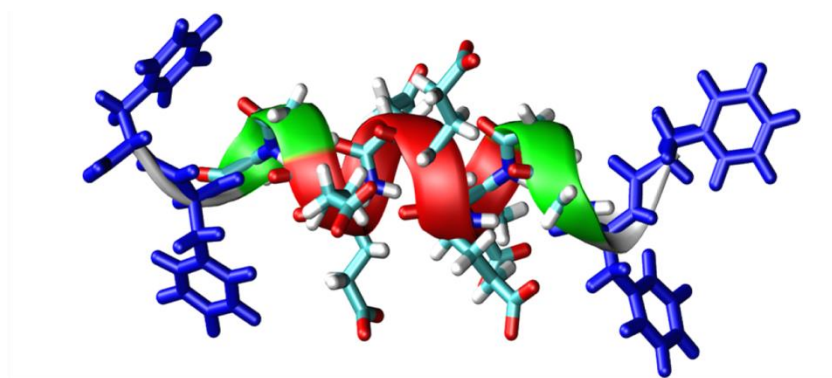


Figure 4-2. The equilibrated structure of the peptide in physiological solution after 10ns of MD simulation.

4.2 Methods

4.2.1 *Molecular Modelling*

The molecular model of the UA2 peptide was generated using the protein builder in the visual molecular dynamics (VMD) package [366]. In this study, all MD simulations were performed using the NAMD program [369]. The peptide intramolecular interactions and peptide-water interactions were evaluated using the CHARMM27 force field [368] with the TIP3P explicit water molecule [380]. All simulations were undertaken at 298 K and 1 atm. Two different systems were modelled as outlined below.

For the first system of peptide in water, without the presence of a graphene, a single peptide was placed in a periodic cubic water box of size $50 \times 55 \times 43 \text{ \AA}^3$. The system was then solvated by water molecules model with sodium ions added to match the negatively charged glutamic acid residues of the bridge and, hence, ensure overall charge neutrality of the simulation cell [381]. Energy minimization and system equilibration was then carried out for 200 ps and 1 ns respectively, until the root mean square deviation (RMSD) and the system's total energy became stable.. Then MD production run was undertaken for 10ns in the isothermal-isobaric ensemble to explore peptide conformation in solution. The Langevin thermostat was employed to integrate equations of motion with a time-step of 2 fs. Long-range full electrostatic interactions were handled using the Particle-Mesh Ewald (PME) approach with a cut-off of 1.2 nm.

The second system was constructed by placing a single flexible graphene sheet in a periodic rectangular simulation cell with a box size of $55 \times 50 \times 50 \text{ \AA}^3$, along with the designed peptide (from the first system), and solvated using water. Energy minimization and system equilibration were carried out in a similar manner to that of the first system. The NPT ensemble was used for the production MD run, with simulation conditions as specified above for the first system. Periodic boundary conditions ensured that the graphene sheet modelled here was of infinite size. To ensure the feasibility of binding the peptide with graphene plane and in order to establish the generality of the adsorption mechanism, 45 simulations were undertaken for the same conditions other than using different initial peptide configuration. The initial configurations were generated by inserting the peptide above the centre of the graphene surface such that its centre of mass (CoM) was 20 \AA above the graphene surface. The peptide was then rotated in increments of 18 degrees around two axes that pass through its centre of mass and are perpendicular to each other while at the same time being parallel to the graphene sheet and aligned with its edges. In addition to 40 configurations generated in this way, 5 more initial configurations were created in which the peptide was randomly oriented. (representative snapshots shown in Supplementary Figure 4-3). The simulations for all 45 different configurations were continued until 100ns.

4.2.2 Microscopy

4.2.2.1 Materials

Natural graphite (325 mesh, 99.8%) was obtained from Alfa Aesar. For the GO and rGO preparation (whose dispersions are shown in Supplementary Figure 4-1), H₂SO₄, H₃PO₄, KMnO₄, H₂O₂, HCl and hydrazine (N₂H₄) and Ammonia (NH₃) were used as received from Sigma Aldrich except the peptide. The peptide was synthesized in-house using a solid phase standard Fmoc chemistry procedure with a rotary sintered glass funnel [370, 371]. Peptide had ~90% purity.

4.2.2.2 Transmission Electron Microscopy (TEM)

The morphology of the rGO before and after peptide adsorption was also examined using a Philips CM100 TEM. The TEM samples were prepared by placing a small drop of (10 times diluted suspension in Milli-Q water: 0.05mg ml⁻¹) of rGO on a carbon coated copper grid. After imaging of the rGO sample, a small drop of peptide was added on the same grid, left undisturbed overnight to allow peptide adsorption and then drying.

4.2.2.3 Atomic Force Microscopy (AFM)

The surface topography of reduced graphene oxide (rGO), whose preparation is reported Supplementary Information, and its height profile before and after the peptide adsorption were examined by AFM (NT-MDT Ntegra Solaris) in tapping mode. The rGO-only samples were prepared by drop-casting a 10 times diluted suspension of the rGO Milli-Q water (0.05mg ml⁻¹) onto a cleaned mica substrate. Samples were then allowed to dry in air before imaging immediately thereafter. The rGO-peptide samples were prepared by adding a droplet of diluted peptide solution (0.01μM) immediately after the rGO-only sample has been placed on the mica giving 20 minutes to allow the peptide to completely adsorb on to the rGO.

4.3 Results and Discussions

4.3.1 *Peptide structure in the solution phase*

The peptide structural stability in the solution phase was explored by the time evolution of the helicity over 10ns of MD production run. As exhibited in Supplementary Figure 4-2 (black line), the degree of the peptide helicity is nearly constant at an average of 90% within 10ns of simulation compared to the helicity of the initial equilibrated structure. Although GLU had the highest propensity to form the helical structure, the neighboring GLY and PHE except the N- and C-Terminus residues also contributed in part to the helical structure of the designed peptide. This also confirms the stability of the peptide in neutral pH water. The root mean square deviation (RMSD) is another technique to quantify the structural change in the peptide after being relaxed and equilibrated for 10ns (Shown in Supplementary Figure 4-2, red line). The RMSD of peptide backbone leveled off at average value of $\sim 0.88 \text{ \AA}$ with fluctuation of $\pm 0.28 \text{ \AA}$ about the mean value demonstrating that the level of changes is very low and again confirming the high structural stability of the designed peptide in the ionic water solution.

4.3.2 *Adsorbed peptide structure*

4.3.2.1 Modelling

In all 45 simulations, the peptide was observed to adsorb onto the graphene surface without any significant change in its secondary or tertiary structures. Four examples of initial configuration together with the adsorbed structure of the peptide on graphene are shown in Supplementary Figure 4-3, in which at least two of its four aromatic residues PHE(1), PHE(2), PHE(13) and PHE(14), (shown in blue, black, pink brown stacks, respectively) bind to the graphene, typically with the aromatic ring parallel to the surface. Similar to previous reports [350-352, 363, 379], the affinity for such carbon aromatic ring containing groups for a graphitic surface is not unexpected. Adsorption of peptides with any orientation was found to be intrinsically strong with similar surface interactions on the graphene hydrophobic surface even in the initial adsorption stage. This process led to a similar spreading of peptide on the surface, making both anchor groups in contact with the

surface leading to a very strong and basically irreversible adsorption (see shown in Supplementary Figure 4-3).

To better understand the adsorption behavior, we have investigated the binding geometry of the PHE aromatic rings as well as the ring-tilt angle with respect to the normal of graphene surface. The distribution of tilting angle between the normal of PHE rings and graphene surface correlating with the ring-surface distance throughout the simulation are shown by contour plots in Figure 4-3. The darker regions in each plot indicate that the rings predominately sit parallel to the surface (with a tilting angle close to zero) when they are within its vicinity. Some fluctuation is seen in the tilting angle plots which are due to the flexibility of the graphene sheets. However the PHE aromatic rings are quickly able to attain back their parallel ordering form. The complete parallel orientation occurs when the ring reaches to 3.3Å to the surface where the π - π stacking interaction occurs between any carbon aromatic rings. (The best example of π - π stacking interaction is graphite whose graphene interlayer spacing is 3.35Å) There are some minor separated regions seen for PHE13 and PHE14 which are the sign of their aromatic rings popping off from the surface. These could be attributed to the oscillation of C-terminus as its negatively charged and influenced by high negative charge density of the interfacial water, which is illustrated in Figure 4-4a and b. As a result the PHE residues at this end of peptide try to fluctuate between flat and no-flat mode until they find proper spatial arrangement on the surface which will be discussed later in the section of graphene-peptide interaction. However, we believe that this occurrence does not have any significant issue on peptide stability in its adsorbed state.

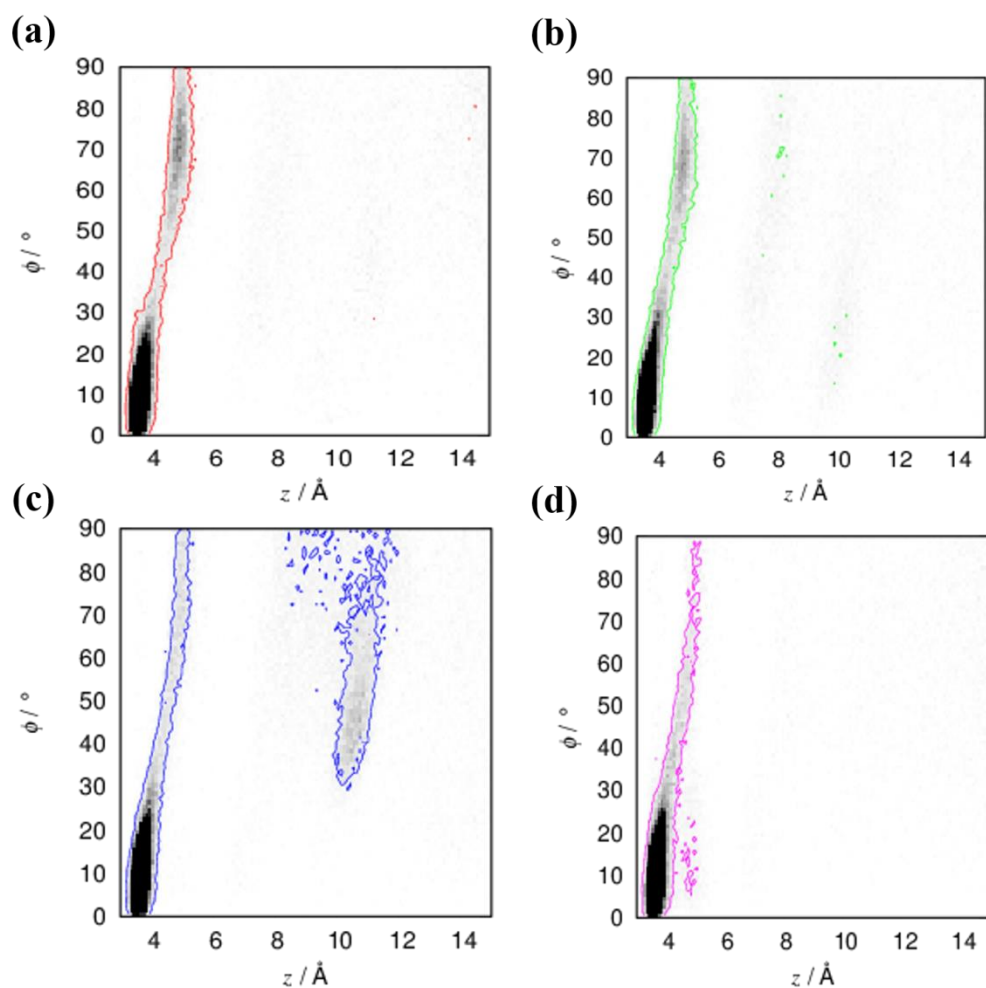


Figure 4-3. Contour plot for distribution of tilting angle between the normal of PHE rings and graphene surface correlating with the ring-surface distance for (a) PHE1, (b) PHE2, (c) PHE13 and (d) PHE14. (Derived from all 45 MD simulations.)

Although in all the 45 simulations undertaken, the π - π stacking interaction were the leading factor to initiate the peptide adsorption on the surface, there appears to be another strong interaction occurs between the surface and peptide which pulls the peptide down toward the graphene surface. Figure 4-4a reveals the origin of this interaction that also induces peptide stability on the surface. In part, the origin is the layering of the water molecules adjacent to the graphene surface as is revealed in Figure 4-4a, which has the effect of projecting the graphene surface around 10 Å into the solution. More importantly, however, is the orientational ordering of the water adjacent to the graphene surface. It has been shown that water behaves in an unusual way at graphene and graphite surfaces as they form ordered layers of opposite charges [362, 382] that could potentially impact

biomolecule dynamics [335, 351], particularly for peptides containing polar residues. However, those studies have focused on water layering and peptide conformational changes over fix graphene sheets. Similarly, for our case of flexible graphene sheet, Figure 4-4a revealed the multiple peaks in the hydrogen atom density profile and its difference from that of the oxygen atoms. The hydrogen and oxygen atoms carry partial charges of opposite sign (the net charge is shown in Figure 4-4b) , and this orientational ordering means that the graphene surface is endowed with charged layers that in effect bringing electrostatic interactions into play for the peptide charged residue and the solid surface.

Here we found that the second factor responsible for the strong adsorption of the UA2 is the strength of the interaction between the graphene surface and the GLU (7 and 8) which anchor on top of the first water layer (seen in Figure 4-4a at *height* $\sim 4\text{\AA}$ above graphene). The GLU side-chain distribution in Figure 4-4c is in agreement with the GLU normal distance above graphene shown in Supplementary Figure 4-4. This demonstrates that the GLU residues with negatively charged side-chains did not initiate the lockdown (adsorption in the first water layer) due to the large negative charge associated with the first water layer oxygen atoms. GLU (7 and 8) only anchor on top of the first water layer and the water molecule can pass through them and the graphene surface as is shown in the inset image of in Figure 4-4. However, the GLU (7 and 8) side-chain could not overcome the negative charge barrier seen *at height between 3 to 4 \AA* in Figure 4-4b, but their average interaction energy with the graphene surface is as large as $8.85 \text{ kcal.mol}^{-1}$ in last 60 ns of simulation, and only $3.5 \text{ kcal.mol}^{-1}$ less than the already lockdown PHE residues (shown in Supplementary Figure 4-5). This suggests the presence of the GLU residue plays a central role in stabilizing the UA2 in the vicinity of the graphene surface, and aids the PHE and GLY residues to remain in their lockdown phase. Such strong interaction between charged residues and charged water layers are addressed as solvent-mediated interactions [335, 351] in which the charged layer of interfacial water could potentially impact biomolecule dynamics [335, 351], particularly for peptides containing polar residues. Beside all, the hydrophilic properties of GLU combined with hydrophobic behaviors of graphene and peptide hydrophobic bound residues endow a reasonable amphiphilicity to the graphene binding peptide structure.

These explorations revealed that the dynamics of peptide adsorption and desorption on the surface are controlled by the property and the texture of the surfaces, adjacent water molecules' orientations, and the design of the peptide. Hence, surface design and modification may also enhance the possibility of regulating the peptide adsorption and/or desorption behaviors.

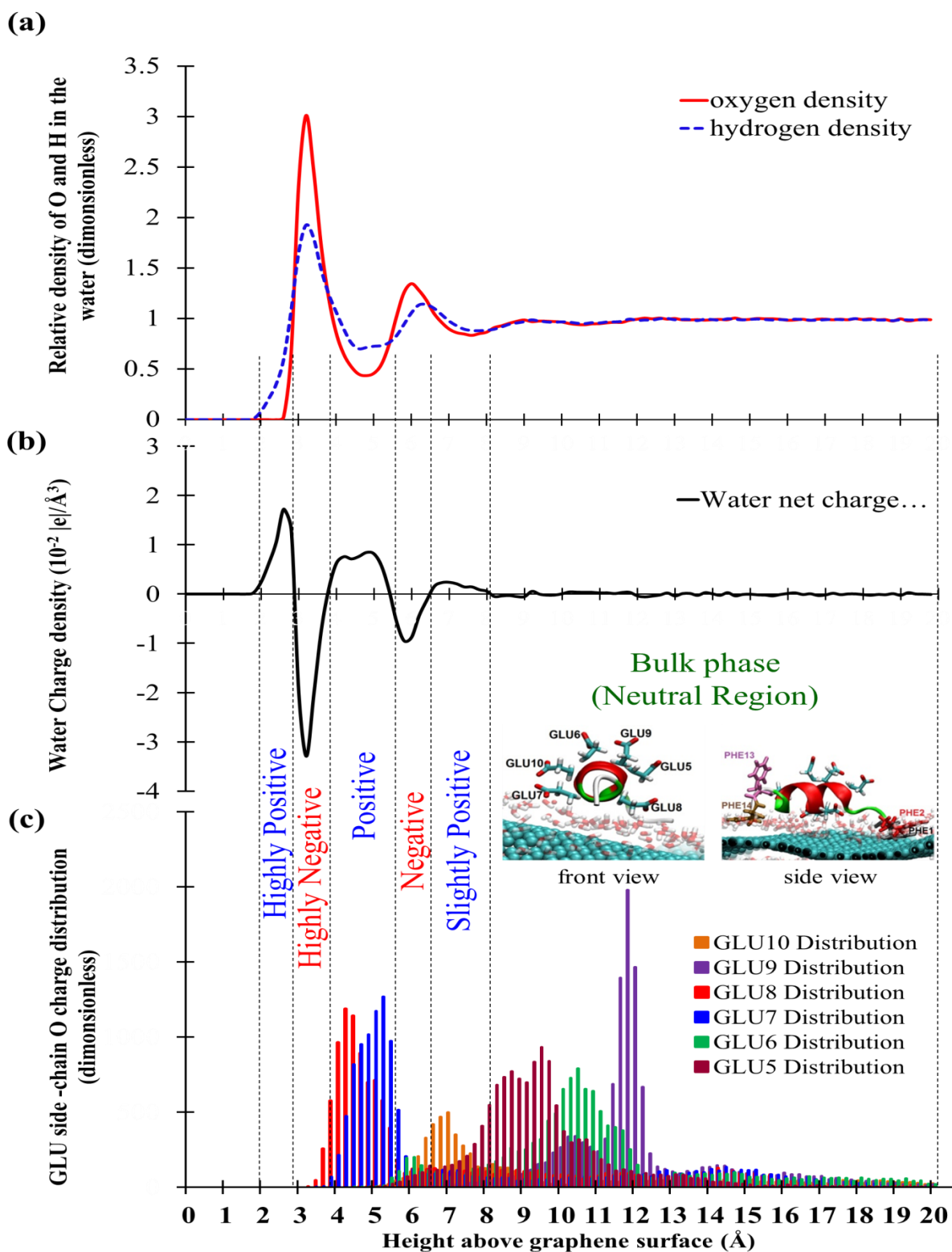


Figure 4-4. Variation with normal distance above the solid surface of: (a) relative density of the oxygen (solid line) and hydrogen (broken line) in the water and (b) water net charge density (c) GLU residues' side-chain distribution.

4.3.2.2 Experiment

The TEM images of single rGO sheet and GRP-UA2 are shown in Figure 4-5a and b, respectively. Comparing these two images, the plain rGO sheet exhibited more transparent and smoother texture with few wrinkles. The graphene sheet lost the transparency and showed rough surface topology with mesh-like layering. Comparison of these two micrographs suggests that the mesh-like layering is the peptide on the graphene surface.

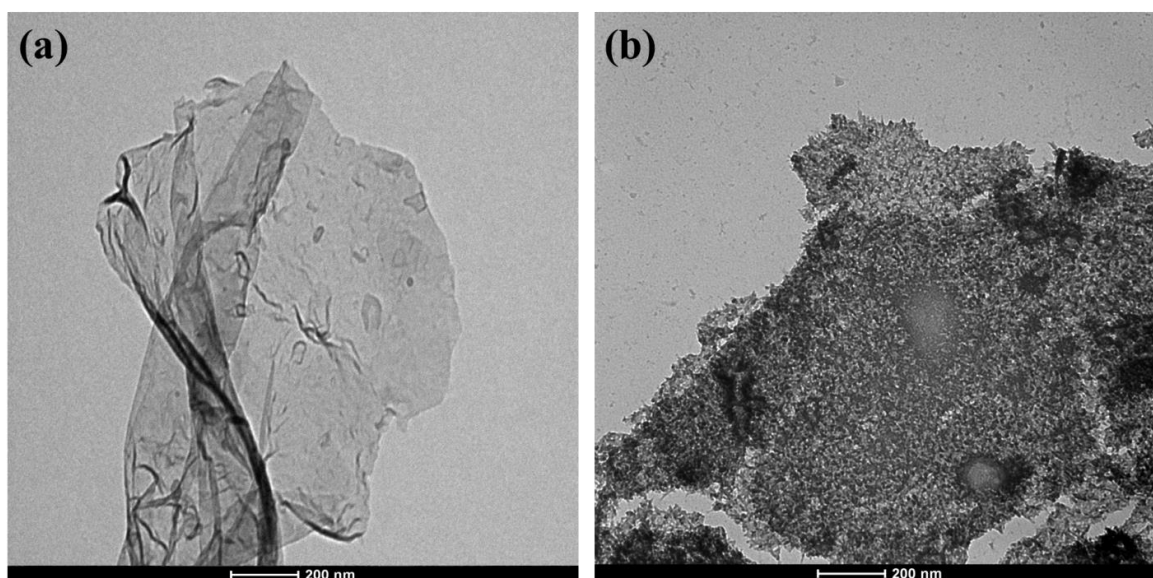


Figure 4-5. TEM images of (a) single rGO sheet and (a) GRP-UA2.

We also confirmed the peptide binding to the graphene surface by AFM imaging before and after adding the UA2 (shown in Figure 4-6 left and right respectively). AFM 2D (top) and 3D (bottom) images show the uniform peptide binding to the graphene surface without any aggregation. The AFM height traces (middle) show a uniform increase in rGO thickness from ~ 0.9 nm to ~ 1.5 nm after treating with UA2. The height difference is very close to our results from simulation which was 6.16\AA by the average for the distance of the peptide center of mass normal to the surface in its completely bound mode. In agreement with AFM investigations of peptide binding to graphitic surface reported elsewhere [320] [348], our results demonstrate that the peptides through hydrophobic residues strongly interact with the surface without any significant perturbation to its secondary structure. Combining the AFM and TEM results thereby imply that the UA2 peptide molecules bind effectively and uniformly on the graphene surfaces with a final laid down adsorbed structure.

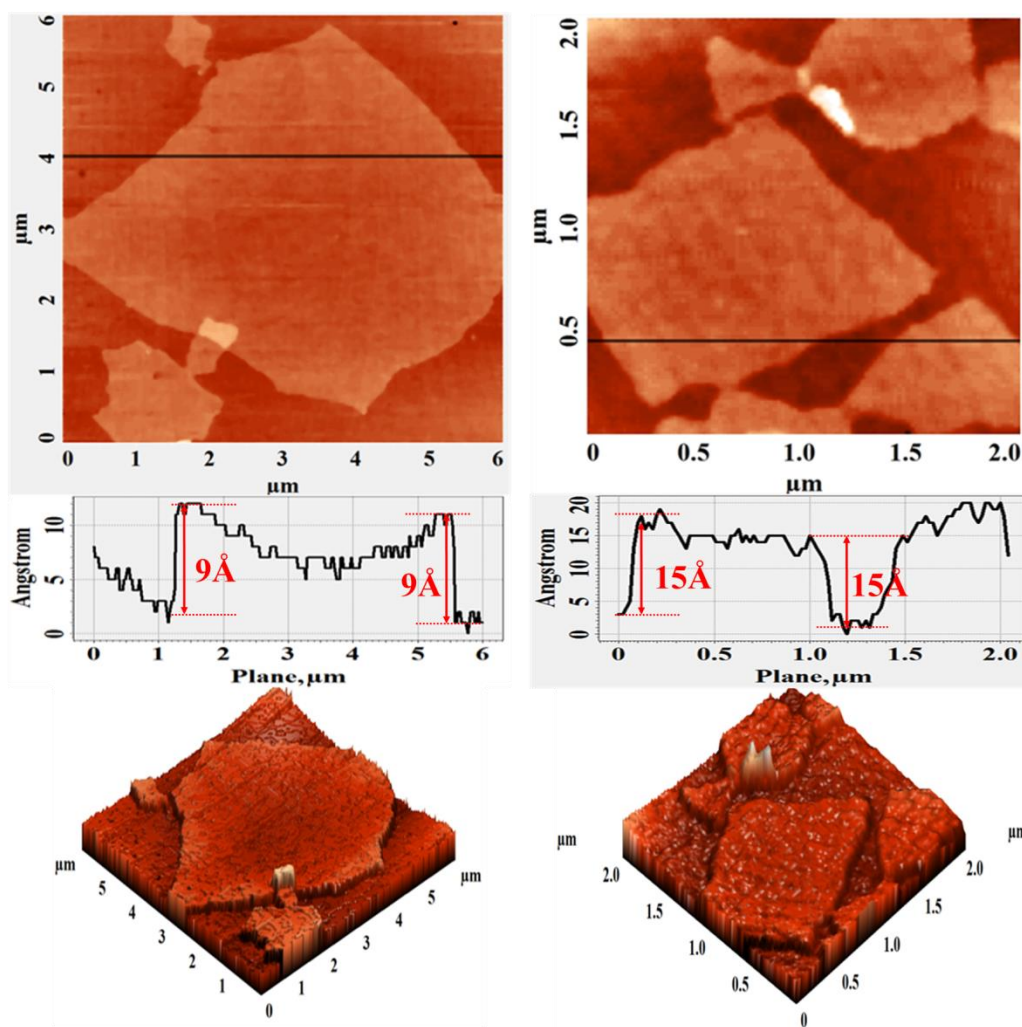


Figure 4-6. AFM 2D and 3D images and height profile of the X cross-sections indicated in black for rGO sheets (left) and GRP-UA2 (right).

4.3.3 Adsorption Mechanism

4.3.3.1 Exemplar trajectory

We investigated long enough simulation time to cover all events for a single peptide to migrate from bulk state to the completely adsorbed (lockdown) state on the graphene surface. Representative snapshots of graphene and peptide at different simulation times to show the adsorption kinetic process introducing the events are exhibited in Figure 4-7. The contributions of the aromatic containing residues in the adsorption of the designed peptide onto the graphene are also shown. Thus, at $t = 0$, the peptide in the bulk solution phase and the graphene were well separated. The UA2 approached the third water layer on graphene

very quickly within only 1.5ns, which we call it as interfacial diffusion event. The snapshot at $t= 2.0$ ns exhibits that the UA2 further diffused into the second water layer called anchoring event. The UA2 then rapidly elapsed the anchoring at $t=2.5$ ns and enters to the first water layer, called contacting event (see Figure 4-7). Our criterion to state that a residue or a peptide is in completely adsorbed (lockdown) state was derived from the literatures which defined a minimum dwell time of 10ns for species on the graphene surface [383, 384]. The first adsorbing state or lockdown event occurs at $t = 3.0$ ns when residue PHE(2) forms a flat binding mode with graphene through the π - π stacking interaction, which is considered as a very strong interaction between graphitic material and the aromatic residues. This interaction is only governed by the surface properties, hence addressed as direct surface interaction. The second lock-down of the peptide residue which is attributed to the residue PHE(1), occurs approximately 0.5ns after the first. The peptide, by overcoming the energy barrier after a slightly conformational change at about 20ns begins anchoring by the residue PHE(14) and gradually moving down closer to the graphene surfaces. The complete adsorption takes place when the residue PHE(14) has been bound with the surface at almost 35ns. However, the residue PHE(13) did not bind with graphene surface and although PHE(1) started to fluctuate on the surface at about 37th ns. Here we demonstrate that only two Phenylalanine residues are adequate to bind and keep the peptide adsorbed on the surface for 100ns of MD run. Moreover, it is believed that the residues' movement helps the peptide to adopt its favourable orientation [347]. In this study, we have shown that the UA2 maintained its favorable α -helical structure and that binding with graphene surface had no meaningful influence on perturbation of GRP-UA2 overall conformational dynamics.

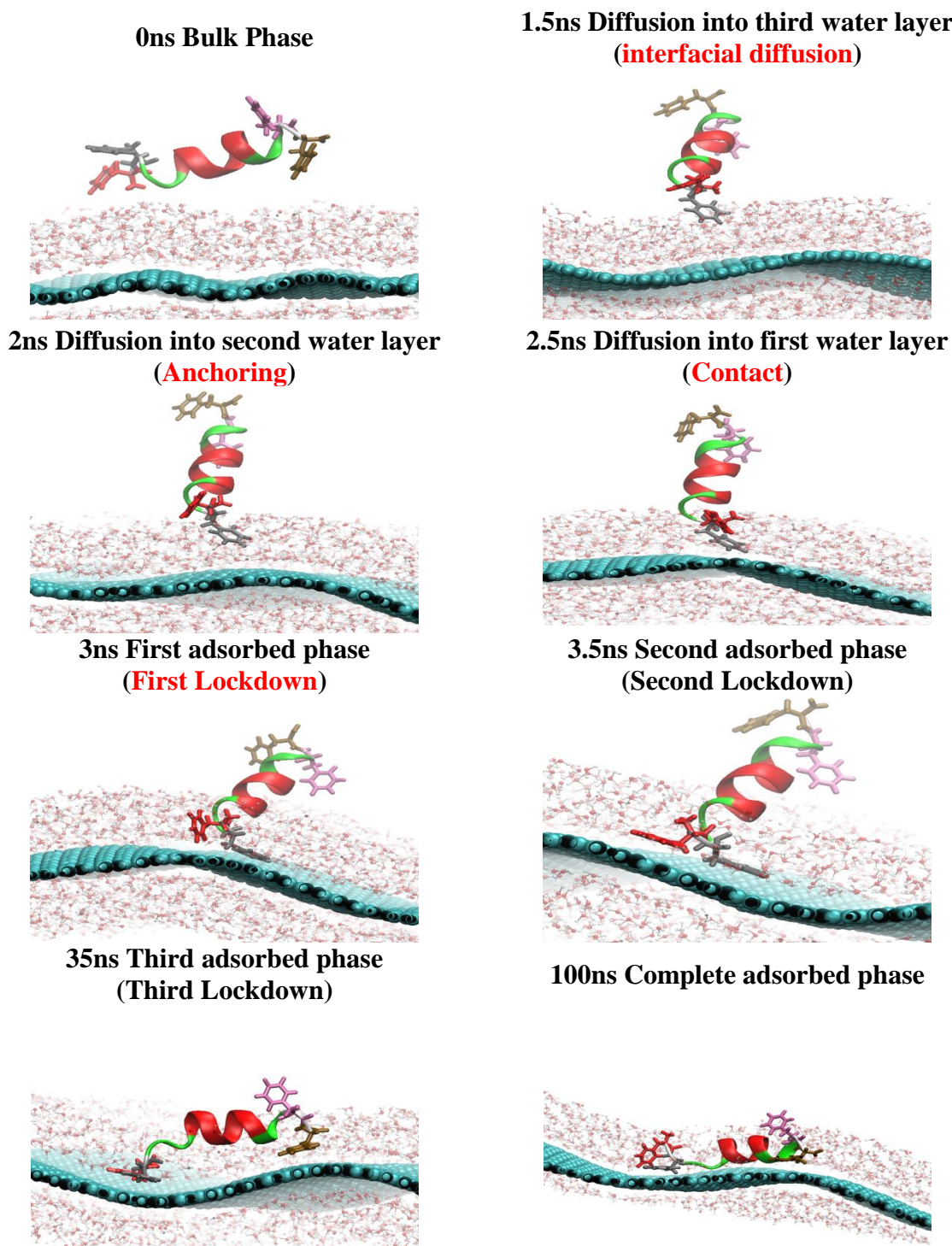


Figure 4-7. Side view snapshots of the representative UA2 adsorption on graphene surface. The snapshots of the designed UA2 in the side view are displayed by the new cartoon model, and the graphene is displayed by a VDW model.

Conformational dynamics and mechanism of UA2 adsorption on graphene surface was studied by analyzing the trajectory of an exemplar MD simulation (the same system used the section of adsorbed state structure). The detailed dynamics of the peptide

structural change were investigated from the time evolution of the helicity change and calculating the peptide RMSD as shown in Supplementary Figure 4-6. The high stability of the α -helix of about 70% (compared to the peptide structure in bulk water) observed in our MD simulations is in good agreement with the RMSD value as low as 1.90 ± 0.51 Å, both indicating that the helical structure of the UA2 is dynamically stable in solution even after being initially adsorbed on the graphene surface.

To investigate the detailed peptide–graphene interactions in GRP-UA2 and the effects on the UA2 conformation, the interaction energies for each type of residues are plotted in Supplementary Figure 4-5a–c. The interaction between graphene and hydrophobic residues (PHE1, PHE(2), PHE(13) and PHE(14)) implies that all of these residues reached their lowest energy level except PHE(13) (see the green curve in Supplementary Figure 4-5a) which has not bound with the graphene surface. The PHE(2) and PHE(14) residues make the dominant interaction between the UA2 and graphene surface with the approximate dwells of 96.5ns and 65ns via the van der Waals and hydrophobic interactions (shown by the red and blue curves in Supplementary Figure 4-5a). A similar phenomenon has also been observed in previous reports [320, 347, 385], which revealed that the van der Waals interaction between aromatic groups of biomolecules and graphitic carbon surfaces are the dominant factor for their adsorption on the surface. Combining the results from Supplementary Figure 4-5a and b, it is evident that the second residue initiates interacting with graphene surface after the first lockdown group is next to PHE (either PHE or GLY) which again confirms that non-polar residues are prioritized to initiate the adsorption.

The interesting stepwise and time dependence of the GRP-UA2 interaction energy for the solvated peptide are exhibited in Supplementary Figure 4-5a–c. The stepwise feature reflects stepwise adsorption dynamics of each of the UA2 residues at the graphene surface. From the observation of interaction energy changes (Supplementary Figure 4-5) and the trajectory animation (shown in Figure 4-8), one understands that the UA2 adsorption on the surface is always accompanied with some conformational rearrangement and reorientation of the residues that are close to the surfaces. Hence, the decrease of interaction energy is not linear. The similar stepwise adsorption behaviors on graphitic

surfaces were proposed in a 2 ns MD study for the adsorption of human serum albumin on the surface of carbon nanotubes [347] with 15ns for the adsorption of de novo designed α -helical peptide on the graphene surface [383]. However, in this study we found that the stepwise adsorption dynamics takes place over a much longer time scale, and the dwell time in one single step can last for 60 ns for any residue that is already in lockdown (seen in Supplementary Figure 4-5). By comparing Supplementary Figures 4-5 and 4-6, it can be ascertained that changes in initial α -helical structure, particularly from 35ns to 40 ns of the MD run (when the other end of peptide is bound to the surface), are strongly correlated with the peptide–graphene interaction energy in GRP-UA2. This indicates that a stepwise adsorption of peptide residues may induce α -helix unfolding to some extent [383]. The slight structure change of α -helices from 15ns to 20ns (shown in Supplementary Figure 4-6) originated from the partial unfolding of the α -helices that occurs with GLY(3) residue. This was then followed by a substantial drop in interaction energy after the adsorption of the second residue, PHE(2). Another change in the UA2 conformation between 35ns to 40ns is correlated to an oscillation of the graphene-GLY(12) interaction energy over the same time range, when the other end of the UA2 lockdown is on the surface via PHE(14). In addition to the GRP-UA2 interaction, the UA2 spatial rearrangement on the surface is the other reason for the small loss of helicity. All these minor changes in peptide structure might therefore be due to graphene surface disruption that occurs when the peptide reaches to its fully adsorbed state and the closest distance to graphene surface. Nevertheless, the UA2 retrieved its α -helical structure by the spatial rearrangements completed at 40th ns and showed a very high structural stability until 100ns of the MD run.

It is noteworthy that slight oscillations are seen for the graphene-GLU(7 and 8) interactions, when they initiate interacting with the surface together with GLY(3) (shown in Supplementary Figure 4-5c). The reasons for how the hydrophilic GLU residues interacts with the hydrophobic graphene surface and how far they go down in the water to the surface will be discussed further in the next section where we investigate the water structure above the graphene surface.

The interaction energy of GRP-UA2 for all different initial configurations decreases with the increasing adsorption fraction of UA2, as one example is shown in Figure 4-8. To determine the fraction of adsorbed atoms, we consider an atom adsorbed (or lockdown) when it displaced the first water layer from the graphene surface (within 5Å of the graphene surface) and has remained there approximately constant for at least 10 ns. Support for this criterion was obtained from existing computational studies of adsorption of de novo designed α -helical peptide [383] and insulin [384] on graphene surface using MD simulation approaches.

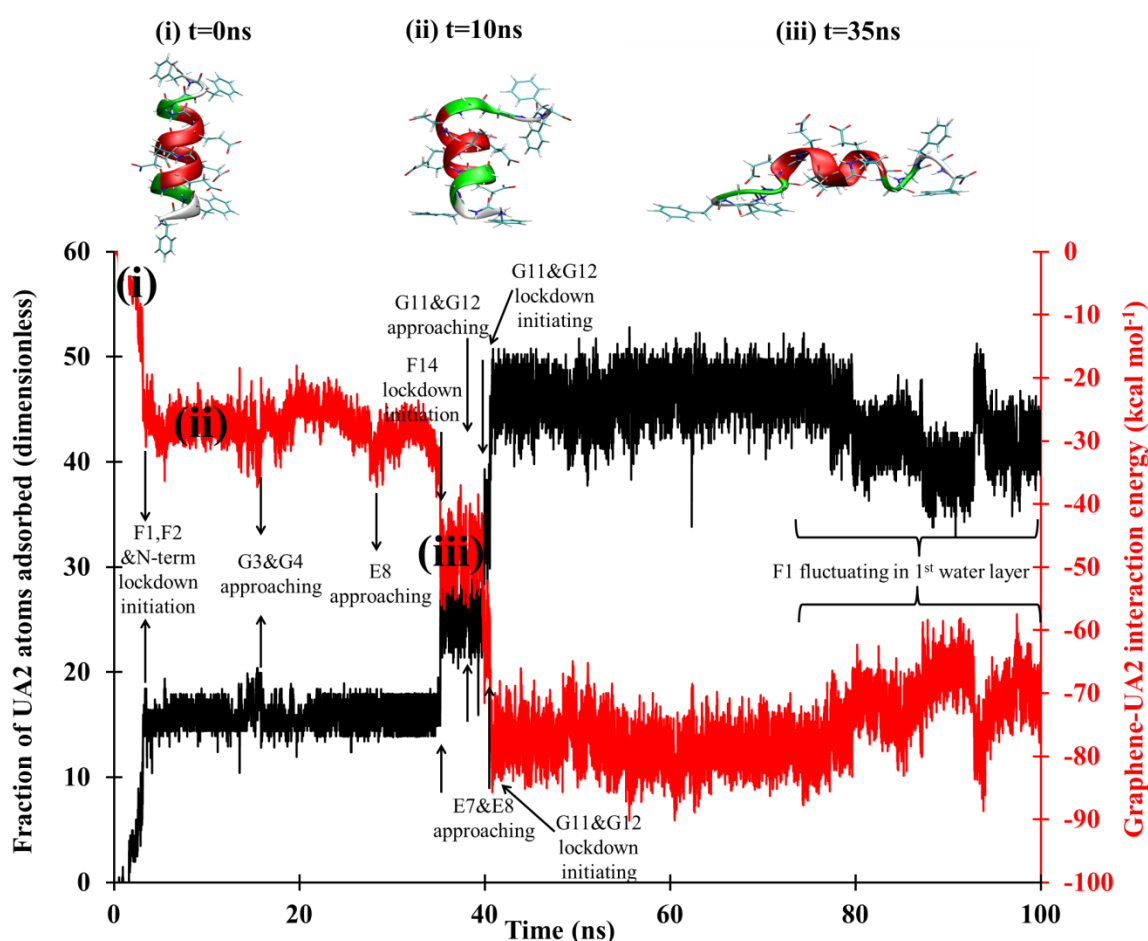


Figure 4-8. Trajectory of the exemplar MD simulation from initiation of the lockdown phase to the complete peptide adsorption: Correlation of the fraction of UA2 adsorbed atoms with interaction energy. Snapshots three different event where the peptide undergoes major changes in structure from: (i) initial states at bulk water to (ii) lockdown state of one end and (iii) lockdown of the other end (complete adsorption).

From the observations of the whole peptide in Figure 4-8 and each individual residues in Supplementary Figure 4-5, one can realize the stepwise adsorption of the peptide residues on the surface where the PHE(1 and 2), for an example of peptide binding graphene, initiate lockdown at first water layer and contact with the graphene surface in less than 5ns. This rapid movement of the peptide from bulk phase towards the surface was observed in every simulation, despite the nearest residues to the surface initially being outside the cut-off range of the peptide-solid surface dispersion interaction (*i.e.* beyond 12 Å). After PHE(1 and 2), the non-polar residue of GLY(3) and GLU(8) are the next candidates that approach the graphene surface. An obvious increase and drop have been, respectively seen for the fraction of adsorbed atoms and interaction energy at $t=35$ ns, whilst the other end of the peptide lies down on the graphene surface via PHE (14). Then GLY(11 and 12) and GLU(7 and 8) approached the surface such that GLY(11 and 12) lockdown occurred in the first layer, but the GLU(7 and 8) only anchored between first and second water layer. As a result, the UA2 had approximately 50% adsorbed atoms in the first water layer for even more than 40ns, thereby having great affinity to the graphene surface.

4.3.3.2 Statistical analysis of ensemble of simulations

In order to generalize the hypothesis of PHE residues acting as lockdown initiator, statistical analysis of all 45 simulation were conducted and are shown in Figure 4-9. As mentioned earlier the criterion to state that a residue side-chain or a terminal is in lockdown state defined as their minimum dwell time of 10 ns in first water layer ($\sim 5\text{\AA}$ above graphene). Perhaps unsurprisingly, only the side-chain of the PHE residues, initiate going down toward the graphene surface to lock itself onto the surface (20 to 28.88%) as is shown by black bars in Figure 4-9. As with their initial diffusion into the third water layer, this bias towards the PHE residues is due to their great capacity to form non-covalently π - π stacking interaction with the graphitic surface materials [360]. However, statistical analysis revealed that all the PHE residue equally interact with the surface, although a slightly higher fraction is evident for the side-chains of PHE(1 and 14) compare to PHE(2 and 13) that are located at both ends of the peptide. The reason for this might be that besides the π - π stacking interactions, the residues PHE(1) and PHE(14) have charged N-

term and C-term, which can interact with the negative and positive charged regions on second water layer (seen in Figure 4-4b) via electrostatic interaction.

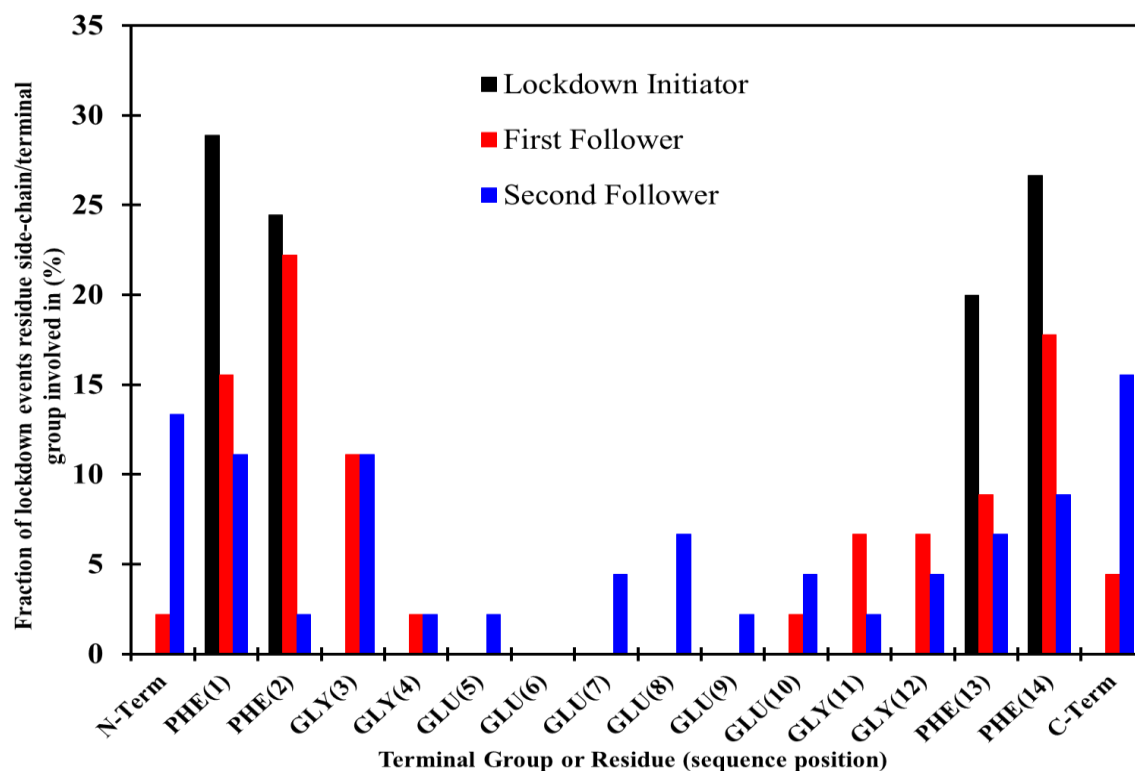


Figure 4-9. The fraction of 45 simulations in which the indicated terminal/residue side-chain groups initiated adsorbed (lockdown state) and their first and second follower.

Whilst PHE residue with non-polar side-chains have the largest propensity to initiate lockdown, Figure 4-9 and Figure 4-10 in line with each other show that for most of the simulations, the probability of a residue being the first follower or the second to lockdown relates more to the residue next to the first lockdown residue (either PHE or GLY), and is therefore exponentially related to the distance from the initial lockdown residue. It seems that the nature of the UA2 residues plays an important role in ordering adsorption so that the non-polar residues are more likely to be attracted to the graphene surface. The polar residue, however, appeared to be a candidate for the second follower groups which only anchor between the first and second water layer and would otherwise be unlikely to lock itself onto the surface. Figure 4-9 also demonstrate that the N-term and C-term are the most favored groups as second follower to the initiating lockdown group with the probability of 13.33% and 15.55%, respectively. The negative C-term after the complete adsorption of PHE(14) always takes on a stable adsorbed form and stays in the positive

charged region of the first water layer as it cannot overcome the large negative charge barrier of the first water layer above the graphene surface. On the contrary, the positive N-term, after adsorption of the PHE(1), is found to stick and fluctuate only between the negative charge region of first and second water layer (*i.e.* between $3 < \text{height} < 5 \text{ \AA}$). These movements of the N-term may sometimes take along the PHE(1) side-chain from the first to the second water layer and vice versa, thereby fluctuating the PHE(1) residue on the graphene surface (seen between $80 < t < 100 \text{ ns}$ in Figure 4-8 and Supplementary Figure 4-5).

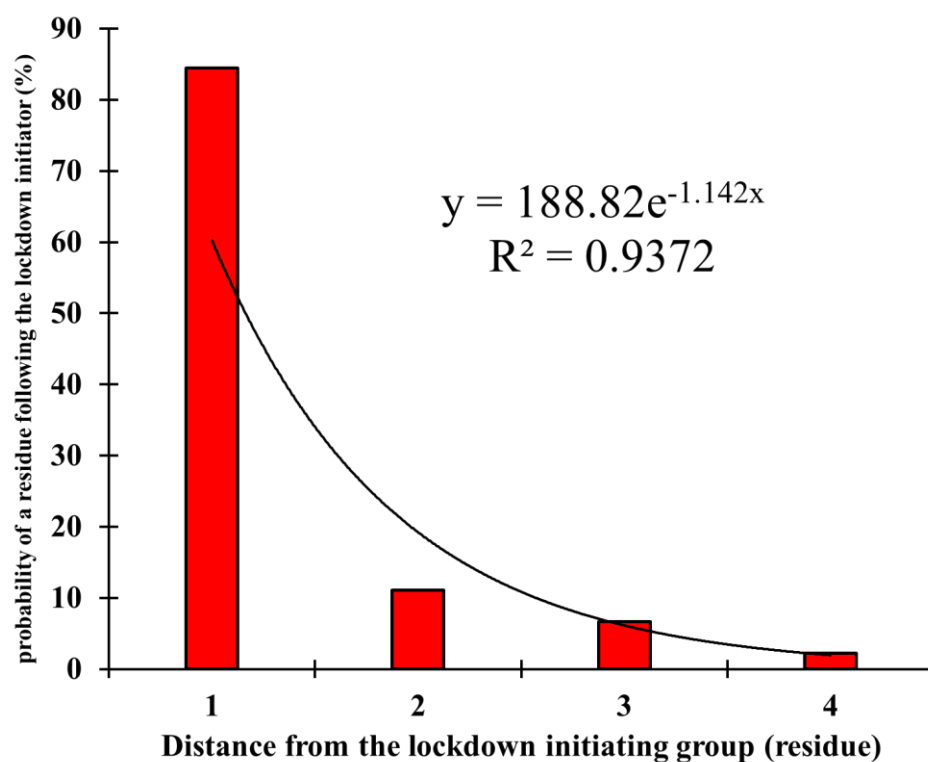


Figure 4-10. The probability of a residue following the adsorption initiator into the adsorbed (lockdown) state as a function of its distance from the initiator in number of residues. The exponential fit to the data is characterized by a coefficient of determination of $R^2 = 0.9372$.

To investigate the role of each residue on perturbations to the UA2 α -helical structure, we plot in Figure 4-11 the fraction of initial α -helix as a function of amino acid residues (all quantities are averaged over 100ns of 45 simulations). Figure 4-11 is in agreement with Supplementary Figure 4-5, shows that the perturbation to UA2 is caused by strong interactions between non-polar residues and graphene, and that this is stepwise and almost symmetric between the N-terminal and the C-terminal regions. The PHE residues as

anchor groups (adsorption initiators) including N-terminal and C-terminal lose >70% of their α -helix content, whereas the following residues GLY(3) and GLY(12) still have approximately 50% of the α -helix content left.

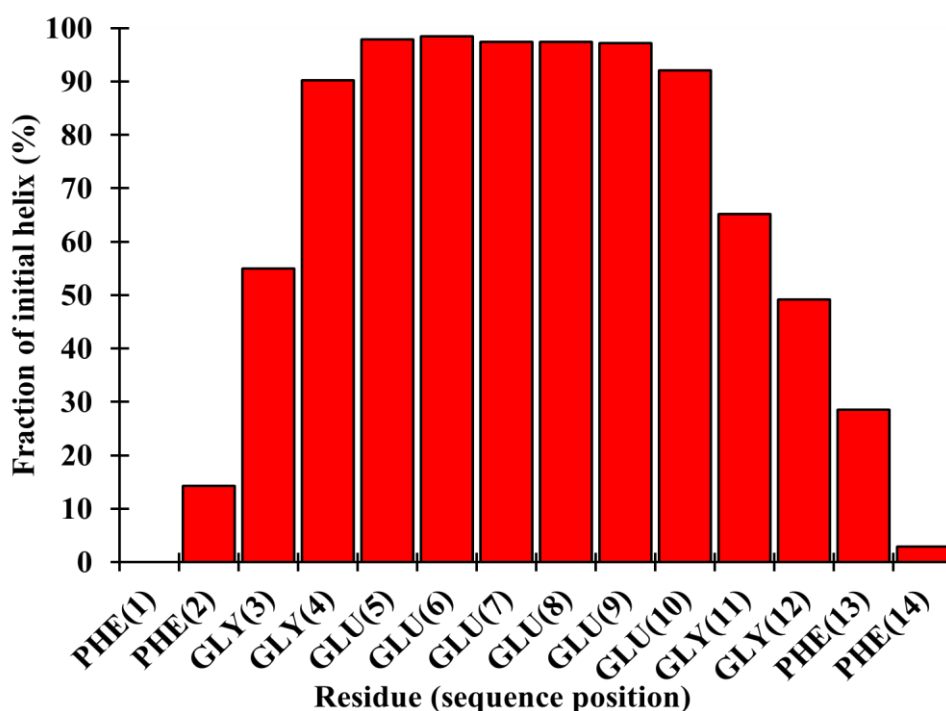


Figure 4-11. Time-averaged fraction of initial α -helix of each residue over the 100 ns for 45 MD runs

In line to Figure 4-11, the statistical analysis in Figure 4-9 indicates that there is no adsorption preference between the N-terminus and the C-terminus to the graphene surface. We attribute this to the similarly strong interactions of the N- and C-terminal residues with the uncharged graphene surface. The side-chains of residues PHE(1 and 2) and PHE(13 and 14) contain the aromatic ring contributing in π - π stacking interactions (van der Waals interactions). The following residues next to them, and GLY(3) and GLY(12) are non-polar, so they may be adsorbed at the graphene surface due to hydrophobic interactions. These strong interactions between UA2 residues and graphene would therefore disrupt the native intra-peptide interactions, thus inducing α -helix perturbation occurs from either end, regardless of what initiated the UA2 adsorption. The results from GLU side-chain distribution evident in Figure 4-4c also shows that GLU residues were almost equally spread out within the positive charged regions and the bulk of water without any disruption

to the UA2 helical structure. This in conjunction with results from Figure 4-11 confirms how the position of the GLU residues is important for retaining the UA2 α -helical structure, thereby maintaining the structural stability. All of these conclude that the peptide conformational change mainly occurs due to its direct contact with the surface rather than being influenced by the interfacial water layering profile. Sequencing the residues is therefore also a vital factor to be considered in the peptide design.

4.4 Conclusions

In summary, we have systematically studied the adsorption and conformational dynamics of the designed α -helical peptide, UA2, at the flexible graphene surface by carrying out 45 all-atom MD simulations in water for 100 ns time scale. The average helicity of 85% for UA2 after 10ns of simulation confirmed the stability of the peptide solely in the water solution with a neutral pH. The simulations of GRP-UA2 showed that both N- and C-terminal residues have similar preferences to adsorb at graphene surface because of the strong π - π stacking interactions of PHE residues that symmetrically designed both ends of the UA2. The PHE residues through direct surface interactions after diffusing into the third and second water layers, lockdown on the graphene surface by replacing several water molecules in the first water layer. GLU negative charged side-chains are also the second leading factor for the UA2 stabilizing on the graphene surface through solvent mediated interactions, however, the closest they go toward the surface is the positive charged region between first and second water layer. Analysis of the peptide-graphene interactions in GRP-UA2 demonstrates that the surface oscillation of the graphene sheets does not significantly perturb the water density profile or the native intra-peptide interactions, except for a slight change in the UA2 helicity where the UA2 very quickly retrieved its helical conformation. Our experiment results through TEM and AFM images have shown the peptide affinity and assembly on the flexible graphene surface. The height profile measurement of GRP-UA2 has also confirmed the lie down orientation of peptide via demonstrating the height increase of ~ 6 Å compared to that of the plain graphene sheet. Finally, the results of this study also show that our approach can be useful for further investigation of a wide variety of graphene binding peptide for the self-assembly of the graphene nanosheets, and the fabrication of graphene multilayered nano-

constructs. We believe that symmetric design of peptide having aromatic containing residues at each end may aid with their symmetrical binding with pair of graphene sheets if it is placed in between sheets. This would result in graphene self-assembly, forming bilayer and multilayer nano-constructs. As graphene nano-construct preparations advance in adsorption industrial applications, the graphene binding peptide with controlled peptide sizes will benefit various applications, such as in heavy metal and dye removal from wastewater, gas adsorption and controlled drug delivery.

Acknowledgements

M.V.K gratefully acknowledges the Australian Postgraduate Award (APA) International Postgraduate Research Scholarship (IPRS) from the University of Adelaide. The support of the Australian Research Council Discovery Program (DP20111888) is also gratefully acknowledged. The supercomputing resources for this work were provided by eResearchSA and both the NCI National Facility at the Australian National University and the iVEC Facility at Murdoch University under the National Merit Allocation Scheme.

Supplementary information

1. Preparation of graphene oxide (GO) and reduced graphene oxide (rGO)

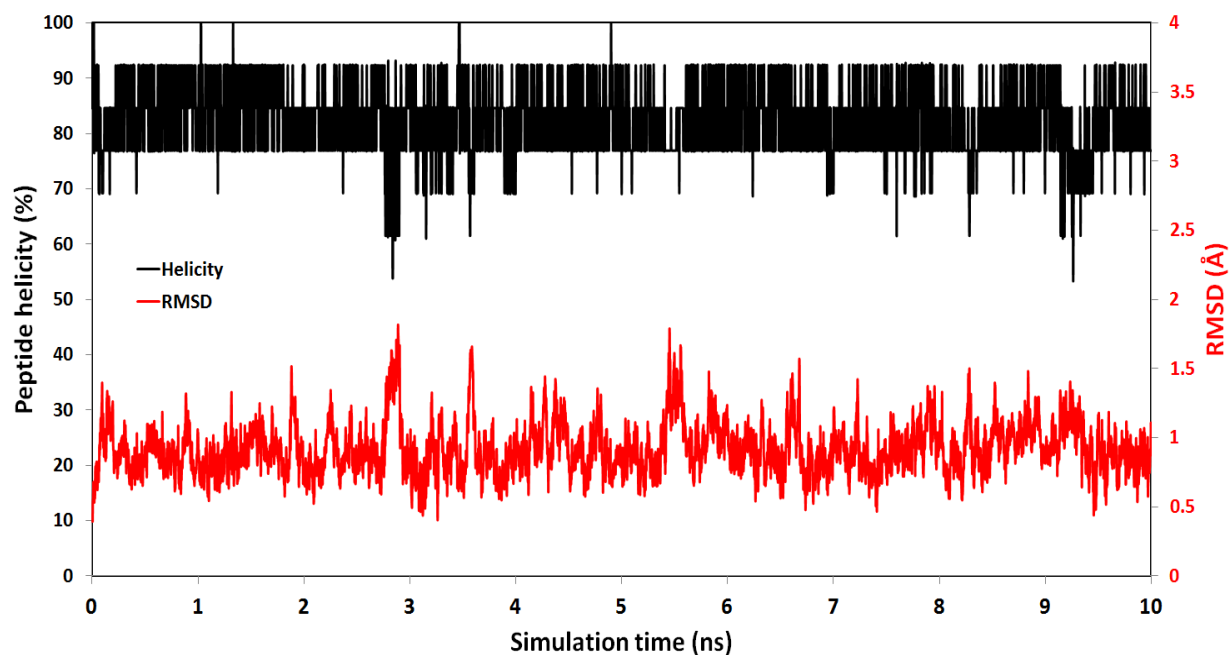
Graphite oxide or Graphene oxide (GO) was prepared by oxidation of natural graphite according to the improved Hummer's method^[88]. In a typical procedure for chemically reducing GO to prepare rGO, the as-synthesised GO was used to prepare homogeneous dispersion (0.5 mg ml⁻¹) in a 25mL flask. Then, 25 μ l of hydrazine solution (35 wt% in water, Aldrich) and 75.0 μ l of ammonia solution (28 wt% in water, Crown Scientific) were added to the flask. The dispersion was shaken vigorously and stirred for a few minutes, then placed in an oil bath (~95 °C) for 1 hr. The brownish dispersion of GO (shown in Figure 4-1, left,) turned to black rGO (shown in Figure 4-1, right). The rGO dispersion prepared was diluted 200 times with Milli-Q water for further use in AFM and TEM characterizations.



Supplementary Figure 4-1. GO (left) and rGO (right) dispersions.

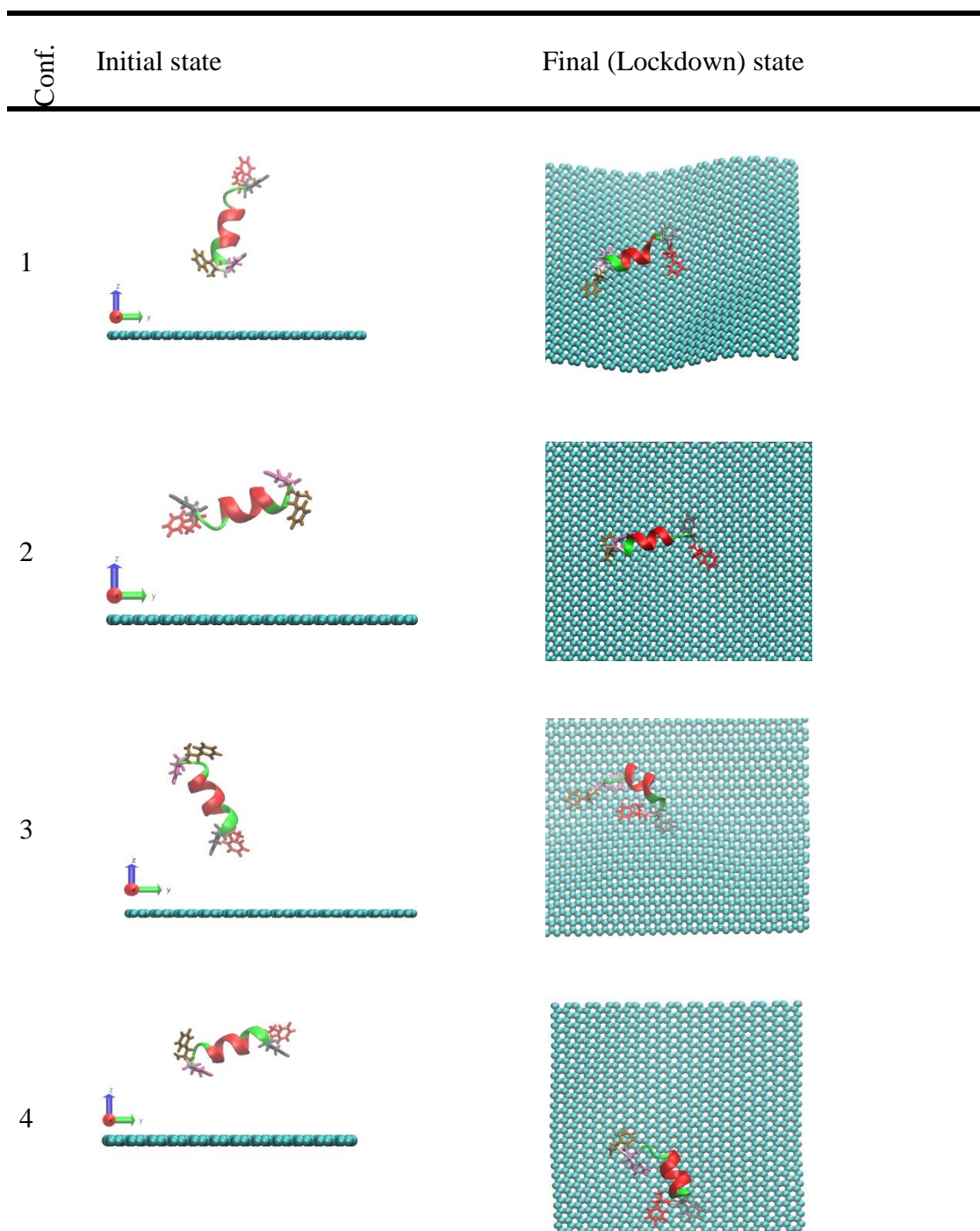
2. Peptide structural stability

The average peptide helicity of 85% and average RMSD value of 0.97 Å for peptides backbone (shown in Supplementary Figure 4-2) confirm the high structural stability of the designed peptide in the ionic water solution.

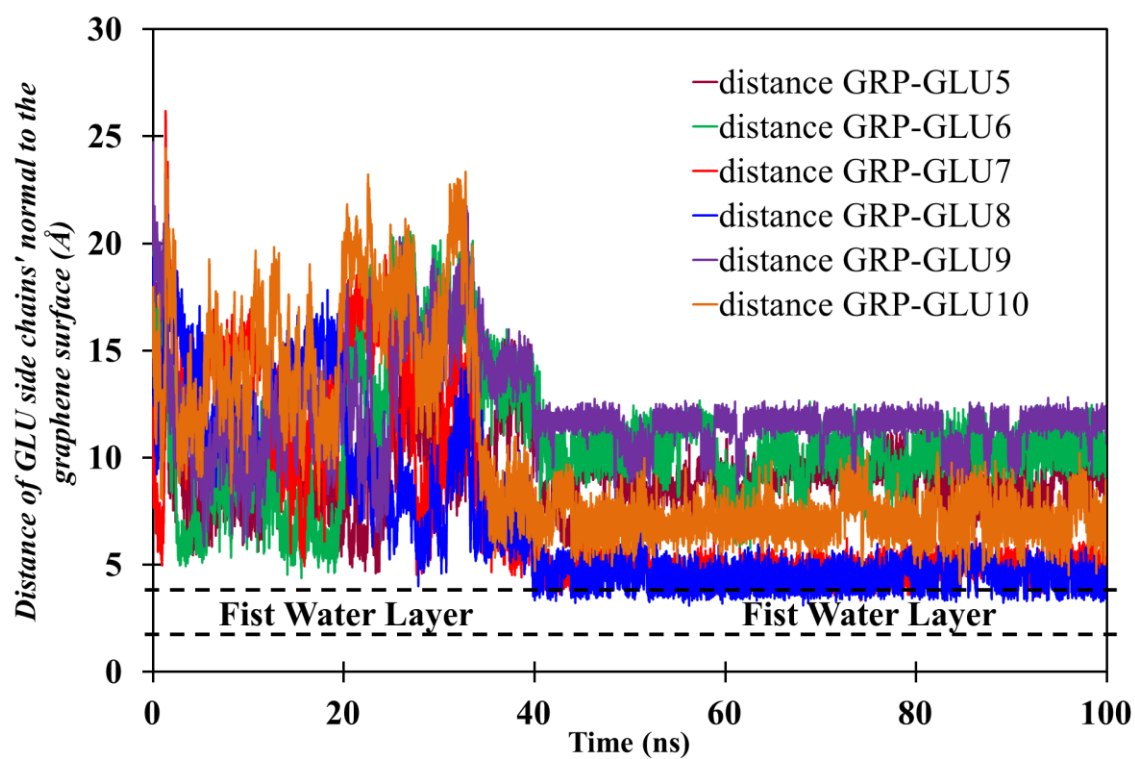


Supplementary Figure 4-2. Variation of α -helicity (black) and RMSD (red) of the solvated UA2 over a sample simulation

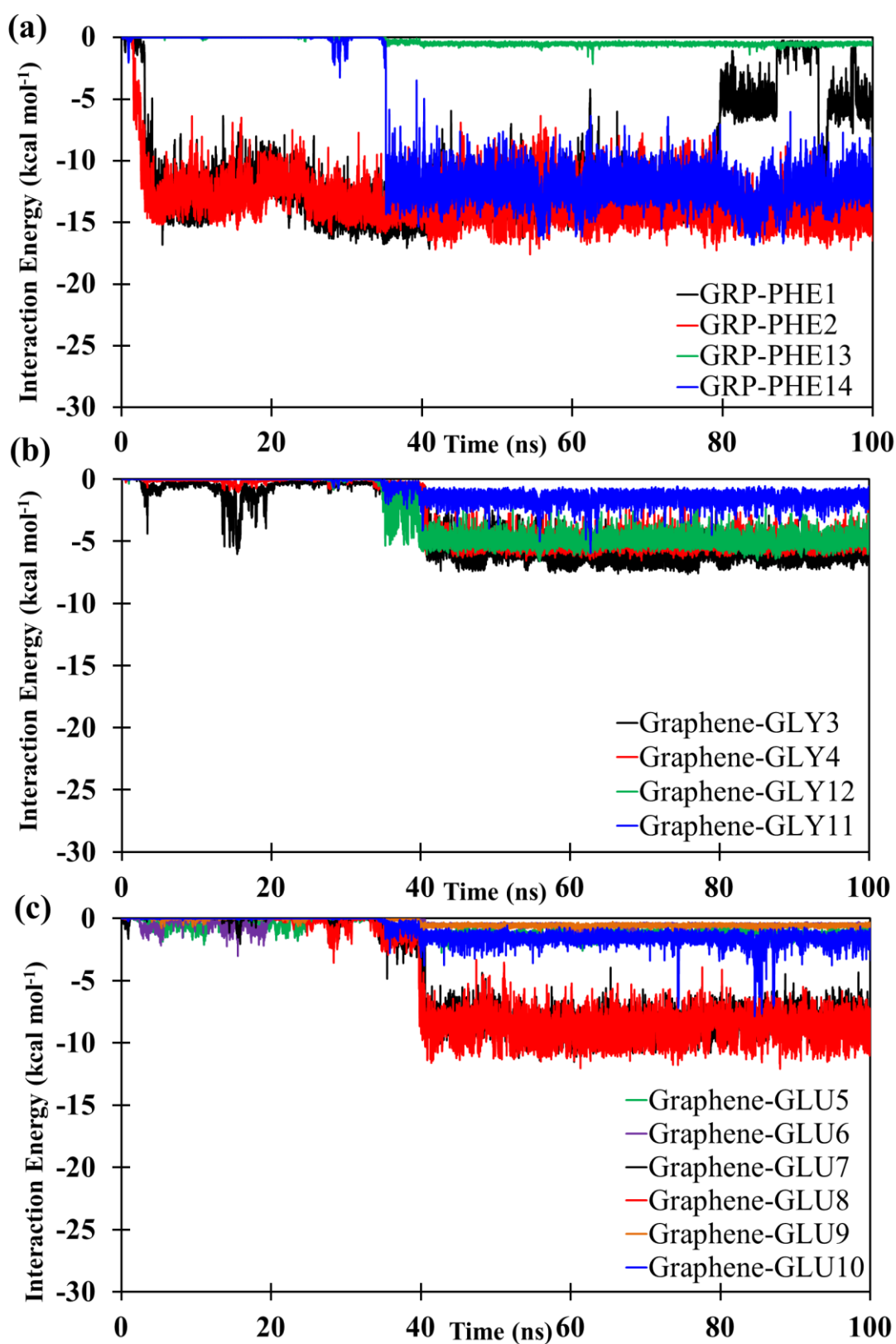
3. Examples of peptide initial (in bulk) and final (adsorbed state) configurations



Supplementary Figure 4-3. Simulation representative snapshots for the UA2 peptide with different initial orientations interacting with graphene surface. Water molecules are not displayed for clarity.



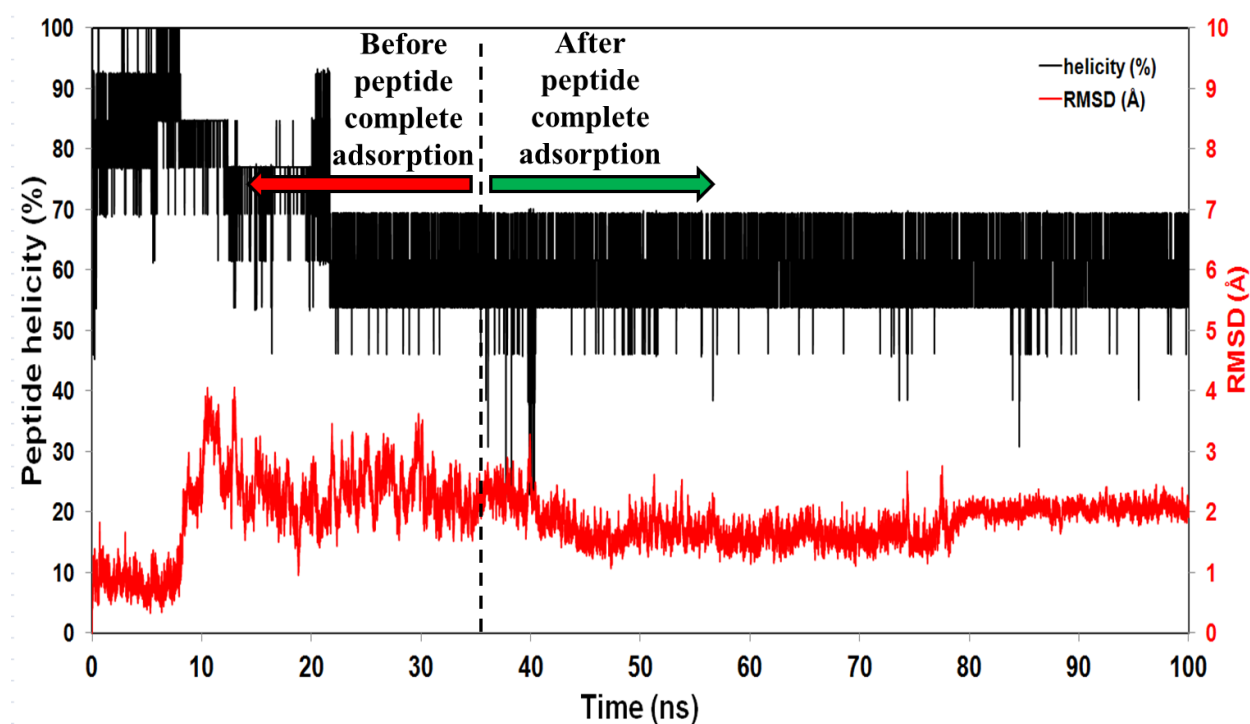
Supplementary Figure 4-4. The normal distance of GLU side-chain to the graphene surface.



Supplementary Figure 4-5. Interaction energy between UA2 residues ((a) PHE, (b) GLY and (c) GLU) and graphene surface.

4. Dynamics of the peptide structural change

The detailed dynamics of the peptide structural change were investigated from the time evolution of the helicity change and calculating the peptide RMSD as shown in Supplementary Figure 4-6 by the black and red lines, respectively. The average helicity value of 70% at complete adsorbed state confirms that the UA2 retained its α -helical structure. The high stability of the α -helix observed in our MD simulations is in good agreement with the RMSD average value which is as low as 1.90 Å. It is noteworthy that the small RMSD corresponds to weak disruption of UA2 conformation from interaction of the UA2 with the graphene surface. The major change of the helicity value takes place in between 35th ns and 40th ns of MD run which corresponds to a local α -helix unfolding-refolding of the UA2. A minor fluctuation of helicity is also seen between 10th ns and 20th ns, in which a partial unfolding-refolding of α -helix occurs, indicating that the helical structure of the UA2 is dynamically stable in solution even after being initially adsorbed on the graphene surface.



Supplementary Figure 4-6. Variation of α -helicity (black) and RMSD (red) of the adsorbed UA2 over 100ns of MD simulation.

Chapter 5: Peptide-mediated Self-assembly of Graphene and Related Materials to form Nanoporous Hydrogel with Tuneable Pore Size

Abstract

Graphene-related materials with tuneable pore sizes in the nanoscale range offer the potential to address significant challenges in biomolecule separation, controlled delivery of drugs [18], selective biosensors [386], rechargeable batteries [387], supercapacitors [388, 389] and solar cells [390]. Layered assemblies of graphene-related sheets with physical [48, 306, 319] and chemical [38, 391, 392] cross-linkers between the sheets has been recognized as one possible strategy for making such nanoporous materials. However, current approaches give very limited control over the pore size distribution, particularly with regards control of the mean pore size and the degree of spread around it. Here, we demonstrate that through use of a designed peptide, a layered nanoporous graphene-related hydrogel with a specific desired pore size can be formed *via* self-assembly in a highly scalable way from an aqueous solution containing the graphene-related material and peptide. The principles of the peptide design are given along with the synthesis method of thick and transparent thin hydrogel films and their characteristics. It is also shown that the porosity within the hydrogel films is retained when freeze-dried. It is finally shown that the material can be used to exquisitely separate biomolecules in the nanometer range. The proposed approach can in principle be used to construct a robust hydrogel material of virtually any pore size to suit the needs of users in nanomedicines, nanobiotechnology, nanoelectronics, biosensors and biomolecular and nanoparticle separations.

5.1 Introduction

Graphene, due to its facile scalable synthesis from inexpensive graphite and its outstanding mechanical, chemical, electrical, optical and thermal properties, has attracted immense interest since its physical isolation earlier this century [55, 393]. Layered graphene-based materials that are able to accommodate molecules and nanoscale entities

between the individual graphene or related (*e.g.* graphene oxide or reduced GO) sheets has more recently also been of considerable interest [144, 393-395] because they offer the possibility of combining one or more of the outstanding properties of the graphene-related material with a high surface area-to-volume ratio. Such nanoporous graphene-based materials have significant potential in electrode materials of energy storage devices where the electrolyte ions diffusivity and rapid electron transport capability is necessary [23, 46, 298] in gas and energy storages where the accessibility to the active surface areas is the key issue [27], and in drug delivery where the poor solubility of the drug, the yield of drug uptake, and release rate are the main concerns [29].

Nanoporous, layered graphene-related materials may be formed through a manual layer-by-layer (M-LBL) [42, 44, 396] approach or self-assembly (SA) [24, 32, 43, 301]. The latter is far more scalable than the former and, therefore, of greater interest [397, 398]. Layered graphene-related materials produced through the SA protocols can in turn be classified into two categories: those with spacers, and those without. In the absence of spacers, the self-assembly driving force is the π - π stacking (a type of van der Waals) interaction between graphene sheets. The pore size between the sheets can be altered *via* the reaction conditions used in graphene preparation [26], and also by the filtration pressure applied for the fabrication of layered graphene film [271]. However, this approach is intrinsically limited to small pore sizes (varying from 0.39 nm for rGO [32, 33] to ~1.2 nm for GO depends on the density of oxygen containing group) with limited control. The use of spacing units between the graphene sheets provides a basis for addressing both these issues.

A variety of inter-sheet spacers have been used to date. The first group are inorganic nanoscale elements such as carbon black [35], randomly [270, 285, 293-297] and vertically aligned [38, 39, 298] carbon nanotubes, mesoporous carbon nanoparticles [37], iron oxide nanorods [40], ruthenium dioxide nanoparticles [41], gold nanoparticles [42-44, 310, 311] and tin oxide nanoparticles [45] or nanorods [399]. Polymers constitute a second group of spacers, including those that react with the graphene [291, 400, 401] and those that are polymerized *in situ*. Neither of these two groups of spacer provides a high degree of control over the pore size distribution (PSD) due to the challenges faced in controlling the

spacer size. Metal ions are a third group of spacers; these not only push apart the sheets but also cross-link them laterally [93]. Whilst tighter control over the PSD is achieved in this approach, the pore size range is limited to around a nanometre and the porosity is susceptible to collapse if the ions leach out with a change in solution conditions. Linkers chemically bound to the graphene sheets can address this issue whilst also giving greater control over the PSD, but the pore sizes are still limited to a narrow range and the chemical binding to the graphene can also cause undesired property changes.[334]

Peptides have previously been used to direct the self-assembly of polymer-based hydrogels with desired characteristics [377]. In a similar vein, it is proposed here to use designed peptides to induce the self-assembly of graphene-related sheets to form a layered hydrogel with specifically desired inter-sheet distance (pore size) as illustrated schematically in Figure 5-1a. This concept is illustrated here through a peptide, denoted hereafter UA2, that endows the graphene-based hydrogel with a pore size of 2.6 nm.

The design principles of the peptide are explained below;

5.2 Results and discussions

5.2.1 Peptide design

The peptide is made up of three components as illustrated in Figure 5-1b. The first is a relatively rigid, hydrophilic region that bridges the majority of the distance between the two graphene-related sheets it is bound to. In the case of the UA2 peptide used to demonstrate the principles here, the bridge is composed of poly(glutamic acid); this has been selected because the side-chain of glutamic acid (Glu, E) carries a negative charge under pH neutral conditions and its propensity to form an α -helix [377, 378]. Our recent work [382] has also suggested the negative charge of the glutamic acid (Glu, E) may prevent it penetrating the water layer that is directly adjacent to carbon surfaces. The second component of the peptide prefers to leave the solution phase and interact physically with the graphene-related sheet with sufficient strength to ensure the peptide remains attached to the sheet. In the UA2 peptide, there are instances of this component at either end as illustrated in Figure 5-1b. Molecular modelling of met-enkephalin on graphite [363] indicates that phenylalanine (Phe, F) may be a suitable anchor residue, whilst other recent

work [349, 382] suggests that tyrosine (Tyr, Y) or tryptophan (Trp, W) may also be suitable. [349, 382] Each anchor of the UA2 peptide is composed of two Phe residues, which molecular modelling suggests is sufficient to ensure the anchor remains irreversibly adsorbed to the graphene-related sheet [382]. The final component of the peptide design is the region between the bridge and anchor, which must be sufficiently flexible to allow the aromatic group(s) of the anchor residues to fully engage with the graphene-related sheet whilst not being so long that it allows both anchors to adsorb onto the same sheet with the hydrophilic bridge still remaining in the solution phase. Once again, using experience from our prior molecular modelling work [363], this was fulfilled in the UA2 peptide by two glycine (Gly, G) residues. The distance between the graphene-related sheets (the pore size) can clearly be varied by changing the number of residues in the three different components of the peptide, although in the case of a design such as the UA2 peptide the bridge is the main route by which pore size can be varied. Molecular modelling (see sections 1 and 2 of Supplementary Information) indicates that the UA2 peptide sequence of $F_2G_2E_6G_2F_2$ should yield an inter-sheet distance of around 2.6 nm.

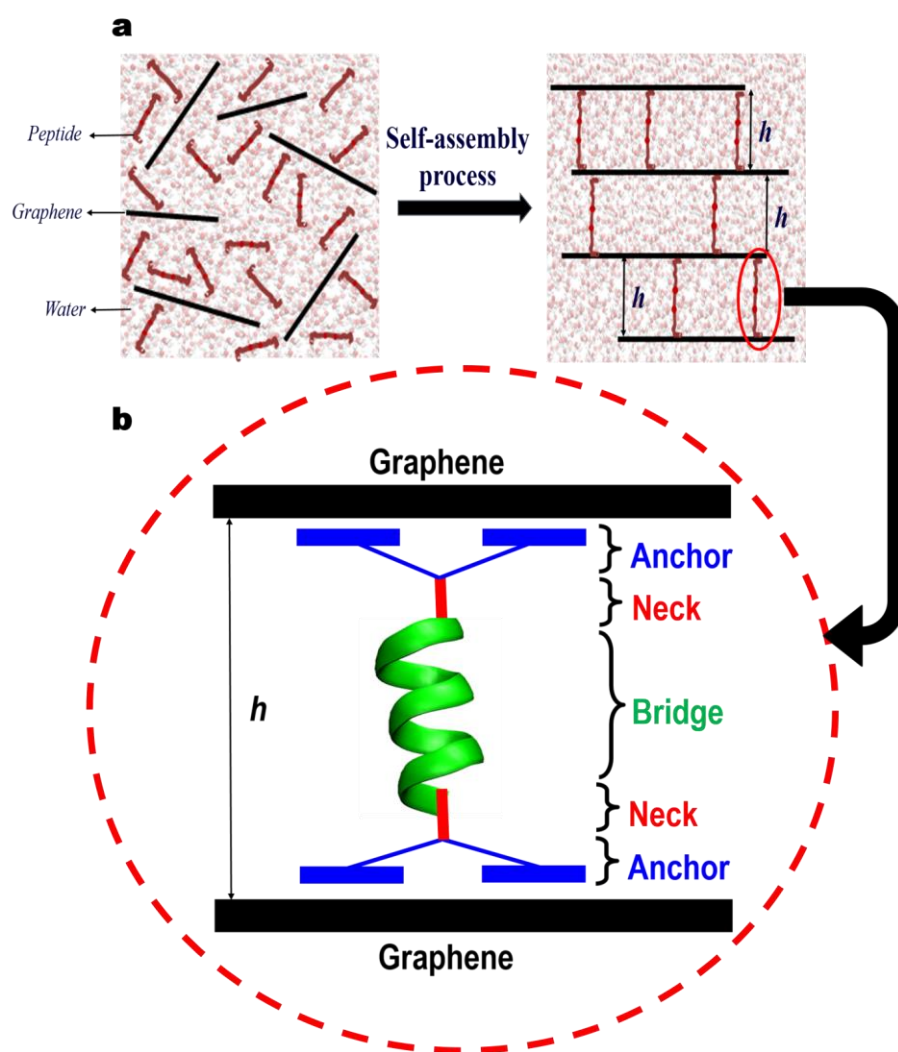


Figure 5-1. (a) Self-assembly of graphene related hydrogel with tuneable pore size and (b) the components of the peptide design used to self-assemble the graphene-based nanoporous hydrogel with a specific pore size.

5.2.2 Hydrogel synthesis

Hydrogel films are made using a vacuum filtration approach as outlined in methodology section and the process is shown in section 3 of the Supplementary Information. Films of widely varying thickness can be made with ease by simply varying the concentration of the graphene-related material and peptide in the solution that is subject to filtration. Free standing strongly hydrogel films prepared by reduced graphene oxide (rGO) binding peptide, denoted hereafter rGOPH, such as that shown in Figure 5-2a are obtained when they are of the order of 15 μm or more thick. These rGOPH films and similar made from GO and partially reduced GO are robust and paper-like (*i.e.* flexible and

non-brittle) provided they do not dry out; if this does occur, they disintegrate. The films retain the structural integrity and much of their porosity even after strong agitation in boiling water for at least 30 minutes (see Supplementary Movie 5-3). Dried films that retain the desired pore size can also be formed by freeze drying of the hydrogel films as outlined in the methodology section. Thin, transparent hydrogel films such as that shown in Figure 5-2b can also be formed provided the film is transferred to a rigid backing (*e.g.* glass slide) post-filtration (see section 4 of Supplementary Information); films as thin as ~300 nm have been formed to date, although in principle thinner films should be possible. These thinner films are delicate to the touch, but are otherwise quite stable even being dried out provided they are attached to the glass substrate.

5.2.3 Hydrogel characterisation

The cross-sectional SEM image from the hydrogel fracture edge in Figure 5-2c clearly reveals the homogeneous and highly oriented layered macrostructure of the graphene nanosheets parallel to each other, and similar to the one obtained without presence of peptide [402]. The TEM image in Figure 5-2d shows the spiky and mesh-like layering of the peptide over the graphene surface (this is comparable with the TEM image of hydrogel without presence of peptide, shown in section 5 Supplementary Information, which only contained the transparent graphene sheets).

AFM was used to establish the inter-sheet spacing as *per* the procedure outlined in the methodology section. Figure 5-2e shows a typical AFM image of an rGO hydrogel after being well crushed and dispersed in water and deposited on a mica surface. Scanning the probe over the surface yielded height profiles such as that shown in Figure 5-2f, which indicate the distance between the rGO sheets is around 2.6 nm. Many scans yielded an average inter-sheet distance (*i.e.* pore size) of 2.595 ± 0.176 (see Supplementary Table 5-1), which is consistent with the $26.26 \pm 0.80 \text{ \AA}$ nm obtained from the molecular simulation underpinning the peptide design (see section 2 of Supplementary Information). This is a significant enhancement in the pore size compared to that of hydrogel made solely by rGO (denoted as rGOH) and without presence of peptide. Our AFM measurements and MD simulation results (see in section 5 and 6 Supplementary

Information) in consistent with each other demonstrated that the inter-layer distance of the graphene plane in rGOH is ~ 0.7 nm which is in the range reported elsewhere [32-34].

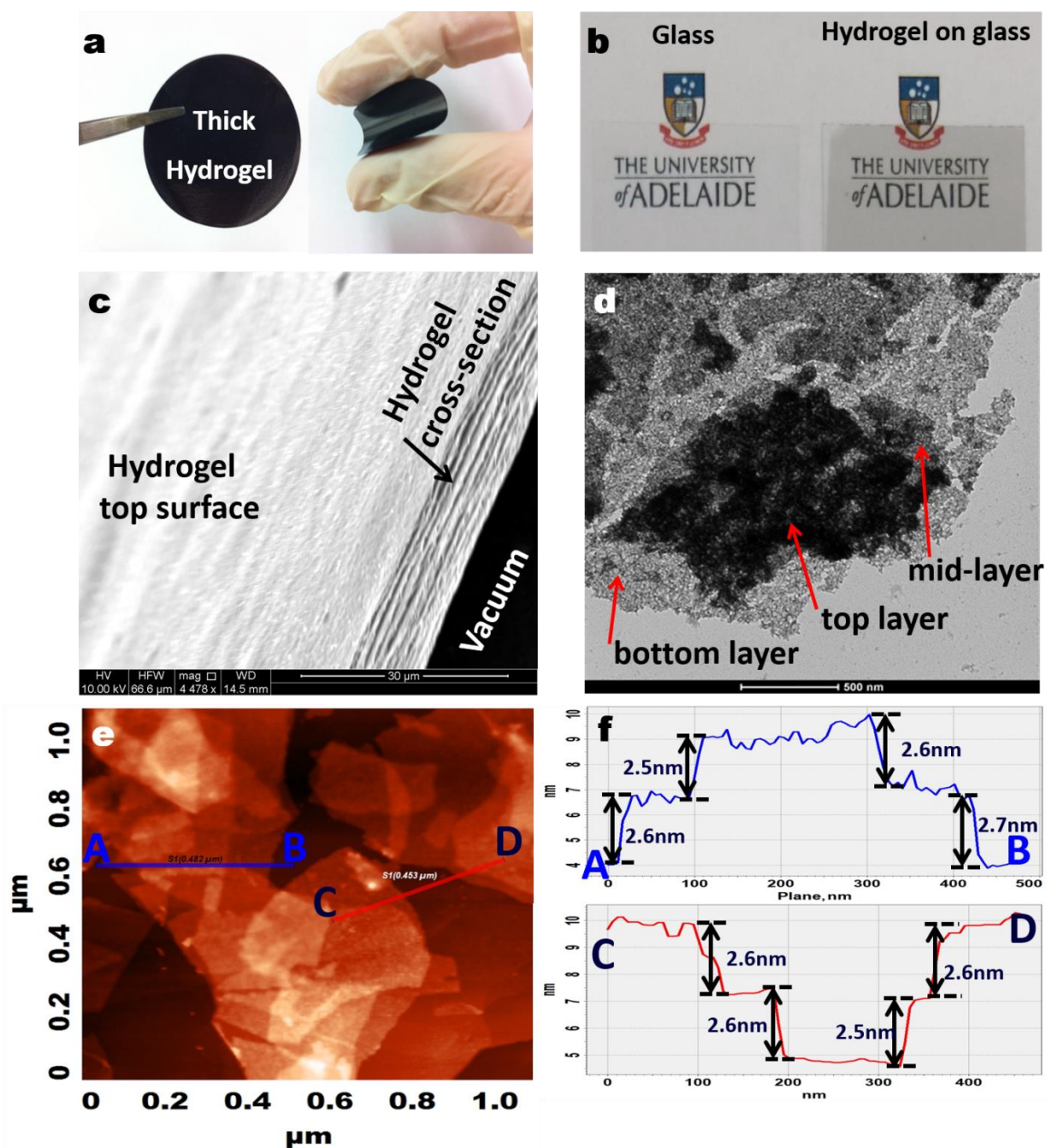


Figure 5-2. Photographs of (a) thick and (b) transparent hydrogel films (c) Cross-section view SEM image of rGOPH (d) TEM image of multi-layered rGOPH from the top view (red arrows correspond to individual layering of graphene sheets covered by peptide), (e) Tapping-mode AFM image (blue and red lines are random sections for pore measurements) and (f) height profile of rGOPH which illustrates an inter-layer spacing of ~ 2.6 nm comparable with that of in rGOH,

5.2.4 Dry-state characterization of porosity (nitrogen adsorption)

To investigate stability of self-assembled 3D lattice, porosity of rGOPH film is also studied in dry phase using nitrogen adsorption experiments. Nitrogen adsorption isotherms for freeze-dried rGOPH sample, shown in Figure 5-3a, exhibits a combination of type I and II adsorption isotherms based on IUPAC classification [403]. This primarily indicates a relatively small contribution of micropores and a substantial contribution of mesopores for the sample. The isotherm also shows a H4 type hysteresis loop indicating presence of narrow slit-like pores [403, 404]. The calculated BET [405] surface area, micropore volume [406], and total pore volume for the sample are $66 \text{ m}^2.\text{g}^{-1}$, $0.02 \text{ cm}^3.\text{g}^{-1}$, and $0.13 \text{ cm}^3.\text{g}^{-1}$, respectively.

To discuss the calculated PSD for the sample, we suggest classifying pore size range into four possible categories retrieved from simulations as discussed in the Supplementary Information Section 7 (Supplementary Table 5-2) and identified in Figure 5-3b Stacked graphene layers and graphene layers with 1 layer of water molecule between them, form pore sizes within Category 0 which is not detectable by nitrogen adsorption. Category 1 includes perfect graphene layers with two layers of water molecules between them (1nm based on simulations), defects in stacked graphene layers, and lying down protein molecules between two graphene layers (1.2 nm based on the simulations). The first peak in PSD in Figure 5-3b shows presence of these groups of pores in our rGOPH sample. Category 2 consists of the perfect pores form from the insertion of upright protein molecules between graphene layers. As it is shown in Figure 5-3b, the peptide insertion into the structure results in the formation of a considerably large distribution of pores within Category 2 (with the peak cantered by 2.52 nm), proving successful protein binding with graphene layers from its both ends. Based on the simulation results, pores larger than 3 nm are non-existent. However, PSD from nitrogen adsorption show a shoulder extending up to 4 nm. We assume these pores are due to the void spaces between multi-layer graphene units.

The positions of peaks in PSD results on dry-state sample show promising consistency with the simulations and with the wet-state AFM results, indicating that the

freeze-drying process does not have any negative impacts on the porous structure. This is evidence of the high mechanical stability of the sample pore structure.

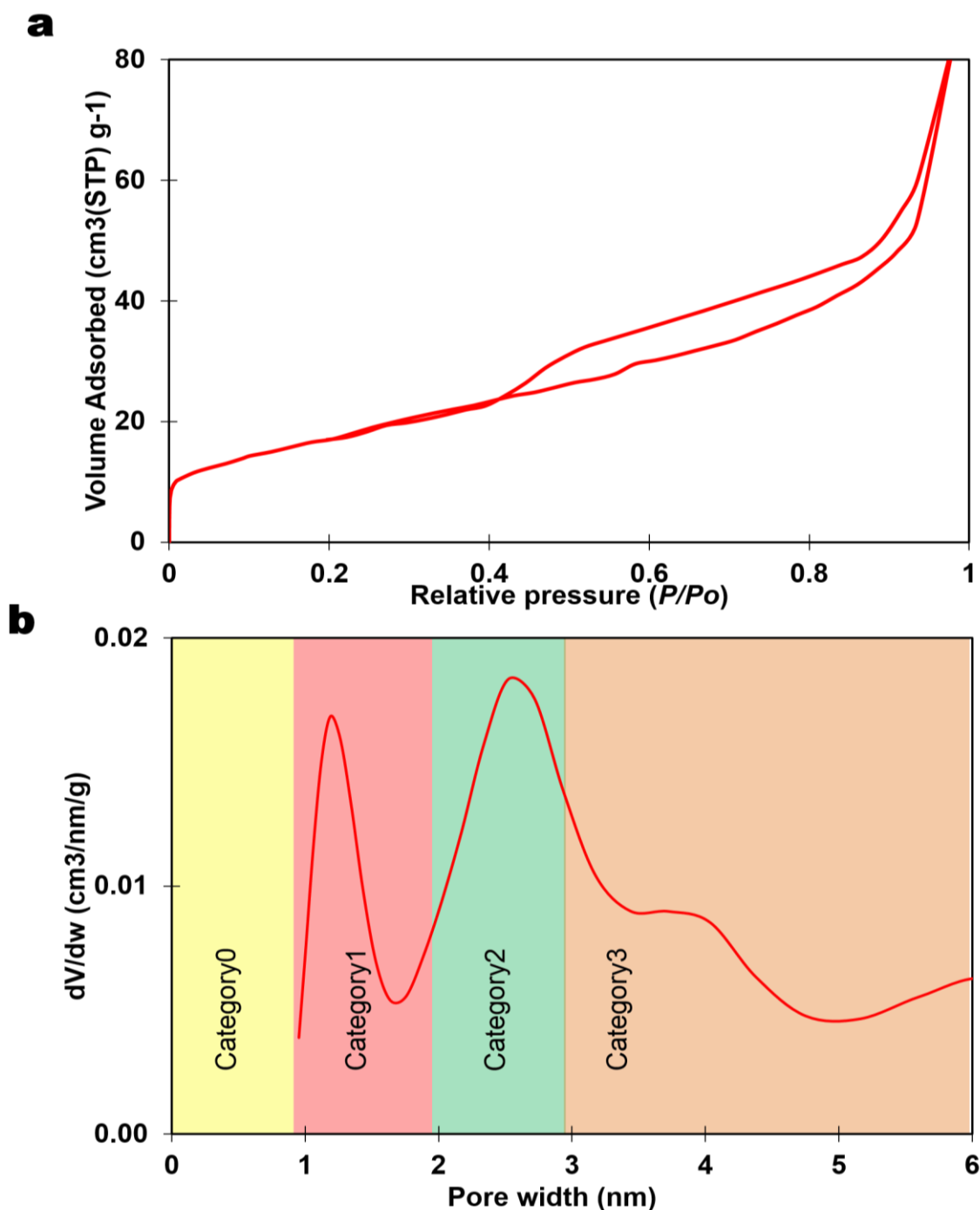


Figure 5-3. (a) Nitrogen adsorption isotherms, and (b) Pore size distribution derived from nitrogen adsorption isotherm on dried rGOPH film based on the Quenched Solid Density Functional Theory (QSDFT) method [407]. Pores are classified as Category0: non-detectable pores, Category1: Stack mediated pores, Category2: Peptide mediated pores and Category3: inter-particles void.

5.2.5 Demonstration of size-exclusion and kinetic separation

To illustrate the potential of the hydrogel materials in the biomolecule separation context, the rate of take-up of fluorescent-labeled dextran molecules of three different sizes was investigated. As demonstrated in Figure 5-4a, which shows the variation of the concentration of the dextran molecules in the solution with time after introduction of the hydrogel, the rate of take-up of the FD4 molecule (~1.4 nm) [408] is greater than that of the FD10 molecule (~2.3 nm) [409], whilst the FD20 molecule (~3.3 nm) [410] is not taken-up at all, in line with the fact that it is larger than the pore size within the material. The photographs of FD4, FD10, and FD20 before and after 24hrs of hydrogels introduction shown in Figure 5-4b are the evidence to such observations. The contrast between the FD4/10 on the one hand and FD20 on the other very clearly demonstrates the capacity for the material to separate molecules on the size exclusion principle. The differing rates of take-up of the FD4 and FD10 molecules also demonstrate the material can be used to effect separation based on kinetic effects.

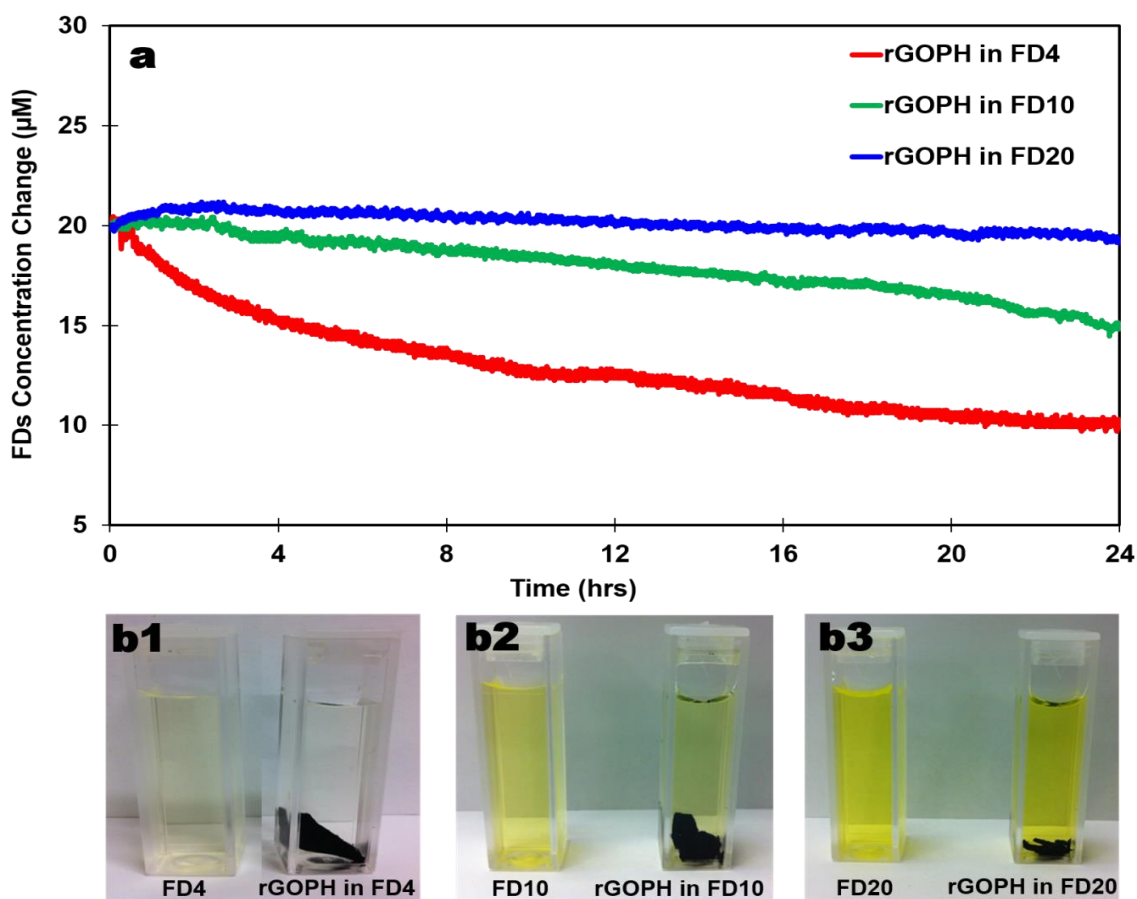


Figure 5-4. (a) Time evolution of the FITC-labeled dextran concentration change in hydrogels (adsorption profile) and (b) the representative colors of the dye solutions before and after the dye adsorption.

5.3 Conclusions

In summary, this study presents a novel design for utilizing π - π stacking interactions in the LBL self-assembly of graphene nanosheets to build new uniform 3D structured hydrogels with tuneable pore sizes and structural characteristics. The hydrogel was made simply by mixing the graphene dispersion with the UA2 peptide, without the need for either surfactant stabilizers or co-solvent to dissolve the peptide. This facile approach worked beneficially for enhancing the hydrophobic properties of graphene, π - π stacking interactions and therefore, successful binding to the UA2 through its aromatic residues (Phe). In agreement with simulation results, the TEM and AFM for a few layers scale, UV-Vis and N₂-adsorptions for the bulk material demonstrated that the desired pore size was achieved in LBL assembled hydrogel. The porous structures of the materials were stable in

both dry- and wet-states. In conclusion, the novel LBL self-assembled hydrogel, not only exhibits very good physiochemical properties for size selective biomolecules separation, but also opens up new vistas of applications in the areas of nanomedicines, nanobiotechnology and nanoelectronics. We believe that the work presented here has provided one significant step forward to our aim of bringing graphene based materials closer to real-world applications.

5.4 Methods

5.4.1 MD simulation

Graphene and UA2 were, respectively generated using the graphene and protein builder in the VMD package.[366] In keeping with the neutral pH considered throughout the work here, the zwitterionic form of the UA2 molecule with negatively charged sidechains of the glutamic acid residues was modelled. The intra-graphene and peptide-graphene interactions were modelled by the CHARMM27 all-atom force field [368] and the water molecules treated using the TIP3P model. The representative MD simulations of rGOH and rGOPH were performed using NAMD [369] (see details in supplementary information section 1 and 6).Synthesis

5.4.1.1 Preparation of rGOH thick films

The rGO dispersion was prepared by chemical reduction of a GO solution. Details of the synthesis procedure for GO and rGO dispersions and their characterizations are reported in Section 3 of the Supplementary Information. To prepare the rGOH film, a 25 mL of rGO dispersion (0.5 mg.mL^{-1}) was filtered through a Millipore mixed cellulose esters filter membrane (47 mm in diameter, $0.45 \mu\text{m}$ pore size,) by vacuum filtration. The vacuum was disconnected when the filtration was over and no free rGO dispersion was left on the filtrate cake. The resultant rGOH film was then immediately transferred to a Petri dish and immersed in Milli-Q water overnight to remove the remaining ammonia and unreacted hydrazine. A relatively thick film was carefully peeled from the filter membrane using tweezers and was used for most measurements. The rGOH film was stored in Milli-Q water prior to any characterization to prevent the water evaporation. The film was cut to

size using a razor blade for various tests. The thickness of the rGOH film can be controlled simply by adjusting the concentration and/or volume of the rGO dispersion.

5.4.1.2 Preparation of peptide solution

The UA2 peptide was synthesised using a solid phase standard Fmoc chemistry procedure with a rotary sintered glass funnel [370, 371]. The UA2 with concentrations of $0.1\mu\text{M}$ was prepared by dissolving into 150mM sodium chloride solution made in Milli-Q water. The salt was used for better solubility of the peptide and no co-solvent was used. It is known that using the high concentration of NaCl perturbs the peptide conformations and promotes peptides to form beta-sheets by reducing electrostatic repulsion [372-374]. However, the results from our simulation have shown that the UA2 is very stable in NaCl solution even at concentration as high as 0.3M.

5.4.1.3 Preparation of rGOPH thick film

Non-covalent adsorption of UA2 onto the graphene sheets occurred by adding the 25 mL of rGO dispersion ($0.5\text{ mg}\cdot\text{mL}^{-1}$) to the 25 mL of UA2 ($0.10\mu\text{M}$). The mixture of rGO and UA2 was then stirred for about 30 min and filtered through a mixed cellulose esters filter membrane (47 mm in diameter, $0.45\mu\text{m}$ pore size, Millipore) by vacuum filtration. The resultant rGOPH film was then washed three times and immediately transferred to a Petri dish and immersed in Milli-Q water overnight to remove the remaining unbound peptides. (See supplementary section 4 for the preparation method of transparent rGOH and rGOPH).

5.4.2 Characterizations

Morphology of the rGOH and rGOPH were investigated by SEM images using a FEG Environmental (QUANTA_450) scanning electron microscope. The TEM images were obtained using a Philips CM100 transmission electron microscope operated at 80-kV. Surface topography and height profile of the rGOH and rGOPH were examined by atomic force microscope (AFM, NT-MDT Ntegra Solaris) in tapping mode. The AFM samples were prepared by drop-casting a diluted suspension onto a cleaned Mica substrate and imaged immediately.

5.4.2.1 Hydrogel pore size confirmation in the dry-state via nitrogen adsorption

Thick film samples were freeze-dried prior to porosity characterization. The wet-state rGOH and rGOPH films were transferred into cylindrical containers. Only the bottom of the container was immersed into liquid nitrogen, and the wet film was frozen immediately. A lab-scale freeze-drying device ALPHA 1-2LD plus (CHRIST, Germany) was used to dry the frozen films at the temperature of 188K and under 10^{-2} Pa of pressure for 24hrs. Freeze-dried samples were degassed prior to the adsorption experiments at ambient temperature and a background vacuum of 10^{-5} kPa for 12hrs. Nitrogen gas adsorption experiments were carried out at 77K using a Belsorp-max gas adsorption apparatus. Ultra high purity (>99.999%) helium and nitrogen from Coregas Australia were used for dead-space measurements and adsorption experiments, respectively.

5.4.2.2 Hydrogel pore size confirmation in the wet-state via real time UV-vis

The pore size of the prepared thick hydrogels in the wet-state were further confirmed by loading FITC-labeled dextrans as test biomolecules with wide range of spherical sizes; FITC-dextran-4k (FD4, Sigma; mol. wt. 4000, Stokes radii ~1.4 nm), FITC-dextran-10k (FD10 s, Sigma; mol. wt. 10,000, Stokes radii ~2.3 nm), and FITC-dextran-20k (FD20 s, Sigma; mol. wt. 20,000, Stokes radii ~3.3 nm). The pore size assessment experiments were performed by placing 20mg of hydrogels in 3 mL cuvette containing FD4, FD10, and FD20, with a concentration of 20 μ M dissolved in Milli-Q water. The adsorption efficiencies were monitored on UV-vis spectrometer (Ocean Optics-CHEMUSB4) at a wavelength of 490nm for the excitation of FITC-dextran [411].

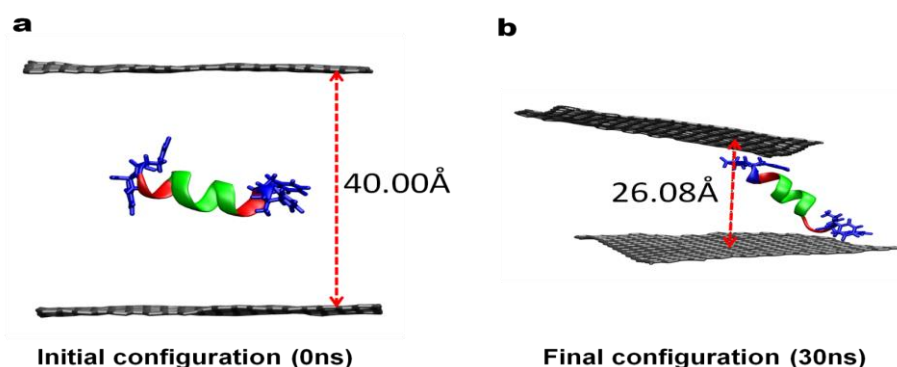
Acknowledgements

M.V.K gratefully acknowledges the Australian Postgraduate Award (APA) International Postgraduate Research Scholarship (IPRS) from the University of Adelaide. The support of the Australian Research Council Discovery Program (DP20111888) is also gratefully acknowledged. The supercomputing resources for this work were provided by eResearchSA and both the NCI National Facility at the Australian National University and the iVEC Facility at Murdoch University under the National Merit Allocation Scheme.

Supplementary information

Section 1. MD simulation method for graphene self-assembly

The simulation system was constructed by placing two graphene sheets in a periodic rectangular simulation cell, with a box size of $60.5 \times 62.5 \times 80 \text{ \AA}^3$, along with as-designed peptide (α -helix with the amino acid sequence of FFGGEEEEEGGFF). The graphene sheets modelled here have the finite size of $41.75 \times 42.55 \text{ \AA}^2$. The system was then solvated using the TIP3P water model [412] and sodium ions were added to ensure overall charge neutrality of the cell[381]. Then energy minimization and system equilibration were carried out for 200 ps and 1 ns, respectively, until the root mean square deviation (RMSD) and the system's total energy become stable. This indicated that the equilibrium state was reached. Then MD production run underwent for 30 ns in the isothermal-isobaric ensemble, number of moles, pressure and temperature (NPT) ensemble, to explore graphene-peptide interactions and conformations in solution. The Langevin dynamics and CHARMM force field were employed to integrate equations of motion with a time-step of 2 fs. Long-range full electrostatics were handled using the Particle-Mesh Ewald (PME) approach with a cut-off of 1.2 nm. The self-assembly process of two graphene nanosheets via the peptide as cross-linker (with a pore size of almost 2.6 nm) is shown in Supplementary Movie 5-1 as video. The snapshots of the graphene assembly before and after binding with peptide were shown in Supplementary Figure 5-1a and b. The graphene-peptide-graphene sandwiched structure was successfully maintained until the 30th ns of MD simulation.



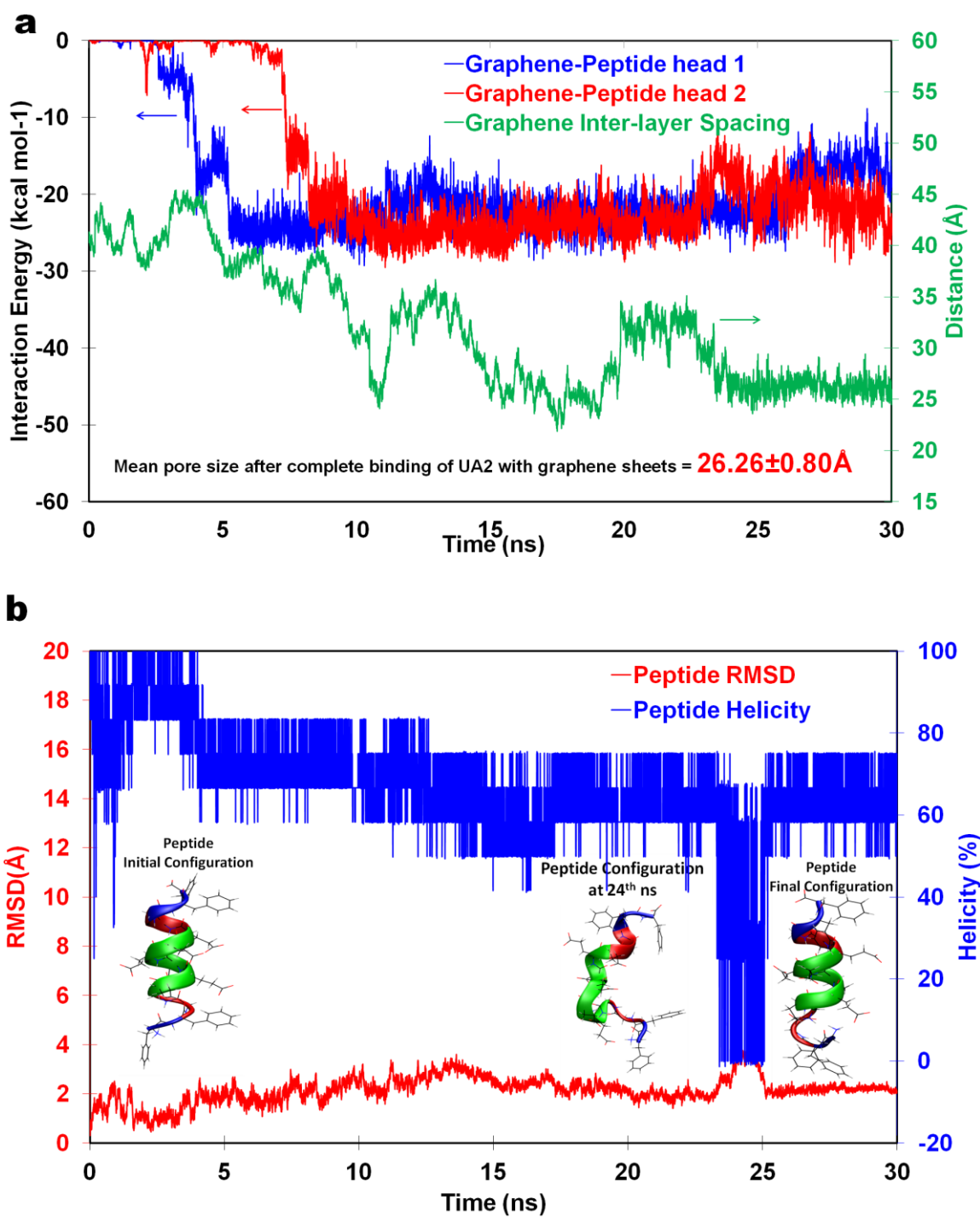
Supplementary Figure 5-1. The snapshots for the graphene nanosheets self-assembly using the peptide molecule: (a) the initial and (b) final configurations.

Section 2. Investigations of graphene-peptide interactions, graphene interlayer distance and peptide structural stability from MD Simulation

To investigate the detailed graphene-peptide interactions in rGOPH, the interaction energies for the UA2 with each graphene sheets are plotted in Supplementary Figure 5-2a. The interaction between graphene and aromatic ring containing residues (head groups) implies that UA2 reached their lowest energy level after binding with graphene surfaces and promoting the graphene self-assembly. The UA2 bound with the graphene surfaces with its first and second head groups at 5 and 8 ns respectively, via the dominant interaction of π - π stacking interactions and the hydrophobic interaction, and then remained stable at its lowest energy for more than 20 ns over 30 ns of simulation. A similar phenomenon was also observed in many previous reports[320, 347, 385, 413-415] which revealed that the π - π stacking interactions (van der Waals interaction) between aromatic groups of biomolecules and graphene-like surfaces are the dominant factor for their adsorption on the surface. A slight fluctuation of energy occurred between 24th and 25th ns which was due to peptide temporary disarrangement, however it quickly rearranged itself and reached the minim energy level without any significant disruption to the self-assembled structure. The green line in Supplementary Figure 5-2a exhibits the time evolution of distance between two graphene sheets over 30ns of simulation. The average interlayer distance of the rGOPH computed from the position of two graphene sheets after complete binding with UA2 is $26.26 \pm 0.80 \text{ \AA}$ which is in agreement with the range confirmed by the AFM experiments.

The impacts of graphene-peptide interactions on the UA2 structure and configuration were also investigated from the time evolution of the helicity change and calculating the peptide root-mean-square deviation (RMSD) as shown in Supplementary Figure 5-2b in blue and red lines, respectively. The average helicity value of 70% at complete adsorbed state confirms that the UA2 retained its α -helical structure. Similarly, with graphene-peptide interactions a little fluctuation was observed in peptide helicity from 24th to 25th ns. This originated from peptide disarrangement between graphene sheets, however, the peptide could quickly rearrange, obtain the helical structure and preserve it throughout the entire simulation. The inset images in Supplementary Figure 5-2b aid visualization and

understanding of the events of peptide disarrangement and rearrangement from MD simulation. The high stability of the α -helical structure observed in our MD simulations is in agreement with the RMSD average value which is as low as 2.15 Å. It is noted that the very small RMSD corresponds to weak disruption of UA2 configuration from interactions with both graphene sheets. With respect to helicity change between 24th and 25th ns of the MD simulation, a minor change of the RMSD value was expected to take place. However, no significant changes occurred in the self-assembly process of graphene sheets, indicating that the helical structure of the UA2 is dynamically stable in solution even when interacting with the graphene surface.

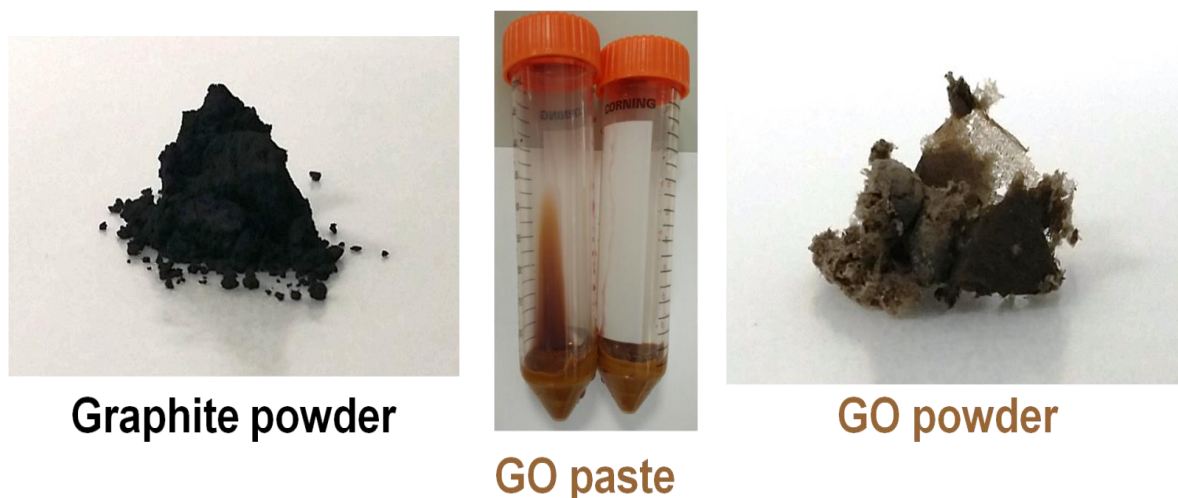


Supplementary Figure 5-2. (a) Time evolution of graphene interlayer distance¹³ and the interaction energy between UA2 peptide and below (blue) and top (red) graphene sheets, (b) Variation of α -helicity (blue) and RMSD (red) of rGOPH over a sample simulation. Insets are snapshots for the peptide initial, 24th ns and final configuration in MD simulation.

Section 3. Preparations and Characterizations GO and rGO

Section 3.1. Preparation of graphene oxide (GO)

Graphite oxide or Graphene oxide (GO) was prepared by oxidation of natural graphite according to the improved Hummer's method^[88]. Briefly, a 9:1 mixture of concentrated sulphuric acid and phosphoric acid (120:13 mL) was cooled overnight to 4 °C. The already cooled acid mixture was slowly added to the graphite powder (1 g) and potassium permanganate (6 g) during stirring at room temperature. Then, the mixture was heated to 50 °C for about 12 h to form a thick paste (as shown in Supplementary Figure 5-3). After the reaction had completed, the paste was cooled down to room temperature and quickly poured onto ice cubes (150 mL) with 30% hydrogen peroxide (1 mL) for an hour. The mixture was then washed and filtered with distilled water and hydrochloric acid (32 %) followed by repeated washing with ethanol and eventually with Milli-Q water. For each successive wash, the obtained brown dispersion was centrifuged at 4400 rpm for 2 hrs to remove residual salts and any un-exfoliated graphite oxide. The obtained GO was vacuum dried overnight at room temperature.

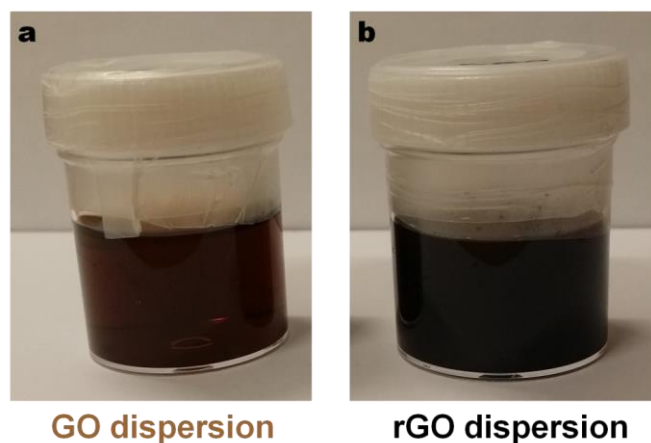


Supplementary Figure 5-3. Graphite to graphene oxide

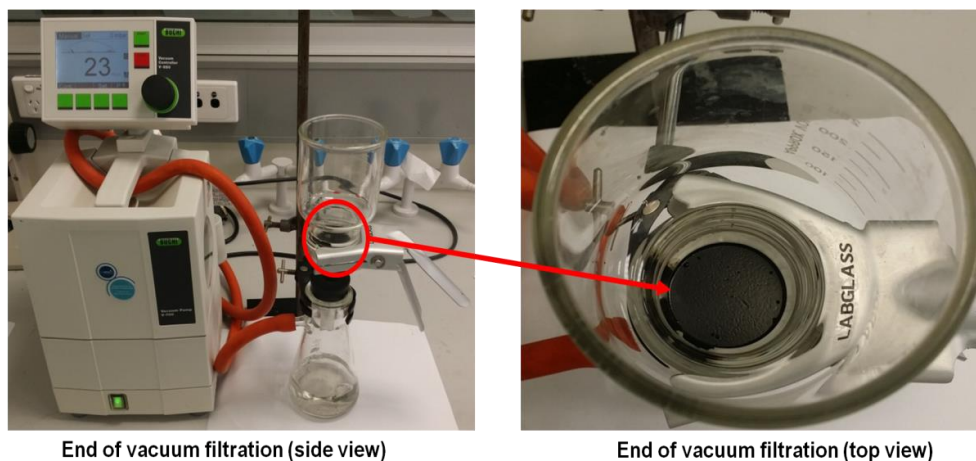
Section 3.2. Preparation of reduced graphene oxide (rGO)

In a typical procedure for chemically reducing GO to prepare rGO, the GO from previous step was used to prepare homogeneous dispersion (0.5 mg ml^{-1}) in a 25 mL flask. Then, 54 μl of hydrazine solution (35 wt% in water, Aldrich) and 75.0 μl of ammonia

solution (28 wt% in water, Crown Scientific) were added to the flask. The dispersion was shaken vigorously and stirred for a few minutes, then placed in an oil bath (~90 °C) for 1 hr. The brownish dispersion of GO (shown in Supplementary Figure 5-4a) turned to black rGO (shown in Supplementary Figure 5-4b). The rGO dispersions prepared were used for further characterization and hydrogel film fabrication.



Supplementary Figure 5-4. (a) GO and (b) rGO dispersions.

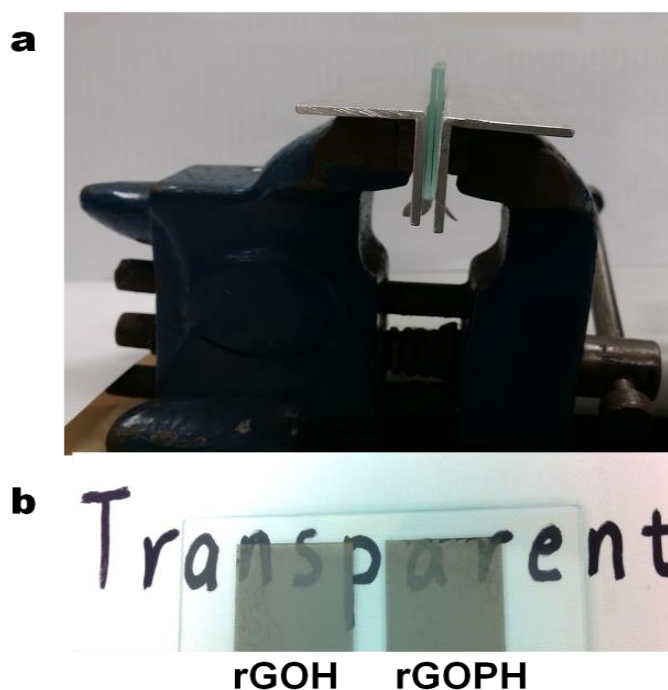


Supplementary Figure 5-5. Filtering apparatus (left) filtrate cake or hydrogel.

Section 4. Preparation of the transparent rGOH and rGOPH

Dilute dispersions of rGO ($0.0025\text{mg}\cdot\text{mL}^{-1}$ rGO in 200mL Milli-Q water) and rGOP ($0.0025\text{mg}\cdot\text{mL}^{-1}$ in 200 mL of a solution of the peptide $0.0005\ \mu\text{M}$) were prepared and were then vacuum filtered on a mixed cellulose ester membrane (47 mm in diameter, $0.45\ \mu\text{m}$ pore size, Millipore). The thickness of film can be carefully controlled from tens to few hundred nanometres by varying the concentration of dispersions. The rGOH and rGOPH

films were then adhered to the glass substrate so that the hydrogel sides were touching the glass substrate. They were then put under weight by utilizing a vice clamp at room temperature overnight (as is shown in Supplementary Figure 5-6a). The weight was then removed and the membrane was dissolved in acetone to leave the thin transparent hydrogel films on the substrate (as shown in Supplementary Figure 5-6b).



Supplementary Figure 5-6. Optical images of (a) vice clamp holding the graphene film between two glass substrate (b) transparent film of rGOH and rGOPH.

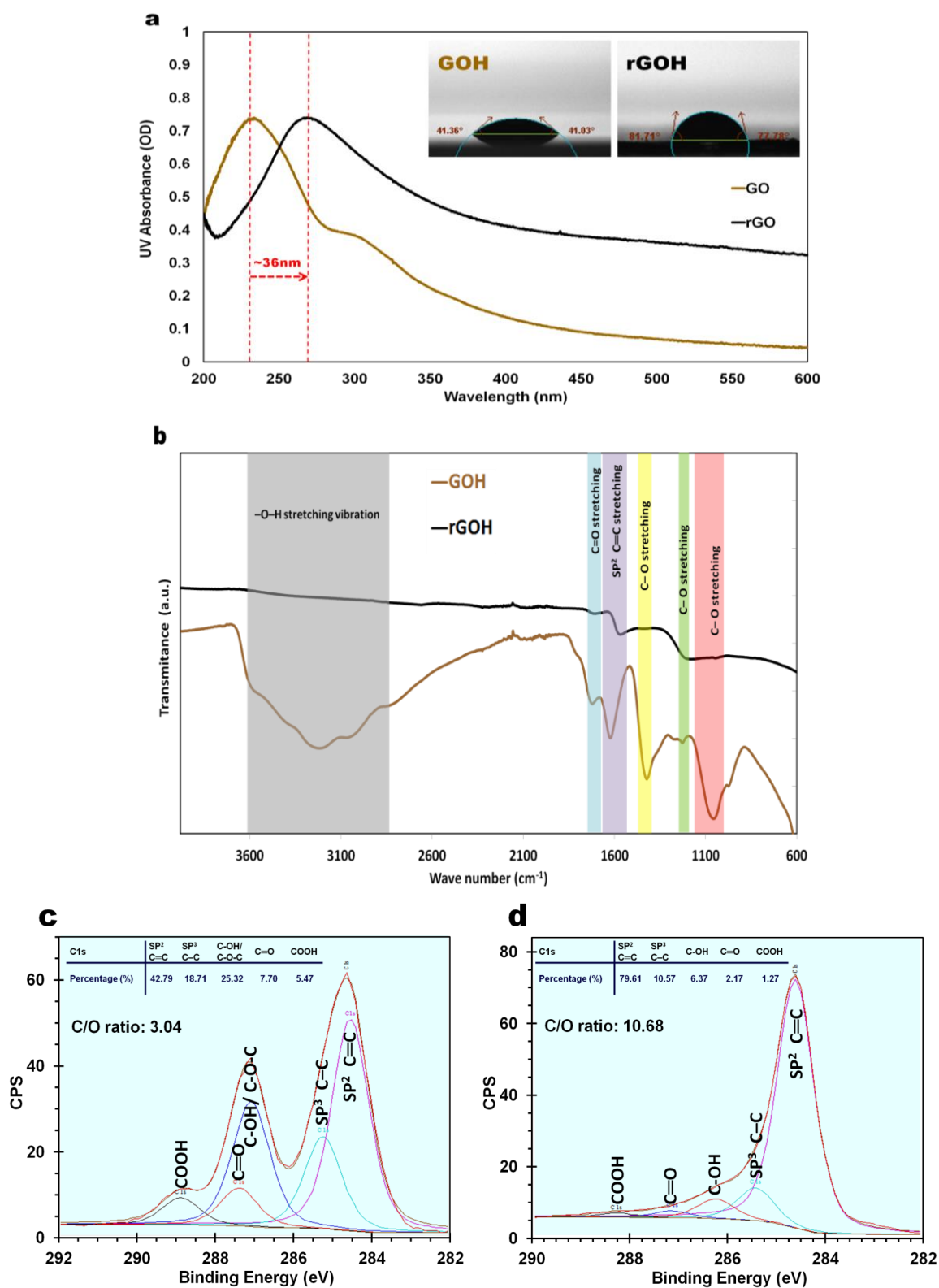
Section 5. Characterizations of GOH and rGOH

UV-vis spectrometer (Ocean Optics-CHEMUSB4) was employed to monitor the reaction process of the formation of stable graphene from GO to rGO dispersion. As shown in **Supplementary Figure 5-7a**, the absorption peak of the GO dispersion at 233 nm gradually redshifts to 269 nm, indicating that the reduction reaction was successful, and that the electronic conjugation within the graphene sheets is restored with hydrazine reduction. Inset images in **Supplementary Figure 5-7a** are contact angle measurements (using an Attension Theta optical tensiometer) to establish the correlation between the reduction process and material characteristics. Increasing the average contact angle from

41.20 for GOH film to 79.75 for rGOH film suggests the change in the wettability of the sample and confirms the efficient oxygen removal from the graphene surface.

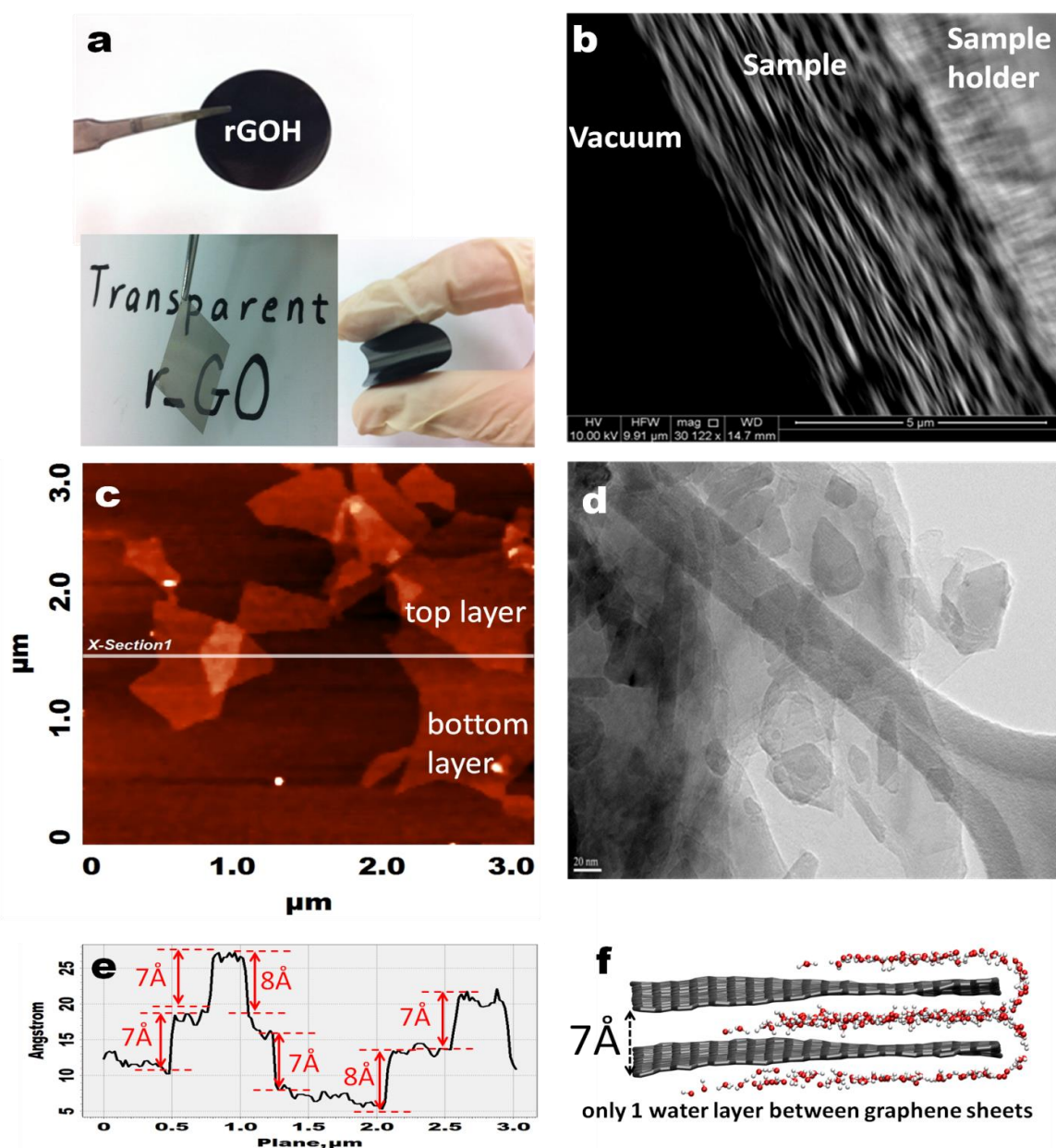
Supplementary Figure 5-7b shows the typical Fourier Transform Infrared Spectroscopy (FTIR) spectra of GO and the hydrazine treated rGO obtained by Nicolet 6700 FTIR. With GO, the characteristic peaks appear for hydroxyl (-OH stretching group at $\sim 3218\text{ cm}^{-1}$), carbonyl C=O stretching (1730 cm^{-1}), aromatic C=C (1620 cm^{-1}), carboxy C-O (1415 cm^{-1}), epoxy C-O (1228 cm^{-1}), and C-O (1070 cm^{-1}) which are all within the ranges reported elsewhere [416-418]. After chemical reduction, the peaks for the oxygen functional groups were reduced efficiently and the remaining noteworthy peak is attributed to the aromatic carbon double bonds (C=C) group.

XPS measurements in agreement with UV-vis and FTIR spectroscopy could provide sound evidence of the successful reduction of GO. The XPS spectra of GO and rGO films shown in **Supplementary Figure 5-7c** and **d** respectively, indicate that the carbon backbones, namely carbon sp^2 at $284.4\text{--}284.9\text{ eV}$ and carbon sp^3 at $285.3\text{--}285.8\text{ eV}$, of GO paper before reduction were functionalized with oxygen containing groups such as epoxide/hydroxyl groups (C-O : $286.1\text{--}286.7\text{ eV}$), carbonyl group (C=O : $287.4\text{--}287.9\text{ eV}$), and carboxyl group (O-C=O : $288.8\text{--}291\text{ eV}$) [417, 419]. The deconvoluted C1s XPS spectra in **Supplementary Figure 5-7d** reflect heavy reductions of oxygenated species arising mainly from the removal of C-O and C=O groups along with the restoration of sp^2 graphitic carbon, and decreases in sp^3 carbon and carboxyl groups. After the chemical reduction, almost all epoxide bonds (which have slightly greater binding energy than the hydroxyl group) were broken after reacting with hydrazine and converted to hydroxyl group according to step 1 of reduction reported by Wang et al. [420] Therefore, the oxygen species of C-O had a shift toward 286 eV attributing to C-OH . As they reported for the step 2 of reduction, the hydroxyl group is the second target. After reacting with hydrazine, a significant proportion of them are reduced, and some remain unreacted (as shown **Supplementary Figure 5-7c**). The carbonyl (C=O) and the carboxyl (O=C-O) also reduced significantly, which indicates an efficient reduction process.



Supplementary Figure 5-7. (a) The absorption peak of the GO and rGO dispersions (Inset images are Milli-Q water droplets on GOH and rGOH films), (b) FT-IR spectra of GOH and rGOH, (c) Deconvoluted XPS C1s spectra of (c) GOH and (d) rGOH.

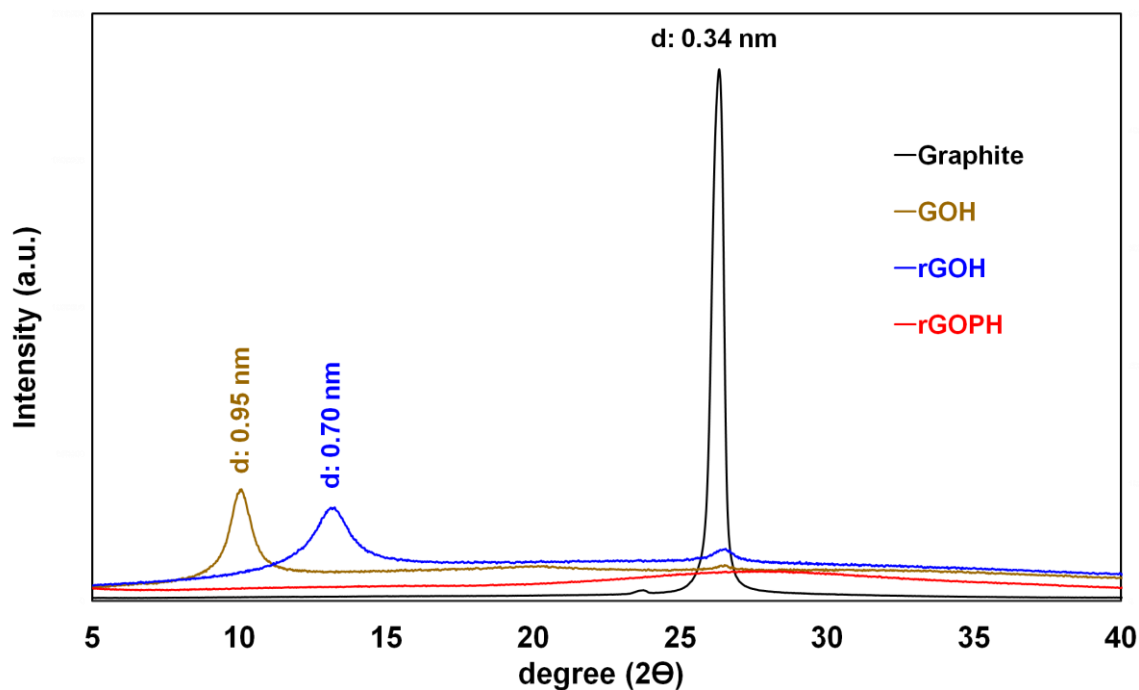
Using vacuum filtration approach we could obtain high-quality free-standing rigid and flexible film of reduced graphene oxide hydrogel (rGOH) and also a very thin transparent hydrogel but attached to a glass substrate (shown in Supplementary Figure 5-8a). This rGOH is sufficiently robust to be handled by hand and cut using normal scissors. The cross-sectional scanning electron microscope (SEM) image from the rGOH fracture edge in Supplementary Figure 5-8b clearly reveals the homogeneous and highly oriented layered structure of the graphene nanosheets parallel to each other, and similar to one achieved in previous work.[402] The morphology of as-prepared rGOH with its multilayer 3D structure was also characterized using atomic force microscope (AFM) (Supplementary Figure 5-8c) and transmission electron microscope (TEM) images (Supplementary Figure 5-8d), which both show how single layers of graphene arrange in parallel and on top of each other via the strong Van der Waals interactions between each two sheets. The small broken sheets layered on top occur due to conducting high ultrasound for the TEM sample preparation. The height profile of the rGOH shown in Supplementary Figure 5-8e, demonstrates that the inter-layer distance of the graphene plane in hydrogel is ~ 0.7 nm. Although for bare and defect-free graphene planes (basically, for un-reacted graphite), the natural interlayer distance is around 0.34nm, for rGO, owing to the presence of some un-removed O and OH groups, the natural interlayer distance is around 0.7nm.[27, 273, 278] This inter-planar distance of graphene sheets in hydrogel was also confirmed by our molecular dynamics (MD) simulation (Supplementary Figure 5-8f). This shows that hydration of graphene (the presence of 1 layer water in between graphene sheets) leads to interlayer spacing of about ~ 0.7 nm (see supplementary Movie 5-2 for the trajectory of graphene sheet self-assembly). This sits in the range reported by Nakajima et al,[273] for which the graphene interlayer distance varied between 6.87 to 8.72 Å depending on the extent of oxygen containing group and the hydration level. However, this could increase up to 1.2 nm for GO due to its great hygroscopic nature and large number of oxygen functional group.[34]



Supplementary Figure 5-8. (a) Photographs of rGOH film in both transparent and thick form, (b) SEM image of rGOH obtained from the cross section view, (c) Tapping-mode AFM image, and (d) TEM image of multi-layered rGOH from the top view, (e) Height profile of rGOH which illustrates a graphene interlayer spacing of about $\sim 7\text{\AA}$, and (f) side view snapshots of the representative rGOH from MD simulation.

Supplementary Figure 5-9 shows the wide-angle X-ray diffraction (WAXRD) patterns of graphite, GOH, rGOH and rGOPH. Compared with pristine graphite, the inter-layer spacing of GOH increased notably from 0.34 to 0.95 nm, indicating weakening of the inter-layer π - π stacking interactions. However, the inter-layer spacing decreased to 0.70 nm for rGOH after the reduction of GO and the elimination of oxygen containing

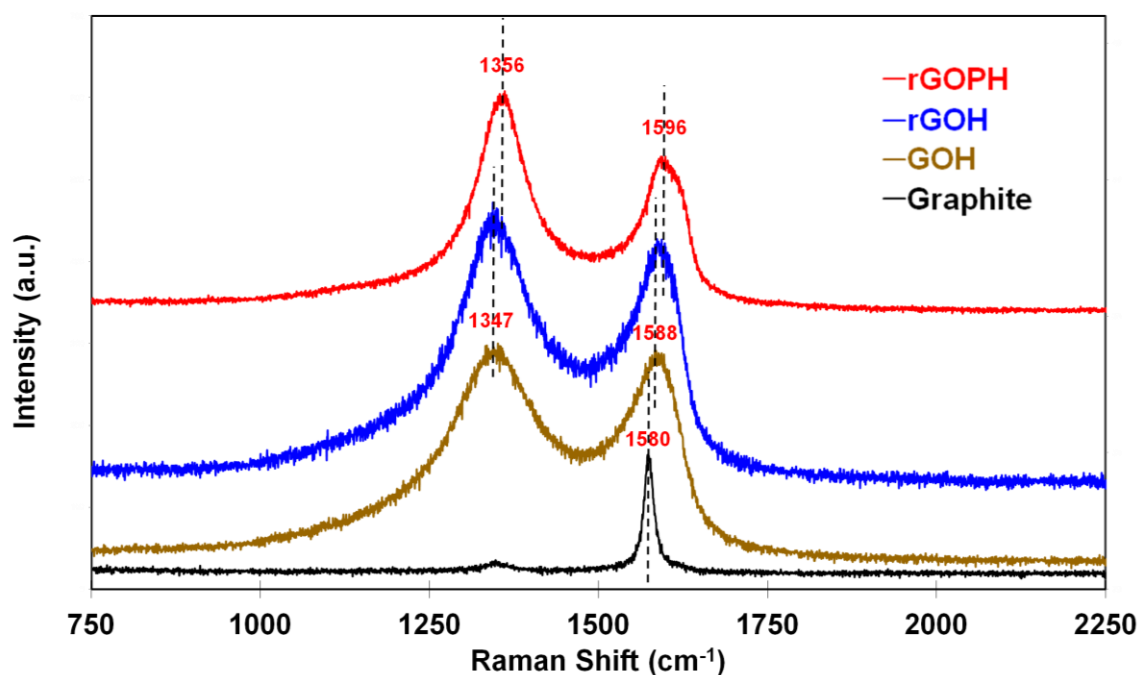
groups. This interlayer spacing is in agreement with MD simulation results and the AFM measurements of inter-sheets distance for rGOH. Both GOH and rGOH show a minor peak at about 2θ of 26° and this could be attributed to the existence of some graphene stackings. The rGOPH lacks any significant peak in WXR D except a very broad peak at about 2θ of 26° indicating that most of graphene interlayer spacing has been successfully filled with peptide. There are also some minor stackings which are negligible.



Supplementary Figure 5-9. WXR D patterns of graphite (black), GOH (brown), rGOH (blue) and rGOPH (red).

Supplementary Figure 5-10 represents the typical Raman spectra of graphite and GOH, rGOH and rGOPH film. The Raman spectrum of the pristine graphite, as expected, displays a prominent G (the E_{2g} mode of sp^2 carbon atoms) peak as the only feature at about 1580cm^{-1} . For both samples of GOH and rGOH, the two peaks at about 1347 and 1588cm^{-1} can be assigned to the D- and G-band, which respectively correspond to the vibrations of sp^3 carbon atoms of disordered graphene nanosheets (such as ripples, edges, and defects) and the vibrations of sp^2 carbon atom domains of graphite. The G band of graphite is broadened and shifted from 1580 to 1588cm^{-1} after the oxidation process indicating a better exfoliation of graphene layers [421] in GOH and rGOH. In addition, the D-band and the G-band produced a small red shift (9 and 8cm^{-1} , respectively) in rGOPH

compared with GOH and rGOH. Previous studies provide robust evidence that the interaction of graphene with other components might change the Raman peak frequencies [421-423]. Therefore, we hypothesize that such a significant shift in the position of the G band is probably due to the interaction between rGO and peptide during the self-assembly process.



Supplementary Figure 5-10. Raman spectra of graphite (black), GOH (brown), rGOH (blue) and rGOPH (red).

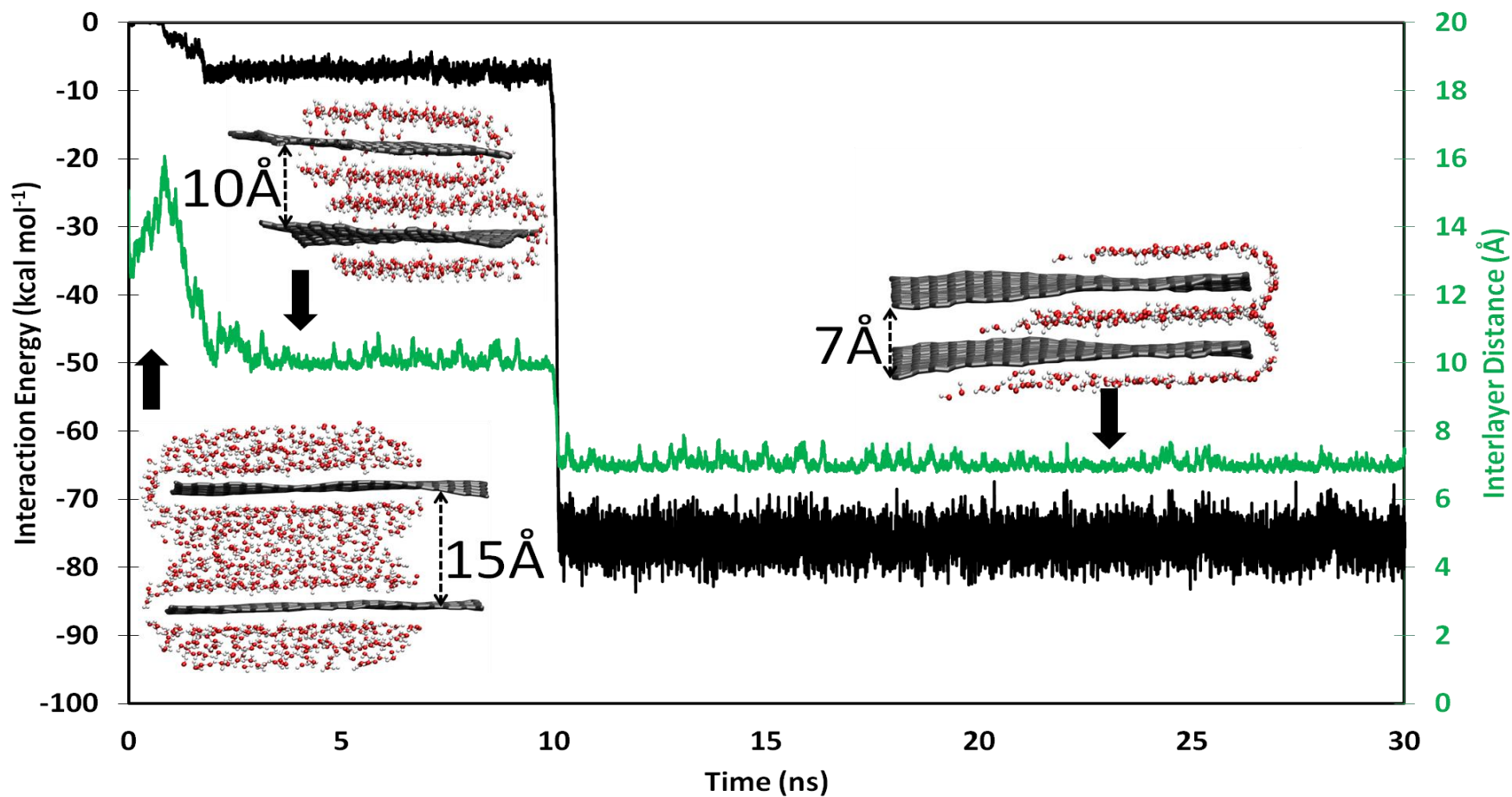
Further investigation is required to clarify this hypothesis. The intensity ratios of D- and G-bands (ID/IG) is used to determine the quality of graphitization or defective disorders on the crystalline structure of graphite. Compared with graphite, the ID/IG of GOH is drastically increased from 0.21 to 1.01, which is due to the increase of the disordered structure in the graphene sheets during oxidization[421]. After reduction of GO to rGO, the ID/IG of the rGOH increased to 1.09. This is due to the removal of some oxygen-containing functional groups[98, 423, 424] which alters the surface structure of GO with more defects and decreases the average size of the in-plane sp^2 domains (an increase of the edge defects) upon reduction [98, 425]. In addition, non-covalent modification of the graphene surface has been shown to contribute to the increase of ID/IG [421, 425]. For the rGOPH, the ID/IG is slightly increased to 1.15, which is indicative of

the increasing disorder after peptides bind with the graphene surface. This helps with further exfoliation of graphene layers and of course increasing their interlayer spacing.

Section 6. MD simulation method for graphene self-assembly dispersed in water

For the system composed of graphene and water, two nanosheets of graphene with the finite sizes of $41.75 \times 42.55 \text{ \AA}^2$ were placed in a periodic cubic box of $70.5 \times 72.5 \times 45.0 \text{ \AA}^3$. The system was then solvated using the TIP3 water model and the energy minimization was carried out for 200 ps. Molecular dynamics in the isothermal-isobaric ensemble, moles, pressure and temperature (NPT) ensemble was used to explore graphene conformation and the self-assembly in solution. The Langevin thermostat and CHARMM force field were employed to integrate equations of motion with a time-step of 2 fs. The particle mesh Ewald (PME) method was used to calculate the electrostatic interactions with a cut-off distance of 1.2 nm. The system underwent a 30 ns production run, with frames saved every 2 ps.

The self-assembly process of two graphene nanosheets (with a separation of 0.7 nm in the normal direction) was shown in Supplementary Movie 5-2 as video. The snapshots of the evolution of the graphene assembly as well as the interlayer water relative density were shown in Supplementary Figure 5-11. The graphene–water–graphene sandwiched structure was successfully maintained until the 30th ns of MD simulation.



Supplementary Figure 5-11. Time evolution of graphene interlayer distance (**green**) and the interaction energy between two graphene nanosheets (**black**). (Insets are the evolutionary snapshots of two graphene nanosheets self-assembly and the interlayer water relative density.)


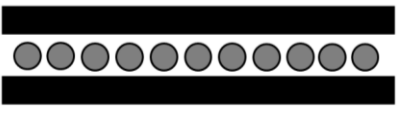
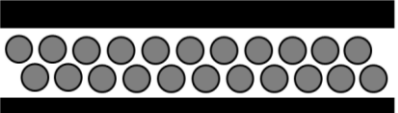
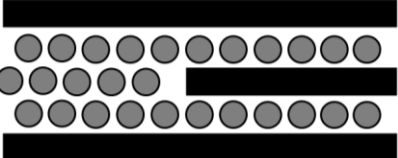
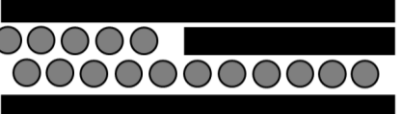
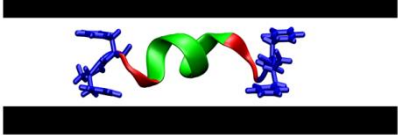
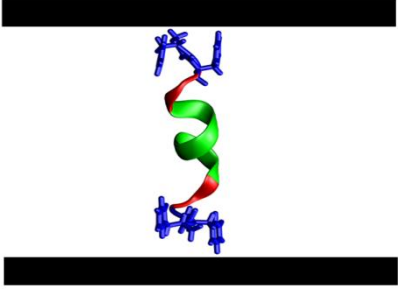

Supplementary Table 5-1. Mean pore size measurements from different AFM height profile images of rGOPH.

Sample	Pore size (nm)
1	2.6
2	2.8
3	2.7
4	2.5
5	2.6
6	2.7
7	2.4
8	2.2
9	2.5
10	2.5
11	2.5
12	2.7
13	2.4
14	2.8
15	2.9
16	2.9
17	2.6
18	2.5
19	2.5
20	2.6
Mean Pore size=	2.595±0.176

Section 7. Dry-state analysis of PSD

To discuss the origins of the peaks shown in Figure 4d of the article, we wish to categorize available pores for our samples into four individual groups for considering all the possibilities for pore formation. A summary of the classification with schematic view of the pores is reported in Supplementary Table 5-2.

Supplementary Table 5-2. Possible pores in wet-state hydrogels.

Category	Scheme	Description
0 not detectable by adsorption experiments (<0.9 nm)	0.34 nm 	Two fully-stacked graphene layers
	0.7 nm 	Two graphene layers with one layer of water between them
1 Stack mediated pores (0.9 – 1.5nm)	1 nm 	Two graphene layers with two layers of water between them
	1.4 nm 	Defect examples
	1.04 nm 	
	1.2 nm 	Protein molecule inserted between graphene layers (undesirable orientation)
	2.6 nm 	Peptide molecule inserted properly between graphene layers (desirable orientation)
3 Inter-particles void (>3.0 nm)		Voids between multi-layered graphene units (>3nm)

Chapter 6: Peptide Mediated Self-Assembly of Graphene based Hydrogels: Preparation, Optimization and Drug Delivery Application

Abstract

Amphiphilic hydrogels, such as graphene based hydrogels are known as a promising agent for sustainable drug delivery systems. However, it is a challenge to control their porous structures and pore sizes as these two factors significantly influence drug delivery behavior. A layered nanoporous graphene hydrogel named “rGOPH” with tuneable pore sizes produced through peptide-directed self-assembly was shown to be a promising candidate for the controlled delivery of an anti-cancer drug, doxorubicin (DOX). In particular, the hydrogel prepared with optimum degree of reduction of graphene oxide (GO), which was defined by design of experiment (DOE) analysis, showed the highest DOX loading capacity of about $\sim 500 \mu\text{g DOX/mg rGOPH}$. Pore sizes of less than $\sim 1 \text{ nm}$ would be achieved when the GO sheets were slightly and highly reduced, whereas the optimal reduction of GO led to the desired pore size of $\sim 2.6 \text{ nm}$ which aided with taking up more drug into the nanoporous structure. The effect of hydrogel pore size on drug delivery process has also been studied in this work. Utilizing the molecular dynamics (MD) simulations along with experiments demonstrated that the larger pore size ($\sim 2.6 \text{ nm}$) in the hydrogel network provides favorable accessibility for the diffusion of water as well as drug molecules. The DOX adsorption kinetic study for hydrogels revealed that the adsorption mechanisms were physisorption within their nanoporous structure as they well followed the pseudo-first order dynamic equation.

6.1 Introduction

Interest has focused on graphene nanomaterials because of their tunable biocompatibility and environmental responsiveness together with unique electronic, optical, mechanical, and chemical properties. Graphene based hydrogels have subsequently been extensively explored as promising biomaterials for biosensor,[426, 427] tissue engineering, [128, 428] gene [429] and drug delivery. [128, 267] Graphene oxide (GO)

[430, 431] and reduced graphene oxide (rGO) [432] as different subclasses of graphene have been widely studied for amphiphilic hydrogels preparations in the realm of nanomedicine delivery. High specific surface area, π - π stacking, hydrophobic interactions and electrostatic of graphene based hydrogels can be exploited to attain high loading of poorly soluble drugs such as anticancer drugs without losing potency or efficiency.[128] Both GO and rGO owing to their extremely high specific surface area and possessing active functional groups are able to interact with various drug molecules, such as doxorubicin (DOX) [28, 196, 197, 246-249], camptothecin (CPT), [196, 245, 249-253] 5-fluorouracil (5-FU) [254-256] and Ibuprofen [258]. Amongst these, the common anticancer drug DOX has received the most attention for exploiting both π - π stacking (containing 5 aromatic rings) and hydrogen bonding interaction with graphene derivatives [28, 196, 197, 246-249].

In the field of fabricating porous media, it is extremely important to construct them with an ordered microstructure and uniform pore size, [14, 30, 31] particularly for drug delivery applications, as the uniform spatial structure and pore distribution will ensure that drugs are homogeneously loaded and distributed. The use of mesoporous, microporous and nanoporous graphene based hydrogels as carriers in drug delivery systems is a part of a growing body of research [18, 263, 267, 268]. Similar to other porous media, tuning the pore size in graphene based hydrogels is vital in the sense that the loading and release of drugs may be conducted in a more controllable, reproducible and predictable manner. The idea of using varieties of spacers (cross-linkers) such as carbon based materials, [35-38, 293] polymers and [46, 291] metallic based particles [40, 41, 93] in order to prepare graphene based hydrogels has been interesting to increase the graphene interlayer spacing (pore size) and even control the hydrogel pore size. These kind of graphene based materials neither have an accurately uniform pore size nor are biocompatible to be tested as drug delivery agent. Thus, the focus of researchers moved toward using biomolecules such as amino acids or peptides [292, 317] as the spacer. They are favorable due to their high biocompatibility, controllability in their designs and binding with graphene sheets. One of the very few examples of peptide binding graphene hydrogel which peptide mediate the graphene gelation is peptide-graphene oxide hybrid hydrogel prepared by Wu et al.,[49] for drug delivery. Although their peptide was intelligently designed to bind with

graphene sheets and aid with their gelation, the pore size could not be controlled and it was randomly distributed in micrometer scale. To the extent of our knowledge, preparing the graphene hydrogel with highly accurate tunability in mesopore size and their inclusion of drugs in a reproducible and predictable manner has not been reported elsewhere when the peptide is not used.

In our previous work (in Chapter 5), a novel amphiphilic hydrogel named “rGOPH” with tunable pore size was produced via peptide mediated self-assembly of graphene sheets. In this study, the effects of preparation parameters on hydrogel pore structure as well as the loading capacity of DOX as a sample drug are statistically considered. Thus, pore engineering on graphene based hydrogels was investigated by conducting numerous experiments varying experimental parameters (such as hydrazine amount and temperature for the GO reduction, and peptide concentration) for preparation of rGOPH. We have used a wide range of hydrazine amounts and temperature here based on literature to better understand the effect of oxygen containing functional groups in the peptide mediated self-assembly of graphene sheets. The range of peptide concentration as one of the main variables for rGOPH preparation was set based on our preliminary screening experiment (in Chapter 5). The interactions between variables influencing the dependent parameter (response) which is the DOX loading capacity and their optimizations were then studied using statistical design of experiments (DOE) which will be explained in details in methodology section. Molecular dynamics (MD) simulation of rGOPHs was utilized as a tool to study the inter-molecular interactions in hydrogels and better interpret the occurrence in different experiments.

In addition, the influence of the hydrogel pore size on drug adsorption mechanism has been studied. As a fundamental method to monitor the adsorption efficiency, we used the adsorption kinetics to predict the adsorption characteristics and mechanisms. Furthermore, the effect of pore size on DOX loading yield and mechanism were investigated using MD simulations. Here, we believe that real time monitoring of DOX adsorptions into hydrogels and analysis of their kinetics will benefit from understanding the inter- and intra-molecular interaction mechanism between the DOX and graphene

based hydrogels and serves as the basis for the establishment of drug delivery systems in nano-constructs.

6.2 Experimental Details

6.2.1 Materials

Natural graphite (325 mesh, 99.8%) was obtained from Alfa Aesar. H_2SO_4 , H_3PO_4 , KMnO_4 , H_2O_2 , HCl and hydrazine (N_2H_4) and Ammonia (NH_3) used in GO and hydrogel preparation were all purchased from Sigma Aldrich except the peptide which was synthesized in our laboratory. All the Chemicals were directly used without further purification.

6.2.2 Methods

GO dispersion was produced by a modified Hummers' method [86] as originally presented by Kovtyukhova and colleagues [24], using graphite as a starting material. Details of the synthesis procedure for GO dispersions and their characterizations were reported in the supplementary information of Chapter 5. GO was converted back to conducting graphene (or rGO) by reacting with different amounts of hydrazine at different temperatures as guided by DOE. The reduced graphene oxide was then used to prepare the reduced graphene oxide hydrogel (rGOH) and reduced graphene oxide binding peptide hydrogel rGOPH films via directional flow caused by vacuum filtration. The residual hydrazine was removed via soaking and washing with Milli-Q water for several times. More details on how to prepare the rGOH and rGOPH hydrogels can be found in chapter 5. In this study, 20 samples of rGOPH were prepared by varying three main parameters (hydrazine amount and temperature for the GO reduction, and peptide concentration for the pore size enhancement) in order to investigate their influences on controlling pore sizes as well as drug loading capacity.

After preparing wet hydrogel films, they were freeze-dried only prior to characterization of the films. The wet-state rGOH and rGOPH films were transferred into cylindrical containers and only the bottom of the container was immersed into liquid nitrogen and the wet film became frozen immediately. A lab-scale freeze-drying device

ALPHA 1-2LD Plus (CHRIST, Germany) was used to dry the frozen films at the temperature of 188K and under the pressure of 10^{-2} Pa for 24 hrs.

6.2.3 Characterization

6.2.3.1 GO and rGO surface charge measurements

The dispersion/aggregation states of GO and rGO sheets upon the parameters of hydrazine amount and reduction temperature were monitored by measuring their surface charges (zeta potentials) using a Malvern Zetasizer Nano-ZS particle analyzer.

6.2.3.2 Contact angle measurements

Contact angle measurements (using an Attension Theta optical tensiometer) to establish the correlation between the reduction process and material hydrophobicity.

6.2.3.3 Fourier transform infrared (FTIR) spectroscopy analyses

FTIR spectra of all freeze-dried hydrogel films were recorded on a Bruker Tensor27 spectrometer. Spectra were obtained in an optical range of $400\text{--}4000\text{ cm}^{-1}$ by averaging 3 scans at a resolution of 5 cm^{-1} with 1 min interval to minimize the effects of dynamic scanning.

6.2.3.4 Atomic force microscopy (AFM) investigations

Surface topography and height profile of the rGOH and rGOPH were recorded by a MultiMode® 8 (Bruker) AFM in tapping mode. Image and height profile analyses of the AFM images were performed using the Nanoscope software. The AFM samples were prepared by drop-casting a diluted suspension of each hydrogel onto a fresh-cleaved Mica substrate and were then imaged.

6.2.3.5 X-ray photoelectron spectroscopy (XPS) analyses

XPS of the hydrogel films was carried out using a Kratos (UK) Axis-Ultra spectrometer with a monochromatic Al $K\alpha$ source (1487 eV) operating at 15 kV and 14 mA. The analysis of the photoelectron spectra was conducted using CasaXPS (V2.3.5)

software. Freeze-dried hydrogels samples were degassed prior to the nitrogen adsorption experiments at ambient temperature and a background vacuum of 10^{-5} kPa for 12 hrs. Nitrogen gas adsorption experiments were carried out at 77K using a Belsorp-max gas adsorption apparatus. Ultra high purity (>99.999%) helium and nitrogen from Coregas Australia were used for dead-space measurements and adsorption experiments, respectively.

6.2.4 Loading of DOX in hydrogels

The loading of DOX on the freestanding rGOH and rGOPH films were done by immersing films (in wet state) into DOX solutions in Milli-Q water, as shown in Figure 6-1. For each real time observation, 3 mL of DOX solution ($50 \mu\text{g}\cdot\text{mL}^{-1}$) was added into cuvette and then 15 mg of each film (in wet state) was placed on the bottom of the cuvette. Absorbance of DOX at a wavelength of 490 nm [187, 433] was monitored continuously for 24 hrs by a UV–VIS spectrometer (USB4000-UV-VIS - Ocean Optics). The one day loading capacity was calculated according to the following equation [28]:

$$\text{Loading capacity} = \frac{W_{\text{initialDOX}} - W_{\text{finalDOX}}}{W_{\text{hydrogel}}} \quad (6-1)$$

where $W_{\text{initial DOX}}$ is the weight of DOX initially added, $W_{\text{final DOX}}$ is the weight of DOX left in the cuvette after 24 hrs and W_{hydrogel} is the weight of rGOH and rGOPH samples which is approximately 15 mg for each experiment. (The amount of DOX after the loading can be calculated from the calibration curve shown in Supplementary Figure 6-1)

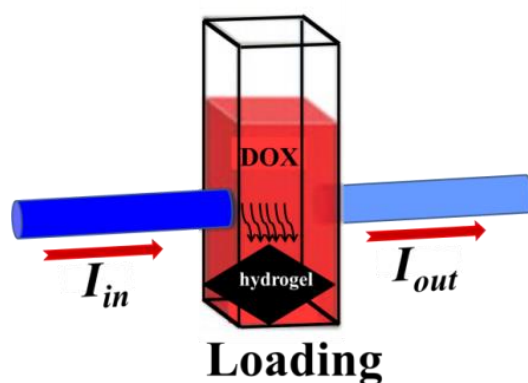


Figure 6-1. Schematic drawing of the real time monitoring of DOX loading on hydrogels placed inside a cuvette.

6.2.5 Statistical analyses on the effecting parameters for DOX loading

The statistical design of experiments (DOE) is a time and money saving method achieved by significantly reducing the number of trials required to study a multi-variable phenomenon. This is extremely useful when screening probable variables for cases involving second-order models [434]. In addition, the DOE is used to compute the multiple interactions between the main variables and also their influences on the response of a process. Response surface method (RSM) is a collection of mathematical and statistical techniques that generates three dimensional plots and displays statistical analyses about how the responses are influenced by the process variables. RSM was also applied to the optimum operating conditions for the system and to identify the region, which satisfies the operating specifications [435].

The most popular RSM design is the central composite design (CCD) for analysis of experimental data. The CCD is applied to estimate the coefficients of a particular model equation. The CCD method is efficient and flexible, providing sufficient information on the effects of variables and overall experimental error with a minimum number of experiments [435]. Center points in CCD design are usually repeated 4-6 times to get a good estimate of experimental error (pure error). Six center points will be created by default for experimental designs with three variables. Central composite designs generally require 3 levels for each variable: $-\text{Alpha}$, -1 , 0 , 1 and $+\text{Alpha}$. In this study, Alpha value is taken as one resulting at 3 levels, Lowest (-1), middle (0), highest ($+1$) which is more specifically known as central composite face centered design (CCFD). Full factorial design

for a study with three variables requires 20 experimental trials. RSM has successfully been applied to study and optimize the experiments with graphene for instance in chemical synthesis of graphene based nanocomposites [436, 437], biomolecule immobilization on graphene surface [438], and vitamin B₁₂ adsorption of graphene oxide [439].

The objective of using DOE in the present work is to investigate the DOX loading capacity of rGOPH using the CCFD. The main parameters (variables) investigated were for the degree reduction of GO based on literature. The amount of hydrazine to obtain rGO from the low to extremely high degree of reduction were chosen 25 and 75 μ L which sits in the ranges used by Dan Li et al. and Fernandez-Merino et al,[118, 440] . The temperature dependence of GO reduced by hydrazine was investigated using suggested ranges of temperature from literature [441, 442] for rGO synthesis with reasonable dispersibility.

The statistical analyses were performed using Design-Expert [443] software (version 6.0.7, Stat-Ease Inc., Minneapolis, USA). The response surface method (RSM) of statistical analysis system and design expert was used to statically analyze the experimental data. A CCFD was applied with three design parameters (variables); the hydrazine amount for GO reduction (A), the reduction temperature (B), and peptide concentration (C). The variable levels are such that the upper level corresponds to code +1, the lower level to code -1 and the middle level to code zero. The coded level and actual value of these variables have been generated and tabulated by the DOE analysis (shown in Table 6-1) in which the value of -1 and 1 shows the minimum and maximum range of each variable and 0 is the center point.

Table 6-1. Coded and actual values of variables of the design for graphene oxide reduction and rGOPH preparation.

Variable	notation	Unit	Coded levels of the variables		
			-1	0	1
Reduction Temperature	(A)	°C	85	90	95
Amount of Hydrazine	(B)	μL	25	50	75
Peptide Concentration	(C)	μM	0.04	0.07	0.10

The 20 runs of statistical experiments suggested by CCFD method with actual values are presented in Supplementary Table 6-1. The response selected was loading capacity of DOX on rGOPH. After running these 20 trials, the corresponding quadratic models for the above response and parameters were computed. The purpose of these experiments was to determine the functional relationship for the yield of drug loading in relation to these 3 variables. These are carried out for developing the model and optimizing the rGOPH preparation parameters.

The results obtained were then used to elucidate regression model fitting and the statistical analysis to ensure the adequacy of the model in representing results. The mathematical relationship relating variables to the responses can be calculated by the general quadratic equation model as follows:

$$Y_i = \beta_0 + \sum_{i=1}^k \beta_i X_i + \sum_{i=1}^k \beta_{ii} X_i^2 + \sum_{i < j}^k \beta_{ij} X_i X_j + \varepsilon \quad (6-2)$$

where Y_i represents the predicted response (dependant variable), X_i and $X_i X_j$, respectively, are the independent variables and their interactions which influence the response variable Y_i ; β_0 is the constant coefficient, β_i , β_{ii} and β_{ij} are coefficients for the linear, quadratic and interaction effects, respectively. ε is the standard error. There are three variables are involved, hence, k is 3 in this study.

The quality of the developed model was determined by the coefficients of determination (R-squared), while the analysis of variance (ANOVA)[444], as the most efficient parametric method available, helped to evaluate the statistical significance of the model by the values of regression and mean square of residual error. ANOVA is a method

of testing for the equality of three or more population means by analyzing sample variances. The ANOVA table, including lack of fit, Fisher's F-test and its associated probability $p(F)$, is used to determine the significance of the first degree (linear), second degree (quadratic), and cross-product (interaction) terms of the polynomial. After ensuring the validity of the model, the equation was used to predict the optimum values, to plot the two-dimensional contour plot to determine the interactions between the parameters, and the three-dimensional response surfaces. The generated mathematical model was also validated by conducting experiments at DOE given optimal conditions.

6.2.6 MD simulations

Graphene and peptide were, respectively generated using the graphene and protein builder in the visual molecular dynamics (VMD) package [366]. The DOX molecule structure was generated using Zinc database[445]; its topology and CHARMM force field parameters were constructed by SwissParam[367]. Neutral pH considered in each simulation is similar to its corresponding experimental condition, and the UA2 molecule has charged N-terminal (NH_3^+) and C-terminal (COO^-) ends. Graphene-graphene and peptide-graphene interactions were modelled by the CHARMM27 all-atom force field^[368], and MD simulations were performed by the NAMD program [369] (see details in supplementary information, section 3).

6.3 Results and discussion

6.3.1 DOX loading capacities under different pH values

The loading behaviors of DOX (at the initial DOX concentration of $50 \mu\text{g}\cdot\text{mL}^{-1}$) toward the rGOPH films were investigated at pH 5.4, 7.4 and 9.4 adjusted by PBS buffer. The adsorption of DOX in each hydrogel was monitored by the DOX UV absorption peak at 490 nm through the established standard curve (Supplementary Figure 6-1). As shown in Figure 6-2, the rGOPH exhibits the expected distinct pH-dependent behavior with different loading factor toward. The DOX loading ratio was the largest in neutral condition ($510.4 \mu\text{g}$) as compared with the acidic ($283.6 \mu\text{g}$) and basic conditions ($390.2 \mu\text{g}$). Such behavior may be interpreted as the different degree of hydrogen-bonding interaction between drug

molecules and oxygen containing groups of hydrogels under different pH conditions [28, 248]. It is noteworthy that all three samples to be tested in different pH values were cut from the same hydrogel film (with the same degree of reduction of GO and peptide concentration), there should be almost the same size of dominant hydrophobic (π - π stacking) interactions between them and DOX. Thus, the only differentiating factor in loading capacity is the number of hydrogen bonding groups.

As shown in Table 6-2, the acidic condition can only provide four and the least hydrogen bonds, as $-\text{NH}_2$ of DOX forms $-\text{NH}_3^+$ with H^+ and therefore cannot participate in hydrogen bonding. Although, there are eight types of possible hydrogen bondings under both neutral and basic conditions, the latter generates a lesser number of hydrogen bonds, as six out of eight types of hydrogen bonds involve peptide and the concentration of peptide in hydrogels is not comparable with that of graphene sheets. Moreover, in a basic condition, $-\text{COOH}$ of graphene sheets which is one of main hydrogen bonding initiators becomes deprotonated to $-\text{COO}^-$ and cannot participate in forming hydrogen bonds with $-\text{OH}$ or $-\text{NH}_2$ groups of DXR. Hence, in view of achieving the hydrogel with the largest loading capacity, we then chose neutral pH for DOX loading on rGOPHs of statistical experiments.

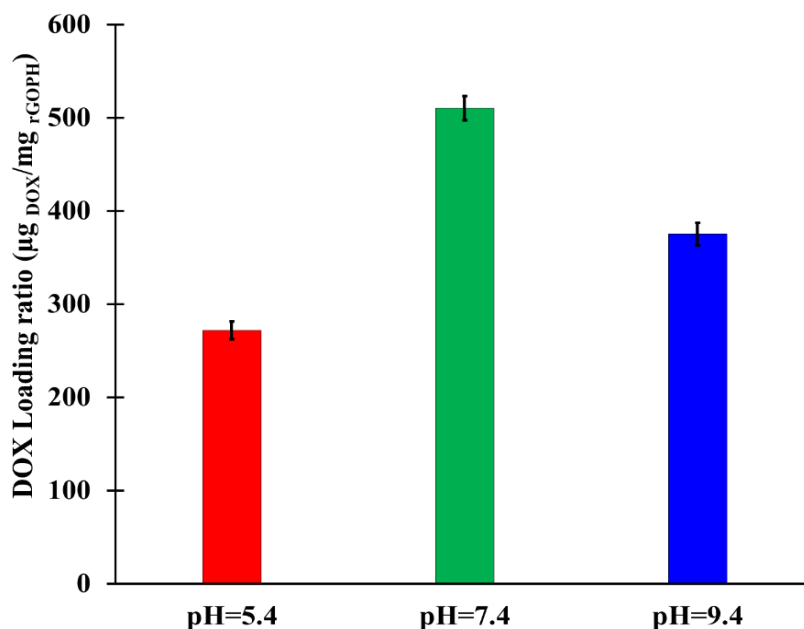


Figure 6-2. The loading capacity of DOX in rGOPH (prepared at optimized conditions) at different pH values adjusted by PBS buffer.

Table 6-2. Groups form hydrogen bonds in rGOPH and DOX at different pH values.

pH	rGOPH	DOX	Types of possible hydrogen bonds
5.4	$-\text{COOH}_{\text{graphene}}$, $-\text{OH}_{\text{graphene}}$, $-\text{NH}_{\text{peptide}}$, $-\text{C}=\text{O}_{\text{peptide}}$	$-\text{OH}$	4
7.4	$-\text{COOH}_{\text{graphene}}$, $-\text{OH}_{\text{graphene}}$, $-\text{NH}_{\text{peptide}}$, $-\text{C}=\text{O}_{\text{peptide}}$	$-\text{NH}_2$, $-\text{OH}$	8
9.4	$-\text{OH}_{\text{graphene}}$, $-\text{NH}_2_{\text{peptide C-term}}$, $-\text{NH}_{\text{peptide}}$, $-\text{C}=\text{O}_{\text{peptide}}$	$-\text{NH}_2$, $-\text{OH}$	8

6.3.2 Model equation development and DOE statistical analysis

The loading behaviors of DOX on both rGOH and rGOPH were studied at neutral pH. The concentration of DOX was determined by monitoring the absorption peak at about 490 nm through the established DOX UV calibration curve (Supplementary Figure 6-1). The DOX loading efficiency for each hydrogel was investigated at a constant initial DOX concentration ($50 \mu\text{g.mL}^{-1}$) with respect to the different hydrogel preparation parameters (reported in Table 6-3).

Table 6-3. Experimental design and the actual response of the DOX loading on rGOPH samples.

Run	Variable Type	Variables			Response
		A, (°C)	B, (μL)	C, (μM)	Dox Loading variable, (μg DOX/ mg dry hydrogel)
1	Fact	85	25	0.04	244.4
2	Fact	95	25	0.04	109.7
3	Fact	85	75	0.04	292.6
4	Fact	95	75	0.04	71.5
5	Fact	85	25	0.10	263.9
6	Fact	95	25	0.10	261.5
7	Fact	85	75	0.10	348.2
8	Fact	95	75	0.10	307.2
9	Axial	85	50	0.07	419.3
10	Axial	95	50	0.07	327.1
11	Axial	90	25	0.07	394.6
12	Axial	90	75	0.07	410.2
13	Axial	90	50	0.04	305.7
14	Axial	90	50	0.10	417.3
15	Center	90	50	0.07	469.2
16	Center	90	50	0.07	510.5
17	Center	90	50	0.07	469.6
18	Center	90	50	0.07	501.8
19	Center	90	50	0.07	477.9
20	Center	90	50	0.07	505.6

Figure 6-3 shows the comparison between the Actual (experimental) value and DOE predicted value for DOX loading capacity. It is clear that the fitted regression equation for our experiments has shown a good fit of the model with the R-squared (R^2) value of 0.9886. This indicates that 98.86% of the total variation in DOX loading capacity was attributed to the experimental parameters studied, and hence, could be explained by the fitted model. The R^2 always lies between 0 and 1 and as suggested by Joglekar and May (1987)[446], the R^2 should be greater than 0.80 for the good fit of a model.

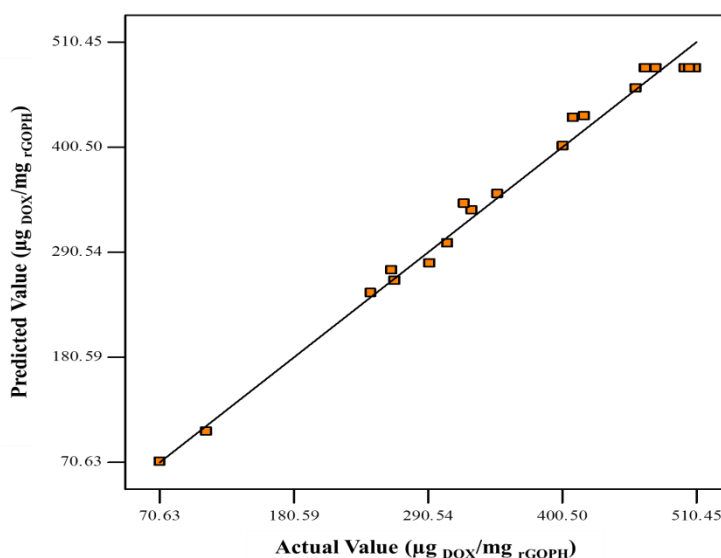


Figure 6-3. The experimental DOX loading capacity plotted against the predicted values calculated from the DOE-RSM model.

Using DOE, the multiple regression analysis was applied to establish the polynomial coefficients. The final equation for determination of the DOX loading capacity can be summarized as follows:

$$\begin{aligned}
 \text{Loading factor } \left(\frac{\mu\text{g DOX}}{\text{mg hydrogel}} \right) = & -49.16A + 18.84B + 60.34C \\
 & - 99.51A^2 - 66.62B^2 - 81.48C^2 - 15.62AB + 39.04AC + 14.98BC + 482.54
 \end{aligned}
 \tag{6-3}$$

where A, B and C are reduction temperature, hydrazine amount and peptide concentration, respectively. The adequacy and significance of the predicted quadratic model were further established by performing ANOVA as given in Supplementary Table 6-2. Some additional statistical parameters mainly standard deviation (SD) and coefficient of variation (CV) are given in Supplementary Table 6-3. To better understand and visualize the effects of each parameter and their interaction effects, the contour and 3D behaviors of the response (DOX adsorption) can be plotted as a function of the two variables at a time while maintaining the other variable at fixed levels (center-point). The quadratic response surface plot in the optimization of each two variables are illustrated and explained in separate sections below. All profiles represent similar surfaces where the maximum response is located inside the experimental variable ranges, indicating that variation of each variable level does directly influence the studied system.

6.3.2.1 Effect of the temperature and Hydrazine amount on DOX loading capacity

According to the contour and 3D surface plots, as shown in Figure 6-4, the amount of DOX loading on the rGOPH gradually increases and then starts to decrease with the increasing temperature and amount of hydrazine. The optimum temperature and hydrazine amount for the rGO preparation to have the maximum DOX loading efficiency were found to be 89 °C and 54 μ L, respectively.

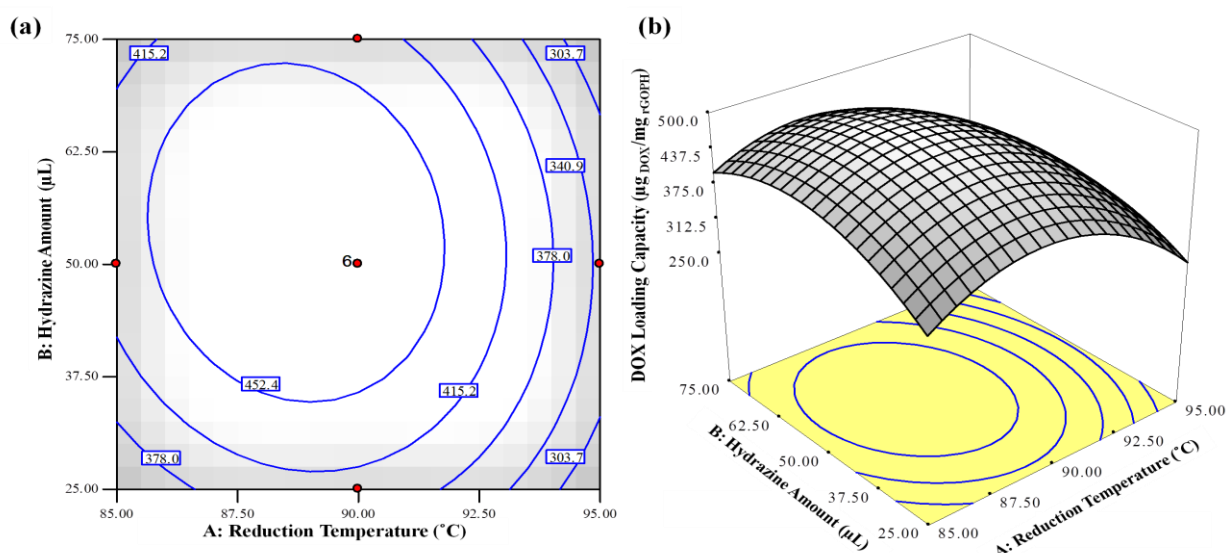


Figure 6-4. Response surfaces for DOX loading capacity against A:reduction temperature and B:amount of hydrazine depicted as contour (a) and three-dimensional (b) plots. The variable C was kept at its zero (centerpoint) level.

The two important parameters impact on the degree of reduction are the temperature and the amount of hydrazine (reducing agent). The reduction degree seems to be very influential on the structure and properties of graphene multilayered films. The water contact angle and FT-IR analysis as qualitative methods (in Supplementary Figure 6-2 and 6-4, respectively) and Zeta Potentials measurement (in Supplementary Figure 6-3) as quantitative methods were applied to monitor the properties and chemistry of GO sheets upon different degrees of reduction. These characterizations together confirmed highly hydrophilic behavior and lowest degree of reduction of the graphene sheets reduced at either the lowest temperature or the lowest hydrazine amount (at 85 °C or with 25 μ L hydrazine). The slightly reduced GO prepared at this condition is named “rGO-SR”. On the contrary, the rGO produced at the highest temperature and hydrazine amount (at 85 °C or with 25 μ L hydrazine) is highly hydrophobic, hence, named “rGO-HR”. There is

another hydrogel prepared at the optimum conditions of these two parameters (89 °C and 54 μ L) which is optimally reduced and named “rGO-OR”. Section 2 of supplementary information together with supplementary Figures 6-2, 6-3 and 6-4 evidence and give more details about how GO degree of reduction influences on properties, stability and chemistry of the material.

The degree of reduction also influences the peptide adsorption on graphene surface, thereby affecting the self-assembly of graphene layers. As is reflected in the contact angle measurement, Zeta potentials and FT-IR, the lower the temperature and the hydrazine amount, the more oxygen functionalities and hydrophilicity for the graphene sheets. Hence, the peptide with hydrophobic end groups is unlikely to bind with such a highly hydrophilic surface. According to Bai et al. [447] and Konkena et al.[448], highly hydrophilic graphene sheets precipitate on top of each other via strong hydrogen bonding among oxygen-containing functionalities. This is also the case when graphene sheets are over reduced by increasing the temperature and using excessive hydrazine. Excellent reduction of graphene sheets occurs when most functional groups leave the surface and the most sp^2 carbon are regenerated on the graphene surface. When the graphene sheets are too reduced, the chance of their stacking becomes higher due to a greater π - π stacking interaction. Although the similar π - π stacking is the interaction in between the graphene sheet and peptide ends, this is not just enough to overcome the strong π - π interaction between highly reduced graphene sheets. In the instances of rGO precipitation or excessive aggregation interactions between graphene sheets, the chance for the peptide to reside in between graphene sheets is very low. The AFM image and corresponding height profile for rGOPH-SR and rGOPH-HR strongly evidence their aggregations. The graphene interlayer spacing for rGOPH-SR and rGOPH-HR are at average of \sim 0.7 nm and \sim 0.9 nm, respectively. These two values fit in the range between 0.68 nm and 1.2 nm which were reported for interlayer spacing of graphene sheets with the lowest and highest amount of oxygen functionalities, respectively [34, 273].

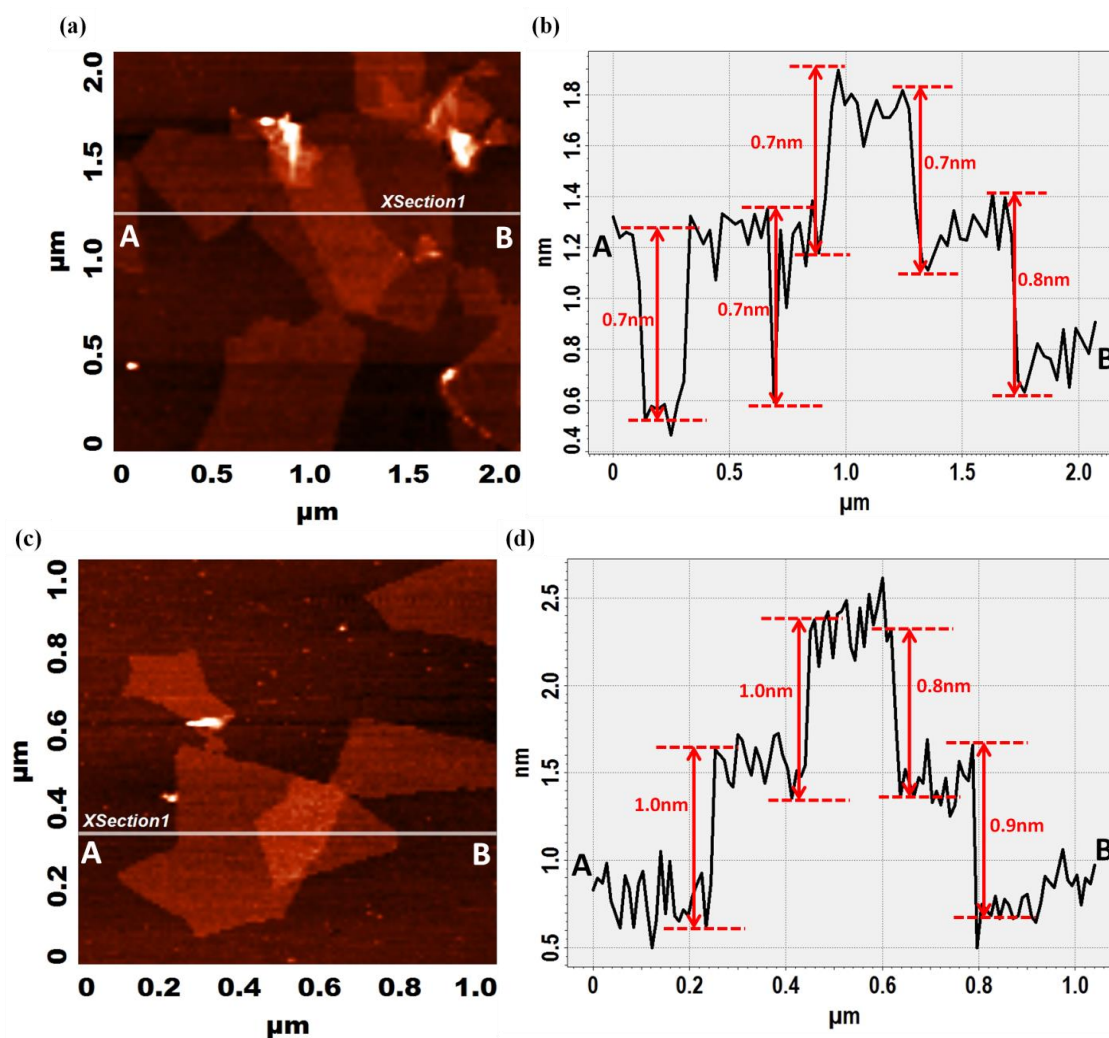


Figure 6-5. Tapping-mode 2D AFM images of (a) rGOPH-HR and (c) rGOPH-SR; Height profile of (b) rGOPH-HR and (d) rGOPH-SR.

XPS was performed in order further confirm the ejection/retention of the peptide from/at the graphene interlayers of different hydrogels. Figure 6-6a shows an XPS wide-scan spectrum obtained for various hydrogel films with three major peaks found that from left to right are attributed to the O 1s and N 1s and C 1s characteristics. Their corresponding oxygen, nitrogen and carbon atomic concentration are given in Figure 6-6b. Considering that the peptide concentration in three rGOPH films were the same with insignificant molar ratio compared with rGO, the rGOPH-SR with the lowest concentration of carbon (76.31%) and the highest concentration of oxygen (20.15%) indicate the lowest degree of GO reduction. In contrast the rGOPH-HR contains the highest concentration of carbon (87.65%) and the lowest concentration of oxygen (10.06%) which are the

indications of the highest degree of reduction. The atomic concentration of nitrogen in hydrogels was used in order to measure their peptide content. Although no peptide was used in the plain rGOH, it has 1.56% of nitrogen, which suggests the incorporation of some insignificant nitrogen atoms on the graphene surface after being treated with hydrazine. The N 1s peaks of rGOH (shown in Figure 6-6c) after deconvolution revealed that all of nitrogen atoms are in the form C-N as with a peak at 399.1 eV. [449] After subtracting 1.56% from nitrogen concentration of each rGOPH, it is revealed that rGOPH-SR and rGOPH-HR contain an insignificant amount of peptides as they both lose peptides during the self-assembly of graphene sheets. In contrast, a significant amount of nitrogen in rGOPH-OR (more than three times large than that of rGOPH-SR) is a strong support to the hypothesis of peptide retention in the hydrogels during the self-assembly process. In order to ensure that the origin of difference between the nitrogen concentration of rGOH and rGOPH is the presence of peptide, the N 1s peak of each rGOPH was deconvoluted and shown in Figure 6-6d, e and f. The rGOPHs have two extra peaks than the plain rGOH. The deconvoluted peaks found at 400.3 eV and 401.7eV, in rGOPH films, respectively correspond to the amide bond nitrogen (CO-NH) [450, 451] and protonated amino groups (NH₃⁺) [450, 452, 453] present in the peptide molecules.

According to our MD simulation (shown in Figure 6-7a) of a peptide between two plain graphene sheets representing as highly reduced GO, the phenylalanine (PHE)-graphene interaction energy at each end of protein is about 25 kcal mol⁻¹ (in binding state) which is almost 30 times smaller than that between two graphene sheets ~730 kcal mol⁻¹ (in stacking state). As a consequence, the graphene sheets during stacking, squeeze out most of the peptides from interlayers and tend to form irreversible agglomerates or even re-stack to form graphite like material. In another MD simulation, we demonstrate that introducing some oxygen containing groups on the graphene surfaces will endow hydrophilic properties as well as the electrostatic repulsions between them.

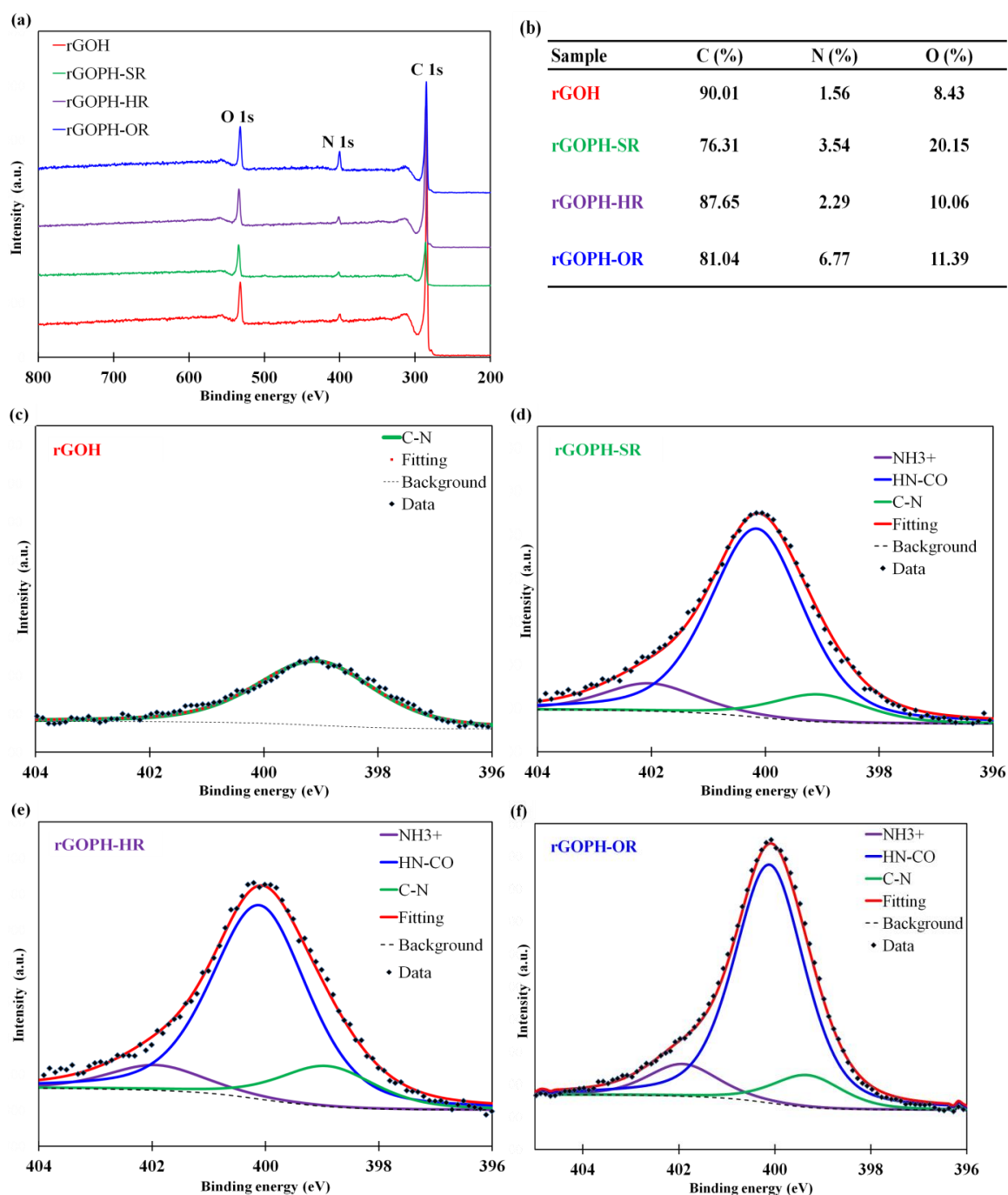


Figure 6-6. (a) The wide-scan X-ray photoelectron spectra (XPS) of various hydrogels. (b) the content of each hydrogel, The XPS spectra of the N1s for (c) rGOH, (d) rGOPH-SR, (e) rGOPH-HR and (f) rGOPH-OR.

As shown in Figure 6-7b, there is no interaction energy that could overcome the PHE-graphene interaction. The oxygen functionalities aided with preventing graphene aggregation. The graphene binding peptide also has a significant role in controlling the graphene interlayer spacing of about ~ 2.6 nm until the 50th ns of the simulation. Here, we

emphasize that different amount of oxygen functionalities generate different levels of intermolecular interactions in the system and influence the peptide mediated self-assembly of graphene based hydrogels.

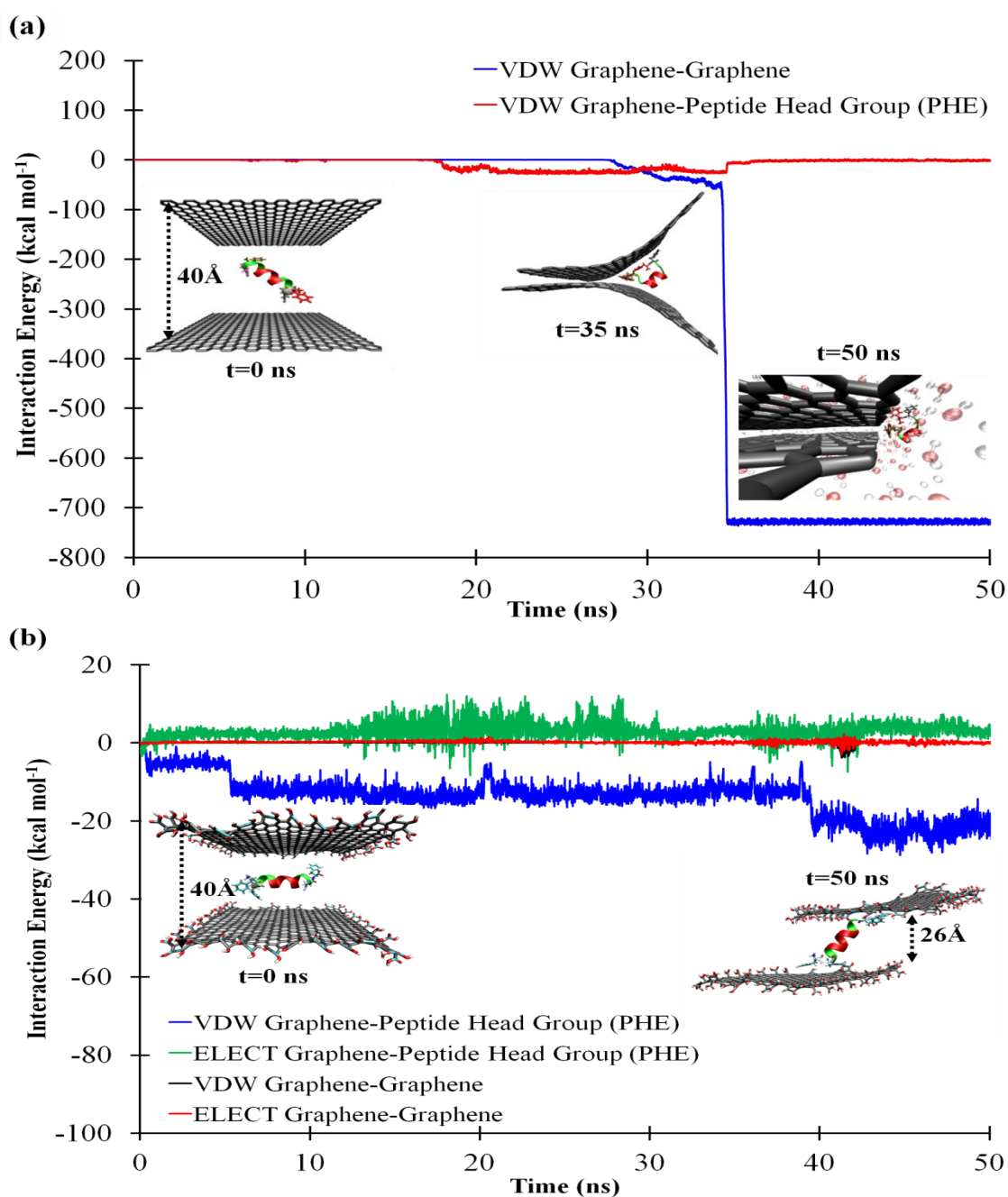


Figure 6-7. Time evolution of interactions in (a) graphene-graphene and (b) graphene-peptide MD simulation systems.

When two graphene sheets stack, their interactions reduce the pore size by squeezing most of the peptide out of the interlayer spacing. (That is, at the competition of binding, the

graphene-graphene interaction wins over that of the graphene-peptide). MD simulation results shown in Supplementary Figure 6-5a and b confirmed that this is a common occurrence, regardless of the peptide concentration. These results demonstrated that placing two or three graphene sheets could not prevent graphene restacking and all peptides were pushed out by very large graphene-graphene van der Waals interaction. As mentioned earlier, when the graphene sheets aggregate or re-stack, their interlayer spacing is less than 1 nm. Hence, there is not enough accessible space for the penetration and accommodation of DOX (with the size of ~1 nm at the largest dimension) into the hydrogel. The adsorption of DOX occurs mostly on the outer accessible surfaces of rGOPH, although a little takes place between the graphene layers. The DOX loading capacity is therefore very low.

With the optimally reduced GO, the chances for the peptide to successfully bind and retain the position in between the graphene sheets is much higher. Therefore, the interlayer spacing (pore size) is larger than that of stacking case, hence, a larger volume is accessible for accommodating the drug molecules. Besides possessing a large accessible pore volume, the optimally reduced graphene oxide can benefit from both hydrophobic and hydrophilic sites generated on the surface, thereby highly favoring the DOX loading capacity.

6.3.2.2 Effect of reduction degree and peptide concentration on DOX loading capacity

The DOX loading capacity against the variables of the temperature and peptide concentration for both contour and three-dimensional depictions is shown in Figure 6-8. The lowest loading capacity was obtained where the reduction temperature was the highest (95 °C), regardless of peptide concentration. The peptide concentration and the reduction temperature had a significant interaction toward the response, when the temperature was below 90 °C. This is also in agreement with our assumption of the decrease in pore size as a result of graphene aggregation when the reduction temperature is higher than 90 °C. Our simulation results revealed that, under such conditions, the van der Waals interaction (π - π stacking interaction) between graphene sheets is high enough (more than 700 kcal mol⁻¹) to stack them and squeeze out the peptide from their interlayer spaces, regardless of the peptide concentration. This has also been observed in our MD simulations (shown in

Supplementary Figure 6-5), by adding two and then three peptides in graphene interlayer space until the graphene surfaces were completely covered with peptide molecules (assuming a high peptide concentration). Both simulation results demonstrated that the peptides initially bind strongly enough to graphene surfaces to keep them apart until a specific point, but then as graphene sheets come closer to meet each other through the edges (where dangling bonds exist), they tend to stack and eventually push out the peptides from interlayer spaces. That is, the graphene stacking interaction - which is a type of van der Waals interaction - is as high as it could be to prevail over the graphene-peptide interactions.

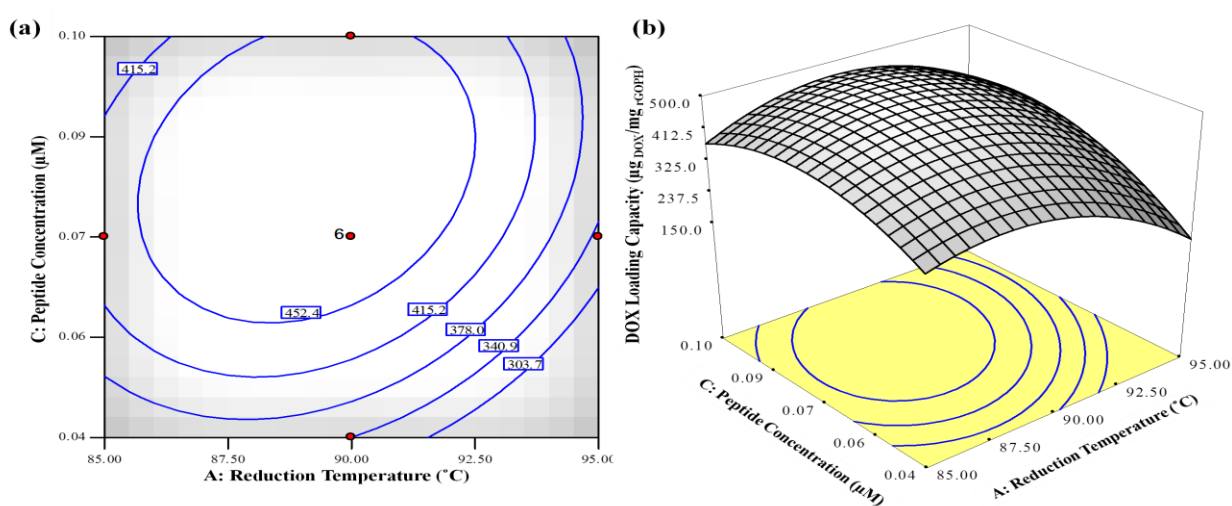


Figure 6-8. Response surfaces for DOX loading capacity against A:reduction temperature and C:peptide concentration depicted as contour (a) and three-dimensional (b) plots. The variable B was kept at its zero (centerpoint) level.

Similarly, the contour and three-dimensional characteristics of the DOX loading capacity against the variables of the hydrazine amount and peptide concentration are plotted in Figure 6-9. The hydrazine amount interaction with the peptide concentration exhibited similar features as the temperature. At any constant peptide concentration, the lowest and the highest hydrazine amount leads to the lowest loading capacity of DOX. This re-emphasizes that the highly hydrophilic or highly hydrophobic graphene sheets are not good candidates for the peptide mediated self-assembly of graphene based hydrogels.

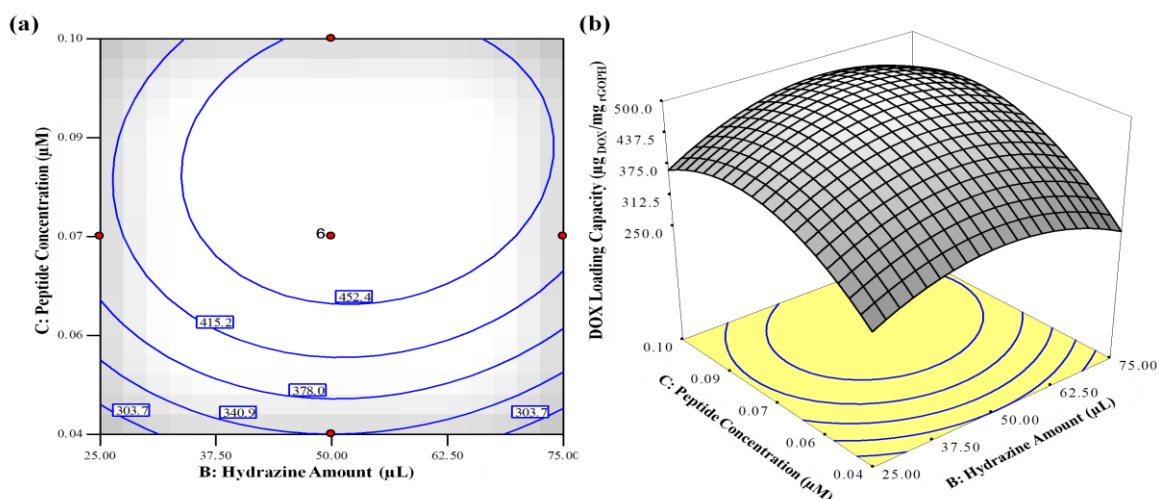


Figure 6-9. Response surfaces for DOX loading capacity against B: amount of hydrazine and C: peptide concentration depicted as contour (a) and three-dimensional (b) plots. The variable A was kept at its zero (center-point) level.

Furthermore, the effect of peptide concentration on controlling pore size was investigated by mixing rGO-OR with peptide with different concentrations of 0.04, 0.08 and 0.1 μM . The AFM image and corresponding height profile are shown in Figure 6-10a and b. The peptide concentration of 0.04 μM resulted in the average pore size of ~ 1.4 nm, assuming that the peptide concentration was not yet enough to overcome the strong π - π stacking interactions of graphene sheets. However, the assumption for such an occurrence is that the peptides are still in between graphene sheets, but mostly in a laid down position rather than positioning upright. Figure 6-11 demonstrated the graphene interlayer pore size measured by AFM for the peptide concentrations of 0.08 and 0.10 μM . Although both peptide concentrations aided in achieving the desired pore size of ~ 2.6 nm, the 0.08 μM peptide concentration led to the higher capacity of DOX loading. This concentration has also been suggested as an optimum concentration by the DOE analysis.

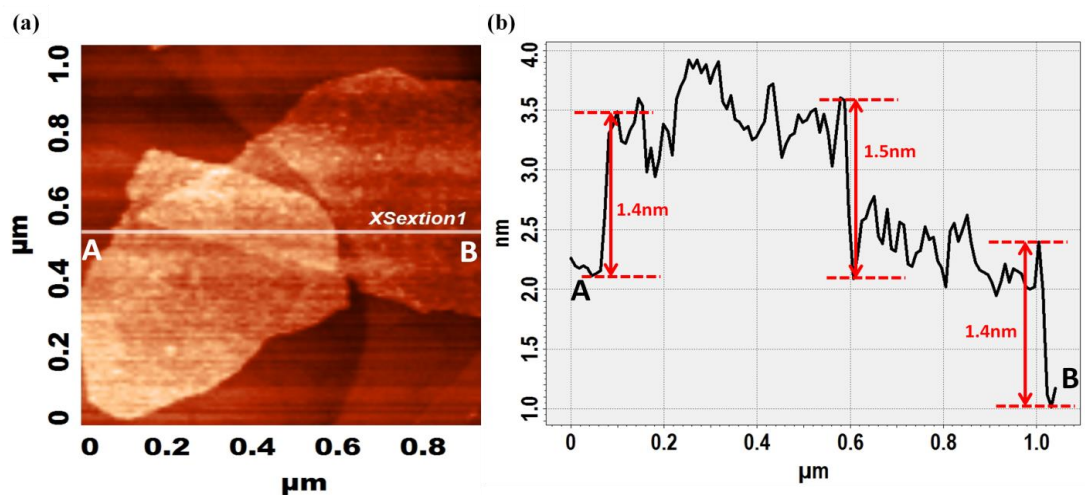


Figure 6-10. (a) Tapping-mode 2D AFM image and (b) height profile of the rGOPH with 0.04 μM of peptide concentration. (X cross-sections labeled from A to B)

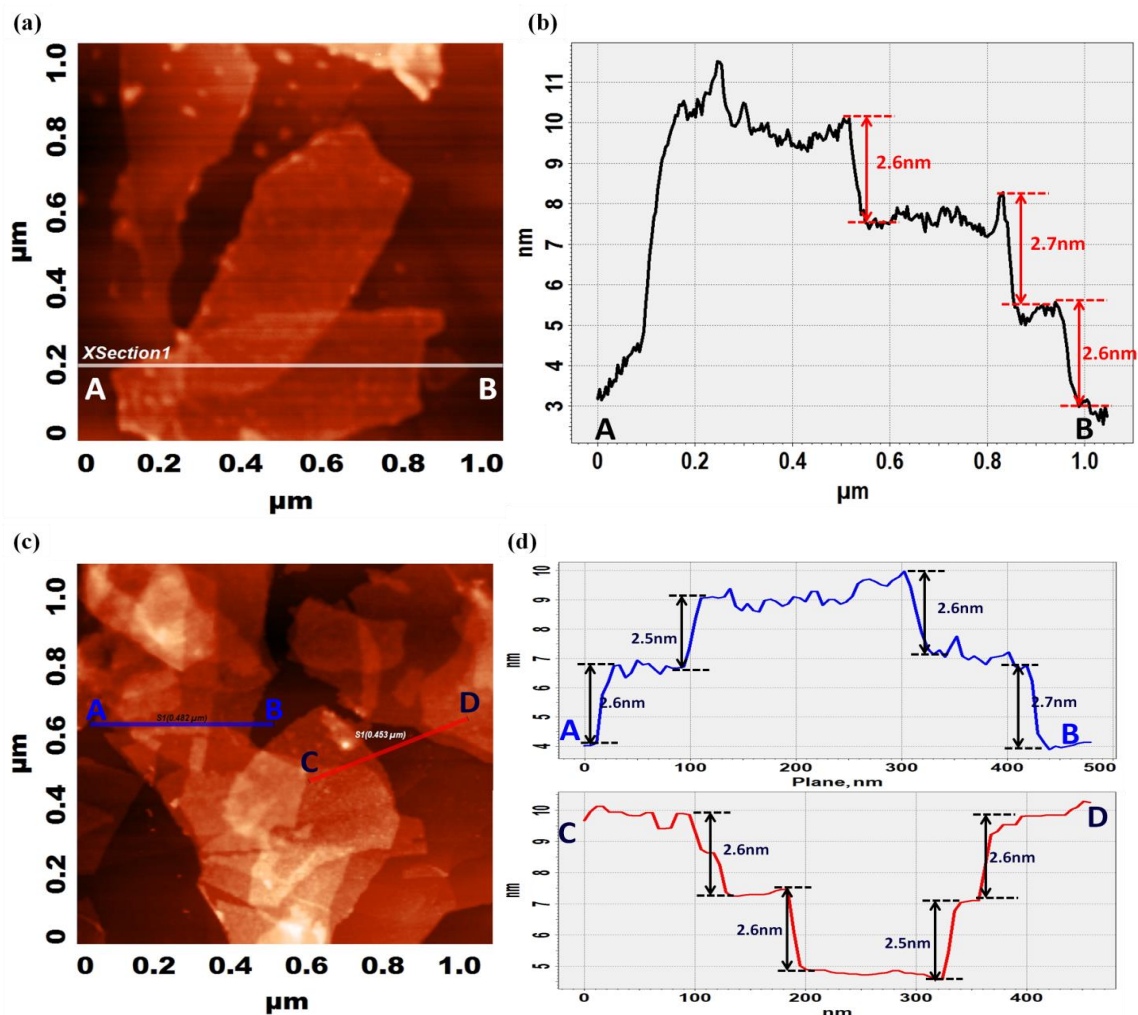


Figure 6-11. (a and c) Tapping-mode 2D AFM images of the rGOPH-OR with of peptide concentration of 0.08 and 0.10 μM , respectively. (b and c) height profile of the rGOPH-OR

with of peptide concentration of 0.08 and 0.10 μM , respectively. (Cross-sections labeled from A to B and from C to D)

Nitrogen adsorption experiments were conducted to investigate the effect of peptide concentration on the pore structure and DOX loading capacity. Three hydrogel samples of underwent nitrogen adsorption; rGOH (without the peptide), rGOPH-0.08 μM (with optimum peptide concentration), and rGOPH-0.10 μM (with the highest peptide concentration). Their corresponding isotherms are plotted in Figure 6-12a. All three isotherms exhibit combinations of type I and II trend based on IUPAC classification[403] indicating the presence of both micropores and mesopores with type H4 hysteresis loop, which is characteristic of narrow slit-shaped pores[403, 404]. The isotherms show a decrease in microporosity and increases in mesoporosity with increasing peptide concentrations. However, as is shown in the embedded table in Figure 6-12b, total pore volume is almost the same for rGOH and rGOPH-0.08 μM with a slight decrease for rGOPH-0.10 μM . The equivalent BET surface area[405] also reduces with the peptide concentration. This behavior is expected, as accommodating peptides of more than a certain concentration at the graphene interlayer space decreases the accessible pore volume, and consequently, the accessible surface area to the DOX molecules.

Figure 6-12b illustrates the calculated pore size distribution (PSD) based on the slit model and the Quenched Solid Density Functional Theory (QSDFT) method[407]. The calculated PSD for rGOH shows a sharp narrow peak at around 1 nm, with a relatively wide shoulder that extends to 4 nm. Although the plain rGOH without peptide at the graphene interlayers exhibited by far the largest pore volume, most pores are less accessible - or even inaccessible - to the DOX molecule because of their size of about ~ 1 nm. This is why the rGOH exhibited the lowest DOX loading capacity (see Supplementary Figure 6-6 for the comparison of DOX loading capacity). The calculated PSD for both rGOPH samples (with 0.08 μM and 0.10 μM peptide) are similar with respect to the position of peaks, but quite different in their intensities. They both exhibit an initially narrow distribution of pores ranging from 1.0-1.5 nm, and a second broader distribution between 1.5 nm and 6.0 nm. The inset of Figure 6-12b with a higher magnification of PSD shows that both second peaks for rGOPHs reach their maximum at the desired pore size of ~ 2.6 nm. However, the peak for the hydrogel with 0.08 μM peptide concentration has a

higher intensity than the hydrogel with 0.10 μM contributing to the larger accessible pore volume for taking up the drug molecule. These results are in agreement with our DOX loading capacity experiments where the rGOPH-0.08 μM demonstrated the highest uptake of the drug.

Generally, the existence of peptide between the graphene layers has two opposite impacts on the prepared hydrogel. Although the peptide fills the accessible pores and has a negative effect on available pore volume, it can also bind strongly to the pore walls (graphene layers) and create a desirable pore size - provided that enough peptide concentration is used. We believe a peptide concentration of 0.08 μM results in a desirable pore size, and a reasonable pore volume for DOX adsorption. Although excessive concentrations lead to stronger graphene-peptide bindings, more parallel graphene layering and consequently more controlled pore size, it is discouraged due to the negative effect of pore filling.

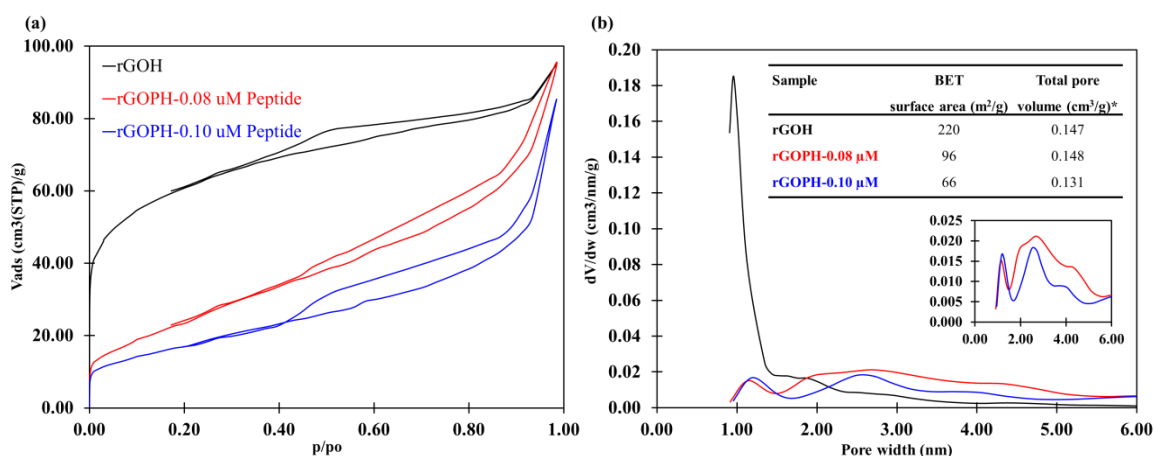


Figure 6-12. (a) Nitrogen adsorption isotherm and (b) PSD analysis of hydrogels; rGOH (without the peptide), rGOPH-0.08 μM (with optimum peptide concentration), and rGOPH-0.10 μM (with the highest peptide concentration)

6.3.3 Pore size effects on DOX loading capacity; MD simulation perspective

In order to investigate the effect of different pore size on the DOX loading capacity, the hydrogel structures were constructed with the graphene interlayer spacing of 1.0 and 2.6 nm, respectively presenting the hydrogels with and without the peptide as interlayer spacer. The idea of choosing these pore sizes was planted through the graphene interlayer spacing measurement from AFM observations. In the case of smaller pore size (shown in

Figure 6-13), the DOX molecules began to make hydrogen bond (shown with red line) with oxygen functionalities within the first 3ns of simulation, just before struggling to penetrate into the pore. Hence, the hydrogen bonding is probably a main driving force for its taking up into the pore, but not the size of the pore. Then the π - π stacking interactions with hydrogen bonding lead the DOX molecules to bind tightly and in flat mode to the graphene surface. The overall DOX fraction in the adsorbed state (on the right snapshot in Figure 6-13 the adsorbed DOX molecules shown with red color bound to graphene surface and non-bound DOX molecules are with different colors) did not exceed 25% within 30ns of simulation.

However, Figure 6-14 shows different results for the hydrogel with the larger pore size, where the DOX molecules did not initiate the stable hydrogen bonding with oxygen containing groups until an almost 20% of the DOX was adsorbed by the pore. This clearly suggests that two similar hydrogels with similar amount of oxygen containing groups, probably show similar adsorption mechanisms, but the larger pore may have the larger intra-particle diffusivity effect. The effect of pore size on the adsorption mechanism will be discussed more in the section of the kinetics of adsorption. Beside the role of π - π stacking, the number of hydrogen bondings increased proportionally with the fraction of DOX being adsorbed by the graphene hydrogel. This robustly indicates the importance of such strong interactions in physical adsorption of the drug molecules after their intra-particle diffusion into the pore. In addition to the DOX permeability effects of the hydrogel pore size, the adsorption rate and loading efficiency were investigated. Comparing Figure 6-13 and 14, the hydrogel of 2.6 nm pore size exhibited a faster initial and overall adsorption rate with a loading efficiency almost 2.5 times larger than that of 1.0 nm pore size within 30ns of MD simulations. Interestingly, this ratio of loading efficiency is very similar to what was observed in our experimental data for the DOX adsorption ratio in the rGOPH/rGOH which was about ~2.6 after 24 hrs of adsorption. The inserted photographs of cuvettes in Figure 6-13 and 14, respectively, show the changes of DOX solution colour for the rGOH and rGOPH. The latter significantly changed the colour of the solution, indicating the higher loading efficiency compared to the former.

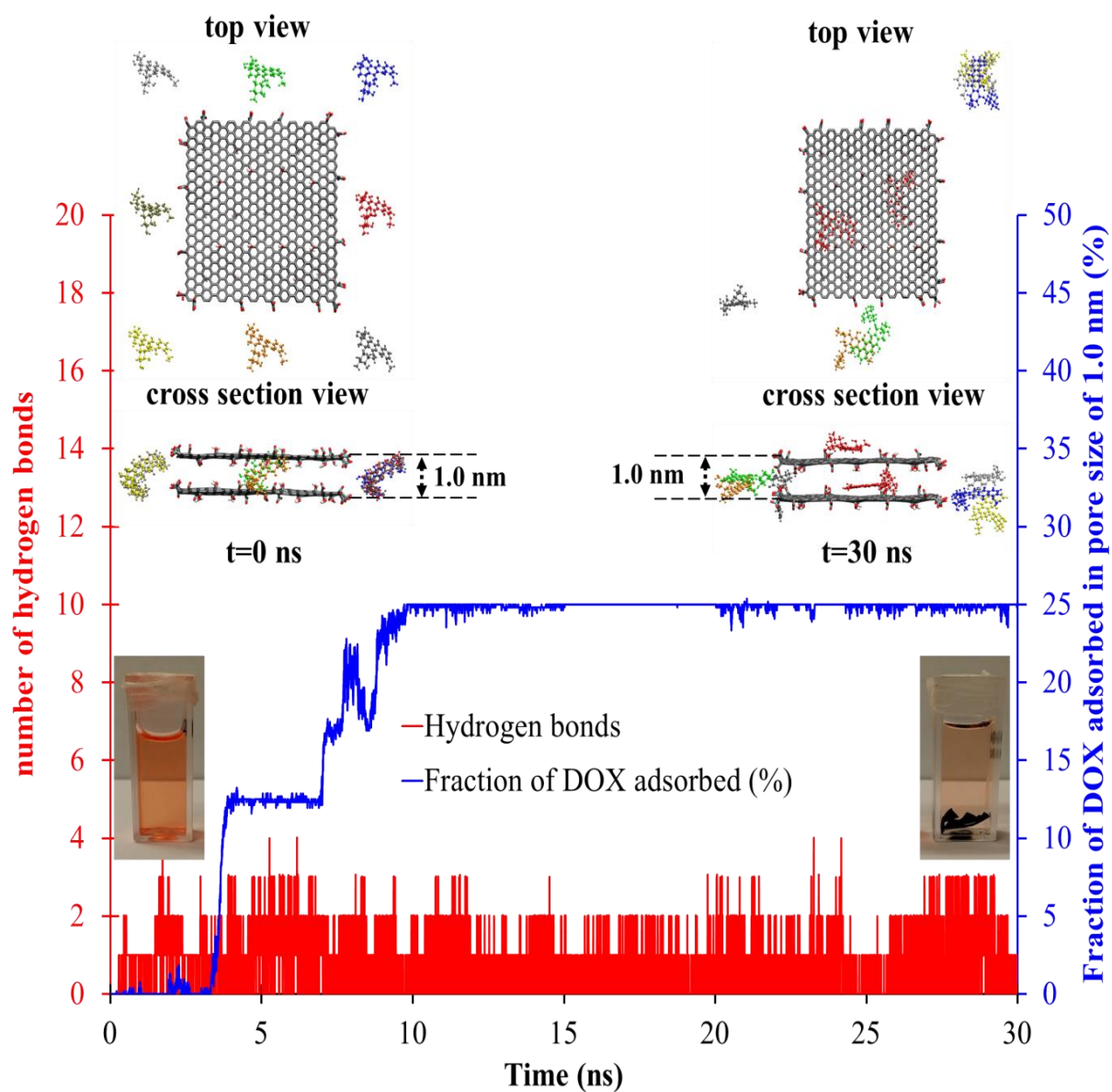


Figure 6-13. The time evolution of the DOX adsorption into the graphene hydrogel with pore size of ~ 1.0 nm. Insets are different views simulation representative snapshots for before and after DOX adsorption. (Water molecules are not displayed for clarity). The inserted photographs of cuvettes show the DOX solutions before and after treating with hydrogel.

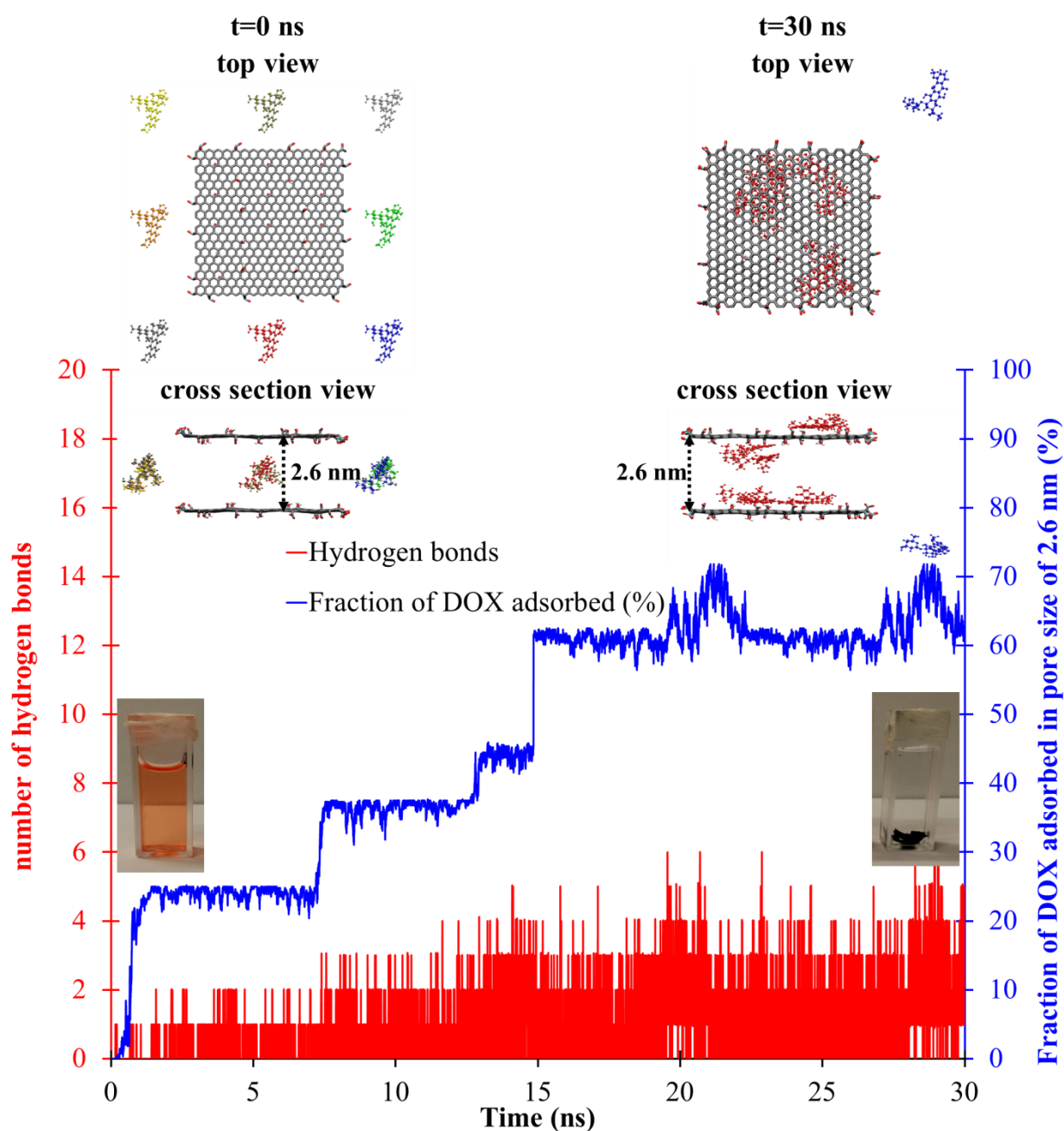


Figure 6-14. The time evolution of the DOX adsorption into the graphene hydrogel with pore size of ~ 2.6 nm. Insets are different views simulation representative snapshots for before and after DOX adsorption. (Water molecules are not displayed for clarity). The inserted photographs of cuvettes show the DOX solutions before and after treating with hydrogel.

6.3.4 Kinetics of adsorption

The adsorption process of DOX as a sorbate from aqueous solution into porous media (hydrogels in our case) may involve several steps: (i) transportation in the solution;

(ii) diffusion through the liquid film surrounding the solid particle, known as external or inter-particle diffusion; (iii) diffusion within the liquid included in the pore, known as internal diffusion or intra-particle diffusion; (iv) adsorption or desorption on the surface of the interior sites, which can involve several mechanism such as physio-chemical sorption, ion exchange and precipitation [454, 455]. The first step refers to the bulk diffusion and has no different rate limitation effect as all the experiments were performed at similar conditions. The second and the third factors, respectively, refer to the external mass transfer and intra-particle mass transfer resistances. The intra-particle is more important in this study as it directly relates to the pore size and shape. The fourth factor is as vital as the third, which suggests the mechanism of adsorption in the pores and whether it is physically controlled (physisorption) or chemically controlled (chemisorption). The different models used were pseudo-first order (physisorption), pseudo-second order (chemisorption) and Weber and Morris or intra-particle model for mass transfer effects.

When film diffusion is rate controlling (simple sorption or physisorption), the pseudo-first order rate equation of Lagergren is applied, which expressed as follows [246, 455]:

$$\log(q_e - q_t) = \log q_e - \frac{k_1}{2.303} t \quad (6-4)$$

where k_1 is the Lagergren rate constant of adsorption (min^{-1}) which varies inversely with the particle size and the film thickness. The plot of $\log(q_e - q_t)$ against t gives a linear relationship from which k_1 and the adsorption capacity of the hydrogels (q_e) are determined from the slope and intercept of the plot, respectively.

The pseudo-second order model, based on the assumption that the rate-limiting step may be chemical sorption or chemisorption involving valency forces through sharing or exchange of electrons between sorbent and sorbate, provides the best correlation of the data [456]. This model can be represented by the following linear form [246, 455]:

$$\frac{t}{q_t} = \frac{1}{k_2 q_e^2} + \frac{t}{q_e} \quad (6-5)$$

where k_2 is the pseudo second-order rate constant of adsorption ($\text{g mg}^{-1} \text{min}$). The values of q_e and k_2 are, respectively, determined from the slope and intercept of the plot of t/q_t against t .

According to Weber and Morriss [457], when the adsorption process is influenced by the intra-particle diffusion, the uptake of the sorbate q_t should vary linearly with the square root of time t . This dependence could be expressed as follows [246, 455]:

$$q_t = k_{ipd} t^{0.5} + C_i \quad (6-6)$$

where k_{ipd} is the rate constants of intra-particle diffusion ($\text{mg g}^{-1} \text{min}^{-0.5}$) and C_i is the intercept at the stage i .

Figure 6-15a-d show the real time DOX loading capacity of four different hydrogels along with their corresponding linear regression in terms of pseudo-first order, pseudo-second order and intra-particle diffusion kinetics, respectively. As shown in Figure 6-15a, the DOX loading capacity in rGOPH-OR was the largest as expected (more than twice as large as that of rGOH and more than 1.5 times larger than that of rGOPH-SR and rGOPH-HR) due to a higher accessible volume to take up the DOX molecules.

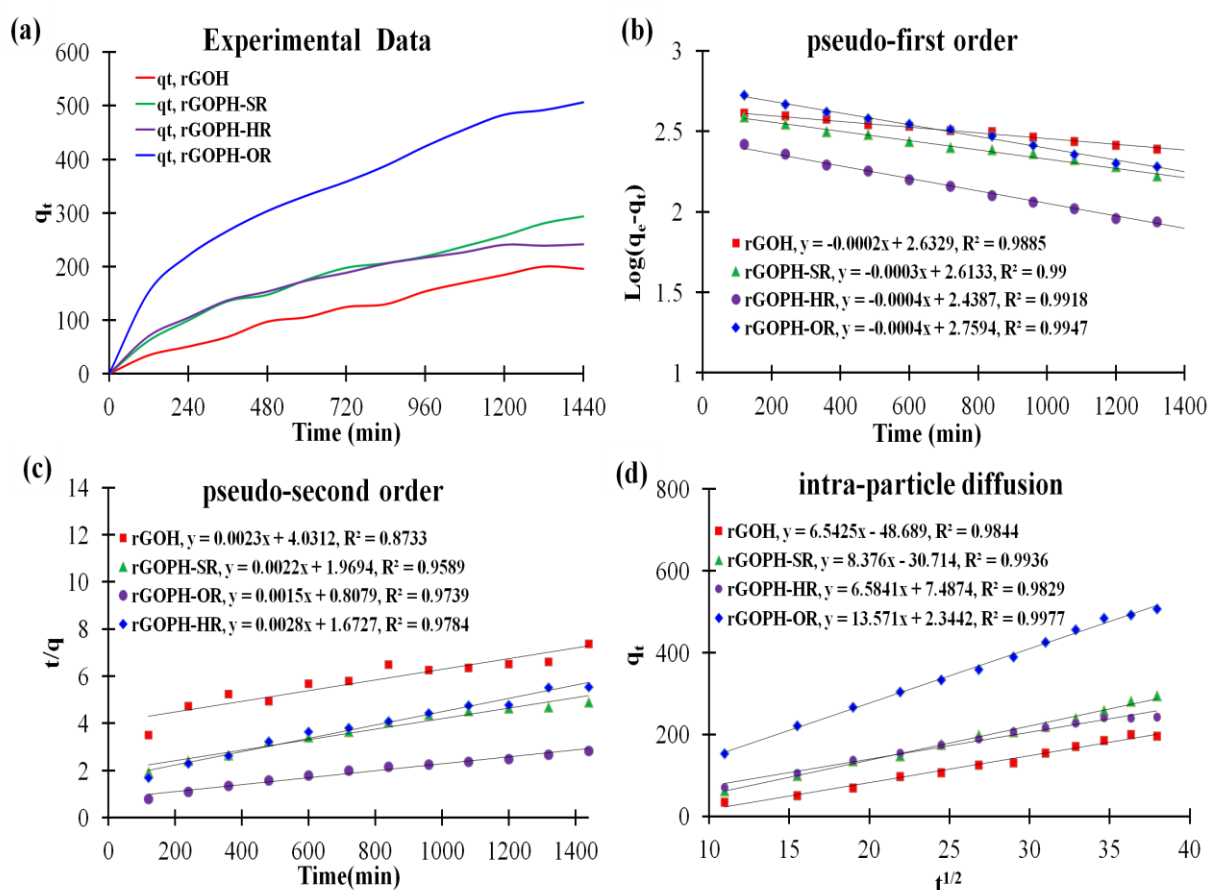


Figure 6-15. (a) Real time monitoring of DOX adsorption by hydrogels, DOX adsorption kinetics of (b) pseudo-first-order, (c) pseudo-second-order, (d) intra-particle diffusion models.

The model with the highest correlation coefficients (R^2) between the observed and the fitted data is selected as the one with the best fit. Comparing the R^2 of pseudo-first order, and pseudo-second order, as indicated in Table 6-4, the adsorption of DOX on all hydrogels follows the similar kinetic model. The pseudo-first order kinetic of rGOH, rGOPH-SR, rGOPH-HR and rGOPH-OR demonstrated a better fit to the experimental adsorption data, that is, higher R^2 compared to their corresponding pseudo-second order (shown in Figure 6-15b and c). Therefore, the adsorption mechanism of DOX onto hydrogels is physisorption or physical binding, including both specific (such as van der Waals, hydrogen bonding, hydrophilic and hydrophobic interactions) and non-specific (simple physical) adsorptions. Among all hydrogels the plain rGOH had the lowest R^2 (0.9885) of the pseudo-first order attributing to have less accessible pores for DOX to diffuse in. However, not having the peptide in the hydrogel significantly reduces its

specific adsorption characteristics. The small R^2 of the pseudo-second order model varying from 0.8733 to 0.9739 clearly reveals that the chemisorption or chemical binding between DOX and hydrogels is unfeasible. This is apparently a good sign as chemisorption is difficult to reverse and a significant amount of energy is required to remove chemically adsorbed molecules. In view of drug delivery applications, particularly for releasing the drug, physisorption is more favorable than chemisorption as reversibility is the advantage of non-covalent functionalization [49, 458, 459]. It is noteworthy that apart from physisorption, the diffusion kinetics could be influenced by another parameter such as intra-particle diffusivity. The hydrogels adsorption data are very well fitted by the Weber and Morriss^[457] kinetic model, with the average R^2 of ~ 0.99 , indicating that the adsorption process here was also intra-particle diffusion controlled (as shown in Figure 6-15d and Table 6-4). With respect to adsorption rate, the rGOPH with K_l and K_{ipd} values of $8.9E-4 \text{ min}^{-1}$ and $13.57 \text{ mg g}^{-1} \text{ min}^{-0.5}$, respectively, had the most rapid uptake of DOX amongst all hydrogels. The rGOPH with K_{ipd} value of almost twice as large as rGOH and higher R^2 value supports our assumption of the impacts of the pore size on the adsorption mechanism stated in previous section. The bigger the pore size the larger the intra-particle diffusivity.

Table 6-4. Kinetic parameters for Pseudo-first-order, Pseudo-second-order and Intra-particle diffusivity.

Sample	Pseudo-first-order model			Pseudo-second-order model			Intra-particle diffusivity	
	K_1	q_e	R^2	K_2	q_e	R^2	K_{ipd}	R^2
rGOH	4.1E-4	429.43	0.9885	2.06E-05	442.31	0.8733	6.54	0.9844
rGOPH-SR	6.8E-4	410.48	0.9900	9.82E-06	447.66	0.9589	8.37	0.9936
rGOPH-HR	9.0E-4	268.16	0.9918	1.52E-05	331.25	0.9784	6.58	0.9829
rGOPH-OR	8.9E-4	574.64	0.9947	1.73E-06	681.72	0.9739	13.57	0.9965

6.4 Conclusions

The rGOPH was found to be effective adsorbents for hydrophobic drug molecules due to its amphiphilic nature of peptide and oxygenated un-substituted graphene domains. The optimization of DOX loading capacity using RSM based CCFD design was demonstrated to be both efficient and economical for optimizing the experimental conditions with the least possible number of experiments. The rGO-OR prepared at optimum condition (89 °C and 54 μ L hydrazine) with moderate hydrophilic/hydrophobic properties aided to achieve the desired pore size of \sim 2.6 nm as well as the highest DOX loading capacity, whereas both highly and slightly reduced GO, due to the highest inter-sheet van der Waals interactions demonstrated the lowest values in pore sizes and DOX loading capacities. The kinetics studies demonstrated that rGOPH had the physisorption characteristics for adsorbing DOX as the experimental data well fitted to pseudo-first order model. The rGOPH due to have a larger pore size providing more accessible adsorption sites showed a quicker adsorption rate and higher loading efficiency compared to that of rGOH, the hydrogel without peptide. The possible adsorption mechanisms are mainly due to hydrogen bondings, π - π stacking interactions between the species of hydrogels and DOX. We believe this systematic study for preparing hydrogels of tunable pore size along with providing fundamental understanding drug adsorption mechanism, benefits the developments of controlled drug delivery systems using graphene based materials.

Acknowledgment

M.V.K gratefully acknowledges the Australian Postgraduate Award (APA) International Postgraduate Research Scholarship (IPRS) from the University of Adelaide. The support of the Australian Research Council Discovery Program (DP20111888) is also gratefully acknowledged. The supercomputing resources for this work were provided by eResearchSA and both the NCI National Facility at the Australian National University and the iVEC Facility at Murdoch University under the National Merit Allocation Scheme.

Supplementary information

Section 1. Statistical experiments and analysis of variance (ANOVA)

Supplementary Table 6-1 shows the 20 runs of statistical experiments based on CCFD to investigate loading capacity of DOX on rGOPH. The purpose of these experiments was to determine the functional relationship for the yield of drug loading capacity in relation to the 3 variables. They also develop the model and optimize the rGOPH preparation parameters.

Supplementary Table 6-1. Experimental matrix for central composite design (CCD) for rGOPH preparation.

Run	Variable Type	Variables		
		A, (°C)	B, (μL)	C, (μM)
1	Factorial	85	25	0.04
2	Factorial	95	25	0.04
3	Factorial	85	75	0.04
4	Factorial	95	75	0.04
5	Factorial	85	25	0.10
6	Factorial	95	25	0.10
7	Factorial	85	75	0.10
8	Factorial	95	75	0.10
9	Axial	85	50	0.07
10	Axial	95	50	0.07
11	Axial	90	25	0.07
12	Axial	90	75	0.07
13	Axial	90	50	0.04
14	Axial	90	50	0.10
15	Center	90	50	0.07
16	Center	90	50	0.07
17	Center	90	50	0.07
18	Center	90	50	0.07
19	Center	90	50	0.07
20	Center	90	50	0.07

The adequacy and significance of the predicted quadratic model were further established by performing Analysis of variance [444] as given in Supplementary Table 6-2. The p-value and F-value were used to determine the significance of each term at a specified level of confidence. The smaller the p-value of each term, the more significant its corresponding coefficient and the greater contribution of that term towards the response variable [436, 460]. The p-values ($\text{Prob} > F$) less than 0.05 imply that the model terms are significant and the p-values greater than 0.10 indicate the insignificance of the model terms which has to be later removed in the model development process. In this instance, all linear, quadratic and cross-product terms (A, B, C, A^2 , B^2 , C^2 , AB, AC and BC) are found to be significant model terms, and had the largest influences on the DOX loading capacity at 95% confidence level of significance as indicated by the lowest p-value (<0.05). The p-value of greater than 0.05 (which was not seen in this study) implies the insignificance of a term's effect on the response model. Therefore, that specific term has to be removed for modifying and further developing the model. According to the ANOVA table, the model F-value is 96.16 which indicates the model is significant. There is only 0.01% chance that a "Model F-value" this large could occur due to noise.

Supplementary Table 6-2. Analysis of variance ^[444] for the response-surface quadratic model of the DOX loading capacity.

Source		Sum of Squares	DF	Mean Square	F-value	p-value (Prob > F)	
Model		3.046E+005	9	33844.56	96.16	< 0.0001	Significant
Linear	A	24167.60	1	24167.60	68.67	< 0.0001	
	B	2202.50	1	2202.50	6.26	0.0314	
	C	36403.53	1	36403.53	103.44	< 0.0001	
Quadratic	A ²	27228.64	1	27228.64	77.37	< 0.0001	
	B ²	12205.21	1	12205.21	34.68	0.0002	
	C ²	18258.28	1	18258.28	51.88	< 0.0001	
Cross-product	AB	1951.35	1	1951.35	5.54	0.0403	
	AC	12193.60	1	12193.60	34.65	0.0002	
	BC	1795.44	1	1795.44	5.10	0.0475	
Residual		3519.45	10	351.94			
Lack of Fit		1728.41	5	345.68	0.97	0.5151	not significant
Pure Error		1791.04	5	358.21			
Cor Total		3.081E+005	19				

The lack of fit, a test to indicate the significance of the replicate error (from the replicate measurements) in comparison to the model dependent error (from the model performance), is the ratio between the lack of fit mean square and the pure error mean square. By using the F-value in our model, we determined the insignificance of the lack of fit error. This is desired, and indicates that how well the model fits with the experimental data.

Some additional statistical parameters are given in Supplementary Table 6-3 to determine the model reliability and reproducibility. The standard deviation (SD) of the fitted model was 18.17. The smaller the standard deviation and the closer the R² value to 1, the more accurate the model will be, and predicted response values will therefore be much closer to the actual values. The coefficient of variation (CV) known as the ratio of the standard error of estimate to the mean value of the observed response is expressed as a percentage. According to and May (1987) [446], A model with the CV less than 10% can

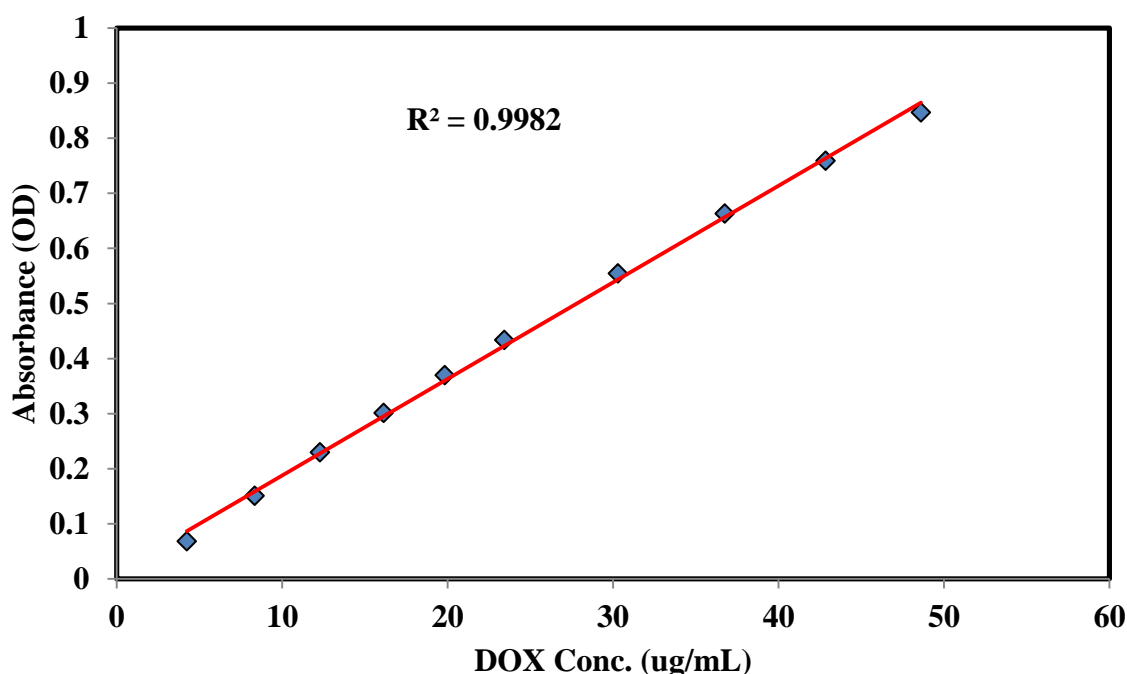
be considered practically reproducible. In our DOX loading experiments, the CV value as low as 5.23% indicates precision and the high reliability of the conducted experiments. The adequate precision measures the signal-to-noise ratio, which is calculated by dividing the difference between the maximum predicted response and the minimum predicted response by the average SD of all predicted responses. As Montgomery (2012)[435] has suggested, for the model to be able to give reasonable performance according to the prediction, it needs to have an adequate precision ratio greater than 4, and the difference between adjusted and predicted R-squared (ΔR -squared) should be <0.2 . In this instance, the adequate precision of 31.05 (which is >4) and ΔR -squared of 0.024 indicate that the model is adequate with a low signal to noise ratio.

Supplementary Table 6-3. Statistical parameters as obtained from ANOVA for the response(DOX loading)-surface fitted model.

Type of variables	value	Type of variables	value
Standard Deviation (SD)	18.76	R-Squared	0.9886
Mean	358.73	Adjusted R-Squared	0.9783
Coefficient of variation C.V. (%)	5.23	Predicted R-Squared	0.9447
Prediction error sum of squares (PRESS)	17028.89	Adequate Precision	31.051

The loading efficiency of DOX was calculated by using DOX UV calibration curve at 490 nm. The correlation between the UV-vis absorbance at 490 nm and the concentration of DOX was normalized by linear regression, and this showed a well-correlated linear relationship ($R^2=0.9982$). The standard curve had a good linear relation, described by the following typical equation:

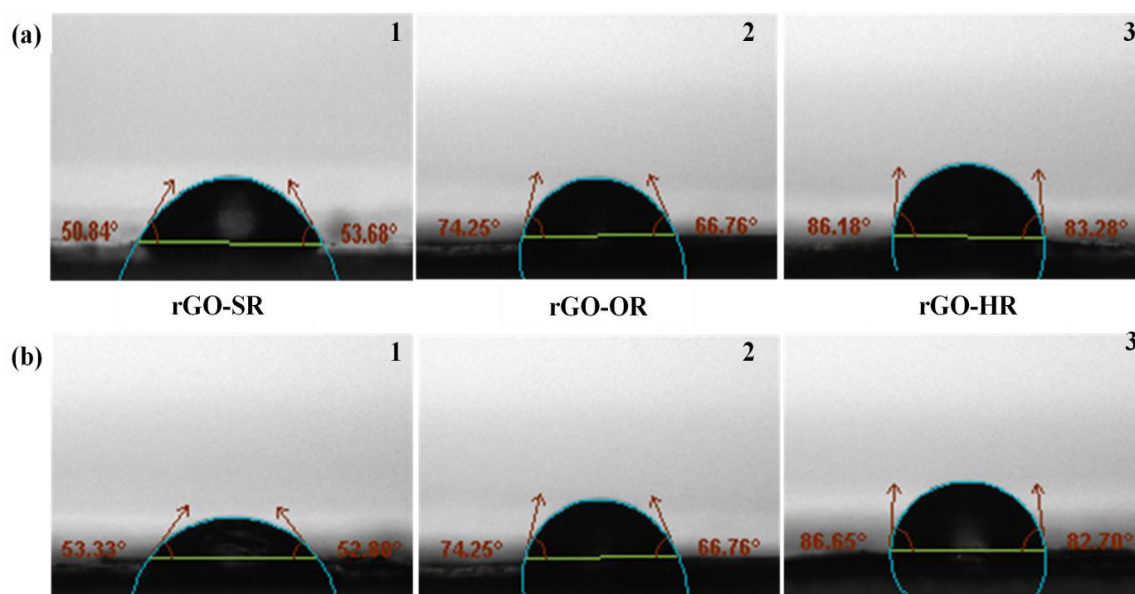
$$y = 0.0175x + 0.0122$$



Supplementary Figure 6-1. UV absorbance versus concentration of DOX. The fit (red curve) was used for calculation of the amount of DOX that was loaded on the hydrogels.

Section 2. Characterizations of rGO-SR, rGO-HR and rGO-OR

Wettability or water contact angle measurements were conducted as a qualitative method to confirm the loss of oxygen groups and increasing the hydrophobicity. However, it is not capable to quantify the degree of oxygen loss. The degree of reduction of the films was further assessed by their hydrophobicity. Supplementary Figure 6-2 shows the wettability of the rGO film (rGO-SR, rGO-HR and rGO-OR) and was obtained by fixing one of the above parameters and varying the other. The average water contact angles of the rGO film treated at an optimum temperature of 89 °C with 25, 54 and 75 μ L of hydrazine were 52.26°, 70.5° and 84.73°, respectively. In the case of fixing the hydrazine amount at optimum value of 54 μ L, the average contact angles on rGO surface were 53.06°, 70.5° and 84.67° for being treated at 85, 89 and 95 °C respectively. Clearly, the rGO surface showed the higher hydrophobicity, indicating a high degree of reduction and more removal of oxygen content by increasing either the reduction temperature or hydrazine amount.

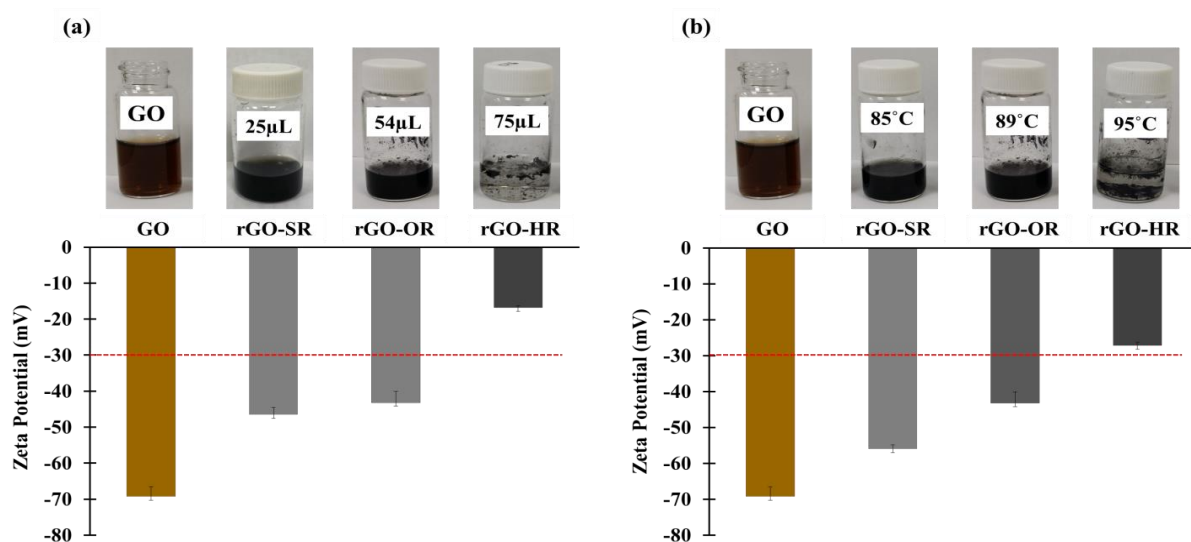


Supplementary Figure 6-2. Water contact angle: (a) rGO treated with 25 μL (1), 54 μL (b) and 75 μL (3) of hydrazine at a constant temperature of 89 $^{\circ}\text{C}$ and (b) rGO treated at 85 $^{\circ}\text{C}$ (1), 89 $^{\circ}\text{C}$ (2) and 95 $^{\circ}\text{C}$ (3) with using a constant amount of hydrazine; 54 μL .

Optimally reduced GO is more stable, does not stack like highly reduced GO, or precipitate like highly oxidized GO.

The top photos in Supplementary Figure 6-3a and b on top, show the effects of the hydrazine amount and the temperature on the degree of oxygen group removal by fixing one parameter at its center level and varying the other one as guided by DOE. All dispersions were left undisturbed for one week to check their stability. Regardless of the reducing temperature, the rGO turned into black colour after adding even a small amount of hydrazine. The rGO prepared with lower and middle levels of each parameter exhibited stability after a week, but those prepared at the higher level conditions (e.g. at 95 $^{\circ}\text{C}$ or with 75 μL of hydrazine), agglomerated and precipitated due to the large loss of graphene surface functionality. In contrast, the GO dispersion was stable for several months due to possessing large amounts of oxygen containing groups. As a quantitative method, the zeta potentials were utilized to confirm and track the loss of oxygen functionalities the aqueous dispersions after reducing the GO and varying different parameters. The bottom figures in Supplementary Figure 6-3b show that all the samples were negatively charged to some extent indicating to contain oxygen functionalities. The zeta potential of GO was initially around -69.3 mV, but started decreasing after adding more hydrazine and increasing the

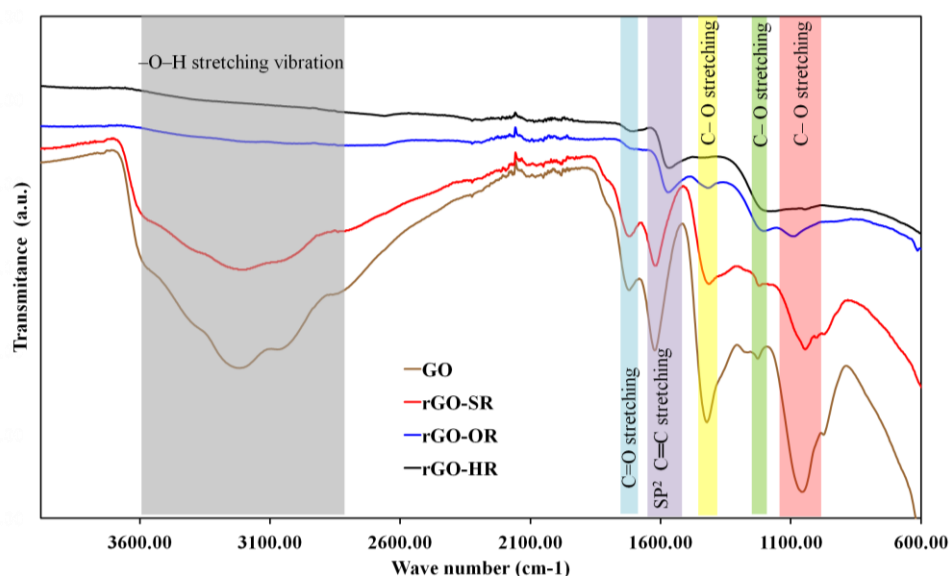
temperature, contributing to the elimination of the oxygen-containing functional groups. According to basic principles of colloidal science,[461] the minimum absolute value of zeta potentials has to be 30 mV to ensure there is sufficient repulsion to reach to the colloidal stability. The American Standard Test Methods (ASTM) [462] on the other hand defines that colloids possess “good stability” if they have zeta potentials of higher than 40 mV. All dispersions prepared here had zeta potentials larger than this range, except those prepared at the highest level of parameters (for example at 95°C with 75 μ L of hydrazine). The zeta potentials of highly reduced GO were even below 30 mV, thereby reducing the electrostatic repulsions, colloidal stability and consequently agglomerating.



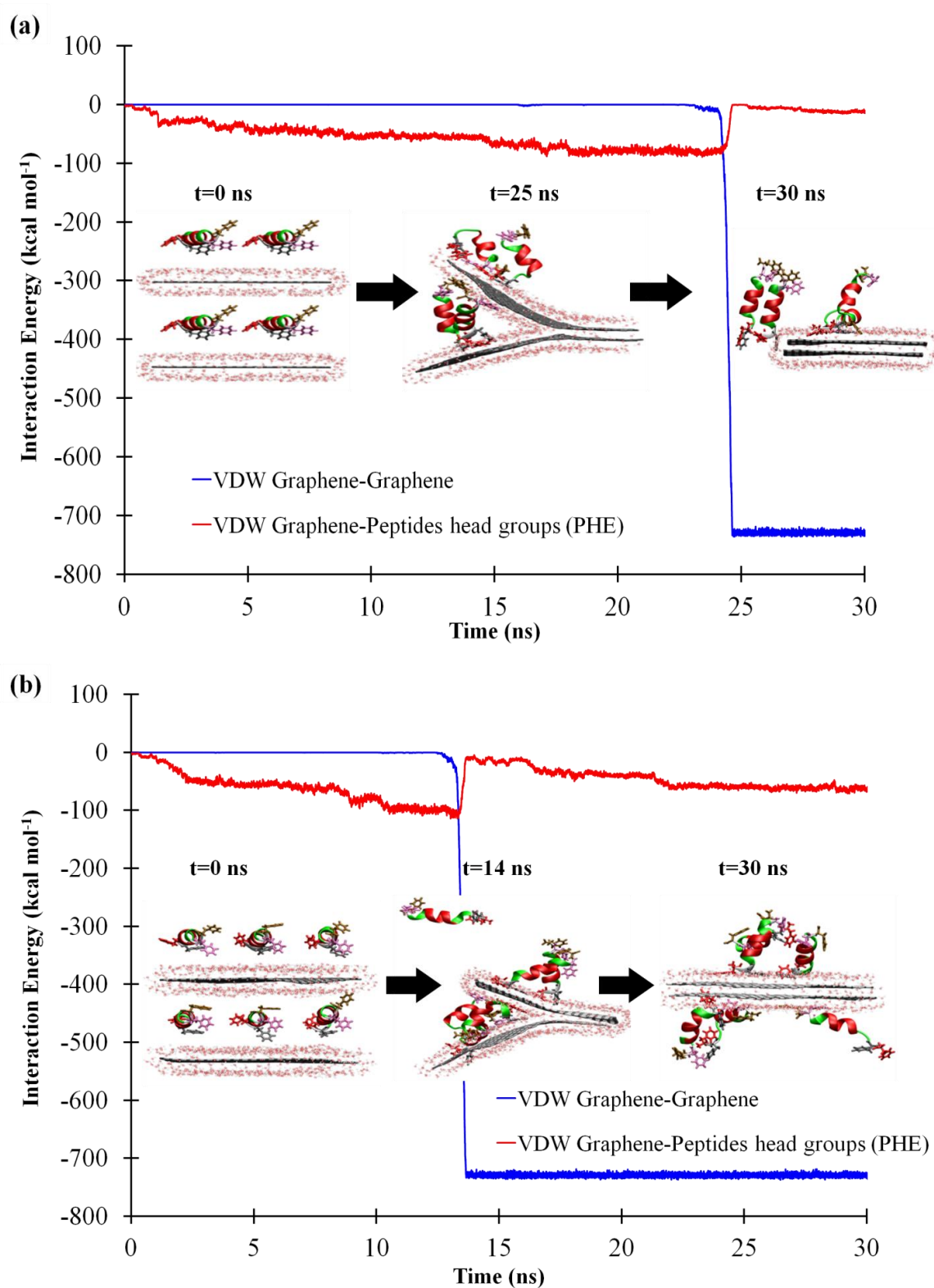
Supplementary Figure 6-3. (a) GO and rGO dispersions ($5 \text{ mg}\cdot\text{mL}^{-1}$) prepared (a) with different amount of hydrazine at constant temperature of 89°C and (b) at different temperature with constant volume of hydrazine (54 μ L). Their corresponding zeta potential graphs are given below the photograph.

These results suggest that the formation of a stable rGO should be attributed to a slight electrostatic repulsion generated by ionization of carboxylic acid (in basic pH~9), but not only the hydrophilicity of GO through the hydrogen bonding with water as was previously presumed. In order to further confirm the origin of this electrostatic repulsion and unveil the graphene surface chemistry, FT-IR analyses of four different samples were investigated. These were GO; slightly reduced GO (rGO prepared with the lowest level of parameters at 85°C with 25 μ L hydrazine) named “rGO-SR”; highly reduced GO (rGO prepared with the highest level of parameters at 95°C with 75 μ L hydrazine) named “rGO-HR”; and optimally reduced GO (rGO prepared with optimum level of parameters at 89°C

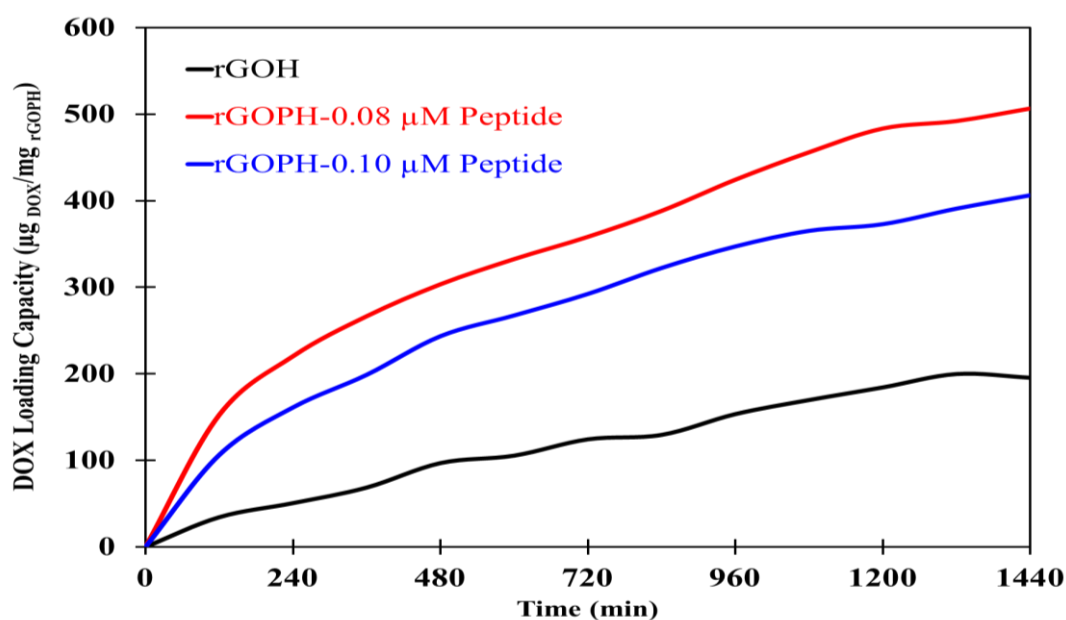
with 54 μL hydrazine and which endowed the highest yield of DOX uptake defined by DOE), named “rGO-OR”. Supplementary Figure 6-4 shows the typical FT-IR spectra of GO and the hydrazine treated rGO with different degrees of reductions. In the instance of GO, the characteristic peaks appear for hydroxyl ($-\text{OH}$ stretching group at $\sim 3218\text{ cm}^{-1}$), carbonyl $\text{C}=\text{O}$ stretching (1730 cm^{-1}), aromatic $\text{C}=\text{C}$ (1620 cm^{-1}), carboxy $\text{C}-\text{O}$ (1415 cm^{-1}), epoxy $\text{C}-\text{O}$ (1228 cm^{-1}), and $\text{C}-\text{O}$ (1070 cm^{-1}) which are all in the ranges reported elsewhere [416-418]. The rGO-SR demonstrated a substantial loss of its oxygen containing group, with the groups with $\text{C}-\text{O}$ stretching in particular. The rGO-OR exhibited similar losses with greater intensities. Our FT-IR results are in agreement with the literature [463-465]. Chemically reduced GO, particularly when treated with hydrazine, loses the majority of the oxidized groups, including the phenolic hydroxyl and epoxide groups, whereas carboxyl groups remain untouched. It is noteworthy that carboxyl groups are unlikely to be reduced by hydrazine under the reaction conditions used in this study. These groups should therefore remain in the form of $-\text{COO}^-$ on rGO while being reduced in the basic environment. In the instance of rGO-HR, the peaks for the oxygen functional groups were reduced efficiently. The remaining significant peaks are attributed to the aromatic carbon double bonds ($\text{C}=\text{C}$) group and a minor $\text{C}=\text{O}$ stretching which represents the presence of carboxyl group. When the $\text{C}=\text{C}$ stretching peak become dominant, it leads to strong $\pi-\pi$ stacking interactions and aggregation of graphene sheet as is evident for the highly reduced samples in Supplementary Figure 6-3a and b.



Supplementary Figure 6-4. FT-IR spectra of GO and rGO-SR, rGO-OR and rGO-HR



Supplementary Figure 6-5. Interaction energies between plain graphene sheets (blue line), between graphene sheets and PHE residues of the (a) two and (b) three peptides located at the interlayer space (red line). Insets are snapshots from the initial, stacking and final states of the MD simulation.



Supplementary Figure 6-6. Real time monitoring of DOX adsorption by hydrogels; rGOH (without the peptide), rGOPH-0.08 μM (with optimum peptide concentration), and rGOPH-0.10 μM (with the highest peptide concentration)

Section 3. MD simulation details

1) Two Graphene sheet with single and multiple designed peptides

Three different simulation systems were constructed by placing two graphene sheets in a periodic rectangular simulation cell, with a box size of $60.5 \times 62.5 \times 80 \text{ \AA}^3$, along with one, two and three designed peptide (α -helix with the amino acid sequence of FFGGEEEEEGGFF) in between graphene sheets with their center of mass (CoM) set at zero. The graphene sheets modelled here have the finite size of $41.75 \times 42.55 \text{ \AA}^2$. The system was then solvated using the TIP3P water model[412]. The density of the water well away from the graphene surface was arranged to be equal to that of bulk water at 298 K and 1 atm. 0.15M Sodium ions were added to ensure overall charge neutrality of the cell[381]. Then energy minimization and system equilibration were carried out for all three systems for 200ps and 1 ns, respectively, until the root mean square deviation (RMSD) and the system's total energy become stable. This indicated that the equilibrium state was reached. Then MD production run for the three system underwent for at least 30 ns in the isothermal-isobaric ensemble, number of moles, pressure and temperature (NPT) ensemble, to explore graphene-peptide interactions and conformations in solution. The

Langevin dynamics and CHARMM force field were employed to integrate equations of motion with a time-step of 2 fs. Long-range full electrostatics were handled using the Particle-Mesh Ewald (PME) approach with a cut-off of 1.2 nm.

2) Two rGO sheets with single peptide

This system was set the same as graphene system with a single designed peptide with an only difference that the surface of each graphene sheet were partially covered by oxygen containing groups (including 34carboxylic and 38hydroxyl functionalities) endowing hydrophilicity to the graphene hydrophobic surface. The Energy minimization and 50 ns MD production run were carried out with the same condition and configuration as systems mentioned above.

3) MD simulation for the effects of pore size in drug adsorption

In order to simulate the hydrogels with pore size of ~ 1.0 nm for rGOH and ~ 2.6 nm for rGOPH, two systems were built by placing two partially oxidized graphene sheets with the distances of 1 and 2.6 nm from each other. To give rigidity to the pore structure, all carbon atoms on the edges of the graphene sheets were constrained within the vicinity of their initial coordination during the entire simulation by a harmonic constraint. The force constant was set at value of 2 for those atoms' restraining potential. 8 DOX molecules were then located outside the pores at a similar distance (~ 1 nm) to the pore entrance. Energies of both systems were minimized and the 30 ns MD production runs were carried out using the same ensemble as graphene peptide system, except adding harmonic constraint parameters.

Chapter 7: A Peptide Mediated Self-Assembled Graphene Hydrogels: Controlled Drug Release and Cytotoxicity

Tests

Abstract

Peptide mediated self-assembled graphene hydrogel, denoted rGOPH, as a novel layered nanomaterial, demonstrated to be a promising carrier for drug delivery due to its high loading capacity. However, the therapeutic potentials of rGOPH, in terms of drug release, biocompatibility and cytotoxicity have not been explored. In this study, we have proven that rGOPH with its pH-responsive release behavior can be used as an efficient nanodrug carrier for cancer therapy. The release behavior of doxorubicin (DOX), as an anticancer model drug, was investigated under various pH values in vitro, and the results exhibited slow drug release profile together with an initial small burst effect. The high mesenchymal stem cells (MSCs) viability of about ~95% indicated the outstanding biocompatibility and low toxicity of this material. This study provides insights into the design of suitable layered graphene based films for biomedical applications.

7.1 Introduction

Among all chemotherapeutic agents, particularly for cancer treatment, doxorubicin (DOX) showed to be exceptionally active to a large variety of cancers including hematological malignancies [466], carcinomas of the breast [467], lung [468], ovary [469], stomach [470] and thyroid [471], as well as sarcomas of bone and soft tissue origin [472]. However, the side-effects such as cardiotoxicity, alopecia, vomiting, leucopenia, and stomatitis of DOX hindered its successful applications. In order to diminish the undesired effects without reducing drug potency, DOX has to be encapsulated into various drug delivery agents [473, 474]. These carrier agents should be able to efficiently uptake drug, protect it and selectively release it in specific sites with minor adverse effects to surrounding tissues [260].

Graphene related (*e.g.* graphene oxide (GO) or reduced GO) sheets as novel carbon nanomaterials have recently been of considerable interest in drug delivery applications as both sides of the nanosheet could be accessible for drug loading [263, 264]. It can be further functionalized to exhibit good aqueous solubility[261] and biocompatibility[160]. The functional groups on graphene sheets can be protonated or deprotonated at different pH values[94, 475] endowing pH dependent release of drugs[28, 246, 259]. The major issue with using GO and rGO in dispersion form is the reactive oxygen species (ROS) [179], which damages healthy cells through generating oxidative stress[476]. Oxygen containing graphene and pristine graphene sheets, respectively through the electrostatic interaction with phosphatidylcholine lipids of the red blood cells (skin fibroblasts) [182] and hydrophobic interaction with monkey renal cells[183] resulted in high oxidative stress and led to apoptosis of the cells. Other study demonstrated that the removal of oxygen functionalities from the GO surface can reduce its cytotoxicity and enhance cell viability [477]. However, the toxicity of graphene based dispersions found to be concentration dependent [179, 182].

In contrast to dispersion form of GO and rGO based materials, some results have shown such materials in the forms of film, paper or slabs can exhibit excellent biocompatibility with limited viability inhibition of the treated cells. For instance, Agarwal and co-workers [192], found that rGO in the film form is biocompatible with rat pheochromocytoma (PC12) cells, human oligodendroglia (HOG) cells, and human fetal osteoblast (hFOB) cells. Also the GO film showed to be a non-toxic platform for proliferating mammalian colorectal adenocarcinoma HT-29 cells [195]. These results suggest that the graphene based films with integrated structure might be more suitable candidates for biological applications as they make less interaction with individual cell membrane and lead to less damage to the healthy cells. On the contrary, graphene sheets in dispersion phase have the high chance to interact with cell membrane and cause large ROS and cell toxicity.

GO [478, 479], rGO [480] and CVD grown graphene [479, 481] films have demonstrated to be great platforms for anchorage-dependent cells such as mesenchymal stem cells (MSCs) which need to adhere to substrates in order to spread, proliferate, and

perform their function [482]. Their adhesion occurs through the hydrophobic interaction between π -electron cloud on graphene and the inner hydrophobic core of proteins. In addition, oxygenated groups on graphene surface via electrostatic interactions can bind to serum proteins, Fibronectin, which enhances the cellular adhesion and proliferation [479]. Hence, graphene surface chemistry plays a major role in biocompatibility toward anchoring MSCs.

Our previous study (in Chapter 6), along with other studies, found DOX, a common anticancer drug model, have high affinity to adsorb on the surface of graphene related materials via π - π stacking and hydrogen bonding,[28, 246-248] suggesting that the constructs made of graphene derivatives may be suitable for drug delivery. A layered graphene hydrogel film with tuneable pore size made of peptide mediated self-assembly of graphene sheets, denoted rGOPH, showed to be a promising candidate for the controlled delivery of DOX. A sample with the highest DOX loading capacity ($\sim 510.5 \mu\text{g}_{\text{DOX}}/\text{mg}_{\text{rGOPH}}$) was chosen to investigate the drug release behavior under different pHs. Such a novel hydrogel, not only benefits from a high accessible volume for taking-up drug molecules, but also contains peptides serving as biocompatible cross-linker. The advantages of the prepared rGOPH over Wu et al. [49] in drug delivery application are the uniform porous structure and controlled chemistry of the material. Wu's hydrogel made of random pores for which near-infrared (NIR) irradiation power and time played key roles adjusting the local temperature of hydrogel for controlling the release behavior. Our hydrogels with tuneable mesoporous structures lead to spontaneous drug release in a more sustained way under a specific pH value. To date, very little is known about the release behavior and cytotoxicity of graphene binding peptide materials. Hence, besides the pH dependent drug release, this study also focuses on the cell viability and biocompatibility of the rGOPH. To accomplish this, we selected anchorage-dependent MSCs as the model cell to investigate the biocompatibility of the obtained rGOPH films over a long period of time in order to demonstrate that such amphiphilic hydrogel films could offer an excellent micro-environment for cell adhesion and proliferation.

7.2 Experimental Details

7.2.1 Materials

In order to investigate the drug release behaviour of the rGOPH, a sample from previous chapter with the highest DOX loading capacity ($\sim 510.5 \mu\text{g DOX/mg rGOPH}$) was chosen as model hydrogel sample. The details of rGOPH synthesis and DOX loading process have been described in Chapter 6.

For cell viability, Dulbecco's Modified Eagle's Medium (DMEM), trypsin-EDTA, penicillin-streptomycin and fetal bovine serum (FBS) were purchased from Gibco-BRL (Grand Island, USA). 3-(4,5-Dimethylthiazol-2-yl)-2,5-diphenyltetrazolium bromide (MTT) was also ordered from Molecular Probes (Oregon, USA).

7.2.2 Methods

7.2.2.1 Release of DOX from rGOPH hydrogels

The drug-loaded hydrogel were prepared by immersing rGOPH in a cuvette containing 3 mL of DOX ($50 \mu\text{g mL}^{-1}$) for 24 hrs. To investigate the release of DOX from hydrogels, the film was taken out from drug loading cuvette and then rinsed for several times with DI water to remove the drug molecules which were attached to the outer surface of the hydrogel. The hydrogel film was then cut into 3 pieces ($\sim 5 \text{ mg}$ for each piece) and immersed in 3 separate cuvettes (shown in Figure 7-1) of 3 mL PBS solutions with pH 5.4, 7.4 and 9.4 to investigate the release profile in acidic, neutral and basic environments. The drug release was assumed to start as soon as the hydrogels were transferred into the reservoir. The release reservoir was kept under constant stirring and $37 \text{ }^\circ\text{C}$. The concentrations of DOX released from hydrogels were quantified using UV-vis spectroscopy. The amount of DOX release was calculated by using the DOX UV calibration curve at 490 nm. The correlation between the 490 nm absorbance and DOX concentration is showed in Figure 7-2.

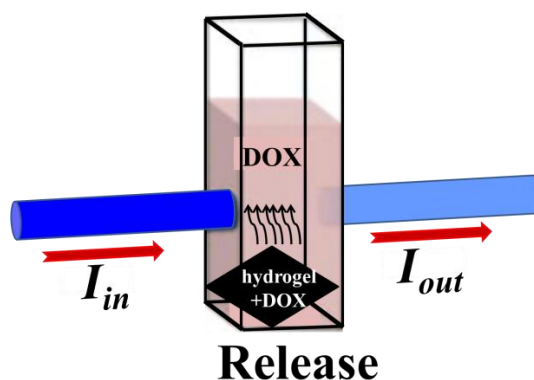


Figure 7-1. Schematic drawing of the real time monitoring of DOX release from hydrogels.

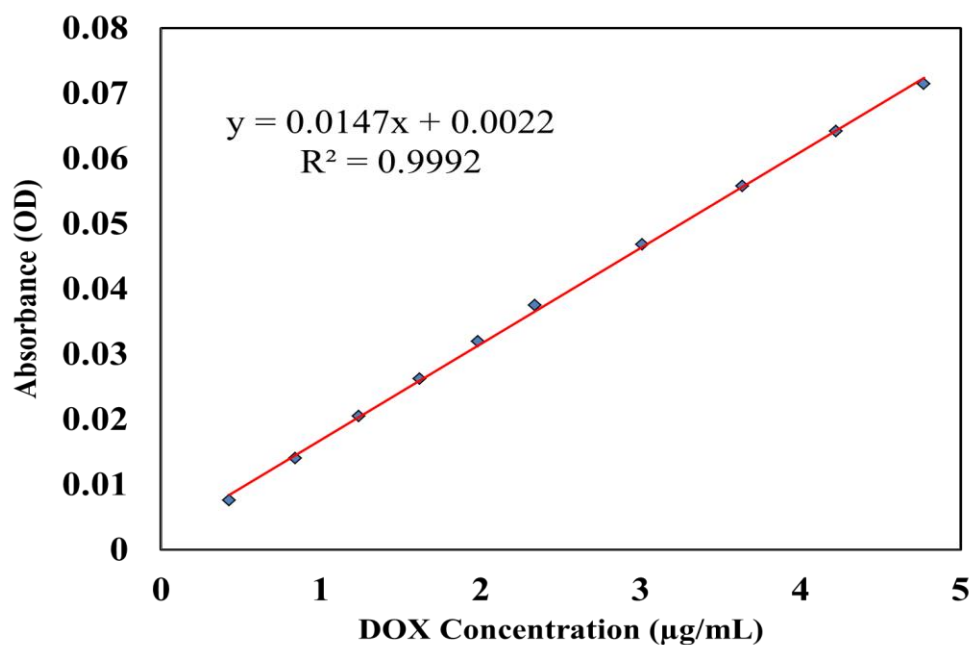


Figure 7-2. UV calibration curve of DOX concentration in PBS buffer at the wavelength of 490 nm.

7.2.2.2 Cell culture

A stem cell line, mesenchymal stem cells (MSCs) (murine, 10T1/2, RIKEN cell bank, Japan) was grown in cell culture flasks containing DMEM supplemented with 10 % FBS, 100 U mL⁻¹ of penicillin, 100 mg mL⁻¹ of streptomycin and 2 mM L⁻¹ L-glutamine. The cells were kept in a humidified incubator at 37 °C in the presence of 5% CO₂ for cell culturing.

7.2.2.3 Cytotoxicity: Analysis of cell viability

Cell viability was assessed using the MTT (3-(4,5-dimethylthiazol-2-yl)-2,5-diphenyltetrazolium bromide) tetrazolium assay in a microplate reader. MSCs were seeded in 96-well microplate at a density of 5.0×10^4 cells/mL in 200 μ L DMEM supplemented with 10% FBS, 100 U mL⁻¹ of penicillin, 100 mg mL⁻¹ of streptomycin and 2mM L⁻¹ L- glutamine for 24 hrs and incubated at 37 °C in a 5% CO₂ humidified incubator. Cells were then cultured in medium with various mass of rGOPH for 24 hrs. Control cells did not receive any hydrogel treatment. Three replicate wells were used for the control and test experiments. Cell viabilities were examined using MTT assays. 10 μ L of MTT (5 mg mL⁻¹ in PBS) were added to each well, including both samples and controls, and then incubated for 4 hrs at 37°C. All the liquid was removed from wells and 150 μ L dimethyl sulfoxide (DMSO) was added to each well to ensure complete solubilisation of formazan crystals. After 1 hr further incubation, the absorbance was measured at 595 nm using a microplate reader (BioTek, USA). Cell viability was expressed as a percentage of the control cell culture value. A control was performed in parallel to monitor the influence of medium on the assays. The cell viability of each treatment was calculated by following equation [247]:

$$\text{Cell viability} = \frac{OD(\text{test sample}) - OD(\text{blank})}{OD(\text{control}) - OD(\text{blank})} \times 100 \quad (7-1)$$

Cell viability values were expressed as mean \pm standard deviation of three independent experiments. Comparisons between two groups were analysed using one-way analysis of variance, with $P < 0.05$ taken as statistically significant.

7.2.2.4 Biocompatibility studies of rGOPH

Two thin transparent films of rGOPH (0.5 mg) were prepared using vacuum filtration and attached to separate glass slides. The rGOPH containing slides were placed into cell culture plate and MSCs at a density of 5.0×10^5 cells/mL in 2 mL DMEM were added. The cell culture plate was then incubated following the same procedure reported in section 7.2.2.2. For biocompatibility study, live/dead cytotoxicity/viability kit was used to stain live and dead cells. 1 μ M of acetomethoxy derivate of calcein (calcein AM) and 2.5

μM of ethidium homodimer-1 (EthD-1) working solutions were prepared freshly according to manufacturer's protocol. At days 1 and 10 of incubation, the growth medium was removed and rGOPH films were washed with 1.0 mL PBS. The liquid was replaced with 2 mL of dye working solution and further incubated at 37°C for 15 min. The dye solution was discarded and samples were carefully washed with PBS to remove unreacted dyes. The cultured cells on the rGOPH films were observed under a Leica SP5 spectral scanning confocal microscope (Leica Microsystems, Germany). Excitation wavelengths were set to 494 and 528 nm and emission wavelengths were at 517 and 617 nm for live (green) and dead (red) cells, respectively.

7.3 Results and discussion

7.3.1 DOX release

Figure 7-3 shows the 10 days DOX release profile of a rGOPH sample investigated at the pH values of 5.4, 7.4 and 9.4. As expected, the GO shows distinctly different release profiles toward DOX at different pH values. The cumulative release of DOX from rGOPH is 63.91% at pH 5.4, 19.04% at pH 7.4, and 6.63% at pH 9.4. The release profiles of DOX from rGOPH at different pH values shows that DOX stacked on graphene hydrogels remained stable in neutral and basic conditions and the laded DOX could be released in acidic condition. After an initial low level burst effect (less than 10%), DOX only continues to be released to any acidic conditions such as tumour sites. The release rate is sustained at an essentially constant value for around 3.5 days.

The accelerated DOX release in the acidic environment can be attributed to the increased protonation and solubility of DOX, similar to the reported pH-dependent loading and releasing properties of other graphene based materials[28, 248]. The pH-dependent DOX release may be related to intermolecular hydrogen-bonding. As all three samples tested were cut from the same hydrogel film, there should be similar level π - π stacking interactions between rGOPH and DOX. Thus, the leading factor in release is the hydrogen bondings. As depicted in **Table 7-1**, there are 4, 8 and 8 types of hydrogen bonding could be formed between DOX and rGOPH, respectively, under basic, neutral and conditions.

Table 7-1. Groups form hydrogen bonds in rGOPH and DOX in different pH values.

pH	rGOPH	DOX	Types of possible hydrogen bonds
5.4	$-\text{COOH}_{\text{graphene}}, -\text{OH}_{\text{graphene}},$ $-\text{NH}_{\text{peptide}}, -\text{C}=\text{O}_{\text{peptide}}$	$-\text{OH}$	4
7.4	$-\text{COOH}_{\text{graphene}}, -\text{OH}_{\text{graphene}},$ $-\text{NH}_{\text{peptide}}, -\text{C}=\text{O}_{\text{peptide}}$	$-\text{NH}_2, -\text{OH}$	8
9.4	$-\text{OH}_{\text{graphene}}, -\text{NH}_2_{\text{peptide C-term}},$ $-\text{NH}_{\text{peptide}}, -\text{C}=\text{O}_{\text{peptide}}$	$-\text{NH}_2, -\text{OH}$	8

In the acidic environment, $-\text{NH}_2$ group of DOX becomes protonated $-\text{NH}_3^+$ and cannot participate in hydrogen bonding. In this case, only 4 types of hydrogen bondings occur between rGOPH and DOX. Furthermore, the protons (H^+) in acidic solution may also compete with the hydrogen-bond-forming groups (either from hydrogel or DOX) and may then weaken the above mentioned hydrogen-bonding interactions [248]. The $-\text{NH}_3^+$ of DOX has the pKa value of 4.6 and loses the proton in neutral environment, hence, it can take part in the formation of hydrogen bonding with functional groups on graphene surface when the pH increased to 7.4. In basic environment, $-\text{COOH}$ of rGOPH loses its hydrogen (becomes deprotonated) to form $-\text{COO}^-$ and no longer participate in hydrogen bonding formation with $-\text{OH}$ and $-\text{NH}_2$ groups of DOX. The $-\text{NH}_3^+$ of the peptide in rGOPH becomes deprotonated and join the hydrogen bonding with DOX. Therefore, the smallest number and weakest hydrogen bonding interactions between rGOPH and DOX is expected in acidic environments, which supports our experimental results where the highest yield of DOX release was obtained from rGOPH at pH=5.4. It is noteworthy for the interaction between the graphene sheets and DOX, π - π stacking may be the most important one because the release rate of DOX from rGOPH significantly decreased after the burst release (first 4 hrs) under acidic conditions, even with decreasing the hydrogen-bonding interactions. The pH-dependent drug releasing behaviors favors the cancer drug delivery applications, since the microenvironments of extracellular tissues of tumors is acidic. That could efficiently facilitate the drug release from rGOPH made in the form of chips localized in the tumor sites.

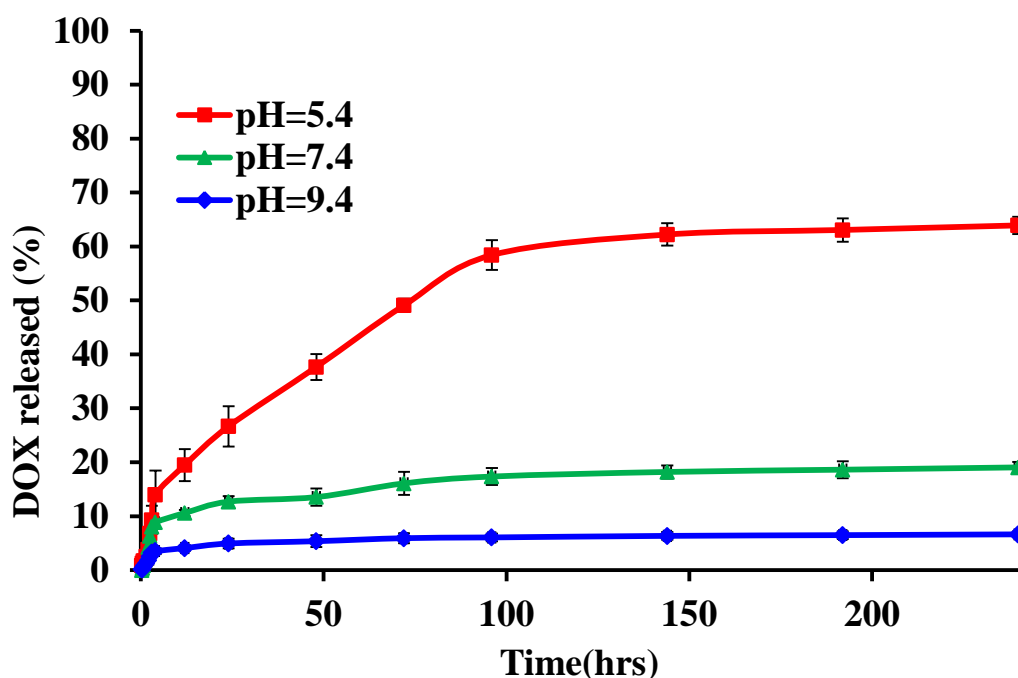


Figure 7-3. The cumulative release of DOX from rGOPH at different pH values.

7.3.2 Effects of hydrogels weight on cell viability

The MSCs were treated with different amounts of rGOPH (5, 10, 15, 20 and 25 mg) for 24 hrs, and the effect of hydrogels on cell viability assessed using MTT assays. According to Figure 7-4, the treated cells showed that cell viability for hydrogels were not dose-dependent. Increasing the hydrogel weight from 5 to 25 mg, the cell viabilities were all above 95%, indicating the low toxicity of the as-synthesized hydrogels. This is probably attributed to the removal of oxygen containing groups during GO reduction process. It is well-known that the number of oxygen containing group proportionally relates to the level oxidative stress mediated by ROS generation [483, 484] which is the main reason of nanomaterial toxicity to healthy cells. Comparing with other studies of using GO or rGO dispersions for treating MSCs [177, 485], our results strongly suggested that successful reduction of GO sheets and their integrated structure in the form of rGOPH film resulted in negligible cytotoxicity in MSCs.

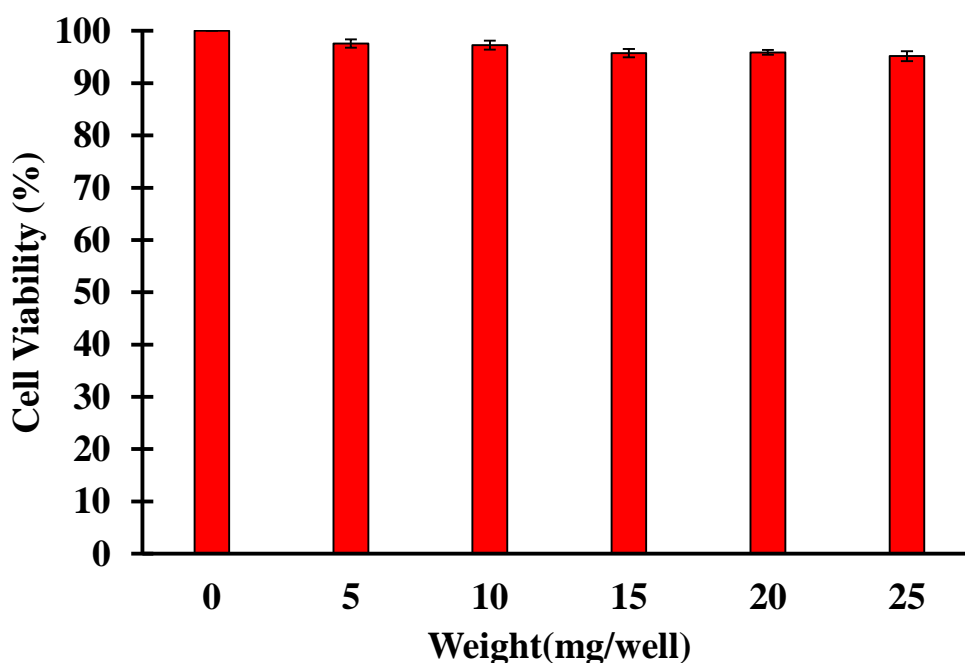


Figure 7-4. The effect of rGOPH (0, 5, 10, 15, 20 and 25 mg) on cell viability of MSCs for 24 hrs. The results represent the means of three separate experiments, and error bars represent the standard error of the mean. Treated groups did not show any statistically significant differences from the control group by Student's t-test ($P < 0.05$).

7.3.3 Effects of DOX and GO/DOX on cell viability

MSCs were treated with DOX and rGOPH/DOX for 24 hrs, and the cell viability effects were assessed using MTT assays. Figure 7-5 compares the cell toxicity of 5 μg of DOX provided *via* 100 μL of a 50 $\mu\text{g}\cdot\text{mL}^{-1}$ DOX solution (DOX-only) and 5 mg of a hydrogel loaded with approximately 50 μg of DOX that releases same amount of DOX (5 μg , by maximum in acidic condition) from previous 24 hrs assessment (rGOPH/DOX). As show in Figure 7-5, at a dosage of 5 mg rGOPH for 24 hrs, we demonstrated that the drug-free hydrogel showed no toxicity (cell viability about $97.5\% \pm 0.8\%$) to cells. The DOX treated cells had an obvious decrease in cell viability (down to $\sim 71.6\% \pm 1.6\%$) confirming that the DOX had a significant toxicity to healthy cells. However, the cell viability increased for the rGOPH/DOX (to $\sim 86.7\% \pm 1.5$) even though the hydrogel contained drug dosage around 30 times larger than DOX-only. That reveals that most of drug molecules are adsorbed in hydrogel so that they could not expose to the cell environment, particularly in neutral pH (pH of healthy cells). These results strongly suggest that the rGOPH not only

being highly biocompatible, but even decrease the toxicity of the DOX toward healthy cells.

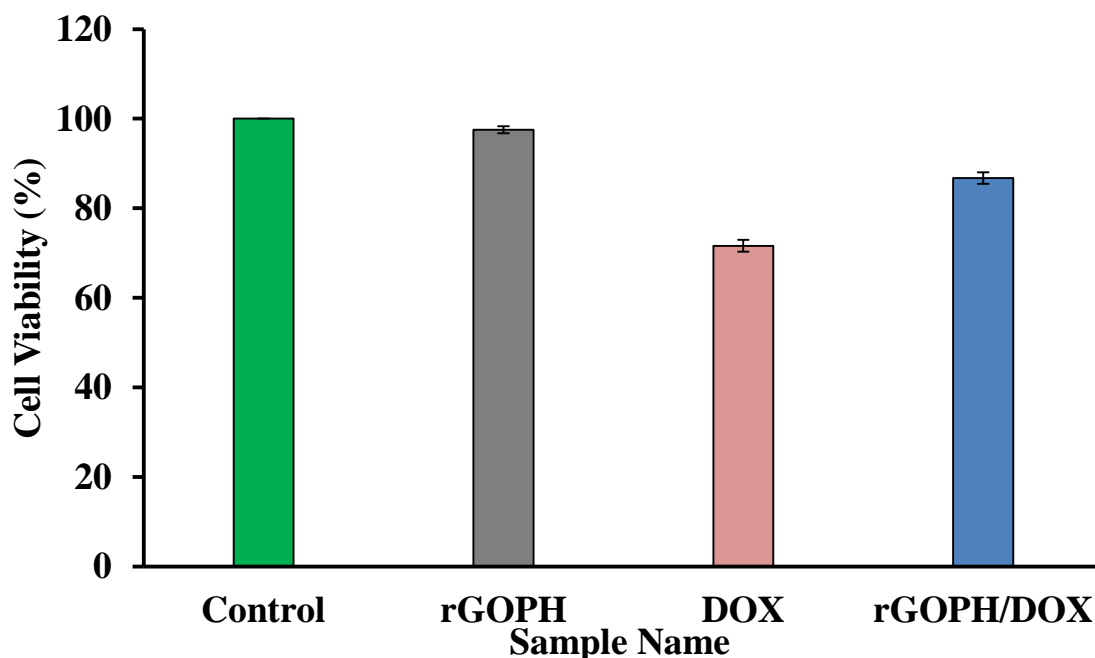


Figure 7-5. The effect of rGOPH, DOX, and rGOPH/DOX on cell viability of MSCs for 24 hrs. The results represent the means of three separate experiments, and error bars represent the standard error of the mean. Treated groups showed statistically significant differences from the control group by Student's t-test ($P < 0.05$).

7.3.4 Biocompatibility studies

Given the potential use of the hydrogel films in biomedical field, MSCs viability cultured on the rGOPH films with highest weight of 25 mg was evaluated using live/dead staining with calcein-AM (to stain live cells with a green color) and ethidium homodimer (to stain dead cells with a red color). Confocal fluorescence microscopy revealed that most of the cells plated were alive on the rGOPH film. For instance, Figure 7-6 from left to right, respectively, shows the confocal fluorescent images of live, dead and mix of live/dead cells on the rGOPH film. The upper row images features the cells after 1day seeding time whereas the lower ones represent the 10 days incubation of the cells treated on rGOPH. The absence of red color cells attributes to the high biocompatibility of the film, the longer the seeding time, the more anchoring of the cell and the stronger attachment to the rGOPH film. Such behavior demonstrates that rGOPH is not only a favorable platform for MSCs, it also aided with retaining the live cells functionalities up to

10 days after seeding. Compared with other studies of the rat pheochromocytoma (PC12) cells[192] and mammalian colorectal adenocarcinoma HT-29 cells [195] treated on graphene based films, our rGOPH film exhibited more than 2 times longer biocompatibility and even with using 50 times larger graphene concentration. Our biocompatibility results are also comparable with GO treated MSCs reported by Elkhenany et al. [478] who found MSCs adhered and proliferated on GO film for over a 10 days period. However, the mass of graphene based film in our study is 5 times larger than what they used. After all of these comparisons, the toxicity of rGOPH film found to be independent of time and the weight of hydrogel and it is assured that there is no serious risk of using them for treating even healthy cells.

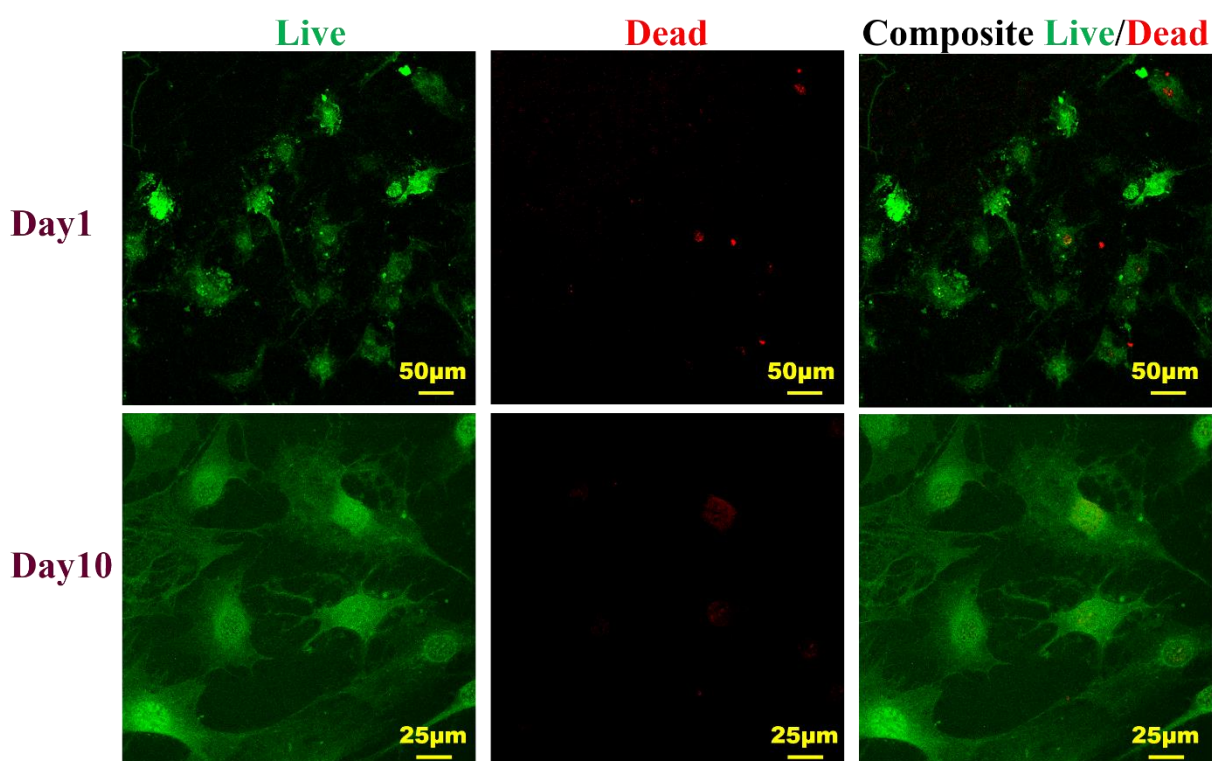


Figure 7-6. Confocal laser scanning microscopy images (live, dead and mix of live/dead images) of MSCs treated with rGOPH(25 mg) at day1 and 10.

7.4 Conclusions

In summary, the pH-dependent release of anticancer drug molecule DOX from rGOPH was investigated in PBS solutions under acidic, neutral and basic conditions. The rGOPH exhibited the highest release rate in acidic environment, thereby, could be a

promising candidate for cancer therapy. MSCs were used to assess the cytotoxicity of rGOPH and rGOPH/DOX. MTT assays found that rGOPH regardless of weight had a negligible toxicity to MSCs and that rGOPH/DOX containing larger dose of DOX was less cytotoxic than pure DOX. This confirms the controlled release behavior of rGOPH which was slow and in a sustained way. Our biocompatibility test results also showed that MSCs independent of the seeding time retained their functionalities on the rGOPH film indicating that such material have no damage risk being localized in healthy cells environment. Our approach is the first utilization of a peptide mediated layered graphene hydrogel with tunable pore size as a drug carrier, and this result opens the door for designing suitable graphene related materials for real biomedical application and many other areas.

Acknowledgment

M.V.K gratefully acknowledges the Australian Postgraduate Award (APA) International Postgraduate Research Scholarship (IPRS) from the University of Adelaide. The support of the Australian Research Council Discovery Program (DP20111888) is also gratefully acknowledged.

Chapter 8: Conclusions

In this work, layered graphene hydrogels were systematically studied from their design and MD simulations to preparations, characterizations and applications.

First, a tetradecamer α -helical peptide (FFGGEEEEEEGGFF), denoted UA2, was designed and synthesised. The peptide helicity and RMSD measurements demonstrated its outstanding structural stability in the ionic water solution with a neutral pH. The statistical analysis from the adsorption mechanism and conformational dynamics of 45 all-atom MD simulations of Graphene/UA2 system confirmed the feasibility and similar preferences of peptide adsorption on flexible graphene surface. The dominant factor for UA2 binding to the graphene surface was the strong π - π stacking interactions of PHE residues that symmetrically designed both ends of UA2 (N- and C-terminal residues). The PHE residues initially through direct surface interactions, lockdown on the graphene surface, however, GLU negative charged side-chains were also the second leading factor for the UA2 stabilizing on the graphene surface and the closest they went toward the surface was the positive charged region between first and second water layer. The surface oscillation of the flexible graphene sheets did not perturb the interfacial water density profile or the native intra-peptide interactions and its helical conformation. The experiment results through TEM and AFM images confirmed the peptide affinity and assembly on the flexible graphene surface. The height profile measurement in agreement with simulation result confirmed the peptide height of about ~ 6 Å indicating that the peptide had the lie down orientation after complete adsorption on the graphene sheet.

UA2 was proposed to have a symmetric design with aromatic containing residues at each end to aid with their symmetrical binding with pair of graphene sheets and induce their assembly after being placed in between them. This was investigated in the second study, in a system through MD simulation with two graphene sheet and single peptide. The simulation results revealed that UA2 through its aromatic residues (PHE) utilizing π - π stacking interactions helped with LBL self-assembly of graphene nanosheets to build a novel 3D construct, with tuneable pore sizes and structural characteristics. Such hydrogel construct was then prepared simply by mixing the graphene dispersion with the UA2

peptide, in thick (opaque) and transparent form (depends on the graphene concentration), without the need for either surfactant stabilizers or co-solvent. The obtained hydrogels with and without presence of peptide were denoted as rGOH and rGOPH, respectively. In agreement with simulation results, the AFM experiments for a few layers scale, UV-Vis and N₂-adsorptions for the bulk material demonstrated that the desired pore size of ~26 Å was achieved in LBL peptide mediated self-assembled hydrogel. The N₂-adsorptions results also elucidated that the porosity within the hydrogel films (either with or without presence of peptide) was retained when freeze-dried under vacuum condition indicating high structural stability of the porous hydrogels. It was eventually shown that such hydrogel material could be used to exquisitely separate biomolecules in the nanometre range. For instance, the rGOPH acted as size-selective adsorbent as it could adsorb the FD4 and FD10 with the respective molecular size of ~1.4 and nm ~2.3 nm, but the FD20 of ~3.3 nm was completely rejected. Such great physiochemical properties and size selective adsorption properties also opens up new vistas of different applications in the areas of nanoelectronics, nanobiotechnology and nanomedicines.

As an application of the prepared hydrogels, loading and controlled delivery of an anti-cancer drug, doxorubicin (DOX), were investigated with regards to the effect of hydrogel preparation parameters and pore sizes. DOX loading capacity of rGOPHs was studied (modelled and optimized) using the DOE analysis of 20 experiments and applying the central composite face-centered design (CCFD) on three main preparation parameters of hydrazine amount, reduction temperature and peptide concentration. The rGOPH exhibited distinct pH-dependent behavior with largest DOX loading ratio in neutral condition (510.4 µg) as compared with the acidic (283.6 µg) and basic conditions (390.2 µg), which is mainly attributed to the different degrees of hydrogen-bonding interaction between DOX and rGOPH under different pH conditions. The rGO prepared at optimum condition (89 °C and 54 µL hydrazine) due to contain sufficient amount of oxygen containing groups aided to achieve the desired pore size of ~2.6 nm as well as the highest DOX loading capacity. In contrast, both highly and slightly reduced GO, due to the higher inter-sheet van der Waals interactions (through either strong hydrogen-bonding or π - π stacking interactions) demonstrated the lowest values in pore sizes and DOX loading capacities. The kinetics studies of DOX loading experimental data demonstrated the

physisorption characteristics of rGOPH after well-fitting to pseudo-first order model. The rGOPH due to have a larger pore size providing more accessible adsorption sites showed a quicker adsorption rate and higher loading efficiency compared to that of rGOH, the hydrogel without peptide. The possible adsorption mechanisms are mainly due to hydrogen bonding, π - π stacking interactions between the species of hydrogels and DOX. Furthermore, the effect of pore size on the DOX loading yield and mechanism were investigated using MD simulations. Interestingly, similar to the experimental data the rGOPH of \sim 2.6 nm pore size exhibited a faster initial and overall adsorption rate with a loading efficiency almost 2.5 times larger than that of rGOH (with 1.0 nm pore size) through 30ns of MD simulations.

Furthermore, in order to investigate the potentials of rGOPH for therapeutic applications, its pH dependent DOX release was conducted in PBS solution under acidic, neutral and basic conditions together with performing cell viability and biocompatibility tests. The rGOPH exhibited the highest release rate in acidic environment, thereby, could be a promising candidate for cancer therapy. In such a condition, the release rate was sustained at a constant value (60%) for around 3.5 days. MSCs were used to assess the cytotoxicity of rGOPH and rGOPH/DOX. MTT assay data found that rGOPH regardless of weight had negligible toxicity to MSCs and that DOX containing rGOPH was less cytotoxic than pure DOX. The biocompatibility results further confirmed retaining of MSCs functionalities even after 10 days being seeded on rGOPH film indicating that there is no serious risk of using them for treating healthy cells. The approach introduced in this study opens the door for designing graphene based materials for biomedical applications and many other areas.

Recommendations

In terms of future work, there is clearly an opportunity to expand on the work concerned with better understanding the roles of different types and amounts of oxygen containing groups on graphene surface (through both simulation and experiment) on controlling the self-assembly process of layered graphene materials, stability of their structures, and the adjustment of pore sizes.

The pore sizes and properties of the graphene layered hydrogel described in this study can be tuned or customised based on the substitution or variation of the amino acid sequences in peptide. These customizations may favour different applications where target molecules are with different sizes and particular properties.

Since the pH dependent drug release behavior of resultant hydrogel materials in this study favours the cancer therapy applications, future works for cytotoxic potency of hydrogels drug loaded hydrogels on various tumor cell lines are suggested. Flow cytometric analysis could be the main tool to count cells number at the different phases of the cell cycle to determine whether these materials induces the cells apoptosis.

References

- [1] Peppas NA, Bures P, Leobandung W, Ichikawa H. Hydrogels in pharmaceutical formulations. *European Journal of Pharmaceutics and Biopharmaceutics*. 2000;50(1):27-46.
- [2] Buddy D R, Allan S H. *Synthetic Hydrogels for Biomedical Applications. Hydrogels for Medical and Related Applications: AMERICAN CHEMICAL SOCIETY* 1976, p. 1-36.
- [3] Peppas NA, Langer R. New challenges in biomaterials. *Science*. 1994;263(5154):1715-20.
- [4] Hu X, Hao L, Wang H, Yang X, Zhang G, Wang G, et al. Hydrogel Contact Lens for Extended Delivery of Ophthalmic Drugs. *International Journal of Polymer Science*. 2011;2011:9.
- [5] Tavazzi S, Ferraro L, Cozza F, Pastori V, Lecchi M, Farris S, et al. Hydrogen Peroxide Mechanosynthesis in Siloxane-Hydrogel Contact Lenses. *ACS Applied Materials & Interfaces*. 2014;6(22):19606-12.
- [6] Sharma B, Fermanian S, Gibson M, Unterman S, Herzka DA, Cascio B, et al. Human cartilage repair with a photoreactive adhesive-hydrogel composite. *Science Translational Medicine*. 2013;5(167).
- [7] Park H, Choi B, Hu J, Lee M. Injectable chitosan hyaluronic acid hydrogels for cartilage tissue engineering. *Acta Biomaterialia*. 2013;9(1):4779-86.
- [8] He C, Kim SW, Lee DS. In situ gelling stimuli-sensitive block copolymer hydrogels for drug delivery. *Journal of Controlled Release*. 2008;127(3):189-207.
- [9] Megeed Z, Haider M, Li D, O'Malley Jr BW, Cappello J, Ghandehari H. In vitro and in vivo evaluation of recombinant silk-elastinlike hydrogels for cancer gene therapy. *Journal of Controlled Release*. 2004;94(2-3):433-45.
- [10] Stankovich S, Dikin DA, Dommett GHB, Kohlhaas KM, Zimney EJ, Stach EA, et al. Graphene-based composite materials. *Nature*. 2006;442(7100):282-6.
- [11] Dikin DA, Stankovich S, Zimney EJ, Piner RD, Dommett GHB, Evmenenko G, et al. Preparation and characterization of graphene oxide paper. *Nature*. 2007;448(7152):457-60.
- [12] L. Brannon-Peppas, N. A. Peppas. The equilibrium swelling behavior of porous and non-porous hydrogels. In: L. Brannon-Peppas, R.S. Harland, eds. *Absorbent Polymer Technology*. Amsterdam: Elsevier 1990, p. 67–75.
- [13] Servant A, Leon V, Jasim D, Methven L, Limousin P, Fernandez-Pacheco EV, et al. Graphene-Based Electroresponsive Scaffolds as Polymeric Implants for On-Demand Drug Delivery. *Advanced Healthcare Materials*. 2014;3(8):1334-43.
- [14] Varghese JS, Chellappa N, Fathima NN. Gelatin–carrageenan hydrogels: Role of pore size distribution on drug delivery process. *Colloids and Surfaces B: Biointerfaces*. 2014;113(0):346-51.
- [15] Xu Y, Sheng K, Li C, Shi G. Self-Assembled Graphene Hydrogel via a One-Step Hydrothermal Process. *ACS Nano*. 2010;4(7):4324-30.
- [16] Bai H, Sheng K, Zhang P, Li C, Shi G. Graphene oxide/conducting polymer composite hydrogels. *J Mater Chem*. 2011;21(46):18653-8.

- [17] Cong H-P, Ren X-C, Wang P, Yu S-H. Macroscopic Multifunctional Graphene-Based Hydrogels and Aerogels by a Metal Ion Induced Self-Assembly Process. *ACS Nano*. 2012;6(3):2693-703.
- [18] Gu X, Ning Y, Yang Y, Wang C. One-step synthesis of porous graphene-based hydrogels containing oil droplets for drug delivery. *RSC Advances*. 2014;4(7):3211-8.
- [19] Zhang X, Sui Z, Xu B, Yue S, Luo Y, Zhan W, et al. Mechanically strong and highly conductive graphene aerogel and its use as electrodes for electrochemical power sources. *J Mater Chem*. 2011;21(18):6494-7.
- [20] Wu Z-S, Yang S, Sun Y, Parvez K, Feng X, Müllen K. 3D Nitrogen-Doped Graphene Aerogel-Supported Fe₃O₄ Nanoparticles as Efficient Electrocatalysts for the Oxygen Reduction Reaction. *Journal of the American Chemical Society*. 2012;134(22):9082-5.
- [21] Han Z, Tang Z, Shen S, Zhao B, Zheng G, Yang J. Strengthening of Graphene Aerogels with Tunable Density and High Adsorption Capacity towards Pb²⁺. *Sci Rep*. 2014;4.
- [22] Bai H, Li C, Wang X, Shi G. A pH-sensitive graphene oxide composite hydrogel. *Chemical Communications*. 2010;46(14):2376-8.
- [23] Chen J-J, Meng J, Zhou Y-B, Wu H-C, Bie Y-Q, Liao Z-M, et al. Layer-by-layer assembly of vertically conducting graphene devices. *Nat Commun*. 2013;4:1921.
- [24] Kovtyukhova NI, Ollivier PJ, Martin BR, Mallouk TE, Chizhik SA, Buzaneva EV, et al. Layer-by-Layer Assembly of Ultrathin Composite Films from Micron-Sized Graphite Oxide Sheets and Polycations. *Chemistry of Materials*. 1999;11(3):771-8.
- [25] Nicolai A, Sumpter BG, Meunier V. Tunable water desalination across graphene oxide framework membranes. *Physical Chemistry Chemical Physics*. 2014;16(18):8646-54.
- [26] Chen S, Duan J, Jaroniec M, Qiao SZ. Hierarchically porous graphene-based hybrid electrodes with excellent electrochemical performance. *Journal of Materials Chemistry A*. 2013;1(33):9409-13.
- [27] Burrell JW, Gadipelli S, Ford J, Simmons JM, Zhou W, Yildirim T. Graphene Oxide Framework Materials: Theoretical Predictions and Experimental Results. *Angewandte Chemie International Edition*. 2010;49(47):8902-4.
- [28] Lin L-S, Cong Z-X, Li J, Ke K-M, Guo S-S, Yang H-H, et al. Graphitic-phase C₃N₄ nanosheets as efficient photosensitizers and pH-responsive drug nanocarriers for cancer imaging and therapy. *Journal of Materials Chemistry B*. 2014;2(8):1031-7.
- [29] Hong J, Shah NJ, Drake AC, DeMuth PC, Lee JB, Chen J, et al. Graphene Multilayers as Gates for Multi-Week Sequential Release of Proteins from Surfaces. *ACS Nano*. 2011;6(1):81-8.
- [30] Chung KY, Mishra NC, Wang CC, Lin FH, Lin KH. Fabricating scaffolds by microfluidics. *Biomicrofluidics*. 2009;3(2).
- [31] El-Sherbiny IM, Yacoub MH. Hydrogel scaffolds for tissue engineering: Progress and challenges. *Global Cardiology Science and Practice*. 2013;2013(3):38.
- [32] Yang X, Zhu J, Qiu L, Li D. Bioinspired Effective Prevention of Restacking in Multilayered Graphene Films: Towards the Next Generation of High-Performance Supercapacitors. *Adv Mater*. 2011;23(25):2833-8.
- [33] Feng X, Chen W, Yan L. Reduced graphene oxide hydrogel film with a continuous ion transport network for supercapacitors. *Nanoscale*. 2015;7(8):3712-8.

- [34] Buchsteiner A, Lerf A, Pieper J. Water Dynamics in Graphite Oxide Investigated with Neutron Scattering. *The Journal of Physical Chemistry B*. 2006;110(45):22328-38.
- [35] Wang G, Sun X, Lu F, Sun H, Yu M, Jiang W, et al. Flexible Pillared Graphene-Paper Electrodes for High-Performance Electrochemical Supercapacitors. *Small*. 2012;8(3):452-9.
- [36] Yan J, Wei T, Shao B, Ma F, Fan Z, Zhang M, et al. Electrochemical properties of graphene nanosheet/carbon black composites as electrodes for supercapacitors. *Carbon*. 2010;48(6):1731-7.
- [37] Lei ZB, Liu ZH, Wang HJ, Sun XX, Lu L, Zhao XS. A high-energy-density supercapacitor with graphene-CMK-5 as the electrode and ionic liquid as the electrolyte. *Journal of Materials Chemistry A*. 2013;1(6):2313-21.
- [38] Zhang LL, Xiong Z, Zhao XS. Pillaring Chemically Exfoliated Graphene Oxide with Carbon Nanotubes for Photocatalytic Degradation of Dyes under Visible Light Irradiation. *ACS Nano*. 2010;4(11):7030-6.
- [39] Zhang LL, Xiong ZG, Zhao XS. A composite electrode consisting of nickel hydroxide, carbon nanotubes, and reduced graphene oxide with an ultrahigh electrocapacitance. *Journal of Power Sources*. 2013;222:326-32.
- [40] Yang WL, Gao Z, Wang J, Wang B, Liu LH. Hydrothermal synthesis of reduced graphene sheets/Fe₂O₃ nanorods composites and their enhanced electrochemical performance for supercapacitors. *Solid State Sciences*. 2013;20:46-53.
- [41] Wu Z-S, Wang D-W, Ren W, Zhao J, Zhou G, Li F, et al. Anchoring Hydrous RuO₂ on Graphene Sheets for High-Performance Electrochemical Capacitors. *Advanced Functional Materials*. 2010;20(20):3595-602.
- [42] Kong BS, Geng JX, Jung HT. Layer-by-layer assembly of graphene and gold nanoparticles by vacuum filtration and spontaneous reduction of gold ions. *Chem Commun*. 2009(16):2174-6.
- [43] Zhang P, Huang Y, Lu X, Zhang S, Li J, Wei G, et al. One-Step Synthesis of Large-Scale Graphene Film Doped with Gold Nanoparticles at Liquid-Air Interface for Electrochemistry and Raman Detection Applications. *Langmuir*. 2014;30(29):8980-9.
- [44] Kuo T-R, Wang D-Y, Chiu Y-C, Yeh Y-C, Chen W-T, Chen C-H, et al. Layer-by-layer thin film of reduced graphene oxide and gold nanoparticles as an effective sample plate in laser-induced desorption/ionization mass spectrometry. *Analytica Chimica Acta*. 2014;809(0):97-103.
- [45] Wang D, Li X, Wang J, Yang J, Geng D, Li R, et al. Defect-Rich Crystalline SnO₂ Immobilized on Graphene Nanosheets with Enhanced Cycle Performance for Li Ion Batteries. *The Journal of Physical Chemistry C*. 2012;116(42):22149-56.
- [46] Li F, Bao Y, Chai J, Zhang Q, Han D, Li N. Synthesis and application of widely soluble graphene sheets. *Langmuir*. 2010;26(14):12314-20.
- [47] Xu Y, Wu Q, Sun Y, Bai H, Shi G. Three-Dimensional Self-Assembly of Graphene Oxide and DNA into Multifunctional Hydrogels. *ACS Nano*. 2010;4(12):7358-62.
- [48] Wang L, Sofer Z, Luxa J, Pumera M. Nitrogen doped graphene: influence of precursors and conditions of the synthesis. *J Mater Chem C*. 2014;2(16):2887-93.
- [49] Wu J, Chen A, Qin M, Huang R, Zhang G, Xue B, et al. Hierarchical construction of a mechanically stable peptide-graphene oxide hybrid hydrogel for drug delivery and pulsatile triggered release in vivo. *Nanoscale*. 2015.
- [50] Novoselov KS, Geim AK, Morozov SV, Jiang D, Zhang Y, Dubonos SV, et al. Electric Field Effect in Atomically Thin Carbon Films. *Science*. 2004;306(5696):666-9.

- [51] Stoller MD, Park S, Zhu Y, An J, Ruoff RS. Graphene-Based Ultracapacitors. *Nano Letters*. 2008;8(10):3498-502.
- [52] Nair RR, Blake P, Grigorenko AN, Novoselov KS, Booth TJ, Stauber T, et al. Fine Structure Constant Defines Visual Transparency of Graphene. *Science*. 2008;320(5881):1308.
- [53] Lee C, Wei X, Kysar JW, Hone J. Measurement of the elastic properties and intrinsic strength of monolayer graphene. *Science*. 2008;321(5887):385-8.
- [54] Balandin AA, Ghosh S, Bao W, Calizo I, Teweldebrhan D, Miao F, et al. Superior thermal conductivity of single-layer graphene. *Nano Letters*. 2008;8(3):902-7.
- [55] Geim AK, Novoselov KS. The rise of graphene. *Nat Mater*. 2007;6(3):183-91.
- [56] Bonaccorso F, Lombardo A, Hasan T, Sun Z, Colombo L, Ferrari AC. Production and processing of graphene and 2d crystals. *Materials Today*. 2012;15(12):564-89.
- [57] Van Bommel AJ, Crombeen JE, Van Tooren A. LEED and Auger electron observations of the SiC(0001) surface. *Surface Science*. 1975;48(2):463-72.
- [58] Tejeda A, Taleb-Ibrahimi A, Heer Wd, Berger C, Conrad EH. Electronic structure of epitaxial graphene grown on the C-face of SiC and its relation to the structure. *New Journal of Physics*. 2012;14(12):125007.
- [59] Cambaz ZG, Yushin G, Osswald S, Mochalin V, Gogotsi Y. Noncatalytic synthesis of carbon nanotubes, graphene and graphite on SiC. *Carbon*. 2008;46(6):841-9.
- [60] Jacobson P, Stöger B, Garhofer A, Parkinson GS, Schmid M, Caudillo R, et al. Nickel Carbide as a Source of Grain Rotation in Epitaxial Graphene. *ACS Nano*. 2012;6(4):3564-72.
- [61] Weatherup RS, Amara H, Blume R, Dlubak B, Bayer BC, Diarra M, et al. Interdependency of Subsurface Carbon Distribution and Graphene–Catalyst Interaction. *Journal of the American Chemical Society*. 2014;136(39):13698-708.
- [62] Karu AE, Beer M. Pyrolytic formation of highly crystalline graphite films. *Journal of Applied Physics*. 1966;37(5):2179-81.
- [63] Perdereau J, Rhead GE. LEED studies of adsorption on vicinal copper surfaces. *Surface Science*. 1971;24(2):555-71.
- [64] Kholin NA, Rut'kov EV, Tontegode AY. The nature of the adsorption bond between graphite islands and iridium surface. *Surface Science*. 1984;139(1):155-72.
- [65] Li X, Cai W, An J, Kim S, Nah J, Yang D, et al. Large-area synthesis of high-quality and uniform graphene films on copper foils. *Science*. 2009;324(5932):1312-4.
- [66] Li X, Cai W, Colombo L, Ruoff RS. Evolution of graphene growth on Ni and Cu by carbon isotope labeling. *Nano Letters*. 2009;9(12):4268-72.
- [67] Kim KS, Zhao Y, Jang H, Lee SY, Kim JM, Ahn JH, et al. Large-scale pattern growth of graphene films for stretchable transparent electrodes. *Nature*. 2009;457(7230):706-10.
- [68] Novoselov KS, Jiang D, Schedin F, Booth TJ, Khotkevich VV, Morozov SV, et al. Two-dimensional atomic crystals. *Proceedings of the National Academy of Sciences of the United States of America*. 2005;102(30):10451-3.
- [69] Lu X, Yu M, Huang H, Ruoff RS. Tailoring graphite with the goal of achieving single sheets. *Nanotechnology*. 1999;10(3):269-72.
- [70] Goler S, Piazza V, Roddaro S, Pellegrini V, Beltram F, Pingue P. Self-assembly and electron-beam-induced direct etching of suspended graphene nanostructures. *Journal of Applied Physics*. 2011;110(6):064308.

- [71] Das A, Chakraborty B, Sood AK. Raman spectroscopy of graphene on different substrates and influence of defects. *Bull Mater Sci.* 2008;31(3):579-84.
- [72] Casiraghi C, Hartschuh A, Lidorikis E, Qian H, Harutyunyan H, Gokus T, et al. Rayleigh imaging of graphene and graphene layers. *Nano Letters.* 2007;7(9):2711-7.
- [73] Lotya M, King PJ, Khan U, De S, Coleman JN. High-concentration, surfactant-stabilized graphene dispersions. *ACS Nano.* 2010;4(6):3155-62.
- [74] Israelachvili J. *Intermolecular and surface force.* Third ed. Boston: Academic Press; 2011.
- [75] Lyklema J. The surface tension of pure liquids: Thermodynamic components and corresponding states. *Colloids and Surfaces A: Physicochemical and Engineering Aspects.* 1999;156(1-3):413-21.
- [76] Ghatee MH, Pakdel L. Surface tension regularity of non-polar, polar, and weak electrolyte liquid hydrocarbons. *Fluid Phase Equilibria.* 2005;234(1-2):101-7.
- [77] Hernandez Y, Nicolosi V, Lotya M, Blighe FM, Sun Z, De S, et al. High-yield production of graphene by liquid-phase exfoliation of graphite. *Nature nanotechnology.* 2008;3(9):563-8.
- [78] Parvez K, Wu Z-S, Li R, Liu X, Graf R, Feng X, et al. Exfoliation of Graphite into Graphene in Aqueous Solutions of Inorganic Salts. *Journal of the American Chemical Society.* 2014;136(16):6083-91.
- [79] Rao KS, Senthilnathan J, Liu Y-F, Yoshimura M. Role of Peroxide Ions in Formation of Graphene Nanosheets by Electrochemical Exfoliation of Graphite. *Sci Rep.* 2014;4.
- [80] Zhou M, Tang J, Cheng Q, Xu G, Cui P, Qin L-C. Few-layer graphene obtained by electrochemical exfoliation of graphite cathode. *Chemical Physics Letters.* 2013;572(0):61-5.
- [81] Su C-Y, Lu A-Y, Xu Y, Chen F-R, Khlobystov AN, Li L-J. High-Quality Thin Graphene Films from Fast Electrochemical Exfoliation. *ACS Nano.* 2011;5(3):2332-9.
- [82] Xiu-Yun C. Graphene-like nanosheets synthesized by natural flaky graphite in Shandong, China. *Int Nano Lett.* 2013;3(1):1-5.
- [83] Chua CK, Pumera M. Chemical reduction of graphene oxide: a synthetic chemistry viewpoint. *Chemical Society reviews.* 2014;43(1):291-312.
- [84] Brodie BC. Sur le poids atomique du graphite. *Ann Chim Phys.* 1860; 59:466-72.
- [85] Staudenmaier L. Verfahren Zur Darstellung der Graphitsäure *Ber Dtsch Chem Ges.* 1898;131(2):1481-7.
- [86] Hummers WS, Offeman RE. Preparation of Graphitic Oxide. *Journal of the American Chemical Society.* 1958;80(6):1339-.
- [87] Sun Y, Wang S, Li C, Luo P, Tao L, Wei Y, et al. Large scale preparation of graphene quantum dots from graphite with tunable fluorescence properties. *Physical Chemistry Chemical Physics.* 2013;15(24):9907-13.
- [88] Marcano DC, Kosynkin DV, Berlin JM, Sinitskii A, Sun Z, Slesarev A, et al. Improved Synthesis of Graphene Oxide. *ACS Nano.* 2010;4(8):4806-14.
- [89] Chen J, Yao B, Li C, Shi G. An improved Hummers method for eco-friendly synthesis of graphene oxide. *Carbon.* 2013;64(0):225-9.
- [90] Chen J, Li Y, Huang L, Li C, Shi G. High-yield preparation of graphene oxide from small graphite flakes via an improved Hummers method with a simple purification process. *Carbon.* 2015;81(0):826-34.

- [91] Mattevi C, Eda G, Agnoli S, Miller S, Mkhoyan KA, Celik O, et al. Evolution of Electrical, Chemical, and Structural Properties of Transparent and Conducting Chemically Derived Graphene Thin Films. *Adv Funct Mater.* 2009;19(16):2577-83.
- [92] Cai W, Piner RD, Stadermann FJ, Park S, Shaibat MA, Ishii Y, et al. Synthesis and Solid-State NMR Structural Characterization of ¹³C-Labeled Graphite Oxide. *Science.* 2008;321(5897):1815-7.
- [93] Park S, Lee K-S, Bozoklu G, Cai W, Nguyen ST, Ruoff RS. Graphene Oxide Papers Modified by Divalent Ions—Enhancing Mechanical Properties via Chemical Cross-Linking. *ACS Nano.* 2008;2(3):572-8.
- [94] Shih C-J, Lin S, Sharma R, Strano MS, Blankshtein D. Understanding the pH-Dependent Behavior of Graphene Oxide Aqueous Solutions: A Comparative Experimental and Molecular Dynamics Simulation Study. *Langmuir.* 2011;28(1):235-41.
- [95] Li X, Zhang G, Bai X, Sun X, Wang X, Wang E, et al. Highly conducting graphene sheets and Langmuir-Blodgett films. *Nature nanotechnology.* 2008;3(9):538-42.
- [96] Hasan SA, Rigueur JL, Harl RR, Krejci AJ, Gonzalo-Juan I, Rogers BR, et al. Transferable Graphene Oxide Films with Tunable Microstructures. *ACS Nano.* 2010;4(12):7367-72.
- [97] Li X, Wang X, Zhang L, Lee S, Dai H. Chemically derived, ultrasmooth graphene nanoribbon semiconductors. *Science.* 2008;319(5867):1229-32.
- [98] Stankovich S, Dikin DA, Piner RD, Kohlhaas KA, Kleinhammes A, Jia Y, et al. Synthesis of graphene-based nanosheets via chemical reduction of exfoliated graphite oxide. *Carbon.* 2007;45(7):1558-65.
- [99] Lomeda JR, Doyle CD, Kosynkin DV, Hwang W-F, Tour JM. Diazonium Functionalization of Surfactant-Wrapped Chemically Converted Graphene Sheets. *Journal of the American Chemical Society.* 2008;130(48):16201-6.
- [100] Schniepp HC, Li J-L, McAllister MJ, Sai H, Herrera-Alonso M, Adamson DH, et al. Functionalized Single Graphene Sheets Derived from Splitting Graphite Oxide. *The Journal of Physical Chemistry B.* 2006;110(17):8535-9.
- [101] Niyogi S, Bekyarova E, Itkis ME, McWilliams JL, Hamon MA, Haddon RC. Solution properties of graphite and graphene. *Journal of the American Chemical Society.* 2006;128(24):7720-1.
- [102] Zhang T, Liu P, Sheng C, Duan Y, Zhang J. A green and facile approach for the synthesis of water-dispersible reduced graphene oxide based on ionic liquids. *Chemical Communications.* 2014;50(22):2889-92.
- [103] Paredes JI, Villar-Rodil S, Martínez-Alonso A, Tascón JMD. Graphene Oxide Dispersions in Organic Solvents. *Langmuir.* 2008;24(19):10560-4.
- [104] Ghosh R, Midya A, Santra S, Ray SK, Guha PK. Chemically Reduced Graphene Oxide for Ammonia Detection at Room Temperature. *ACS Applied Materials & Interfaces.* 2013;5(15):7599-603.
- [105] Gómez-Navarro C, Weitz RT, Bittner AM, Scolari M, Mews A, Burghard M, et al. Electronic Transport Properties of Individual Chemically Reduced Graphene Oxide Sheets. *Nano Letters.* 2007;7(11):3499-503.
- [106] Dreyer DR, Park S, Bielawski CW, Ruoff RS. The chemistry of graphene oxide. *Chemical Society reviews.* 2010;39(1):228-40.
- [107] Barg S, Perez FM, Ni N, do Vale Pereira P, Maher RC, Garcia-Tuñón E, et al. Mesoscale assembly of chemically modified graphene into complex cellular networks. *Nat Commun.* 2014;5.

- [108] Bai H, Li C, Shi G. Functional Composite Materials Based on Chemically Converted Graphene. *Advanced Materials*. 2011;23(9):1089-115.
- [109] Chen H, Song Z, Zhao X, Li X, Lin H. Reduction of free-standing graphene oxide papers by a hydrothermal process at the solid/gas interface. *RSC Advances*. 2013;3(9):2971-8.
- [110] Liu G-J, Fan L-Q, Yu F-D, Wu J-H, Liu L, Qiu Z-Y, et al. Facile one-step hydrothermal synthesis of reduced graphene oxide/Co₃O₄ composites for supercapacitors. *J Mater Sci*. 2013;48(24):8463-70.
- [111] Shi J-L, Du W-C, Yin Y-X, Guo Y-G, Wan L-J. Hydrothermal reduction of three-dimensional graphene oxide for binder-free flexible supercapacitors. *Journal of Materials Chemistry A*. 2014;2(28):10830-4.
- [112] Zhou Y, Bao Q, Tang LAL, Zhong Y, Loh KP. Hydrothermal Dehydration for the “Green” Reduction of Exfoliated Graphene Oxide to Graphene and Demonstration of Tunable Optical Limiting Properties. *Chemistry of Materials*. 2009;21(13):2950-6.
- [113] Zhang J, Yang H, Shen G, Cheng P, Zhang J, Guo S. Reduction of graphene oxide vial-ascorbic acid. *Chemical Communications*. 2010;46(7):1112-4.
- [114] Bagri A, Mattevi C, Acik M, Chabal YJ, Chhowalla M, Shenoy VB. Structural evolution during the reduction of chemically derived graphene oxide. *Nat Chem*. 2010;2(7):581-7.
- [115] Gao W, Alemany LB, Ci L, Ajayan PM. New insights into the structure and reduction of graphite oxide. *Nat Chem*. 2009;1(5):403-8.
- [116] Daeha J, Chunder A, Lei Z, Saiful IK. High yield fabrication of chemically reduced graphene oxide field effect transistors by dielectrophoresis. *Nanotechnology*. 2010;21(16):165202.
- [117] Wilson NR, Pandey PA, Beanland R, Rourke JP, Lupo U, Rowlands G, et al. On the structure and topography of free-standing chemically modified graphene. *New Journal of Physics*. 2010;12.
- [118] Li D, Müller MB, Gilje S, Kaner RB, Wallace GG. Processable aqueous dispersions of graphene nanosheets. *Nature nanotechnology*. 2008;3(2):101-5.
- [119] Xuekun L, Minfeng Y, Hui H, Rodney SR. Tailoring graphite with the goal of achieving single sheets. *Nanotechnology*. 1999;10(3):269.
- [120] Brauer G. *Handbook of Preparative Inorganic Chemistry*. second ed. New York: Academic Press; 1963.
- [121] Park S, Hu Y, Hwang JO, Lee E-S, Casabianca LB, Cai W, et al. Chemical structures of hydrazine-treated graphene oxide and generation of aromatic nitrogen doping. *Nat Commun*. 2012;3:638.
- [122] Mungse HP, Sharma OP, Sugimura H, Khatri OP. Hydrothermal deoxygenation of graphene oxide in sub- and supercritical water. *RSC Advances*. 2014;4(43):22589-95.
- [123] Thakur S, Das G, Raul PK, Karak N. Green One-Step Approach to Prepare Sulfur/Reduced Graphene Oxide Nanohybrid for Effective Mercury Ions Removal. *The Journal of Physical Chemistry C*. 2013;117(15):7636-42.
- [124] Ganguly A, Sharma S, Papakonstantinou P, Hamilton J. Probing the Thermal Deoxygenation of Graphene Oxide Using High-Resolution In Situ X-ray-Based Spectroscopies. *The Journal of Physical Chemistry C*. 2011;115(34):17009-19.
- [125] Becerril HA, Mao J, Liu Z, Stoltenberg RM, Bao Z, Chen Y. Evaluation of Solution-Processed Reduced Graphene Oxide Films as Transparent Conductors. *ACS Nano*. 2008;2(3):463-70.

- [126] David L, Singh G. Reduced Graphene Oxide Paper Electrode: Opposing Effect of Thermal Annealing on Li and Na Cyclability. *The Journal of Physical Chemistry C*. 2014;118(49):28401-8.
- [127] Song N-J, Chen C-M, Lu C, Liu Z, Kong Q-Q, Cai R. Thermally reduced graphene oxide films as flexible lateral heat spreaders. *Journal of Materials Chemistry A*. 2014;2(39):16563-8.
- [128] Goenka S, Sant V, Sant S. Graphene-based nanomaterials for drug delivery and tissue engineering. *Journal of Controlled Release*. 2014;173(0):75-88.
- [129] Loh KP, Bao Q, Ang PK, Yang J. The chemistry of graphene. *J Mater Chem*. 2010;20(12):2277-89.
- [130] Taherian F, Marcon V, Van Der Vegt NFA, Leroy F. What is the contact angle of water on graphene? *Langmuir*. 2013;29(5):1457-65.
- [131] Xue Y, Liu Y, Lu F, Qu J, Chen H, Dai L. Functionalization of graphene oxide with polyhedral oligomeric silsesquioxane (POSS) for multifunctional applications. *Journal of Physical Chemistry Letters*. 2012;3(12):1607-12.
- [132] Hsieh CT, Chen WY. Water/oil repellency and work of adhesion of liquid droplets on graphene oxide and graphene surfaces. *Surface and Coatings Technology*. 2011;205(19):4554-61.
- [133] Yang ST, Chang Y, Wang H, Liu G, Chen S, Wang Y, et al. Folding/aggregation of graphene oxide and its application in Cu²⁺ removal. *Journal of Colloid and Interface Science*. 2010;351(1):122-7.
- [134] Nika DL, Pokatilov EP, Askerov AS, Balandin AA. Phonon thermal conduction in graphene: Role of Umklapp and edge roughness scattering. *Physical Review B*. 2009;79(15):155413.
- [135] Jiang J-W, Lan J, Wang J-S, Li B. Isotopic effects on the thermal conductivity of graphene nanoribbons: Localization mechanism. *Journal of Applied Physics*. 2010;107(5):054314.
- [136] Bolotin KI, Sikes KJ, Jiang Z, Klima M, Fudenberg G, Hone J, et al. Ultrahigh electron mobility in suspended graphene. *Solid State Communications*. 2008;146(9-10):351-5.
- [137] Mahanta NK, Abramson AR. Thermal conductivity of graphene and graphene oxide nanoplatelets. *InterSociety Conference on Thermal and Thermomechanical Phenomena in Electronic Systems, ITherm*; p. 1-6.
- [138] Artiles MS, Rout CS, Fisher TS. Graphene-based hybrid materials and devices for biosensing. *Advanced Drug Delivery Reviews*. 2011;63(14-15):1352-60.
- [139] Nguyen P, Berry V. Graphene interfaced with biological cells: Opportunities and challenges. *Journal of Physical Chemistry Letters*. 2012;3(8):1024-9.
- [140] Cohen-Karni T, Langer R, Kohane DS. The smartest materials: The future of nanoelectronics in medicine. *ACS Nano*. 2012;6(8):6541-5.
- [141] Cohen-Karni T, Qing Q, Li Q, Fang Y, Lieber CM. Graphene and nanowire transistors for cellular interfaces and electrical recording. *Nano Letters*. 2010;10(3):1098-102.
- [142] Kravets VG, Grigorenko AN, Nair RR, Blake P, Anissimova S, Novoselov KS, et al. Spectroscopic ellipsometry of graphene and an exciton-shifted van Hove peak in absorption. *Physical Review B*. 2010;81(15):155413.
- [143] Wang F, Hamdi M. Strictly non-blocking conditions for the central-stage buffered Clos-network. *IEEE Communications Letters*. 2008;12(3):206-8.

- [144] Park S, Ruoff RS. Chemical methods for the production of graphenes. *Nature nanotechnology*. 2009;4(4):217-24.
- [145] Elias DC, Nair RR, Mohiuddin TMG, Morozov SV, Blake P, Halsall MP, et al. Control of Graphene's Properties by Reversible Hydrogenation: Evidence for Graphane. *Science*. 2009;323(5914):610-3.
- [146] Bonaccorso F, Sun Z, Hasan T, Ferrari AC. Graphene photonics and optoelectronics. *Nature Photonics*. 2010;4(9):611-22.
- [147] Ma X, Tao H, Yang K, Feng L, Cheng L, Shi X, et al. A functionalized graphene oxide-iron oxide nanocomposite for magnetically targeted drug delivery, photothermal therapy, and magnetic resonance imaging. *Nano Res*. 2012;5(3):199-212.
- [148] Shen AJ, Li DL, Cai XJ, Dong CY, Dong HQ, Wen HY, et al. Multifunctional nanocomposite based on graphene oxide for in vitro hepatocarcinoma diagnosis and treatment. *Journal of Biomedical Materials Research - Part A*. 2012;100 A(9):2499-506.
- [149] Sanchez VC, Jachak A, Hurt RH, Kane AB. Biological interactions of graphene-family nanomaterials: An interdisciplinary review. *Chemical Research in Toxicology*. 2012;25(1):15-34.
- [150] Bianco A. Graphene: Safe or toxic? the two faces of the medal. *Angewandte Chemie - International Edition*. 2013;52(19):4986-97.
- [151] Lu CH, Zhu CL, Li J, Liu JJ, Chen X, Yang HH. Using graphene to protect DNA from cleavage during cellular delivery. *Chemical Communications*. 2010;46(18):3116-8.
- [152] Wang Y, Li Z, Hu D, Lin CT, Li J, Lin Y. Aptamer/graphene oxide nanocomplex for in situ molecular probing in living cells. *Journal of the American Chemical Society*. 2010;132(27):9274-6.
- [153] Wu M, Kempaiah R, Huang PJJ, Maheshwari V, Liu J. Adsorption and desorption of DNA on graphene oxide studied by fluorescently labeled oligonucleotides. *Langmuir*. 2011;27(6):2731-8.
- [154] Titov AV, Král P, Pearson R. Sandwiched Graphene–Membrane Superstructures. *ACS Nano*. 2010;4(1):229-34.
- [155] Donaldson K, Aitken R, Tran L, Stone V, Duffin R, Forrest G, et al. Carbon nanotubes: A review of their properties in relation to pulmonary toxicology and workplace safety. *Toxicological Sciences*. 2006;92(1):5-22.
- [156] Sanchez VC, Pietruska JR, Miselis NR, Hurt RH, Kane AB. Biopersistence and potential adverse health impacts of fibrous nanomaterials: What have we learned from asbestos? *Wiley Interdisciplinary Reviews: Nanomedicine and Nanobiotechnology*. 2009;1(5):511-29.
- [157] Liu X, Hurt RH, Kane AB. Biodurability of single-walled carbon nanotubes depends on surface functionalization. *Carbon*. 2010;48(7):1961-9.
- [158] Allen BL, Kichambare PD, Gou P, Vlasova II, Kapralov AA, Konduru N, et al. Biodegradation of single-walled carbon nanotubes through enzymatic catalysis. *Nano Letters*. 2008;8(11):3899-903.
- [159] Kagan VE, Konduru NV, Feng W, Allen BL, Conroy J, Volkov Y, et al. Carbon nanotubes degraded by neutrophil myeloperoxidase induce less pulmonary inflammation. *Nature Nanotechnology*. 2010;5(5):354-9.
- [160] Kotchey GP, Allen BL, Vedala H, Yanamala N, Kapralov AA, Tyurina YY, et al. The enzymatic oxidation of graphene oxide. *ACS Nano*. 2011;5(3):2098-108.

- [161] Duch MC, Budinger GRS, Liang YT, Soberanes S, Urich D, Chiarella SE, et al. Minimizing Oxidation and Stable Nanoscale Dispersion Improves the Biocompatibility of Graphene in the Lung. *Nano Letters*. 2011;11(12):5201-7.
- [162] Schinwald A, Murphy FA, Jones A, MacNee W, Donaldson K. Graphene-Based Nanoplatelets: A New Risk to the Respiratory System as a Consequence of Their Unusual Aerodynamic Properties. *ACS Nano*. 2011;6(1):736-46.
- [163] Zhang X, Yin J, Peng C, Hu W, Zhu Z, Li W, et al. Distribution and biocompatibility studies of graphene oxide in mice after intravenous administration. *Carbon*. 2011;49(3):986-95.
- [164] Yang K, Wan J, Zhang S, Zhang Y, Lee S-T, Liu Z. In Vivo Pharmacokinetics, Long-Term Biodistribution, and Toxicology of PEGylated Graphene in Mice. *ACS Nano*. 2010;5(1):516-22.
- [165] Zhang L, Wang Z, Xu C, Li Y, Gao J, Wang W, et al. High strength graphene oxide/polyvinyl alcohol composite hydrogels. *J Mater Chem*. 2011;21(28):10399-406.
- [166] Liang J, Huang Y, Zhang L, Wang Y, Ma Y, Guo T, et al. Molecular-Level Dispersion of Graphene into Poly(vinyl alcohol) and Effective Reinforcement of their Nanocomposites. *Adv Funct Mater*. 2009;19(14):2297-302.
- [167] Fan H, Wang L, Zhao K, Li N, Shi Z, Ge Z, et al. Fabrication, Mechanical Properties, and Biocompatibility of Graphene-Reinforced Chitosan Composites. *Biomacromolecules*. 2010;11(9):2345-51.
- [168] Kang S, Herzberg M, Rodrigues DF, Elimelech M. Antibacterial Effects of Carbon Nanotubes: Size Does Matter! *Langmuir*. 2008;24(13):6409-13.
- [169] Kang S, Pinault M, Pfefferle LD, Elimelech M. Single-Walled Carbon Nanotubes Exhibit Strong Antimicrobial Activity. *Langmuir*. 2007;23(17):8670-3.
- [170] Akhavan O, Ghaderi E. Toxicity of graphene and graphene oxide nanowalls against bacteria. *ACS Nano*. 2010;4(10):5731-6.
- [171] Akhavan O, Ghaderi E. *Escherichia coli* bacteria reduce graphene oxide to bactericidal graphene in a self-limiting manner. *Carbon*. 2012;50(5):1853-60.
- [172] Hu W, Peng C, Luo W, Lv M, Li X, Li D, et al. Graphene-Based Antibacterial Paper. *ACS Nano*. 2010;4(7):4317-23.
- [173] Wang G, Qian F, Saltikov C, Jiao Y, Li Y. Microbial reduction of graphene oxide by *Shewanella*. *Nano Res*. 2011;4(6):563-70.
- [174] Salas EC, Sun Z, Lüttge A, Tour JM. Reduction of Graphene Oxide via Bacterial Respiration. *ACS Nano*. 2010;4(8):4852-6.
- [175] Wang K, Ruan J, Song H, Zhang J, Wo Y, Guo S, et al. Biocompatibility of Graphene Oxide. *Nanoscale Research Letters*. 2011;6(1):1-8.
- [176] Akhavan O, Ghaderi E, Emamy H. Nontoxic concentrations of PEGylated graphene nanoribbons for selective cancer cell imaging and photothermal therapy. *J Mater Chem*. 2012;22(38):20626-33.
- [177] Akhavan O, Ghaderi E, Emamy H, Akhavan F. Genotoxicity of graphene nanoribbons in human mesenchymal stem cells. *Carbon*. 2013;54:419-31.
- [178] Zhang Y, Ali SF, Dervishi E, Xu Y, Li Z, Casciano D, et al. Cytotoxicity Effects of Graphene and Single-Wall Carbon Nanotubes in Neural Phaeochromocytoma-Derived PC12 Cells. *ACS Nano*. 2010;4(6):3181-6.
- [179] Chang Y, Yang S-T, Liu J-H, Dong E, Wang Y, Cao A, et al. In vitro toxicity evaluation of graphene oxide on A549 cells. *Toxicology Letters*. 2011;200(3):201-10.

- [180] Tang YJ, Ashcroft JM, Chen D, Min G, Kim C-H, Murkhejee B, et al. Charge-Associated Effects of Fullerene Derivatives on Microbial Structural Integrity and Central Metabolism. *Nano Letters*. 2007;7(3):754-60.
- [181] Szabó T, Berkesi O, Forgó P, Josepovits K, Sanakis Y, Petridis D, et al. Evolution of Surface Functional Groups in a Series of Progressively Oxidized Graphite Oxides. *Chemistry of Materials*. 2006;18(11):2740-9.
- [182] Liao K-H, Lin Y-S, Macosko CW, Haynes CL. Cytotoxicity of Graphene Oxide and Graphene in Human Erythrocytes and Skin Fibroblasts. *ACS Applied Materials & Interfaces*. 2011;3(7):2607-15.
- [183] Sasidharan A, Panchakarla LS, Chandran P, Menon D, Nair S, Rao CNR, et al. Differential nano-bio interactions and toxicity effects of pristine versus functionalized graphene. *Nanoscale*. 2011;3(6):2461-4.
- [184] Lv M, Zhang Y, Liang L, Wei M, Hu W, Li X, et al. Effect of graphene oxide on undifferentiated and retinoic acid-differentiated SH-SY5Y cells line. *Nanoscale*. 2012;4(13):3861-6.
- [185] Gurunathan S, Han JW, Park JH, Kim JH. An in vitro evaluation of graphene oxide reduced by *Ganoderma* spp. in human breast cancer cells (MDA-MB-231). *International journal of nanomedicine*. 2014;9(1):1783-97.
- [186] Liu Z, Robinson JT, Sun X, Dai H. PEGylated Nanographene Oxide for Delivery of Water-Insoluble Cancer Drugs. *Journal of the American Chemical Society*. 2008;130(33):10876-7.
- [187] Sun X, Liu Z, Welsher K, Robinson JT, Goodwin A, Zaric S, et al. Nano-Graphene Oxide for Cellular Imaging and Drug Delivery. *Nano Res*. 2008;1(3):203-12.
- [188] Akhavan O, Ghaderi E. Graphene Nanomesh Promises Extremely Efficient In Vivo Photothermal Therapy. *Small*. 2013;9(21):3593-601.
- [189] Zhou T, Zhang B, Wei P, Du Y, Zhou H, Yu M, et al. Energy metabolism analysis reveals the mechanism of inhibition of breast cancer cell metastasis by PEG-modified graphene oxide nanosheets. *Biomaterials*. 2014;35(37):9833-43.
- [190] Xu Z, Wang S, Li Y, Wang M, Shi P, Huang X. Covalent Functionalization of Graphene Oxide with Biocompatible Poly(ethylene glycol) for Delivery of Paclitaxel. *ACS Applied Materials & Interfaces*. 2014;6(19):17268-76.
- [191] Liu Y, Luo Y, Wu J, Wang Y, Yang X, Yang R, et al. Graphene oxide can induce in vitro and in vivo mutagenesis. *Sci Rep*. 2013;3.
- [192] Agarwal S, Zhou X, Ye F, He Q, Chen GCK, Soo J, et al. Interfacing Live Cells with Nanocarbon Substrates. *Langmuir*. 2010;26(4):2244-7.
- [193] Oh S, Brammer KS, Li YSJ, Teng D, Engler AJ, Chien S, et al. Stem cell fate dictated solely by altered nanotube dimension. *Proceedings of the National Academy of Sciences*. 2009;106(7):2130-5.
- [194] Bettinger CJ, Langer R, Borenstein JT. Engineering Substrate Topography at the Micro- and Nanoscale to Control Cell Function. *Angewandte Chemie International Edition*. 2009;48(30):5406-15.
- [195] Ruiz ON, Fernando KAS, Wang B, Brown NA, Luo PG, McNamara ND, et al. Graphene Oxide: A Nonspecific Enhancer of Cellular Growth. *ACS Nano*. 2011;5(10):8100-7.
- [196] Zhang L, Xia J, Zhao Q, Liu L, Zhang Z. Functional Graphene Oxide as a Nanocarrier for Controlled Loading and Targeted Delivery of Mixed Anticancer Drugs. *Small*. 2010;6(4):537-44.

- [197] Song E, Han W, Li C, Cheng D, Li L, Liu L, et al. Hyaluronic Acid-Decorated Graphene Oxide Nanohybrids as Nanocarriers for Targeted and pH-Responsive Anticancer Drug Delivery. *ACS Applied Materials & Interfaces*. 2014;6(15):11882-90.
- [198] Yang K, Zhang S, Zhang G, Sun X, Lee S-T, Liu Z. Graphene in Mice: Ultrahigh In Vivo Tumor Uptake and Efficient Photothermal Therapy. *Nano Letters*. 2010;10(9):3318-23.
- [199] Yang K, Wan J, Zhang S, Zhang Y, Lee S-T, Liu Z. In Vivo Pharmacokinetics, Long-Term Biodistribution, and Toxicology of PEGylated Graphene in Mice. *ACS Nano*. 2011;5(1):516-22.
- [200] Yang K, Gong H, Shi X, Wan J, Zhang Y, Liu Z. In vivo biodistribution and toxicology of functionalized nano-graphene oxide in mice after oral and intraperitoneal administration. *Biomaterials*. 2013;34(11):2787-95.
- [201] Zhang S, Yang K, Feng L, Liu Z. In vitro and in vivo behaviors of dextran functionalized graphene. *Carbon*. 2011;49(12):4040-9.
- [202] Ward MA, Georgiou TK. Thermoresponsive polymers for biomedical applications. *Polymers*. 2011;3(3):1215-42.
- [203] Morkhade D, Fulzele S, Satturwar P, Joshi S. Gum copal and gum damar: Novel matrix forming materials for sustained drug delivery. *Indian Journal of Pharmaceutical Sciences*. 2006;68(1):53-8.
- [204] Siegel R, Rathbone M. Overview of Controlled Release Mechanisms. In: Siepmann J, Siegel RA, Rathbone MJ, eds. *Fundamentals and Applications of Controlled Release Drug Delivery*: Springer US 2012, p. 19-43.
- [205] Sathish Ummadi, B. Shravani, N. G. Raghavendra Rao, M. Srikanth Reddy, B. Sanjeev, Nayak TR. Overview on Controlled Release Dosage Form. *International Journal of Pharma Sciences*. 2013;3(4):258-69.
- [206] Fu Y, Kao WJ. Drug Release Kinetics and Transport Mechanisms of Non-degradable and Degradable Polymeric Delivery Systems. *Expert Opin Drug Del*. 2010;7(4):429-44.
- [207] Sarika Pundir, Ashutosh Badola, Deepak Sharma. Sustained Release Matrix Technology and Recent Advance in Matrix Drug Delivery System: A Review. *International Journal of Drug Research and Technology*. 2013;3(1):12-20.
- [208] Lin C-C, Metters AT. Hydrogels in controlled release formulations: Network design and mathematical modeling. *Advanced Drug Delivery Reviews*. 2006;58(12-13):1379-408.
- [209] Ragab DM, Rohani S, Consta S. Controlled release of 5-fluorouracil and progesterone from magnetic nanoaggregates. *International journal of nanomedicine*. 2012;7:3167-89.
- [210] Siepmann J, Lecomte F, Bodmeier R. Diffusion-controlled drug delivery systems: calculation of the required composition to achieve desired release profiles. *Journal of Controlled Release*. 1999;60(2-3):379-89.
- [211] Peppas NA. *Hydrogels in Medicine and Pharmacy*. Boca Raton, Florida: CRC Press 1986, p. 180.
- [212] Cohen MH, Turnbull D. Molecular transport in liquids and glasses. *The Journal of Chemical Physics*. 1959;31(5):1164-9.
- [213] Mackie JS, Meares P. The Diffusion of Electrolytes in a Cation-Exchange Resin Membrane. I. Theoretical; 1955.

- [214] Zhang H, Hao R, Ren X, Yu L, Yang H, Yu H. PEG/lecithin-liquid-crystalline composite hydrogels for quasi-zero-order combined release of hydrophilic and lipophilic drugs. *RSC Advances*. 2013;3(45):22927-30.
- [215] Sinn Aw M, Kurian M, Losic D. Non-eroding drug-releasing implants with ordered nanoporous and nanotubular structures: concepts for controlling drug release. *Biomaterials Science*. 2014;2(1):10-34.
- [216] Siepmann J, Siepmann F. Modeling of diffusion controlled drug delivery. *Journal of Controlled Release*. 2012;161(2):351-62.
- [217] Peppas NA. Physiologically responsive hydrogels. *Journal of Bioactive and Compatible Polymers*. 1991;6(3):241-6.
- [218] Brannon-Peppas L, Peppas NA. Equilibrium swelling behavior of pH-sensitive hydrogels. *Chemical Engineering Science*. 1991;46(3):715-22.
- [219] Katchalsky A. Rapid swelling and deswelling of reversible gels of polymeric acids by ionization. *Experientia*. 1949;5(8):319-20.
- [220] Katchalsky A, Lifson S, Exsenberg H. Equation of swelling for polyelectrolyte gels. *Journal of Polymer Science*. 1951;7(5):571-4.
- [221] Tanaka T. Phase transitions in gels and a single polymer. *Polymer*. 1979;20(11):1404-12.
- [222] Skouri R, Schosseler F, Munch JP, Candau SJ. Swelling and elastic properties of polyelectrolyte gels. *Macromolecules*. 1995;28(1):197-210.
- [223] Huang Y, Zeng M, Ren J, Wang J, Fan L, Xu Q. Preparation and swelling properties of graphene oxide/poly(acrylic acid-co-acrylamide) super-absorbent hydrogel nanocomposites. *Colloids and Surfaces A: Physicochemical and Engineering Aspects*. 2012;401(0):97-106.
- [224] Tai Z, Yang J, Qi Y, Yan X, Xue Q. Synthesis of a graphene oxide-polyacrylic acid nanocomposite hydrogel and its swelling and electroresponsive properties. *RSC Advances*. 2013;3(31):12751-7.
- [225] Song X, Oksanen M, Sillanpää MA, Craighead HG, Parpia JM, Hakonen PJ. Stamp Transferred Suspended Graphene Mechanical Resonators for Radio Frequency Electrical Readout. *Nano Letters*. 2011;12(1):198-202.
- [226] Zaixing J, Dan X, Yue L, Jun L, Qiang L, Menglin C, et al. Facilitating the mechanical properties of a high-performance pH-sensitive membrane by cross-linking graphene oxide and polyacrylic acid. *Nanotechnology*. 2013;24(33):335704.
- [227] Tanaka T. Collapse of gels and the critical endpoint. *Physical Review Letters*. 1978;40(12):820-3.
- [228] Hirotsu S, Hirokawa Y, Tanaka T. Volume-phase transitions of ionized N-isopropylacrylamide gels. *The Journal of Chemical Physics*. 1987;87(2):1392-5.
- [229] Pang X, Cui S. Single-Chain Mechanics of Poly(N,N-diethylacrylamide) and Poly(N-isopropylacrylamide): Comparative Study Reveals the Effect of Hydrogen Bond Donors. *Langmuir*. 2013;29(39):12176-82.
- [230] Kuramoto N, Shishido Y, Nagai K. Thermosensitive and redox-active polymers: Preparation and properties of poly(N-ethylacrylamide-co-vinylferrocene) and poly(N,N-diethylacrylamide-co-vinylferrocene). *Journal of Polymer Science Part A: Polymer Chemistry*. 1997;35(10):1967-72.
- [231] Gonçalves da Silva AMPS, Lopes SIC, Brogueira P, Prazeres TJV, Beija M, Martinho JMG. Thermo-responsiveness of poly(-diethylacrylamide) polymers at the air-

- water interface: The effect of a hydrophobic block. *Journal of Colloid and Interface Science*. 2008;327(1):129-37.
- [232] Gan LH, Gan YY, Deen GR. Poly(N-acryloyl-N'-propylpiperazine): A New Stimuli-Responsive Polymer. *Macromolecules*. 2000;33(21):7893-7.
- [233] Roy I, Gupta MN. Smart Polymeric Materials: Emerging Biochemical Applications. *Chemistry & Biology*. 2003;10(12):1161-71.
- [234] Reyntjens W, Jonckheere L, Goethals E, Du Prez F. Thermosensitive polymer structures based on segmented copolymer networks. *Macromolecular Symposia*. 2001;164(1):293-300.
- [235] Van Durme K, Van Mele B, Bernaerts KV, Verdonck B, Prez FEDU. End-group modified poly(methyl vinyl ether): Characterization and LCST demixing behavior in water. *Journal of Polymer Science, Part B: Polymer Physics*. 2006;44(2):461-9.
- [236] Confortini O, Du Prez FE. Functionalized thermo-responsive polyvinyl ether by living cationic random copolymerization of methyl vinyl ether and 2-chloroethyl vinyl ether. *Macromolecular Chemistry and Physics*. 2007;208(17):1871-82.
- [237] Beltran S, Baker JP, Hooper HH, Blanch HW, Prausnitz JM. Swelling equilibria for weakly ionizable, temperature-sensitive hydrogels. *Macromolecules*. 1991;24(2):549-51.
- [238] Ma X, Li Y, Wang W, Ji Q, Xia Y. Temperature-sensitive poly(N-isopropylacrylamide)/graphene oxide nanocomposite hydrogels by in situ polymerization with improved swelling capability and mechanical behavior. *European Polymer Journal*. 2013;49(2):389-96.
- [239] Li Y, Rodrigues J, Tomas H. Injectable and biodegradable hydrogels: gelation, biodegradation and biomedical applications. *Chemical Society reviews*. 2012;41(6):2193-221.
- [240] Lashuel HA, LaBrenz SR, Woo L, Serpell LC, Kelly JW. Protofilaments, filaments, ribbons, and fibrils from peptidomimetic self-assembly: Implications for amyloid fibril formation and materials science. *Journal of the American Chemical Society*. 2000;122(22):5262-77.
- [241] Schneider A, Garlick JA, Egles C. Self-assembling peptide nanofiber scaffolds accelerate wound healing. *PLoS ONE*. 2008;3(1).
- [242] Hamada K, Hirose M, Yamashita T, Ohgushi H. Spatial distribution of mineralized bone matrix produced by marrow mesenchymal stem cells in self-assembling peptide hydrogel scaffold. *Journal of Biomedical Materials Research - Part A*. 2008;84(1):128-36.
- [243] Pollock JF, Healy KE. Mechanical and swelling characterization of poly(N-isopropyl acrylamide -co- methoxy poly(ethylene glycol) methacrylate) sol-gels. *Acta Biomaterialia*. 2010;6(4):1307-18.
- [244] Dreher MR, Raucher D, Balu N, Michael Colvin O, Ludeman SM, Chilkoti A. Evaluation of an elastin-like polypeptide-doxorubicin conjugate for cancer therapy. *Journal of Controlled Release*. 2003;91(1-2):31-43.
- [245] Bao H, Pan Y, Ping Y, Sahoo NG, Wu T, Li L, et al. Chitosan-functionalized graphene oxide as a nanocarrier for drug and gene delivery. *Small*. 2011;7(11):1569-78.
- [246] Wu S, Zhao X, Li Y, Du Q, Sun J, Wang Y, et al. Adsorption properties of doxorubicin hydrochloride onto graphene oxide: Equilibrium, kinetic and thermodynamic studies. *Materials*. 2013;6(5):2026-42.
- [247] Wu S, Zhao X, Cui Z, Zhao C, Wang Y, Du L, et al. Cytotoxicity of graphene oxide and graphene oxide loaded with doxorubicin on human multiple myeloma cells. *International journal of nanomedicine*. 2014;9(1):1413-21.

- [248] Yang X, Zhang X, Liu Z, Ma Y, Huang Y, Chen Y. High-Efficiency Loading and Controlled Release of Doxorubicin Hydrochloride on Graphene Oxide. *The Journal of Physical Chemistry C*. 2008;112(45):17554-8.
- [249] Shen H, Zhang L, Liu M, Zhang Z. Biomedical applications of graphene. *Theranostics*. 2012;2(3):283-94.
- [250] Pan YZ, Bao HQ, Sahoo NG, Wu TF, Li L. Water-Soluble Poly(N-isopropylacrylamide)-Graphene Sheets Synthesized via Click Chemistry for Drug Delivery. *Adv Funct Mater*. 2011;21(14):2754-63.
- [251] Saikia N, Deka RC. Ab initio study on the noncovalent adsorption of camptothecin anticancer drug onto graphene, defect modified graphene and graphene oxide. *Journal of Computer-Aided Molecular Design*. 2013;27(9):807-21.
- [252] Wu X, Du N, Li H, Zhang R, Hou W. Synthesis and characterization of camptothecin/graphene oxide/hydroxycalcite-like compounds nanohybrids. *Acta Chimica Sinica*. 2014;72(8):963-9.
- [253] Zhang YM, Cao Y, Yang Y, Chen JT, Liu Y. A small-sized graphene oxide supramolecular assembly for targeted delivery of camptothecin. *Chemical Communications*. 2014;50(86):13066-9.
- [254] Fan X, Jiao G, Gao L, Jin P, Li X. The preparation and drug delivery of a graphene-carbon nanotube-Fe₃O₄ nanoparticle hybrid. *Journal of Materials Chemistry B*. 2013;1(20):2658-64.
- [255] Fan X, Jiao G, Zhao W, Jin P, Li X. Magnetic Fe₃O₄-graphene composites as targeted drug nanocarriers for pH-activated release. *Nanoscale*. 2013;5(3):1143-52.
- [256] Zhao L, Li H, Shi Y, Wang G, Liu L, Su C, et al. Nanoparticles inhibit cancer cell invasion and enhance antitumor efficiency by targeted drug delivery via cell surface-related GRP78. *International journal of nanomedicine*. 2015;10:245-56.
- [257] Lei L, Liu X, Guo S, Tang M, Cheng L, Tian L. 5-Fluorouracil-loaded multilayered films for drug controlled releasing stent application: Drug release, microstructure, and ex vivo permeation behaviors. *Journal of Controlled Release*. 2010;146(1):45-53.
- [258] Rana VK, Choi MC, Kong JY, Kim GY, Kim MJ, Kim SH, et al. Synthesis and Drug-Delivery Behavior of Chitosan-Functionalized Graphene Oxide Hybrid Nanosheets. *Macromol Mater Eng*. 2011;296(2):131-40.
- [259] Huang T, Zhang L, Chen H, Gao C. A cross-linking graphene oxide-polyethyleneimine hybrid film containing ciprofloxacin: One-step preparation, controlled drug release and antibacterial performance. *Journal of Materials Chemistry B*. 2015;3(8):1605-11.
- [260] Vashist SK, Zheng D, Pastorin G, Al-Rubeaan K, Luong JHT, Sheu F-S. Delivery of drugs and biomolecules using carbon nanotubes. *Carbon*. 2011;49(13):4077-97.
- [261] Zhu Y, Stoller MD, Cai W, Velamakanni A, Piner RD, Chen D, et al. Exfoliation of graphite oxide in propylene carbonate and thermal reduction of the resulting graphene oxide platelets. *ACS Nano*. 2010;4(2):1227-33.
- [262] Lee SH, Dreyer DR, An J, Velamakanni A, Piner RD, Park S, et al. Polymer Brushes via Controlled, Surface-Initiated Atom Transfer Radical Polymerization (ATRP) from Graphene Oxide. *Macromolecular Rapid Communications*. 2010;31(3):281-8.
- [263] Zhang R, Hummelgård M, Lv G, Olin H. Real time monitoring of the drug release of rhodamine B on graphene oxide. *Carbon*. 2011;49(4):1126-32.
- [264] Mudavath SL, Talat M, Rai M, Srivastava ON, Sundar S. Characterization and evaluation of amine-modified graphene amphotericin B for the treatment of visceral

- leishmaniasis: in vivo and in vitro studies. *Drug Design, Development and Therapy*. 2014;8:1235-47.
- [265] Zhu Y, Murali S, Cai W, Li X, Suk JW, Potts JR, et al. Graphene and Graphene Oxide: Synthesis, Properties, and Applications. *Advanced Materials*. 2010;22(35):3906-24.
- [266] Peng F, Su Y, Wei X, Lu Y, Zhou Y, Zhong Y, et al. Silicon-Nanowire-Based Nanocarriers with Ultrahigh Drug-Loading Capacity for In Vitro and In Vivo Cancer Therapy. *Angewandte Chemie International Edition*. 2013;52(5):1457-61.
- [267] Wu J, Chen A, Qin M, Huang R, Zhang G, Xue B, et al. Hierarchical construction of a mechanically stable peptide-graphene oxide hybrid hydrogel for drug delivery and pulsatile triggered release in vivo. *Nanoscale*. 2015;7(5):1655-60.
- [268] Tao C-a, Wang J, Qin S, Lv Y, Long Y, Zhu H, et al. Fabrication of pH-sensitive graphene oxide-drug supramolecular hydrogels as controlled release systems. *J Mater Chem*. 2012;22(47):24856-61.
- [269] Tao Y, Xie XY, Lv W, Tang DM, Kong DB, Huang ZH, et al. Towards ultrahigh volumetric capacitance: graphene derived highly dense but porous carbons for supercapacitors. *Scientific Reports*. 2013;3.
- [270] Huang Z-D, Zhang B, Liang R, Zheng Q-B, Oh SW, Lin X-Y, et al. Effects of reduction process and carbon nanotube content on the supercapacitive performance of flexible graphene oxide papers. *Carbon*. 2012;50(11):4239-51.
- [271] Tang YP, Paul DR, Chung TS. Free-standing graphene oxide thin films assembled by a pressurized ultrafiltration method for dehydration of ethanol. *Journal of Membrane Science*. 2014;458(0):199-208.
- [272] Scholz W, Boehm HP. Untersuchungen am Graphitoxid. VI. Betrachtungen zur Struktur des Graphitoxids. *Zeitschrift für anorganische und allgemeine Chemie*. 1969;369(3-6):327-40.
- [273] Nakajima T, Mabuchi A, Hagiwara R. A new structure model of graphite oxide. *Carbon*. 1988;26(3):357-61.
- [274] Carr KE. Electron microscope study of the formation of graphite oxide. *Carbon*. 1970;8(2):245-7.
- [275] Kyotani T, Suzuki K-y, Yamashita H, Tomita A. Formation of Carbon-Metal Composites from Metal Ion Exchanged Graphite Oxide. *TANSO*. 1993;1993(160):255-65.
- [276] Park S, An J, Jung I, Piner RD, An SJ, Li X, et al. Colloidal Suspensions of Highly Reduced Graphene Oxide in a Wide Variety of Organic Solvents. *Nano Letters*. 2009;9(4):1593-7.
- [277] Du J, Yue RR, Ren FF, Yao ZQ, Jiang FX, Yang P, et al. Simultaneous determination of uric acid and dopamine using a carbon fiber electrode modified by layer-by-layer assembly of graphene and gold nanoparticles. *Gold Bull*. 2013;46(3):137-44.
- [278] Yamaguchi H, Eda G, Mattevi C, Kim H, Chhowalla M. Highly Uniform 300 mm Wafer-Scale Deposition of Single and Multilayered Chemically Derived Graphene Thin Films. *Acs Nano*. 2010;4(1):524-8.
- [279] Mo Y, Wan Y, Chau A, Huang F. Graphene/Ionic Liquid Composite Films and Ion Exchange. *Sci Rep*. 2014;4.
- [280] Zhu Y, Cai W, Piner RD, Velamakanni A, Ruoff RS. Transparent self-assembled films of reduced graphene oxide platelets. *Appl Phys Lett*. 2009;95(10):-.
- [281] Wang X, Zhi L, Müllen K. Transparent, Conductive Graphene Electrodes for Dye-Sensitized Solar Cells. *Nano Lett*. 2007;8(1):323-7.

- [282] Cote LJ, Kim F, Huang J. Langmuir-blodgett assembly of graphite oxide single layers. *Journal of the American Chemical Society*. 2009;131(3):1043-9.
- [283] Brownson DAC, Varey SA, Hussain F, Haigh SJ, Banks CE. Electrochemical properties of CVD grown pristine graphene: monolayer- vs. quasi-graphene. *Nanoscale*. 2014;6(3):1607-21.
- [284] Huang YS, Wu DQ, Han S, Li S, Xiao L, Zhang F, et al. Assembly of Tin Oxide/Graphene Nanosheets into 3D Hierarchical Frameworks for High-Performance Lithium Storage. *Chemsuschem*. 2013;6(8):1510-5.
- [285] Yu D, Goh K, Wang H, Wei L, Jiang W, Zhang Q, et al. Scalable synthesis of hierarchically structured carbon nanotube-graphene fibres for capacitive energy storage. *Nat Nano*. 2014;9(7):555-62.
- [286] Lee DW, Hong TK, Kang D, Lee J, Heo M, Kim JY, et al. Highly controllable transparent and conducting thin films using layer-by-layer assembly of oppositely charged reduced graphene oxides. *J Mater Chem*. 2011;21(10):3438-42.
- [287] Krishnan D, Kim F, Luo J, Cruz-Silva R, Cote LJ, Jang HD, et al. Energetic graphene oxide: Challenges and opportunities. *Nano Today*. 2012;7(2):137-52.
- [288] Qiu Y, Guo F, Hurt R, Külaots I. Explosive thermal reduction of graphene oxide-based materials: Mechanism and safety implications. *Carbon*. 2014;72:215-23.
- [289] Shao JJ, Lv W, Yang QH. Self-Assembly of Graphene Oxide at Interfaces. *Adv Mater*. 2014;26(32):5586-612.
- [290] Mativetsky JM, Liscio A, Treossi E, Orgiu E, Zanelli A, Samorì P, et al. Graphene Transistors via in Situ Voltage-Induced Reduction of Graphene-Oxide under Ambient Conditions. *J Am Chem Soc*. 2011;133(36):14320-6.
- [291] Park S, Dikin DA, Nguyen ST, Ruoff RS. Graphene Oxide Sheets Chemically Cross-Linked by Polyallylamine. *The Journal of Physical Chemistry C*. 2009;113(36):15801-4.
- [292] Wang T, Wang L, Wu D, Xia W, Zhao H, Jia D. Hydrothermal synthesis of nitrogen-doped graphene hydrogels using amino acids with different acidities as doping agents. *J Mater Chem A*. 2014;2(22):8352-61.
- [293] Wimalasiri Y, Zou L. Carbon nanotube/graphene composite for enhanced capacitive deionization performance. *Carbon*. 2013;59(0):464-71.
- [294] Wang Y, Wu YP, Huang Y, Zhang F, Yang X, Ma YF, et al. Preventing Graphene Sheets from Restacking for High-Capacitance Performance. *Journal of Physical Chemistry C*. 2011;115(46):23192-7.
- [295] Cheng Q, Tang J, Ma J, Zhang H, Shinya N, Qin LC. Graphene and carbon nanotube composite electrodes for supercapacitors with ultra-high energy density. *Physical Chemistry Chemical Physics*. 2011;13(39):17615-24.
- [296] Tristán-López F, Morelos-Gómez A, Vega-Díaz SM, García-Betancourt ML, Perea-López N, Elías AL, et al. Large Area Films of Alternating Graphene-Carbon Nanotube Layers Processed in Water. *Acs Nano*. 2013;7(12):10788-98.
- [297] Jiang L, Sheng L, Long C, Fan Z. Densely packed graphene nanomesh-carbon nanotube hybrid film for ultra-high volumetric performance supercapacitors. *Nano Energy*. 2015;11(0):471-80.
- [298] Du F, Yu D, Dai L, Ganguli S, Varshney V, Roy AK. Preparation of Tunable 3D Pillared Carbon Nanotube-Graphene Networks for High-Performance Capacitance. *Chem Mater*. 2011;23(21):4810-6.

- [299] Kim YS, Kumar K, Fisher FT, Yang EH. Out-of-plane growth of CNTs on graphene for supercapacitor applications. *Nanotechnology*. 2012;23(1).
- [300] Wu Q, Xu Y, Yao Z, Liu A, Shi G. Supercapacitors Based on Flexible Graphene/Polyaniline Nanofiber Composite Films. *ACS Nano*. 2010;4(4):1963-70.
- [301] Zhang LL, Zhao S, Tian XN, Zhao XS. Layered Graphene Oxide Nanostructures with Sandwiched Conducting Polymers as Supercapacitor Electrodes. *Langmuir*. 2010;26(22):17624-8.
- [302] Seo S, Min M, Lee SM, Lee H. Photo-switchable molecular monolayer anchored between highly transparent and flexible graphene electrodes. *Nat Commun*. 2013;4:1920.
- [303] Cui XD, Primak A, Zarate X, Tomfohr J, Sankey OF, Moore AL, et al. Reproducible Measurement of Single-Molecule Conductivity. *Science*. 2001;294(5542):571-4.
- [304] Engelkes VB, Beebe JM, Frisbie CD. Length-Dependent Transport in Molecular Junctions Based on SAMs of Alkanethiols and Alkanedithiols: Effect of Metal Work Function and Applied Bias on Tunneling Efficiency and Contact Resistance. *J Am Chem Soc*. 2004;126(43):14287-96.
- [305] Salomon A, Cahen D, Lindsay S, Tomfohr J, Engelkes VB, Frisbie CD. Comparison of Electronic Transport Measurements on Organic Molecules. *Adv Mater*. 2003;15(22):1881-90.
- [306] Chow PK, Eksik O, Koratkar N. Mechanical Property Enhancement of Layered Reduced Graphene Oxide Papers by Non-Covalent Modification with Terephthalic Acid. *Part Part Syst Char*. 2014;31(3):337-41.
- [307] Sk MM, Yue CY. Layer-by-layer (LBL) assembly of graphene with p-phenylenediamine (PPD) spacer for high performance supercapacitor applications. *Rsc Adv*. 2014;4(38):19908-15.
- [308] Lastoskie CM, Quirke N, Gubbins KE. Structure of porous adsorbents: Analysis using density functional theory and molecular simulation. *Studies in Surface Science and Catalysis 1997*, p. 745-75.
- [309] Han S-T, Zhou Y, Wang C, He L, Zhang W, Roy VAL. Layer-by-Layer-Assembled Reduced Graphene Oxide/Gold Nanoparticle Hybrid Double-Floating-Gate Structure for Low-Voltage Flexible Flash Memory. *Adv Mater*. 2013;25(6):872-7.
- [310] Zhang H, Hines D, Akins DL. Synthesis of a nanocomposite composed of reduced graphene oxide and gold nanoparticles. *Dalton Transactions*. 2014;43(6):2670-5.
- [311] Movahed SK, Fakharian M, Dabiri M, Bazgir A. Gold nanoparticle decorated reduced graphene oxide sheets with high catalytic activity for Ullmann homocoupling. *Rsc Adv*. 2014;4(10):5243-7.
- [312] Zhao A, Masa J, Schuhmann W, Xia W. Activation and Stabilization of Nitrogen-Doped Carbon Nanotubes as Electrocatalysts in the Oxygen Reduction Reaction at Strongly Alkaline Conditions. *The Journal of Physical Chemistry C*. 2013;117(46):24283-91.
- [313] Gong K, Du F, Xia Z, Durstock M, Dai L. Nitrogen-Doped Carbon Nanotube Arrays with High Electrocatalytic Activity for Oxygen Reduction. *Science*. 2009;323(5915):760-4.
- [314] Lv R, Li Q, Botello-Méndez AR, Hayashi T, Wang B, Berkdemir A, et al. Nitrogen-doped graphene: beyond single substitution and enhanced molecular sensing. *Sci Rep*. 2012;2.

- [315] Chen P, Xiao T-Y, Qian Y-H, Li S-S, Yu S-H. A Nitrogen-Doped Graphene/Carbon Nanotube Nanocomposite with Synergistically Enhanced Electrochemical Activity. *Adv Mater.* 2013;25(23):3192-6.
- [316] Lee WJ, Maiti UN, Lee JM, Lim J, Han TH, Kim SO. Nitrogen-doped carbon nanotubes and graphene composite structures for energy and catalytic applications. *Chem Commun.* 2014;50(52):6818-30.
- [317] Du N, Liu XY, Narayanan J, Li L, Lim MLM, Li D. Design of Superior Spider Silk: From Nanostructure to Mechanical Properties. *Biophysical Journal.* 2006;91(12):4528-35.
- [318] Lu CH, Li J, Zhang XL, Zheng AX, Yang HH, Chen X, et al. General approach for monitoring peptide-protein interactions based on graphene-peptide complex. *Analytical chemistry.* 2011;83(19):7276-82.
- [319] Zhang M, Yin B-C, Wang X-F, Ye B-C. Interaction of peptides with graphene oxide and its application for real-time monitoring of protease activity. *Chemical Communications.* 2011;47(8):2399-401.
- [320] Katoch J, Kim SN, Kuang Z, Farmer BL, Naik RR, Tatulian SA, et al. Structure of a Peptide Adsorbed on Graphene and Graphite. *Nano Letters.* 2012;12(5):2342-6.
- [321] Kim SN, Kuang Z, Slocik JM, Jones SE, Cui Y, Farmer BL, et al. Preferential Binding of Peptides to Graphene Edges and Planes. *Journal of the American Chemical Society.* 2011;133(37):14480-3.
- [322] Radic S, Geitner NK, Podila R, Käkinen A, Chen P, Ke PC, et al. Competitive Binding of Natural Amphiphiles with Graphene Derivatives. *Sci Rep.* 2013;3.
- [323] Li C, Adamcik J, Mezzenga R. Biodegradable nanocomposites of amyloid fibrils and graphene with shape-memory and enzyme-sensing properties. *Nat Nano.* 2012;7(7):421-7.
- [324] Schamberger PC, Gardella Jr JA. Surface chemical modifications of materials which influence animal cell adhesion—a review. *Colloids and Surfaces B: Biointerfaces.* 1994;2(1-3):209-23.
- [325] Willett RL, Baldwin KW, West KW, Pfeiffer LN. Differential adhesion of amino acids to inorganic surfaces. *Proceedings of the National Academy of Sciences.* 2005;102(22):7817-22.
- [326] Chinn JA, Sauter JA, Phillips RE, Kao WJ, Anderson JM, Hanson SR, et al. Blood and tissue compatibility of modified polyester: Thrombosis, inflammation, and healing. *Journal of Biomedical Materials Research.* 1998;39(1):130-40.
- [327] Lahann J, Klee D, Pluester W, Hoecker H. Bioactive immobilization of r-hirudin on CVD-coated metallic implant devices. *Biomaterials.* 2001;22(8):817-26.
- [328] Sheng Y, Wang W, Chen P. Adsorption of an Ionic Complementary Peptide on the Hydrophobic Graphite Surface. *The Journal of Physical Chemistry C.* 2010;114(1):454-9.
- [329] Paul W, Sharma CP. Blood compatibility and biomedical applications of graphene. *Trends in Biomaterials and Artificial Organs.* 2011;25(3):91-4.
- [330] Goede K, Busch P, Grundmann M. Binding Specificity of a Peptide on Semiconductor Surfaces. *Nano Letters.* 2004;4(11):2115-20.
- [331] Lavieu G, Orci L, Shi L, Geiling M, Ravazzola M, Wieland F, et al. Induction of cortical endoplasmic reticulum by dimerization of a coatomer-binding peptide anchored to endoplasmic reticulum membranes. *Proceedings of the National Academy of Sciences.* 2010;107(15):6876-81.

- [332] Witus LS, Rocha JDR, Yuwono VM, Paramonov SE, Weisman RB, Hartgerink JD. Peptides that non-covalently functionalize single-walled carbon nanotubes to give controlled solubility characteristics. *J Mater Chem*. 2007;17(19):1909-15.
- [333] Su Z, Leung T, Honek JF. Conformational selectivity of peptides for single-walled carbon nanotubes. *Journal of Physical Chemistry B*. 2006;110(47):23623-7.
- [334] Cui Y, Kim SN, Jones SE, Wissler LL, Naik RR, McAlpine MC. Chemical Functionalization of Graphene Enabled by Phage Displayed Peptides. *Nano Letters*. 2010;10(11):4559-65.
- [335] Peter EK, Agarwal M, Kim B, Pivkin IV, Shea J-E. How water layers on graphene affect folding and adsorption of TrpZip2. *The Journal of Chemical Physics*. 2014;141(22):22D511.
- [336] Perry G, Coffinier Y, Boukherroub R, Thomy V. Investigation of the anti-biofouling properties of graphene oxide aqueous solutions by electrowetting characterization. *Journal of Materials Chemistry A*. 2013;1(39):12355-60.
- [337] Hnilova M, Oren EE, Seker UOS, Wilson BR, Collino S, Evans JS, et al. Effect of Molecular Conformations on the Adsorption Behavior of Gold-Binding Peptides. *Langmuir*. 2008;24(21):12440-5.
- [338] Walsh TR, Tomasio SM. Investigation of the influence of surface defects on peptide adsorption onto carbon nanotubes. *Molecular BioSystems*. 2010;6(9):1707-18.
- [339] He S, Song B, Li D, Zhu C, Qi W, Wen Y, et al. A Graphene Nanoprobe for Rapid, Sensitive, and Multicolor Fluorescent DNA Analysis. *Adv Funct Mater*. 2010;20(3):453-9.
- [340] Lu CH, Yang HH, Zhu CL, Chen X, Chen GN. A graphene platform for sensing biomolecules. *Angewandte Chemie - International Edition*. 2009;48(26):4785-7.
- [341] Baweja L, Balamurugan K, Subramanian V, Dhawan A. Hydration Patterns of Graphene-Based Nanomaterials (GBNMs) Play a Major Role in the Stability of a Helical Protein: A Molecular Dynamics Simulation Study. *Langmuir*. 2013;29(46):14230-8.
- [342] Alava T, Mann JA, Théodore C, Benitez JJ, Dichtel WR, Parpia JM, et al. Control of the Graphene-Protein Interface Is Required To Preserve Adsorbed Protein Function. *Analytical Chemistry*. 2013;85(5):2754-9.
- [343] Hu Y, Li F, Han D, Niu L. Graphene for Amino Acid, Peptide, Protein, and Enzyme Detection. *Biocompatible Graphene for Bioanalytical Applications*: Springer Berlin Heidelberg 2015, p. 35-55.
- [344] Sarikaya M, Tamerler C, Jen AKY, Schulten K, Baneyx F. Molecular biomimetics: Nanotechnology through biology. *Nature Materials*. 2003;2(9):577-85.
- [345] Tamerler C, Sarikaya M. Molecular biomimetics: nanotechnology and bionanotechnology using genetically engineered peptides. *Philosophical Transactions of the Royal Society A: Mathematical, Physical and Engineering Sciences*. 2009;367(1894):1705-26.
- [346] Tamerler C, Sarikaya M. Molecular biomimetics: Genetic synthesis, assembly, and formation of materials using peptides. *MRS Bulletin*. 2008;33(5):504-10.
- [347] Shen J-W, Wu T, Wang Q, Kang Y. Induced stepwise conformational change of human serum albumin on carbon nanotube surfaces. *Biomaterials*. 2008;29(28):3847-55.
- [348] Adhikari B, Banerjee A. Short peptide based hydrogels: Incorporation of graphene into the hydrogel. *Soft Matter*. 2011;7(19):9259-66.
- [349] So CR, Hayamizu Y, Yazici H, Gresswell C, Khatayevich D, Tamerler C, et al. Controlling Self-Assembly of Engineered Peptides on Graphite by Rational Mutation. *ACS Nano*. 2012;6(2):1648-56.

- [350] Tomásio SM, Walsh TR. Modeling the binding affinity of peptides for graphitic surfaces. influences of aromatic content and interfacial shape. *J Phys Chem C*. 2009;113(20):8778-85.
- [351] Hughes ZE, Tomasio SM, Walsh TR. Efficient simulations of the aqueous bio-interface of graphitic nanostructures with a polarisable model. *Nanoscale*. 2014;6(10):5438-48.
- [352] Guo J, Yao X, Ning L, Wang Q, Liu H. The adsorption mechanism and induced conformational changes of three typical proteins with different secondary structural features on graphene. *RSC Advances*. 2014;4(20):9953-62.
- [353] Akca S, Foroughi A, Frochtzawaj D, Postma HWC. Competing interactions in dna assembly on graphene. *PLoS ONE*. 2011;6(4).
- [354] Manna AK, Pati SK. Theoretical understanding of single-stranded DNA assisted dispersion of graphene. *Journal of Materials Chemistry B*. 2013;1(1):91-100.
- [355] Yang H, Fung S-Y, Pritzker M, Chen P. Surface-Assisted Assembly of an Ionic-Complementary Peptide: Controllable Growth of Nanofibers. *Journal of the American Chemical Society*. 2007;129(40):12200-10.
- [356] Yang H, Fung SY, Pritzker M, Chen P. Modification of hydrophilic and hydrophobic surfaced using an ionic-complementary peptide. *PLoS ONE*. 2007;2(12).
- [357] Pandey RB, Kuang Z, Farmer BL, Kim SS, Naik RR. Stability of peptide (P1 and P2) binding to a graphene sheet via an all-atom to all-residue coarse-grained approach. *Soft Matter*. 2012;8(35):9101-9.
- [358] Sun X, Feng Z, Hou T, Li Y. Mechanism of Graphene Oxide as an Enzyme Inhibitor from Molecular Dynamics Simulations. *ACS Applied Materials & Interfaces*. 2014;6(10):7153-63.
- [359] Yu X, Wang Q, Lin Y, Zhao J, Zhao C, Zheng J. Structure, Orientation, and Surface Interaction of Alzheimer Amyloid- β Peptides on the Graphite. *Langmuir*. 2012;28(16):6595-605.
- [360] Zuo G, Zhou X, Huang Q, Fang H, Zhou R. Adsorption of villin headpiece onto graphene, carbon nanotube, and C60: Effect of contacting surface curvatures on binding affinity. *J Phys Chem C*. 2011;115(47):23323-8.
- [361] Cicero G, Grossman JC, Schwegler E, Gygi F, Galli G. Water Confined in Nanotubes and between Graphene Sheets: A First Principle Study. *Journal of the American Chemical Society*. 2008;130(6):1871-8.
- [362] Park JH, Aluru NR. Ordering-Induced Fast Diffusion of Nanoscale Water Film on Graphene. *The Journal of Physical Chemistry C*. 2010;114(6):2595-9.
- [363] Mijajlovic M, Penna MJ, Biggs MJ. Free Energy of Adsorption for a Peptide at a Liquid/Solid Interface via Nonequilibrium Molecular Dynamics. *Langmuir*. 2013;29(9):2919-26.
- [364] Latour RA. Molecular Simulation of Protein-Surface Interactions Biological Interactions on Materials Surfaces. In: Puleo DA, Bizios R, eds.: Springer US 2009, p. 69-95.
- [365] Leach AR. *Molecular Modelling. Principles and Applications*. Harlow, UK: Pearson Education; 1996.
- [366] Humphrey W, Dalke A, Schulten K. VMD: Visual molecular dynamics. *Journal of Molecular Graphics*. 1996;14(1):33-8.

- [367] Zoete V, Cuendet MA, Grosdidier A, Michielin O. SwissParam: A fast force field generation tool for small organic molecules. *Journal of Computational Chemistry*. 2011;32(11):2359-68.
- [368] MacKerell AD, Bashford D, Bellott, Dunbrack RL, Evanseck JD, Field MJ, et al. All-Atom Empirical Potential for Molecular Modeling and Dynamics Studies of Proteins†. *The Journal of Physical Chemistry B*. 1998;102(18):3586-616.
- [369] Phillips JC, Braun R, Wang W, Gumbart J, Tajkhorshid E, Villa E, et al. Scalable molecular dynamics with NAMD. *Journal of Computational Chemistry*. 2005;26(16):1781-802.
- [370] Merrifield RB. Solid Phase Peptide Synthesis. I. The Synthesis of a Tetrapeptide. *Journal of the American Chemical Society*. 1963;85(14):2149-54.
- [371] Fields GB, Noble RL. Solid phase peptide synthesis utilizing 9-fluorenylmethoxycarbonyl amino acids. *International Journal of Peptide and Protein Research*. 1990;35(3):161-214.
- [372] Zhang S, Lockshin C, Cook R, Rich A. Unusually stable β -sheet formation in an ionic self-complementary oligopeptide. *Biopolymers*. 1994;34(5):663-72.
- [373] Zhang S, Holmes T, Lockshin C, Rich A. Spontaneous assembly of a self-complementary oligopeptide to form a stable macroscopic membrane. *Proceedings of the National Academy of Sciences*. 1993;90(8):3334-8.
- [374] Georgakilas V, Otyepka M, Bourlinos AB, Chandra V, Kim N, Kemp KC, et al. Functionalization of Graphene: Covalent and Non-Covalent Approaches, Derivatives and Applications. *Chemical Reviews*. 2012;112(11):6156-214.
- [375] Biggs MJ, Kiamahalleh MV, Mijajlovic M, Penna MJ, inventors; Compositions comprising self assembled carbon based structures and related methods. 2014.
- [376] Biggs MJ, Penna MJ, Kiamahalleh MV, Mijajlovic M, inventors; Self-assembled carbon based structures and related methods. 2015.
- [377] Kopeček J, Yang J. Peptide-directed self-assembly of hydrogels. *Acta Biomaterialia*. 2009;5(3):805-16.
- [378] Stanley CB, Strey HH. Osmotically Induced Helix-Coil Transition in Poly(Glutamic Acid). *Biophysical Journal*. 2008;94(11):4427-34.
- [379] M. Mijajlovic, M.J. Penna, Biggs MJ. Free energy of adsorption of proteins at fluid/solid interfaces using molecular simulation. the Proceedings of Chemeca 2011: The 41st Australasian Chemical Engineering Conference.
- [380] Jorgensen WL, Chandrasekhar J, Madura JD, Impey RW, Klein ML. Comparison of simple potential functions for simulating liquid water. *The Journal of Chemical Physics*. 1983;79(2):926-35.
- [381] Ma L, Cui Q. The Temperature Dependence of Salt-Protein Association Is Sequence Specific†. *Biochemistry*. 2006;45(48):14466-72.
- [382] Penna MJ, Mijajlovic M, Tamerler C, Biggs MJ. Molecular-level understanding of the adsorption mechanism of a graphite-binding peptide at the water/graphite interface. *Soft Matter*. 2015.
- [383] Ou L, Luo Y, Wei G. Atomic-level study of adsorption, conformational change, and dimerization of an α -helical peptide at graphene surface. *Journal of Physical Chemistry B*. 2011;115(32):9813-22.
- [384] Liang LJ, Wang Q, Wu T, Shen JW, Kang Y. Molecular dynamics simulation on stability of insulin on graphene. *Chinese Journal of Chemical Physics*. 2009;22(6):627-34.

- [385] Chiu C-c, Dieckmann GR, Nielsen SO. Molecular Dynamics Study of a Nanotube-Binding Amphiphilic Helical Peptide at Different Water/Hydrophobic Interfaces. *The Journal of Physical Chemistry B*. 2008;112(51):16326-33.
- [386] Guo Y, Han Y, Shuang S, Dong C. Rational synthesis of graphene-metal coordination polymer composite nanosheet as enhanced materials for electrochemical biosensing. *J Mater Chem*. 2012;22(26):13166-73.
- [387] Xiao J, Mei D, Li X, Xu W, Wang D, Graff GL, et al. Hierarchically Porous Graphene as a Lithium–Air Battery Electrode. *Nano Letters*. 2011;11(11):5071-8.
- [388] Wu Z-S, Sun Y, Tan Y-Z, Yang S, Feng X, Müllen K. Three-Dimensional Graphene-Based Macro- and Mesoporous Frameworks for High-Performance Electrochemical Capacitive Energy Storage. *Journal of the American Chemical Society*. 2012;134(48):19532-5.
- [389] Zhang L, Zhang F, Yang X, Long G, Wu Y, Zhang T, et al. Porous 3D graphene-based bulk materials with exceptional high surface area and excellent conductivity for supercapacitors. *Scientific Reports*. 2013;3.
- [390] Zhang DW, Li XD, Li HB, Chen S, Sun Z, Yin XJ, et al. Graphene-based counter electrode for dye-sensitized solar cells. *Carbon*. 2011;49(15):5382-8.
- [391] Worsley MA, Kucheyev SO, Mason HE, Merrill MD, Mayer BP, Lewicki J, et al. Mechanically robust 3D graphene macroassembly with high surface area. *Chemical Communications*. 2012;48(67):8428-30.
- [392] Yu D, Dai L. Self-Assembled Graphene/Carbon Nanotube Hybrid Films for Supercapacitors. *The Journal of Physical Chemistry Letters*. 2009;1(2):467-70.
- [393] Geim AK. Graphene: Status and prospects. *Science*. 2009;324(5934):1530-4.
- [394] Englert JM, Dotzer C, Yang G, Schmid M, Papp C, Gottfried JM, et al. Covalent bulk functionalization of graphene. *Nat Chem*. 2011;3(4):279-86.
- [395] Qiu L, Liu JZ, Chang SLY, Wu Y, Li D. Biomimetic superelastic graphene-based cellular monoliths. *Nature Communications*. 2012;3.
- [396] Sarker AK, Hong J-D. Layer-by-Layer Self-Assembled Multilayer Films Composed of Graphene/Polyaniline Bilayers: High-Energy Electrode Materials for Supercapacitors. *Langmuir*. 2012;28(34):12637-46.
- [397] Ye X, Qi L. Two-dimensionally patterned nanostructures based on monolayer colloidal crystals: Controllable fabrication, assembly, and applications. *Nano Today*. 2011;6(6):608-31.
- [398] Ward D Michael. Design of Self-Assembling Molecular Systems: Electrostatic Structural Enforcement in Low-Dimensional Molecular Solids. In: Crandall B, Lewis J, eds. *Nanotechnology Research Perspective*. Cambridge, Mass.: MIT Press 1992.
- [399] Wang DN, Yang JL, Li XF, Geng DS, Li RY, Cai M, et al. Layer by layer assembly of sandwiched graphene/SnO₂ nanorod/carbon nanostructures with ultrahigh lithium ion storage properties. *Energ Environ Sci*. 2013;6(10):2900-6.
- [400] Zhang K, Zhang LL, Zhao XS, Wu J. Graphene/Polyaniline Nanofiber Composites as Supercapacitor Electrodes. *Chemistry of Materials*. 2010;22(4):1392-401.
- [401] Tang L, Li X, Du D, He CJ. Fabrication of multilayer films from regenerated cellulose and graphene oxide through layer-by-layer assembly. *Prog Nat Sci-Mater*. 2012;22(4):341-6.
- [402] Yang X, Qiu L, Cheng C, Wu Y, Ma Z-F, Li D. Ordered Gelation of Chemically Converted Graphene for Next-Generation Electroconductive Hydrogel Films. *Angewandte Chemie International Edition*. 2011;50(32):7325-8.

- [403] Sing KSW, Everett DH, Haul RAW, Moscou L, Pierotti RA, Rouquerol J, et al. Reporting physisorption data for gas/solid systems with special reference to the determination of surface area and porosity. *Pure and Applied Chemistry*. 1985;57(4):603.
- [404] Rouquerol F, Rouquerol J, Sing K. *Adsorption by powders and porous solids* London: Academic Press; 1999.
- [405] Brunauer S, Emmett PH, Teller E. Adsorption of gases in multimolecular layers. *J Am Chem Soc*. 1938;60(2):309-19.
- [406] Sing KSW. Empirical method for analysis of adsorption isotherms. *Chemistry and Industry*. 1968;44.
- [407] Neimark AV, Lin Y, Ravikovitch PI, Thommes M. Quenched solid density functional theory and pore size analysis of micro-mesoporous carbons. *Carbon*. 2009;47(7):1617-28.
- [408] Kamio Y, Saito Y, Utoguchi N, Kondoh M, Koizumi N, Fujii M, et al. Epinephrine is an enhancer of rat intestinal absorption. *Journal of Controlled Release*. 2005;102(3):563-8.
- [409] Li S, Nguyen L, Xiong H, Wang M, Hu TCC, She J-X, et al. Porous-wall hollow glass microspheres as novel potential nanocarriers for biomedical applications. *Nanomedicine: Nanotechnology, Biology and Medicine*. 2010;6(1):127-36.
- [410] Sergei I. Sukharev, Alexander V. Titomirov, Klenchin VA. Electrically-Induced DNA Transfer into Cells. *Electrotransfection in Vivo*. In: Wolff JA, ed. *Gene Therapeutics: Methods and Applications of Direct Gene Transfer*: Birkhäuser Basel 1994.
- [411] Yuan W, Lv Y, Zeng M, Fu BM. Non-invasive measurement of solute permeability in cerebral microvessels of the rat. *Microvascular Research*. 2009;77(2):166-73.
- [412] Jorgensen WL, Chandrasekhar J, Madura JD, Impey RW, Klein ML. Comparison of simple potential functions for simulating liquid water. *The Journal of Chemical Physics*. 1983;79(2):926.
- [413] Alves CCO, Franca AS, Oliveira LS. Evaluation of an adsorbent based on agricultural waste (corn cobs) for removal of tyrosine and phenylalanine from aqueous solutions. *BioMed Research International*. 2013;2013.
- [414] Rajesh C, Majumder C, Mizuseki H, Kawazoe Y. A theoretical study on the interaction of aromatic amino acids with graphene and single walled carbon nanotube. *The Journal of Chemical Physics*. 2009;130(12):124911-6.
- [415] Wang X, Lu J, Xing B. Sorption of Organic Contaminants by Carbon Nanotubes: Influence of Adsorbed Organic Matter. *Environmental Science & Technology*. 2008;42(9):3207-12.
- [416] Xue L, Shen C, Zheng M, Lu H, Li N, Ji G, et al. Hydrothermal synthesis of graphene-ZnS quantum dot nanocomposites. *Materials Letters*. 2011;65(2):198-200.
- [417] Chen W, Yan L, Bangal PR. Chemical Reduction of Graphene Oxide to Graphene by Sulfur-Containing Compounds. *The Journal of Physical Chemistry C*. 2010;114(47):19885-90.
- [418] Park S, An J, Piner RD, Jung I, Yang D, Velamakanni A, et al. Aqueous Suspension and Characterization of Chemically Modified Graphene Sheets. *Chemistry of Materials*. 2008;20(21):6592-4.
- [419] González Z, Botas C, Álvarez P, Roldán S, Blanco C, Santamaría R, et al. Thermally reduced graphite oxide as positive electrode in Vanadium Redox Flow Batteries. *Carbon*. 2012;50(3):828-34.

- [420] Wang R, Wang Y, Xu C, Sun J, Gao L. Facile one-step hydrazine-assisted solvothermal synthesis of nitrogen-doped reduced graphene oxide: reduction effect and mechanisms. *RSC Advances*. 2013;3(4):1194-200.
- [421] Choi E-Y, Han TH, Hong J, Kim JE, Lee SH, Kim HW, et al. Noncovalent functionalization of graphene with end-functional polymers. *J Mater Chem*. 2010;20(10):1907-12.
- [422] Si H, Luo H, Xiong G, Yang Z, Raman SR, Guo R, et al. One-Step In Situ Biosynthesis of Graphene Oxide–Bacterial Cellulose Nanocomposite Hydrogels. *Macromolecular Rapid Communications*. 2014;35(19):1706-11.
- [423] Lv X, Weng J. Ternary Composite of Hemin, Gold Nanoparticles and Graphene for Highly Efficient Decomposition of Hydrogen Peroxide. *Sci Rep*. 2013;3.
- [424] Ahn HS, Jang J-W, Seol M, Kim JM, Yun D-J, Park C, et al. Self-assembled foam-like graphene networks formed through nucleate boiling. *Sci Rep*. 2013;3.
- [425] Tang Z, Zhang L, Zeng C, Lin T, Guo B. General route to graphene with liquid-like behavior by non-covalent modification. *Soft Matter*. 2012;8(35):9214-20.
- [426] Burrs SL, Vanegas DC, Bhargava M, Mechulan N, Hendershot P, Yamaguchi H, et al. A comparative study of graphene-hydrogel hybrid bionanocomposites for biosensing. *Analyst*. 2015;140(5):1466-76.
- [427] Liu L, Zhai J, Zhu C, Gao Y, Wang Y, Han Y, et al. One-pot synthesis of 3-dimensional reduced graphene oxide-based hydrogel as support for microbe immobilization and BOD biosensor preparation. *Biosensors and Bioelectronics*. 2015;63(0):483-9.
- [428] Depan D, Girase B, Shah JS, Misra RDK. Structure–process–property relationship of the polar graphene oxide-mediated cellular response and stimulated growth of osteoblasts on hybrid chitosan network structure nanocomposite scaffolds. *Acta Biomaterialia*. 2011;7(9):3432-45.
- [429] Paul A, Hasan A, Kindi HA, Gaharwar AK, Rao VTS, Nikkhah M, et al. Injectable Graphene Oxide/Hydrogel-Based Angiogenic Gene Delivery System for Vasculogenesis and Cardiac Repair. *ACS Nano*. 2014;8(8):8050-62.
- [430] Song F, Hu W, Xiao L, Cao Z, Li X, Zhang C, et al. Enzymatically cross-linked hyaluronic acid/graphene oxide nanocomposite hydrogel with pH-responsive release. *Journal of Biomaterials Science, Polymer Edition*. 2015.
- [431] Cheng QY, Han BH. Supramolecular hydrogel based on graphene oxides for controlled release system. *Journal of Nanoscience and Nanotechnology*. 2013;13(2):755-60.
- [432] Mottaghitalab F, Farokhi M, Zaminy A, Kokabi M, Soleimani M, Mirahmadi F, et al. A Biosynthetic Nerve Guide Conduit Based on Silk/SWNT/Fibronectin Nanocomposite for Peripheral Nerve Regeneration. *Plos One*. 2013;8(9).
- [433] Bian X, Song ZL, Qian Y, Gao W, Cheng ZQ, Chen L, et al. Fabrication of graphene-isolated-au-nanocrystal nanostructures for multimodal cell imaging and photothermal-enhanced chemotherapy. *Scientific Reports*. 2014;4.
- [434] Rigas F, Dritsa V, Marchant R, Papadopoulou K, Avramides EJ, Hatzianestis I. Biodegradation of lindane by *Pleurotus ostreatus* via central composite design. *Environment International*. 2005;31(2):191-6.
- [435] Montgomery DC. *Design and Analysis of Experiments*, 8th Edition: Wiley; 2012.

- [436] Chieng BW, Ibrahim NA, Yunus WMZW. Optimization of Tensile Strength of Poly(Lactic Acid)/Graphene Nanocomposites Using Response Surface Methodology. *Polymer - Plastics Technology and Engineering*. 2012;51(8):791-9.
- [437] Shafiee M, Ramazani SAA. Optimization of UHMWPE/Graphene Nanocomposite Processing using Ziegler-Natta Catalytic System via Response Surface Methodology. *Polymer - Plastics Technology and Engineering*. 2014;53(9):969-74.
- [438] Kishore D, Talat M, Srivastava ON, Kayastha AM. Immobilization of β -galactosidase onto functionalized graphene nano-sheets using response surface methodology and its analytical applications. *PLoS ONE*. 2012;7(7).
- [439] Moradi M, Zenouzi S, Ahmadi K, Aghakhani A. Graphene oxide-based solid phase extraction of vitamin B12 from pharmaceutical formulations and its determination by X-ray fluorescence. *X-Ray Spectrometry*. 2014;n/a-n/a.
- [440] Fernández-Merino MJ, Guardia L, Paredes JI, Villar-Rodil S, Solís-Fernández P, Martínez-Alonso A, et al. Vitamin C Is an Ideal Substitute for Hydrazine in the Reduction of Graphene Oxide Suspensions. *The Journal of Physical Chemistry C*. 2010;114(14):6426-32.
- [441] Peng-Gang R, Ding-Xiang Y, Xu J, Tao C, Zhong-Ming L. Temperature dependence of graphene oxide reduced by hydrazine hydrate. *Nanotechnology*. 2011;22(5):055705.
- [442] Pham V, Dang T, Cuong T, Hur S, Kong B-S, Kim E, et al. Synthesis of highly concentrated suspension of chemically converted graphene in organic solvents: Effect of temperature on the extent of reduction and dispersibility. *Korean J Chem Eng*. 2012;29(5):680-5.
- [443] Wildöer JWG, Venema LC, Rinzler AG, Smalley RE, Dekker C. Electronic structure of atomically resolved carbon nanotubes. *Nature*. 1998;391(6662):59-62.
- [444] Nel AE, Madler L, Velegol D, Xia T, Hoek EMV, Somasundaran P, et al. Understanding biophysicochemical interactions at the nano-bio interface. *Nat Mater*. 2009;8(7):543-57.
- [445] Irwin JJ, Sterling T, Mysinger MM, Bolstad ES, Coleman RG. ZINC: A Free Tool to Discover Chemistry for Biology. *Journal of Chemical Information and Modeling*. 2012;52(7):1757-68.
- [446] Joglekar A M, May A T. Product excellence through design of experiments. *Cereal Foods World*. 1987;32:857-68.
- [447] Bai H, Li C, Wang X, Shi G. On the Gelation of Graphene Oxide. *The Journal of Physical Chemistry C*. 2011;115(13):5545-51.
- [448] Konkena B, Vasudevan S. Understanding Aqueous Dispersibility of Graphene Oxide and Reduced Graphene Oxide through pKa Measurements. *The Journal of Physical Chemistry Letters*. 2012;3(7):867-72.
- [449] Lei W, Qin S, Liu D, Portehault D, Liu Z, Chen Y. Large scale boron carbon nitride nanosheets with enhanced lithium storage capabilities. *Chemical Communications*. 2013;49(4):352-4.
- [450] Ali MA, Srivastava S, Solanki PR, Reddy V, Agrawal VV, Kim C, et al. Highly Efficient Bienenzyme Functionalized Nanocomposite-Based Microfluidics Biosensor Platform for Biomedical Application. *Sci Rep*. 2013;3.
- [451] Preuss CM, Tischer T, Rodriguez-Emmenegger C, Zieger MM, Bruns M, Goldmann AS, et al. A bioinspired light induced avenue for the design of patterned functional interfaces. *Journal of Materials Chemistry B*. 2014;2(1):36-40.

- [452] Islam MS, Choi WS, Lee H-J, Lee YB, Jeon IC. Free-standing polymer nanoactuators, nanoshutters, and nanofilters. *J Mater Chem*. 2012;22(17):8215-20.
- [453] Stevens JS, Byard SJ, Seaton CC, Sadiq G, Davey RJ, Schroeder SLM. Proton transfer and hydrogen bonding in the organic solid state: a combined XRD/XPS/ssNMR study of 17 organic acid-base complexes. *Physical Chemistry Chemical Physics*. 2014;16(3):1150-60.
- [454] Aksu Z, Tatlı AI, Tunç Ö. A comparative adsorption/biosorption study of Acid Blue 161: Effect of temperature on equilibrium and kinetic parameters. *Chemical Engineering Journal*. 2008;142(1):23-39.
- [455] Abramian L, El-Rassy H. Adsorption kinetics and thermodynamics of azo-dye Orange II onto highly porous titania aerogel. *Chemical Engineering Journal*. 2009;150(2-3):403-10.
- [456] Ho YS, McKay G. Pseudo-second order model for sorption processes. *Process Biochemistry*. 1999;34(5):451-65.
- [457] W. J. Weber, J. C. Morriss. Kinetics of adsorption on carbon from solution. *Journal of the Sanitary Engineering Division*. 1963;89:31-60.
- [458] Kavitha T, Haider Abdi SI, Park S-Y. pH-Sensitive nanocargo based on smart polymer functionalized graphene oxide for site-specific drug delivery. *Physical Chemistry Chemical Physics*. 2013;15(14):5176-85.
- [459] Ren L, Liu T, Guo J, Guo S, Wang X, Wang W. A smart pH responsive graphene/polyacrylamide complex via noncovalent interaction. *Nanotechnology*. 2010;21(33).
- [460] Bezerra MA, Santelli RE, Oliveira EP, Villar LS, Escalera LA. Response surface methodology (RSM) as a tool for optimization in analytical chemistry. *Talanta*. 2008;76(5):965-77.
- [461] Gregory J. The matter in suspension. *Nature*. 1989; 338:182-.
- [462] Zeta Potential of Colloids in Water and Waste Water, American Society for Testing and Materials, ASTM Standard D 4187-82; 1985.
- [463] Xu C, Yuan RS, Wang X. Selective reduction of graphene oxide. *Xinxing Tan Cailiao/New Carbon Materials*. 2014;29(1):61-6.
- [464] Haubner K, Murawski J, Olk P, Eng LM, Ziegler C, Adolphi B, et al. The route to functional graphene oxide. *ChemPhysChem*. 2010;11(10):2131-9.
- [465] Xu C, Yuan R-s, Wang X. Selective reduction of graphene oxide. *Carbon*. 2014;71(0):345.
- [466] Visani G, Isidori A. Doxorubicin variants for hematological malignancies. *Nanomedicine*. 2011;6(2):303-6.
- [467] Bertheau P, Lehmann-Che J, Varna M, Dumay A, Poirot B, Porcher R, et al. p53 in breast cancer subtypes and new insights into response to chemotherapy. *The Breast*. 2013;22, Supplement 2(0):S27-S9.
- [468] Nygren P, Larsson R, Gruber A, Peterson C, Bergh J. Doxorubicin selected multidrug-resistant small cell lung cancer cell lines characterised by elevated cytoplasmic Ca²⁺ and resistance modulation by verapamil in absence of P-glycoprotein overexpression. *British Journal of Cancer*. 1991;64(6):1011-8.
- [469] Green AE, Rose PG. Pegylated liposomal doxorubicin in ovarian cancer. *International Journal of Nanomedicine*. 2006;1(3):229-39.
- [470] Choi JH, Lim HY, Nam DK, Kim HS, Cho DY, Yi JW, et al. Expression of thymidylate synthase in gastric cancer patients treated with 5-fluorouracil and doxorubicin-

- based adjuvant chemotherapy after curative resection. *British Journal of Cancer*. 2001;84(2):186-92.
- [471] Lessin L. Chemotherapy for Anaplastic Thyroid Cancer. In: Wartofsky L, Van Nostrand D, eds. *Thyroid Cancer*: Humana Press 2006, p. 643-6.
- [472] Antman KH. Chemotherapy of advanced sarcomas of bone and soft tissue. *Seminars in Oncology*. 1992;19(6 SUPPL. 12):13-22.
- [473] Negishi Y, Hamano N, Omata D, Fujisawa A, Manandhar M, Nomizu M, et al. Effects of doxorubicin-encapsulating AG73 peptide-modified liposomes on tumor selectivity and cytotoxicity. *Results in Pharma Sciences*. 2011;1(1):68-75.
- [474] Lin J, Shigdar S, Fang DZ, Xiang D, Wei MQ, Danks A, et al. Improved efficacy and reduced toxicity of doxorubicin encapsulated in sulfatide-containing nanoliposome in a glioma model. *PLoS ONE*. 2014;9(7).
- [475] Whitby RLD, Korobeinyk A, Gun'Ko VM, Busquets R, Cundy AB, László K, et al. PH-driven physicochemical conformational changes of single-layer graphene oxide. *Chemical Communications*. 2011;47(34):9645-7.
- [476] Lewinski N, Colvin V, Drezek R. Cytotoxicity of Nanoparticles. *Small*. 2008;4(1):26-49.
- [477] Gurunathan S, Han JW, Abdal Dayem A, Eppakayala V, Kim JH. Oxidative stress-mediated antibacterial activity of graphene oxide and reduced graphene oxide in *Pseudomonas aeruginosa*. *International Journal of Nanomedicine*. 2012;7:5901-14.
- [478] Elkhenany H, Amelse L, Lafont A, Bourdo S, Caldwell M, Neilsen N, et al. Graphene supports in vitro proliferation and osteogenic differentiation of goat adult mesenchymal stem cells: potential for bone tissue engineering. *Journal of Applied Toxicology*. 2015;35(4):367-74.
- [479] Lee WC, Lim CHYX, Shi H, Tang LAL, Wang Y, Lim CT, et al. Origin of Enhanced Stem Cell Growth and Differentiation on Graphene and Graphene Oxide. *ACS Nano*. 2011;5(9):7334-41.
- [480] Jin L, Zeng Z, Kuddannaya S, Yue D, Bao J, Wang Z, et al. Synergistic effects of a novel free-standing reduced graphene oxide film and surface coating fibronectin on morphology, adhesion and proliferation of mesenchymal stem cells. *Journal of Materials Chemistry B*. 2015.
- [481] Kalbacova M, Broz A, Kong J, Kalbac M. Graphene substrates promote adherence of human osteoblasts and mesenchymal stromal cells. *Carbon*. 2010;48(15):4323-9.
- [482] Dubey N, Bentini R, Islam I, Cao T, Castro Neto AH, Rosa V. Graphene: A Versatile Carbon-Based Material for Bone Tissue Engineering. *Stem Cells International*.
- [483] Gurunathan S, Woong Han J, Kim E, Kwon DN, Park JK, Kim JH. Enhanced green fluorescent protein-mediated synthesis of biocompatible graphene. *Journal of Nanobiotechnology*. 2014;12(1).
- [484] Gurunathan S, Han JW, Dayem AA, Eppakayala V, Park M-R, Kwon D-N, et al. Antibacterial activity of dithiothreitol reduced graphene oxide. *Journal of Industrial and Engineering Chemistry*. 2013;19(4):1280-8.
- [485] Talukdar Y, Rashkow JT, Lalwani G, Kanakia S, Sitharaman B. The effects of graphene nanostructures on mesenchymal stem cells. *Biomaterials*. 2014;35(18):4863-77.

Appendix A: Patent Specification (PCT/AU2015/000034)

SELF ASSEMBLED CARBON BASED STRUCTURES AND RELATED METHODS

FIELD OF THE INVENTION

The present invention relates generally to novel layered graphene and related structures and materials; methods for producing, through self-assembly, novel layered graphene and related structures or materials of controlled pore size.

BACKGROUND TO THE INVENTION

Graphene and related materials such as, for example, graphene oxide (GO), reduced graphene oxide (rGO) and chemically-doped graphene have attracted considerable attention due to their exceptional inherent properties that result from, amongst other things, their two dimensional character.¹ For example, the exceptional electrical properties of graphene¹ has made it a target of interest in the development of various electrical components such as batteries and sensors. As one of the strongest materials known, considerable research has also been directed towards use of graphene in composite materials.² In addition, graphene and related materials have been a target of interest in the biomedical field with suggestions that they may prove useful in the field of drug delivery and biosensors.

Due to the hydrophobic character of graphene and some related materials such as highly reduced GO sheets, they quickly 're-stack' (*i.e.* aggregate) when placed in aqueous solutions to form layered, near-graphitic structures with sub-nanometre inter-sheet spacing. Whilst such restacking may often be desirable for applications, the loss of the space between the sheets is a major barrier for many potential applications. Many potential applications of graphene and related materials require or would benefit from the individual sheets of graphene or related materials being assembled into a layered structure with inter-sheet spacing (*i.e.* pores) that is greater than that found in the simple aggregated form.

A number of alternative approaches to production of layered graphene and graphene-related materials with pores between the layers have been researched. The first main approach for producing such materials is through insertion of inorganic spacing elements such as carbon black,³ randomly⁴⁻¹⁰ and vertically aligned^{11,12} carbon nanotubes, mesoporous carbon nanoparticles,¹⁴ iron oxide nanorods,¹⁵ ruthenium dioxide nanoparticles,¹⁶ gold nanoparticles¹⁷⁻²¹ or tin oxide nanoparticles²² or nanorods,²³ either in the solution or vapour phase. A second approach is through insertion of polymers between the sheets, including those that react with the graphene-based material such as polyaniline,²⁴ polyallylamine,²⁵ and regenerated cellulose²⁶ and those that are polymerized between the sheets such as polypyrrole.²⁷ None of these approaches provide a high degree of control over the inter-layer spacing or its uniformity due to the challenges in precisely controlling the size of the spacing units.

A third approach is use of metal ions that not only push apart the individual graphene or graphene-related sheets, but also cross-link them laterally.²⁸ Whilst use of ions gives tighter control over the pore size, the range of pore sizes is very limited indeed and still of the order of 1 nm. The intercalated ions are also easily removed depending on the solution conditions.

A fourth approach is the insertion of molecular linkers between sheets of graphene-related materials *via* chemical reaction between the linker molecules and some of the oxygen and other functionalities on the graphene-related sheets. This has been realized in a number of ways including p-phenylenediamine (PPD),²⁹ Ni(II) aza-macrocyclic complexes,³⁰ benzenediboronic acid,³¹ and 3,3'-diaminobenzidine and related compounds.³² The pore sizes accessible here are small, however, due to the constraint on the size of the molecules involved. Where pores sizes much larger than the molecule are claimed, as in the case of PPD,²⁹ this reflects an unpredictable process over which one would anticipate major issues with control of pore size.

A fifth approach is through use of a monolayer of aryl azobenzene linkers with one end of the linker chemical bound to a graphene sheet and the other physically adsorbed to the

adjacent graphene sheet.³³ Although this approach gives finer control over the distance between two successive graphene sheets in this example, the size range is severely limited by the lack of rigidity in the molecules beyond the short scale.

The above review demonstrates that there are two major issues with the state of the art to date in the field. The first is the inability to control to a high degree the spacing between the individual layers of graphene or graphene-related material (*i.e.* pore size) for anything other than the smallest spacing where use of metal ions facilitate finer control, albeit only under certain controlled conditions. The degree of control over the pore size and its dispersion is poor for anything beyond 1 nm and well into the mesopore size range as defined by IUPAC. This lack of consistency and ability to vary the inter-sheet distance in a systematic way presents as an impediment to the use of graphene and graphene-based materials in a number of fields where it is important to control or dictate in a consistent and controlled way this inter-sheet distance (*i.e.* pore size).

Due to the use of designed peptides in the invention presented here, it is worthy of mention that some have also used biomolecules to form constructs composed of graphene and graphene-related materials. Xu *et al.*³⁴ used DNA to yield a three dimensional GO-based material. There is, however, no claim that the DNA act to separate the GO layers, and this is unlikely to be the case given the claimed material formation mechanism. Others³⁵ have used amino acids to achieve some form of spacing, but this was felt to be *via* electrostatic repulsion/attraction between the charged amino acids akin to the mechanism associated with metal ions. Finally, Wu *et al.*³⁶ have proposed the use of a peptide to self-assemble a GO hydrogel for drug delivery applications. Once again, however, there is no claim that the peptides create pores of a given size by sitting between the individual GO layers, with the peptide design being such as to induce the random assembly of the GO.

Many of the approaches mentioned above involve layer-by-layer manufacturing where the macroscopic material is built up by putting down on a substrate successive layers of graphene or graphene-related material and spacer in an alternating fashion. This process leads to only a small fraction of the graphene or graphene-related material being separated by the spacers, with the remainder being essentially multi-layer graphene or graphene-

related material or even more disordered than this. It also has the disadvantage that it is a cyclic process requiring significantly more than one cycle to be undertaken to achieve the final product. Only a small fraction of the prior art involves a self-assembly process in the manufacture and, even then, they do not lead to structures akin to those proposed here in any way, nor provide the degree of control over the pore size gained here.

It is an object of the present invention to provide a layered graphene or graphene-related material structure in which the space between the layers of graphene or graphene-related materials can be controlled over a wide range of pore sizes.

It is an object of the present invention to overcome, or at least substantially ameliorate, the disadvantages and shortcomings of the prior art.

STATEMENTS OF THE INVENTION

According to an aspect of the invention there is provided a spacer molecule comprising: at least first and second binding parts adapted to non-covalently bond at least a first graphene sheet to a second graphene sheet, said spacer comprising at least 9 amino acid residues and wherein when in a solution comprising two or more graphene sheets said spacer molecule contacts first and second graphene sheets to provide a layered structure and a predetermined space between at least the first graphene sheet and the at least second graphene sheet to provide a porous layered graphene structure.

Reference to “graphene” includes graphene oxide, reduced graphene, doped graphene and related carbon based materials.

In a preferred embodiment of the invention said spacer molecule comprises:

- i) a first end group adapted to non-covalently bond a first graphene sheet;
- ii) a second end group adapted to non-covalently bond a second graphene sheet;
- iii) a spacer middle portion separating first and second end groups comprising at least 9 amino acid residues, wherein when in a solution comprising two or more graphene sheets said spacer molecule contacts first and second

graphene sheets to provide a layered structure and a predetermined space between at least the first graphene sheet and the at least second graphene sheet to provide a porous layered graphene structure.

In a preferred embodiment of the invention said first end group comprises one or more amino acids or modified amino acids.

In a preferred embodiment of the invention said second end group comprises one or more amino acids or modified amino acids.

In a preferred embodiment of the invention said first and/or said second end group comprises one or more aromatic amino acids or modified amino acids.

In a preferred embodiment of the invention said aromatic amino acid is selected from the group consisting of: histidine, phenylalanine, tryptophan, or tyrosine.

In a preferred embodiment of the invention said spacer middle portion comprises 9 to at least 50 amino acids or modified amino acids.

The spacer molecule can include one or more natural or modified amino acids. Modified amino acids can be naturally or non-naturally occurring. The spacer molecule can be polar or non-polar and can include polar or non-polar amino acids or modified amino acids to alter the hydrophobicity or lipophilicity of the porous layered graphene structure. Examples of naturally occurring polar amino acids include glutamine, asparagine, histidine, serine, threonine, tyrosine, cysteine, methionine and tryptophan and modified amino acid variants thereof. Examples of non-polar, or hydrophobic amino acids, include alanine, isoleucine, leucine, phenylalanine, valine, proline and glycine and including modified amino acid variants thereof. The combinations of polar and non-polar amino acids can be used to alter the hydrophobicity or lipophilicity of the porous layered graphene structure.

In a preferred embodiment of the invention said spacer middle portion comprises one or more polar amino acids.

In an alternative preferred embodiment of the invention said spacer middle portion comprises one or more non-polar amino acids.

In a preferred embodiment of the invention said spacer middle portion comprises at least 4, 8, 12, 16, 20, 24, 28, 32, 36, 40 or at least 44 amino acids.

In a preferred embodiment of the invention said spacer middle portion comprises over at least part of its length an alpha helix.

In an alternative preferred embodiment of the invention said spacer middle portion comprises over at least part of its length a beta sheet.

In a further embodiment of the invention said alpha helix comprises the same amino acid residues, for example amino acids selected from the group consisting of: methionine, alanine, leucine, glutamine, lysine or arginine.

It will be apparent this embodiment comprises an alpha helix comprising essentially of, for example poly-arginine or poly-lysine.

In an alternative preferred embodiment of the invention said alpha helix comprises alternating, different amino acids selected from the group consisting of: methionine, alanine, leucine, glutamine, lysine or arginine.

It will be apparent this embodiment comprises an alpha helix with, for example, alternating arginine and lysine amino acids.

In a preferred embodiment of the invention said spacer molecule comprises amino acids selected from the amino acid sequence:

Xaa₁ Xaa₂ Xaa₃ Xaa₄ Xaa₅ Xaa₆ Xaa₇ Xaa₈ Xaa₉ Xaa₁₀ Xaa₁₁ Xaa₁₂ Xaa₁₃ Xaa₁₄ [SEQ ID NO: 1]

wherein

Xaa₁ and/or Xaa₂ is an aromatic amino acid

Xaa₃ and/or Xaa₄ is glycine;

Xaa₅ to Xaa₁₀ comprise at least 5 amino acids selected from the group: methionine, alanine, leucine, glutamine, lysine or arginine;

Xaa₁₁ and/or Xaa₁₂ is glycine; and

Xaa₁₃ and/or Xaa₁₄ is an aromatic amino acid.

In an alternative preferred embodiment of the invention said spacer molecule comprises amino acids selected from the amino acid sequence:

Xaa₁ Xaa₂ Xaa₃ Xaa₄ Xaa₅ Xaa₆ Xaa₇ Xaa₈ Xaa₉ Xaa₁₀ Xaa₁₁ Xaa₁₂ Xaa₁₃ Xaa₁₄ [SEQ ID NO: 1]

wherein

Xaa₁ and/or Xaa₂ is an aromatic amino acid

Xaa₃ and/or Xaa₄ is glycine;

Xaa₅ to Xaa₁₀ comprise at least 5 amino acids selected from the group: tyrosine, phenylalanine, tryptophan, threonine, valine or isoleucine, optionally Xaa₅ to Xaa₁₀ can include one or more aromatic amino acid residue

Xaa₁₁ and/or Xaa₁₂ is glycine; and

Xaa₁₃ and/or Xaa₁₄ is an aromatic amino acid.

In an alternative embodiment of the invention of the invention said spacer comprises the amino acid sequence:

Xaa₁ Xaa₂ Xaa₃ Xaa₄ Xaa₅ Xaa₆ Xaa₇ Xaa₈ Xaa₉ Xaa₁₀ Xaa₁₁ Xaa₁₂ Xaa₁₃ Xaa₁₄ [SEQ ID NO: 1]

wherein Xaa₅ to Xaa₁₀ comprises the same amino acid residues wherein said amino acid residues are selected from the group consisting of: methionine, alanine, leucine, glutamine, lysine or arginine.

In an alternative preferred embodiment of the invention said spacer comprises the amino acid sequence:

Xaa₁ Xaa₂ Xaa₃ Xaa₄ Xaa₅ Xaa₆ Xaa₇ Xaa₈ Xaa₉ Xaa₁₀ Xaa₁₁ Xaa₁₂ Xaa₁₃ Xaa₁₄

wherein Xaa₅ to Xaa₁₀ comprises alternating amino acid residues wherein said amino acid residues are selected from the group consisting of: methionine, alanine, leucine, glutamine, lysine or arginine.

In a preferred embodiment of the invention said spacer comprises the amino acid sequence: FFGGEEEEEEGGFF [SEQ ID NO: 3], or a modified amino acid sequence wherein said modified amino acid sequence is at least 75% identical to the amino acid sequence FFGGEEEEEEGGFF [SEQ ID NO: 3] and that retains or has enhanced graphene binding.

In addition, the invention features peptide sequences having at least 80% identity with FFGGEEEEEEGGFF [SEQ ID NO: 3], or fragments and functionally equivalent peptides thereof. In one embodiment, the peptides have at least 85% identity, more preferably at least 90% identity, even more preferably at least 95% identity, still more preferably at least 97% or 98% identity, and most preferably at least 99% identity with the amino acid sequence set for as FFGGEEEEEEGGFF [SEQ ID NO: 3]. A spacer comprising FFGGEEEEEEGGFF [SEQ ID NO: 3] can be modified by one or more substitutions, additions, deletions, truncations which may be present in any combination. Among preferred modifications are those that vary by conservative amino acid substitutions. Such substitutions are those that substitute a given amino acid by another amino acid of like characters. Most highly preferred are modified peptides which retain the same function and activity as the reference peptide from which it varies.

In a preferred embodiment of the invention said peptide comprising or consisting of an amino acid sequence selected from the group consisting of:

- i) FFGGEEEEEGGFF [SEQ ID NO: 2];
- ii) FFGGEEEEEEEGGFF [SEQ ID NO: 3];
- iii) FFGGEEEEEEEEEEEEEGGFF [SEQ ID NO: 4];
- iv) FFGGQQQQQQGGFF [SEQ ID NO: 5];
- v) FFGGKKKKKKGGFF [SEQ ID NO: 6];
- vi) WWGGEEEEEEGGWW [SEQ ID NO: 7];
- vii) FFGGEKEKEKGGFF [SEQ ID NO: 8];
- viii) FFGGEQKEQKGGFF [SEQ ID NO: 9];
- ix) FFGGEMEMEMGGFF [SEQ ID NO: 10]; and
- x) FFGGQMQMGMGGFF [SEQ ID NO: 11].

According to an aspect of the invention there is provided a layered graphene structure comprising one or more spacers according to the invention.

In a preferred embodiment of the invention said layered graphene structure, includes:

at least a first graphene layer and at least a second graphene layer,

at least one spacer layer, wherein said at least one spacer layer includes at least one spacer unit, the spacer unit including a middle portion and an upper end and a lower end, so as to provide a desired predetermined space between the at least first graphene layer and the at least second graphene layer.

In preference, the layered graphene structure is a hydrogel.

In preference, the spacer is a peptide.

In preference, the middle portion is hydrophilic.

In preference, the middle portion is a substantially rigid structure.

In preference, the middle portion has an alpha-helix structure.

In preference, the middle portion has a beta-sheet structure.

In preference, the upper end and lower end are connected to the middle portion by flexible connecting units.

In preference, the flexible connecting units are glycine.

In preference, the upper end and lower end are amino acids.

In preference, the upper end and lower end are selected from the group of amino acids consisting of histidine, tyrosine, phenylalanine and tryptophan.

In preference, the upper end and lower end are the same.

In an alternative preference, the upper end and lower end are the not the same.

In a preferred embodiment of the invention said structure is porous.

In a preferred embodiment of the invention said structure is mesoporous, for example the pores are at least 2nm in diameter and less than 50nm in diameter.

In alternative preferred embodiment of the invention said structure is macroporous, for example the pores are greater than 50nm in diameter.

In a preferred embodiment of the invention said layered structure is at least 10nm thick.

Preferably said layered structure is between 10-100nm thick.

In an alternative embodiment of the invention said layered structure is greater than 100nm thick.

In a further alternative embodiment of the invention said layered structure is between 100 to 1000nm thick.

In an embodiment of the invention said layered structure is greater than 1000nm thick.

In a further preferred embodiment of the invention said layered structure comprises at least 2 graphene layers.

In a preferred embodiment of the invention said layered structure comprises at least 2 to 100 graphene layers.

In an alternative embodiment of the invention said layered structure comprises greater than 100 graphene layers.

According to a further aspect of the invention there is provided a device comprising a graphene structure according to the invention.

In a preferred embodiment of the invention said device is a drug delivery device wherein said device is further modified to include at least one biologically active agent.

A “drug delivery device” is a generic term to include structures that facilitate the controlled release of a therapeutic agent. Typically, drug delivery devices are adapted to deliver a drug of a particular dosage via a particular route of administration, for example intravenous, intraperitoneal, intramuscular, intracavity, subcutaneous, transdermal or trans-epithelial. Drug delivery devices typically are engineered to release the associated therapeutic agent in a controlled release, for example immediate delayed or sustained release or combinations thereof. A drug delivery device as a gel can be applied directly to, for example, a tumour or other diseased tissue to allow direct release of the drug at or on

the diseased tissue. A drug delivery device could also be a bandage or hydrogel adapted to contact a wound to administer a wound healing agent and/or an anti-microbial agent.

In an alternative preferred embodiment of the invention said device is a medical device.

Medical devices are implanted into patients to treat a variety of diseases and conditions. Medical devices include catheters, stents [ureteral or prostatic stents], cannulas, prosthesis and implants, gels. The surfaces of medical devices can be adapted to release agents, for example therapeutic agents, that treat disease or reduce the likelihood of infection. The implantation of a medical device necessarily requires the exposure of the patient to both immune rejection of the implanted device and also an increased probability of an adventitious infection by a microbial pathogen. The invention therefore anticipates a device according to the invention that includes an agent to prevent immune rejection and/or an antimicrobial agent such as an antibiotic or heavy metal such as silver, gold or copper.

In an alternative preferred embodiment of the invention said therapeutic agent is an anti-cancer agent.

In a preferred embodiment of the invention said drug delivery device comprises a gel.

According to the present invention, although this should not be seen as limiting the invention in any way, there is provided a method of producing a layered graphene structure the method including the steps of:

mixing graphene and a solution of spacer units having a first end group and a second end group in a solution;

non-covalently bonding a first end group of the spacer unit to a first side of at least a first graphene sheet;

non-covalently bonding a second end group of the spacer unit to a first side of at least a second graphene sheet;

wherein the spacer units form a spacer layer, so as to provide a desired predetermined space between the at least first graphene sheet and the at least second graphene sheet.

In preference, the layered graphene structure is self-assembled.

In preference, the spacer units facilitates the self-assembly and stabilisation of the layered graphene structure.

In preference, the spacer unit is at least one amino acid.

In preference, the spacer unit is at least one peptide.

In preference, the spacer unit is at least one polypeptide.

In preference, the first end group and the second end group of the spacer units are selected from the group of functional groups including aromatic and non-aromatic functional groups.

According to a further aspect of the invention there is provided a process for the purification of one or more molecules comprising the steps:

- i) providing a mixture comprising a molecule to be purified;
- ii) contacting said mixture with a layered graphene structure according to the invention and provide conditions to allow association of said one or more molecules with said layered graphene structure to provide a graphene structure comprising said molecule[s];
- iii) contacting the layered graphene comprising molecule[s] with a wash buffer to remove non-specifically associated molecules; optionally
- iv) repeating step ii) and/or iii);

- v) eluting associated molecule[s] from said layered graphene to provide a purified solution of said molecule[s]; and optionally
- vi) repeating step v).

In a preferred method of the invention said layered graphene is part of a column and said molecules are contacted with said layered graphene.

In an alternative preferred method of the invention said layered graphene is contacted with a solution comprising a mixture of said molecules.

“Molecules” refer to organic or inorganic compounds and encompasses proteins [e.g. enzymes, hormones, antibodies or antibody fragments, antigenic proteins and polypeptides found in vaccines, peptides such as peptide hormones, nucleic acids, [e.g. DNA fragments, cDNA, mRNA, plasmid and vector nucleic acid]. Also included are small organic molecules such as chemotherapeutic agents, antibiotics, anti-inflammatories.

The properties of the compositions and layered materials described herein may be tuned or customised based on the substitution or variation of the spacer units. Those skilled in the art would recognize and understand that variations to the spacer units could be readily synthesised using conventional approaches to provide a particular property, for example the ability of the layered structure to act as a filter or detector of an analyte.

In some embodiments, by varying the distance between the sheets of graphene, the resultant material may be used to trap or sequester a desired target molecule within a solution or mixture. In addition, the spacer unit may be further functionalised to interact with the desired target molecule.

In further embodiments, the compositions and layered materials of the present invention may be useful as electron transport materials in photovoltaic devices, such as solar cells. They may be combined with other materials such as electron conducting materials. Alternatively, compositions and layered materials of the present invention may be useful in applications such as conductive coatings, energy storage materials such as secondary

batteries and supercapacitors, artificial photosynthetic devices for producing hydrogen from water and other nano-reactor applications.

In yet further embodiments of the present invention, the spacer units may be designed to respond or react to external stimuli so that the spacing between the graphene sheets are affected, for example, by changes in pH to the liquid in which the present invention is immersed. Changes in pH may change the length of the spacer units resulting in the space between the graphene sheets either increasing or decreasing.

The spacer units may also be designed to be able to reversibly or irreversibly disengage with the adjacent graphene sheets after formation of the composition of the present invention. In this way it may be possible to predetermine a point at which any components held within the present invention are released into its immediate environment or alternatively define a point at which the functioning of the present invention may be halted or adjusted.

The present invention provides a way in which the spacing between the graphene sheets can be controlled by way of modification of the size, shape and composition of the peptide.

Some Specific Embodiments of the Invention

Therapeutic Agents

Small Organic Molecules

A general definition of “chemotherapeutic agent” is an agent that typically is a small chemical compound that preferably kills cells in particular diseased cells or tissue or is at least cytostatic. Agents can be divided with respect to their structure or mode of action. For example, chemotherapeutic agents include alkylating agents, anti-metabolites, anthracyclines, alkaloids, plant terpenoids and topoisomerase inhibitors. Chemotherapeutic agents typically produce their effects on cell division or DNA synthesis. Examples of alkylating agents are cisplatin, carboplatin or oxaliplatin. Examples of anti-metabolites include purine or pyrimidine analogues. Purine analogues are known in the art. For example thioguanine is used to treat acute leukaemia. Fludarabine inhibits the

function of DNA polymerases, DNA primases and DNA ligases and is specific for cell-cycle S-phase. Pentostatin and cladribine are adenosine analogues and are effective against hairy cell leukaemias. A further example is mercaptopurine which is an adenine analogue. Pyrimidine analogues are similarly known in the art. For example, 5-fluorouracil (5-FU), floxuridine and cytosine arabinoside. 5-FU has been used for many years in the treatment of breast, colorectal cancer, pancreatic and other cancers. 5-FU can also be formed from the pro-drug capecitabine which is converted to 5-FU in the tumour. Leucovorin, also known as folic acid, is administered as an adjuvant in cancer chemotherapy and which enhances the inhibitory effects of 5-FU on thymidylate synthase. Alkylating agents are also known in the art and include vinca alkaloids, for example vincristine or vinblastine. Terpenoids have been used for many years and include the taxanes, for example, paclitaxel. In a preferred embodiment said agent is doxorubicin. Prodrugs are also within the scope of the invention. A prodrug is a substance that is converted from an inactive or partially active agent by chemical conversion, for example enzymatic conversion, to an active or more active drug.

The spacer according to the invention can be designed to accept small organic molecules as herein disclosed.

Moreover, antibiotics and antiviral agents are effective in the treatment of microbial, for example bacterial and parasitic pathogens and pathogenic viruses. Examples of classes of antibiotics effective in the control of bacterial pathogens include, by example only, penicillins, cephalosporins, rifamycins, sulphonamides, macrolides and tetracyclines. Also included within the scope of the invention are antibacterial peptides such as dermicidins, cecropins and defensins. Antiviral agents include anti-retroviral drugs such as zidovudine, lamivudine, efavirenz and abacavir; and anti-viral drugs such as ganciclovir, aciclovir and oseltamivir. Anti-protozoan agents include lumefantrine, mefloquine, amodiaquine, sulfadoxine, chloroquine used in the treatment of malaria and also combination therapies that use these agents in combination with artemisinin. These are additional non-limiting examples of agents that can be used with the device according to the invention.

Antibodies

Antibodies include polyclonal and monoclonal antibodies, prepared according to conventional methodology. Typically antibodies are directed to cell surface proteins, for example receptors. However, intracellular delivery of antibodies and antibody fragments is known, for example see WO2007/064727; WO2004/030610; WO03/095641; WO02/07671; WO01/43778; WO96/40248; and WO94/01131 each of which is incorporated by reference in their entirety.

Chimeric antibodies are recombinant antibodies in which all of the V-regions of a mouse or rat antibody are combined with human antibody C-regions. Humanised antibodies are recombinant hybrid antibodies which fuse the complementarity determining regions from a rodent antibody V-region with the framework regions from the human antibody V-regions. The C-regions from the human antibody are also used. The complementarity determining regions (CDRs) are the regions within the N-terminal domain of both the heavy and light chain of the antibody to where the majority of the variation of the V-region is restricted. These regions form loops at the surface of the antibody molecule. These loops provide the binding surface between the antibody and antigen.

Antibodies from non-human animals provoke an immune response to the foreign antibody and its removal from the circulation. Both chimeric and humanised antibodies have reduced antigenicity when injected to a human subject because there is a reduced amount of rodent (i.e. foreign) antibody within the recombinant hybrid antibody, while the human antibody regions do not elicit an immune response. This results in a weaker immune response and a decrease in the clearance of the antibody. This is clearly desirable when using therapeutic antibodies in the treatment of human diseases. Humanised antibodies are designed to have less “foreign” antibody regions and are therefore thought to be less immunogenic than chimeric antibodies.

Various fragments of antibodies are known in the art. A Fab fragment is a multimeric protein consisting of the immunologically active portions of an immunoglobulin heavy chain variable region and an immunoglobulin light chain variable region, covalently

coupled together and capable of specifically binding to an antigen. Fab fragments are generated via proteolytic cleavage (with, for example, papain) of an intact immunoglobulin molecule. A Fab₂ fragment comprises two joined Fab fragments. When these two fragments are joined by the immunoglobulin hinge region, a F(ab')₂ fragment results. An Fv fragment is multimeric protein consisting of the immunologically active portions of an immunoglobulin heavy chain variable region and an immunoglobulin light chain variable region covalently coupled together and capable of specifically binding to an antigen. A fragment could also be a single chain polypeptide containing only one light chain variable region, or a fragment thereof that contains the three CDRs of the light chain variable region, without an associated heavy chain variable region, or a fragment thereof containing the three CDRs of the heavy chain variable region, without an associated light chain moiety; and multi specific antibodies formed from antibody fragments, this has for example been described in US patent No 6,248,516. Fv fragments or single region (domain) fragments are typically generated by expression in host cell lines of the relevant identified regions. These and other immunoglobulin or antibody fragments are within the scope of the invention and are described in standard immunology textbooks such as Paul, *Fundamental Immunology* or Janeway et al. *Immunobiology*. Molecular biology now allows direct synthesis (via expression in cells or chemically) of these fragments, as well as synthesis of combinations thereof. A fragment of an antibody or immunoglobulin can also have bispecific function as described above. The device according to the invention can be adapted by manipulation of pore size to carry antibodies and antibody fragments as herein disclosed.

In general, doses of antibodies (or fragments thereof) of between 10 µg/ml and 500 µg/ml generally will be formulated and administered according to standard procedures. Exemplary doses can range from 10 µg/ml to 250 µg/ml, 30 µg/ml to 250 µg/ml, 50 µg/ml to 250 µg/ml, 30 µg/ml to 100 µg/ml, or 50 µg/ml to 100 µg/ml, such as 10 µg/ml, 20 µg/ml, 30 µg/ml, 40 µg/ml, 50 µg/ml, 60 µg/ml, 70 µg/ml, 80 µg/ml, 90 µg/ml, 100 µg/ml, 250 µg/ml, 400 µg/ml or 500 µg/ml. Other protocols for the administration of compositions will be known to one of ordinary skill in the art, in which the dose amount, schedule of injections, sites of injections, mode of administration and the like vary from

the foregoing. The administration of compositions to mammals other than humans, (e.g. for testing purposes or veterinary therapeutic purposes), is carried out under substantially the same conditions as described above. A subject, as used herein, is a mammal, preferably a human, and including a non-human primate, cow, horse, pig, sheep, goat, dog, cat or rodent.

Pharmaceutical Proteins & Peptides

Similarly, so called protein or peptide biologics can be associated with the device according to the invention. This includes pharmaceutically active proteins.

Examples of pharmaceutical proteins include “cytokines”. Cytokines are involved in a number of diverse cellular functions. These include modulation of the immune system, regulation of energy metabolism and control of growth and development. Cytokines mediate their effects via receptors expressed at the cell surface on target cells. Examples of cytokines include the interleukins such as: IL1, 2, 3, 4, 5, 6, 7, 8, 9, 10, 11, 12, 13, 14, 15, 16, 17, 18, 19, 20, 21, 22, 23, 24, 25, 26, 27, 28, 29, 30, 31, 32 and 33. Other examples include growth hormone, leptin, erythropoietin, prolactin, tumour necrosis factor [TNF] granulocyte colony stimulating factor (GCSF), granulocyte macrophage colony stimulating factor (GMCSF), ciliary neurotrophic factor (CNTF), cardiotrophin-1 (CT-1), leukemia inhibitory factor (LIF) and oncostatin M (OSM), interferon α , interferon β , interferon ϵ , interferon κ and ω interferon.

Examples of pharmaceutically active peptides include GLP-1, anti-diuretic hormone; oxytocin; gonadotropin releasing hormone, corticotrophin releasing hormone; calcitonin, glucagon, amylin, A-type natriuretic hormone, B-type natriuretic hormone, ghrelin, neuropeptide Y, neuropeptide YY₃₋₃₆, growth hormone releasing hormone, somatostatin; or homologues or analogues thereof.

The term “chemokine” refers to a group of structurally related low-molecular weight factors secreted by cells having mitogenic, chemotactic or inflammatory activities. They

are primarily cationic proteins of 70 to 100 amino acid residues that share four conserved cysteine residues. These proteins can be sorted into two groups based on the spacing of the two amino-terminal cysteines. In the first group, the two cysteines are separated by a single residue (C-x-C), while in the second group they are adjacent (C-C). Examples of member of the 'C-x-C' chemokines include but are not limited to platelet factor 4 (PF4), platelet basic protein (PBP), interleukin-8 (IL-8), melanoma growth stimulatory activity protein (MGSA), macrophage inflammatory protein 2 (MIP-2), mouse Mig (m119), chicken 9E3 (or pCEF-4), pig alveolar macrophage chemotactic factors I and II (AMCF-I and -II), pre-B cell growth stimulating factor (PBSF), and IP10. Examples of members of the 'C-C' group include but are not limited to monocyte chemotactic protein 1 (MCP-1), monocyte chemotactic protein 2 (MCP-2), monocyte chemotactic protein 3 (MCP-3), monocyte chemotactic protein 4 (MCP-4), macrophage inflammatory protein 1 α (MIP-1- α), macrophage inflammatory protein 1 β (MIP-1- β), macrophage inflammatory protein 1- γ (MIP-1- γ), macrophage inflammatory protein 3 α (MIP-3- α), macrophage inflammatory protein 3 β (MIP-3- β), chemokine (ELC), macrophage inflammatory protein-4 (MIP-4), macrophage inflammatory protein 5 (MIP-5), LD78 β , RANTES, SIS-epsilon (p500), thymus and activation-regulated chemokine (TARC), eotaxin, I-309, human protein HCC-1/NCC-2, human protein HCC-3.

A number of growth factors have been identified which promote/activate endothelial cells to undergo angiogenesis. These include vascular endothelial growth factor (VEGF A), VEGF B, VEGF C, and VEGF D, transforming growth factor (TGF β), acidic and basic fibroblast growth factor (aFGF and bFGF), and platelet derived growth factor (PDGF).

VEGF is an endothelial cell-specific growth factor which has a very specific site of action, namely the promotion of endothelial cell proliferation, migration and differentiation. VEGF is a complex comprising two identical 23 kD polypeptides. VEGF can exist as four distinct polypeptides of different molecular weight, each being derived from an alternatively spliced mRNA. bFGF is a growth factor that functions to stimulate the proliferation of fibroblasts and endothelial cells. bFGF is a single polypeptide chain with a molecular weight of 16.5Kd. Several molecular forms of bFGF have been discovered

which differ in the length at their amino terminal region. However the biological function of the various molecular forms appears to be the same.

Pro-drug activating polypeptides are also within the scope of the invention. The term pro-drug activating genes refers to nucleotide sequences, the expression of which, results in the production of proteins capable of converting a non-therapeutic compound into a therapeutic compound, which renders the cell susceptible to killing by external factors or causes a toxic condition in the cell. An example of a prodrug activating gene is the cytosine deaminase gene. Cytosine deaminase converts 5-fluorocytosine to 5 fluorouracil, a potent anti-tumour agent. The lysis of the tumour cell provides a localized burst of cytosine deaminase capable of converting 5FC to 5FU at the localized point of the tumour resulting in the killing of many surrounding tumour cells. Additionally, the thymidine kinase (TK) gene (see US5,631,236 and US5,601,818) in which the cells expressing the TK gene product become susceptible to selective killing by the administration of ganciclovir may be employed. Other examples of pro-drug activating enzymes are nitroreductase and cytochrome p450's (e.g. CYP1A2, CYP2E1 or CYP3A4).

Throughout the description and claims of this specification, the words "comprise" and "contain" and variations of the words, for example "comprising" and "comprises", means "including but not limited to", and is not intended to (and does not) exclude other moieties, additives, components, integers or steps. "Consisting essentially" means having the essential integers but including integers which do not materially affect the function of the essential integers.

Throughout the description and claims of this specification, the singular encompasses the plural unless the context otherwise requires. In particular, where the indefinite article is used, the specification is to be understood as contemplating plurality as well as singularity, unless the context requires otherwise.

Features, integers, characteristics, compounds, chemical moieties or groups described in conjunction with a particular aspect, embodiment or example of the invention are to be understood to be applicable to any other aspect, embodiment or example described herein unless incompatible therewith.

An embodiment of the invention will now be described by example only and with reference to the following figures:

Figure 1 summarizes the principles of the invention (the solution molecules and ions required to maintain an appropriate solution condition (*e.g.* neutral) have been omitted for clarity);

Figure 2 shows a view of an example of the present invention, a reduced graphene oxide (rGO) layered hydrogel construct of approximately 5 μ m thickness obtained *via* peptide-directed self-assembly using the peptide FFGGEEEEEEGGFF [SEQ ID NO: 3] and the method described herein (see Methods for details);

Figure 3 shows a view of another example of the present invention, a reduced graphene oxide layered hydrogel construct of approximately 70 nm thickness obtained *via* peptide-directed self-assembly using the peptide FFGGEEEEEEGGFF [SEQ ID NO: 3] and supported on a glass slide (see Methods for details) that is sat on top of some written text on a piece of paper;

Figure 4 shows an SEM image of a freeze dried sample of the hydrogel shown in Figure 2 edge on (see Methods for details);

Figure 5 (top) shows on an AFM image two independent paths A-B and C-D taken by the AFM probe for a sample of the material shown in Figure 2 (see Methods for details), and the AFM probe height along the two paths (middle and bottom) showing the distance

between successive rGO sheets separated by the peptide FFGGEEEEEEGGFF [SEQ ID NO: 3] (*i.e.* the pore size) that has been designed to yield a pore size of 2.6 nm;

Figure 6 shows the variation with time of doxorubicin (DOX) anti-cancer drug uptake (see Methods for details) for different rGO hydrogels formed using the peptide FFGGEEEEEEGGFF [SEQ ID NO: 3] where the degree of reduction of the rGO is different (the take-up for the rGO hydrogel formed in the absence of the peptide is also shown for reference);

Figure 7 shows the DOX release profile at different pH values (see Methods for details) for the optimal rGO hydrogel formed using the peptide FFGGEEEEEEGGFF [SEQ ID NO: 3];

Figure 8 shows the results of an MTT assay based analysis (see Methods for details) to assess the toxicity of different concentrations of the rGO hydrogel formed using the peptide FFGGEEEEEEGGFF [SEQ ID NO: 3];

Figure 9 shows the results of an MTT assay based analysis (see Methods for details) to assess the toxicity of DOX alone and DOX released from the hydrogel formed using the peptide FFGGEEEEEEGGFF [SEQ ID NO: 3]; and

Figure 10 shows the variation with time of uptake of three different sized dextran molecules (see Methods for details) for an rGO hydrogel formed using the peptide FFGGEEEEEEGGFF [SEQ ID NO: 3].

DETAILED DESCRIPTION OF THE INVENTION

Methods

Preparation of graphene oxide

Graphene oxide (GO) was prepared from natural or synthetic graphite according to the improved Hummer's method.³⁷ Briefly, a 9:1 mixture of concentrated sulphuric acid and phosphoric acid (120:13 mL) was cooled overnight to 4 °C. The already cooled acid mixture was slowly added to the graphite powder (1 g) and potassium permanganate (6 g) under stirring at room temperature. Then the mixture was heated to 50 °C for 12 h to form a thick paste. The paste was then cooled to room temperature and then poured onto ice cubes (150 mL of Milli-Q water) with 30% hydrogen peroxide (1 mL). The mixture was then washed and filtered with distilled water and hydrochloric acid (32 %) followed by repeated washing with ethanol and eventually with Milli-Q water. For each successive wash the obtained brown dispersion was centrifuged at 4400 rpm for 2 h to remove residual salts and any un-exfoliated graphite oxide, which is usually present in a very small amount. The obtained GO was vacuum dried overnight at room temperature.

Preparation of reduced graphene oxide

One instance of reduced GO (rGO) was prepared from 25 mL of a homogeneous dispersion of GO (0.5 mg.mL⁻¹). After adding to this solution in a volumetric flask 25 µl of hydrazine solution (35 wt% in water) and 75.0 µl of ammonia solution (28 wt% in water), the dispersion was vigorously stirred for a few minutes before being placed in a silicon oil bath (~95 °C) for 1 hr. Other instances of rGO with different levels of GO reduction from ~20 wt% oxygen down to ~8% wt% oxygen were obtained by varying the hydrazine volume between 25 and 75 µl and the reaction temperature between 85 and 95 °C.

Preparation of layered GO and rGO hydrogel

One instance of the layered rGO hydrogel material with a dominant inter-sheet spacing (*i.e.* pore size) of 2.6 nm was produced by adding 25 mL of rGO dispersion (0.5 mg.mL⁻¹) to 25 mL of a solution of the peptide FFGGEEEEEGGFF [SEQ ID NO: 3] (0.10 µM) and then stirring for 30 min before filtering it through a mixed cellulose ester filter membrane (47mm in diameter, 0.45 µm pore size, Millipore) by vacuum filtration. The resultant hydrogel film was then washed three times and immediately transferred to a Petri dish and immersed in Milli-Q water overnight to remove the remaining unbound peptide.

Other instances of the rGO hydrogel material with a dominant pore size of 2.6 nm were obtained by using rGO dispersions with concentrations varying from 0.0025 mg.mL⁻¹ upwards in the aforementioned process. The thickness of the resultant hydrogel films varied from 10s of nm, which meant they needed to be supported; an as-received glass microscope slide was used for this purpose, but it is anticipated that other materials could also be used. The hydrogel films were transferred from the filter membrane to the glass slide support by tightly clamping the filter membrane supported hydrogel film between two glass slides for 12 h at room temperature before dissolving away the filter membrane with acetone.

GO-based variants of the hydrogel material were also similarly made, although the drainage time was greater for the same applied vacuum pressure due to the greater hydrophilicity of the GO.

Characterization of the hydrogel material mesoscale morphology and pore size

The morphologies of the graphene hydrogel films prepared as described above were investigated using a scanning electron microscope (SEM; QUANTA 450). The hydrogels were cut using a razor blade then dried in a freeze dryer (188K at 10⁻² Pa for 24hrs), and then mounted in a cross-sectional sample holder before being imaged in the SEM.

The spacing between the individual rGO or GO sheets (*i.e.* the pore size) was assessed by atomic force microscopy (AFM; NT-MDT Ntegra Solaris) in tapping mode. The AFM samples were prepared by drop-casting a diluted suspension of crushed hydrogel film onto a cleaned mica substrate. They were imaged immediately after preparation.

Characterization of molecular separation capability of hydrogel material

To demonstrate the capacity of the hydrogel films to separate molecules based on their size, it was exposed to solutions of FITC-labelled dextrans of three different diameters (they are generally claimed to be spherical in nature): FITC-dextran-4k (FD4, Sigma-

Aldrich; mol. wt. 4000, Stokes radius ~1.4 nm); FITC-dextran-10k (FD10, Sigma-Aldrich; mol. wt. 10,000, Stokes radius ~2.3 nm); and FITC-dextran-20k (FD20, Sigma-Aldrich; mol. wt. 20,000, Stokes radius ~3.3 nm). The experiments involved placing 20 mg of the hydrogel into three different 3 mL cuvettes containing 20 μm solutions of FD4, FD10 and FD20 respectively and then monitoring in real time the concentration of the molecule in the solution using a UV-vis spectrometer (CHEMUSB4, Ocean Optics,) operating at 490 nm.

Characterization of drug loading into and release from the graphene hydrogels

The loading of doxorubicin (DOX) anti-cancer drug into the rGO hydrogels was assessed using a technique similar to that used to assess the filtration capability of the hydrogel. After adding 15 mg of the hydrogel to 3 mL of the DOX solution ($50 \mu\text{g}\cdot\text{mL}^{-1}$) in a cuvette, the concentration of the latter was monitored in real time for 24 h by a UV-VIS spectrometer (USB4000-UV-VIS, Ocean Optics) operating at 490 nm. The variation of the drug loading in the hydrogel with time was estimated from this.

To characterise the release of DOX from a hydrogel, the DOX-loaded film was first removed from the drug loading cuvette and rinsed several times with deionized water to remove unbound drug and drug attached to the outer surface of the hydrogels. The film was then divided into three roughly equal parts before then being immersed in three separate cuvettes containing a 3 mL aqueous PBS solution at 37 °C and pH 5.4, 7.4 and 9.4 respectively to mimic the release profile in physiological acidic, neutral and basic environments. The solutions in the cuvettes were constantly stirred whilst being maintained at 37 °C. At predetermined time intervals, 1 mL of the solution from the cuvettes was withdrawn (with 1 mL of fresh PBS solution replacing it) to determine the DOX release using UV-Vis spectroscopy.

Cell viability assessments

The toxicities of the graphene hydrogel, DOX and DOX-loaded hydrogel were assessed using the MTT (3-(4,5-dimethylthiazol-2-yl)-2,5-diphenyltetrazolium bromide) tetrazolium

assay in a microplate reader. The step-by-step experimental details for each assessment are:

Cell culturing: Mesenchymal stem cells (MSC) were first seeded in 96-well microplate at a density of 5.0×10^4 cells/mL in 200 μ L DMEM supplemented with 10% FBS, 100 U mL⁻¹ of penicillin, 100 mg mL⁻¹ of streptomycin and 2 mM L⁻¹ L glutamine for 24 hours and incubated at 37 °C in a 5% CO₂ humidified incubator.

Cell treatment with target to be assessed: Cells were then cultured in medium with the target to be assessed (hydrogel, DOX, DOX-loaded hydrogel) for 24 hours. A control containing only the cells and no hydrogel was also included. Three replicate wells were used *per* sample, including the control.

MTT assay: 10 μ L of MTT (5 mg.mL⁻¹ in PBS) were added to each well, including both samples and controls, and then incubated for 4 h at 37 °C. All the liquid was then removed from wells, transferred into new microplate and 150 μ L dimethyl sulfoxide (DMSO) was added to each well to ensure complete solubilization of formazan crystals.

Cell viability measurement: After 1 h further incubation, the absorbance was measured at 595 nm using a microplate reader (BioTek, USA). Cell viability was expressed as a percentage of the control cell culture value.

Example 1

As illustrated in Figure 1, the invention here centres on a peptide that is designed to self-assemble graphene sheets with a specific distance between the sheets, h , and which is composed of the following:

the end groups (at least two of) that non-covalently bind to the graphene;

the middle part (at least one of) that prefers to sit in the solution phase between the two graphene sheets (*e.g.* it is overall hydrophilic when the solution is aqueous);
and

the flexible connection between the end groups and the middle (at least two of) that provide the right balance of flexibility to ensure the middle prefers to stay in the space between the layers and the end groups attached to the graphene

Example 2

Figure 2 shows an example of an instance of an rGO hydrogel dominated by pores of 2.6 nm width produced using 25 mL of a 0.5 mg.mL⁻¹ rGO dispersion and 25 mL of a 0.10 μM solution of the peptide FFGGEEEEEEGGFF [SEQ ID NO: 3], which was designed to yield a pore size of 2.6 nm. The hydrogel film shown here is an approximately 5 μm thick paper-like material that is flexible and non-brittle.

Example 3

Figure 3 shows an example of an instance of an rGO hydrogel dominated by pores of 2.6 nm width produced using 100 mL of 0.0025 mg.mL⁻¹ rGO dispersion and 100 mL of a 0.0005 μM solution of the peptide FFGGEEEEEEGGFF [SEQ ID NO: 3], which was designed to yield a pore size of 2.6 nm. The hydrogel film is approximately 70 nm thick and, thus, requires support on a surface (a microscope glass slide in this example).

Example 4

The lamellar nature of the hydrogel material at the mesoscale is illustrated by the SEM image in Figure 4.

Example 5

The pore size in the hydrogel made using the peptide FFGGEEEEEEGGFF [SEQ ID NO: 3] (i.e. that shown in Figures 2 and 3) is revealed in Figure 5, which shows that the AFM probe experiences vertical displacements of around 2.6 nm as it crosses the edges of the rGO sheets revealed when the hydrogel is fractured.

Example 6

Figure 6 shows that the amount of doxorubicin (DOX) anti-cancer drug that can be loaded into a hydrogel made using the peptide FFGGEEEEEEGGFF [SEQ ID NO: 3] is a strong function of the level of reduction of the rGO: whilst the highly reduced rGO-based hydrogel is marginally better than the mildly-reduced rGO, significantly higher loadings can be achieved by identifying the optimal degree of reduction. This figure also shows that the pores created by use of the peptide increases substantially the DOX capacity of the hydrogel.

Example 7

Figure 7 shows that after an initial low level burst effect (less than 10%), the DOX only continues to be released to any significant extent under acidic conditions akin to those typical of tumour sites. The release rate is sustained at an essentially constant value for around 3.5 days before release halts. Release beyond this point could possibly be enhanced by further optimisation of the hydrogel.

Example 8

The hydrogel by itself appears to be non-toxic as shown in Figure 8, which shows that cell viability over a 24 hour period was statistically invariant from the control (no hydrogel) for the case where 5, 10, 15, 20 and 25 mg of hydrogel were present.

Example 9

Figure 9 compares the cell toxicity of 5 μg of DOX in 24 hours provided *via* 100 μL of a 50 $\mu\text{g}\cdot\text{mL}^{-1}$ DOX solution (DOX-only) and 15 mg of a hydrogel loaded with approximately 150 μg of DOX that releases 5 μg in the 24 hours assessed (DOX-loaded hydrogel). This shows that the hydrogel-loaded DOX possesses a toxicity that is similar to that of DOX-only. As the hydrogel contains around 30 times this dose with approximately 60% of that being released based on the current realisation (see Figure 7), the hydrogel can deliver the required dose in a sustained way for around 3.5 days without intervention. Longer periods could be achieved by increasing the mass of hydrogel or improving its formulation to ensure more than 60% of the DOX were released from the sample.

Example 9

The ability of the hydrogel to separate bio- and other larger molecules by size is illustrated in Figure 10, which shows the variation through time of the bulk phase concentrations of dextran molecules of three different sizes in solution with the hydrogel shown in Figure 2. As expected, the rate of uptake of FD4, which is around half the size of the pores in the hydrogel (1.4 nm vs. 2.6 nm), is taken up more quickly than that of FD10, which is only slightly smaller than the pore size (2.3 nm vs. 2.6 nm) – this demonstrates kinetics-based separation of bio- and other large molecules. The 3.3 nm size of the FD20 means it cannot enter the 2.6 nm pores that dominate the hydrogel's porosity – this demonstrates separation based on size exclusion.

References

1. Geim, A. K. & Novoselov, K. S. The Rise of Graphene. *Nat Mater* 6, 183-191 (2007).
2. Lee, C., Wei, X., Kysar, J. W. & Hone, J. Measurement of the Elastic Properties and Intrinsic Strength of Monolayer Graphene. *Science* 321, 385-388 (2008).
3. Wang, G., Sun, X., Lu, F., Sun, H., Yu, M., Jiang, W., Liu C. & Lian, J. Flexible Pillared Graphene-Paper Electrodes for High-Performance Electrochemical Supercapacitors. *Small* 8, 452-4592 (2012).
4. Wang, Y. et al. Preventing Graphene Sheets from Restacking for High-Capacitance Performance. *Journal of Physical Chemistry C* 115, 23192-23197 (2011).
5. Cheng, Q. et al. Graphene and carbon nanotube composite electrodes for supercapacitors with ultra-high energy density. *Physical Chemistry Chemical Physics* 13, 17615-17624 (2011).
6. Huang, Z.-D. et al. Effects of reduction process and carbon nanotube content on the supercapacitive performance of flexible graphene oxide papers. *Carbon* 50, 4239-4251, (2012).
7. Wimalasiri, Y. & Zou, L. Carbon nanotube/graphene composite for enhanced capacitive deionization performance. *Carbon* 59, 464-471, (2013).
8. Yu, D. et al. Scalable synthesis of hierarchically structured carbon nanotube-graphene fibres for capacitive energy storage. *Nat Nano* 9, 555-562
9. Tristán-López, F. et al. Large Area Films of Alternating Graphene–Carbon Nanotube Layers Processed in Water. *Acs Nano* 7, 10788-10798, (2013).
10. Jiang, L., Sheng, L., Long, C. & Fan, Z. Densely packed graphene nanomesh-carbon nanotube hybrid film for ultra-high volumetric performance supercapacitors. *Nano Energy* 11, 471-480 (2015).
11. Zhang, L. L., Xiong, Z. & Zhao, X. S. Pillaring Chemically Exfoliated Graphene Oxide with Carbon Nanotubes for Photocatalytic Degradation of Dyes under Visible Light Irradiation. *ACS Nano* 4, 7030-7036 (2010).
12. Zhang, L. L., Xiong, Z. G. & Zhao, X. S. A composite electrode consisting of nickel hydroxide, carbon nanotubes, and reduced graphene oxide with an ultrahigh electrocapacitance. *Journal of Power Sources* 222, 326-332, (2013).

13. Du, F. et al. Preparation of Tunable 3D Pillared Carbon Nanotube–Graphene Networks for High-Performance Capacitance. *Chem Mater* 23, 4810-4816, (2011).
14. Lei, Z. B. et al. A high-energy-density supercapacitor with graphene-CMK-5 as the electrode and ionic liquid as the electrolyte. *Journal of Materials Chemistry A* 1, 2313-2321, (2013).
15. Yang, W. L., Gao, Z., Wang, J., Wang, B. & Liu, L. H. Hydrothermal synthesis of reduced graphene sheets/Fe₂O₃ nanorods composites and their enhanced electrochemical performance for supercapacitors. *Solid State Sciences* 20, 46-53 (2013).
16. Wu, Z.-S. et al. Anchoring Hydrated RuO₂ on Graphene Sheets for High-Performance Electrochemical Capacitors. *Advanced Functional Materials* 20, 3595-3602 (2010).
17. Kong, B. S., Geng, J. X. & Jung, H. T. Layer-by-layer assembly of graphene and gold nanoparticles by vacuum filtration and spontaneous reduction of gold ions. *Chem Commun*, 2174-2176 (2009).
18. Zhang, P. et al. One-Step Synthesis of Large-Scale Graphene Film Doped with Gold Nanoparticles at Liquid–Air Interface for Electrochemistry and Raman Detection Applications. *Langmuir* 30, 8980-8989, (2014).
19. Zhang, H., Hines, D. & Akins, D. L. Synthesis of a nanocomposite composed of reduced graphene oxide and gold nanoparticles. *Dalton Transactions* 43, 2670-2675, (2014).
20. Movahed, S. K., Fakharian, M., Dabiri, M. & Bazgir, A. Gold nanoparticle decorated reduced graphene oxide sheets with high catalytic activity for Ullmann homocoupling. *Rsc Adv* 4, 5243-5247 (2014).
21. Kuo, T.-R. et al. Layer-by-layer thin film of reduced graphene oxide and gold nanoparticles as an effective sample plate in laser-induced desorption/ionization mass spectrometry. *Anal Chim Acta* 809, 97-103, (2014).
22. Wang, D. et al. Defect-Rich Crystalline SnO₂ Immobilized on Graphene Nanosheets with Enhanced Cycle Performance for Li Ion Batteries. *The Journal of Physical Chemistry C* 116, 22149-22156, (2012).

23. Wang, D. N. et al. Layer by layer assembly of sandwiched graphene/SnO₂ nanorod/carbon nanostructures with ultrahigh lithium ion storage properties. *Energy Environ Sci* 6, 2900-2906, (2013).
24. Zhang, K., Zhang, L. L., Zhao, X. S. & Wu, J. Graphene/Polyaniline Nanofiber Composites as Supercapacitor Electrodes. *Chemistry of Materials* 22, 1392-1401(2010).
25. Park, S., Dikin, D. A., Nguyen, S. T. & Ruoff, R. S. Graphene Oxide Sheets Chemically Cross-Linked by Polyallylamine. *The Journal of Physical Chemistry C* 113, 15801-15804, (2009).
26. Tang, L., Li, X., Du, D. & He, C. J. Fabrication of multilayer films from regenerated cellulose and graphene oxide through layer-by-layer assembly. *Prog Nat Sci-Mater* 22, 341-346, (2012).
27. Zhang, L. L., Zhao, S., Tian, X. N. & Zhao, X. S. Layered Graphene Oxide Nanostructures with Sandwiched Conducting Polymers as Supercapacitor Electrodes. *Langmuir* 26, 17624-17628, (2010).
28. Park, S. *et al.* Graphene Oxide Papers Modified by Divalent Ions: Enhancing Mechanical Properties via Chemical Cross-Linking. *ACS Nano* 2, 572-578 (2008).
29. Sk, M. M. & Yue, C. Y. Layer-by-layer (LBL) assembly of graphene with p-phenylenediamine (PPD) spacer for high performance supercapacitor applications. *Rsc Adv* 4, 19908-19915, (2014).
30. Kim, T. K. et al. Three-dimensional pillared metallomacrocycle-graphene frameworks with tunable micro- and mesoporosity. *Journal of Materials Chemistry A* 1, 8432-8437, (2013).
31. Burrell, J. W. et al. Graphene Oxide Framework Materials: Theoretical Predictions and Experimental Results. *Angewandte Chemie International Edition* 49, 8902-8904, (2010).
32. Cui, Y., Cheng, Q. Y., Wu, H. P., Wei, Z. X. & Han, B. H. Graphene oxide-based benzimidazole-crosslinked networks for high-performance supercapacitors. *Nanoscale* 5, 8367-8374, (2013).
33. Seo, S., Min, M., Lee, S. M. & Lee, H. Photo-switchable molecular monolayer anchored between highly transparent and flexible graphene electrodes. *Nat Commun* 4, 1920, (2013).

34. Xu, Y., Wu, Q., Sun, Y., Bai, H. & Shi, G. Three-Dimensional Self-Assembly of Graphene Oxide and DNA into Multifunctional Hydrogels. *ACS Nano* 4, 7358-7362, (2010).
35. Wang, T. et al. Hydrothermal synthesis of nitrogen-doped graphene hydrogels using amino acids with different acidities as doping agents. *J Mater Chem A* 2, 8352-8361, (2014).
36. Wu, J. et al. Hierarchical construction of a mechanically stable peptide-graphene oxide hybrid hydrogel for drug delivery and pulsatile triggered release in vivo. *Nanoscale*, (2015).
37. Marcano, D. C. et al. Improved synthesis of graphene oxide. *ACS Nano* 4, 4806-4814, (2010).

Claims

- 1 A spacer molecule comprising: at least first and second binding parts adapted to non-covalently bond at least a first graphene sheet to a second graphene sheet, said spacer comprising at least 9 amino acid residues and wherein when in a solution comprising two or more graphene sheets said spacer molecule contacts first and second graphene sheets to provide a layered structure and a predetermined space between at least the first graphene sheet and the at least second graphene sheet to provide a porous layered graphene structure.
2. The spacer according to claim 1 wherein said spacer molecule comprises:
 - i) a first end group adapted to non-covalently bond a first graphene sheet;
 - ii) a second end group adapted to non-covalently bond a second graphene sheet;
 - iii) a spacer middle portion separating first and second end groups comprising at least 9 amino acid residues, wherein when in a solution comprising two or more graphene sheets said spacer molecule contacts first and second graphene sheets to provide a layered structure and a predetermined space between at least the first graphene sheet and the at least second graphene sheet to provide a porous layered graphene structure.
3. The spacer according to claim 1 or 2 wherein said first end group comprises one or more amino acids or modified amino acids.
4. The spacer according to any one of claims 1 to 3 wherein said second end group comprises one or more amino acids or modified amino acids.
5. The spacer according to claim 3 or 4 wherein said first and/or said second end group comprises one or more aromatic amino acids or modified amino acids.

6. The spacer according to claim 5 wherein said aromatic amino acid is selected from the group consisting of: phenylalanine, tryptophan, or tyrosine.
7. The spacer according to claim 3 or 4 wherein said first or second end group comprises a histidine amino acid.
8. The spacer according to any one of claims 1 to 7 wherein said spacer middle portion comprises one or more polar amino acids.
9. The spacer according to any one of claims 1 to 7 wherein said spacer middle portion comprises one or more non-polar amino acids.
10. The spacer according to any one of claims 2 to 9 wherein said spacer middle portion comprises 10 to at least 50 amino acids wherein one or more amino acids or modified amino acids. .
11. The spacer according to any one of claims 2 to 10 wherein said spacer middle portion comprises over at least part of its length an alpha helix.
12. The spacer according to any one of claims 2 to 10 wherein said spacer middle portion comprises over at least part of its length a beta sheet.
13. The spacer according to claim 11 wherein said alpha helix comprises the same amino acid residues, for example amino acids selected from the group consisting of: methionine, alanine, leucine, glutamine, lysine or arginine.
14. The spacer according to claim 11 wherein said alpha helix comprises alternating, different amino acids selected from the group consisting of: methionine, alanine, leucine, glutamine, lysine or arginine.
15. The spacer according to any one of claims 1 to 14 wherein said spacer molecule comprises amino acids selected from the amino acid sequence:

Xaa₁ Xaa₂ Xaa₃ Xaa₄ Xaa₅ Xaa₆ Xaa₇ Xaa₈ Xaa₉ Xaa₁₀ Xaa₁₁ Xaa₁₂ Xaa₁₃ Xaa₁₄
[SEQ ID NO: 1],

wherein

Xaa₁ and/or Xaa₂ is an aromatic amino acid

Xaa₃ and/or Xaa₄ is glycine;

Xaa₅ to Xaa₁₀ comprise at least 5 amino acids selected from the group:
methionine, alanine, leucine, glutamine, lysine or arginine;

Xaa₁₁ and/or Xaa₁₂ is glycine; and

Xaa₁₃ and/or Xaa₁₄ is an aromatic amino acid.

16. The spacer according to any one of claims 1 to 14 wherein said spacer molecule comprises amino acids selected from the amino acid sequence:

Xaa₁ Xaa₂ Xaa₃ Xaa₄ Xaa₅ Xaa₆ Xaa₇ Xaa₈ Xaa₉ Xaa₁₀ Xaa₁₁ Xaa₁₂ Xaa₁₃ Xaa₁₄ [SEQ ID NO: 1],

wherein

Xaa₁ and/or Xaa₂ is an aromatic amino acid

Xaa₃ and/or Xaa₄ is glycine;

Xaa₅ to Xaa₁₀ comprise at least 5 amino acids selected from the group:
tyrosine, phenylalanine, tryptophan, threonine, valine or isoleucine, optionally
Xaa₅ to Xaa₁₀ can include at least one aromatic amino acid residue.

17. The spacer according to claim 15 wherein said spacer comprises the amino acid sequence:

Xaa₁ Xaa₂ Xaa₃ Xaa₄ Xaa₅ Xaa₆ Xaa₇ Xaa₈ Xaa₉ Xaa₁₀ Xaa₁₁ Xaa₁₂ Xaa₁₃ Xaa₁₄ [SEQ ID NO: 1],

wherein Xaa₅ to Xaa₁₀ comprising of the same amino acid residues wherein said amino acid residues are selected from the group consisting of: methionine, alanine, leucine, glutamine, lysine or arginine.

18. The spacer according to claim 15 wherein said spacer comprises the amino acid sequence:

Xaa₁ Xaa₂ Xaa₃ Xaa₄ Xaa₅ Xaa₆ Xaa₇ Xaa₈ Xaa₉ Xaa₁₀ Xaa₁₁ Xaa₁₂ Xaa₁₃ Xaa₁₄ [SEQ ID NO: 1]

wherein Xaa₅ to Xaa₁₀ comprising of alternating amino acid residues wherein said amino acid residues are selected from the group consisting of: methionine, alanine, leucine, glutamine, lysine or arginine.

19. The spacer according to any one of claims 2 to 11 wherein said peptide comprises an amino acid sequence selected from the group consisting of:

- i) FFGGEEEEGGFF [SEQ ID NO: 2];
- ii) FFGGEEEEEEGGFF [SEQ ID NO: 3];
- iii) FFGGEEEEEEEEEEEEGGFF [SEQ ID NO: 4];
- iv) FFGGQQQQQQGGFF [SEQ ID NO: 5];
- v) FFGGKKKKKKGGFF [SEQ ID NO: 6];
- vi) WWGGEEEEEGGW [SEQ ID NO: 7];
- vii) FFGGEKEKEKGGFF [SEQ ID NO: 8];
- viii) FFGGEQKEQKGGFF [SEQ ID NO: 9];
- ix) FFGGEMEMEMGGFF [SEQ ID NO: 10]; and
- x) FFGGQMQMGMGGFF [SEQ ID NO: 11].

20. A layered graphene structure comprising one or more spacers according to any one of claims 1 to 19.

21. The layered graphene structure according to claim 20 wherein said layered graphene structure, includes:

at least a first graphene layer and at least a second graphene layer,

at least one spacer layer, wherein said at least one spacer layer includes at least one spacer unit, the spacer unit including a middle portion and an upper end and a lower end, so as to provide a desired predetermined space between the at least first graphene layer and the at least second graphene layer.

22. The layered graphene structure according to claim 20 or 21 wherein said structure is mesoporous.

23. The layered graphene structure according to claim 20 or 21 wherein said structure is macroporous.

24. The layered graphene structure according to any one of claims 20 to 23 wherein said layered structure is at least 10nm thick.

25. The layered graphene structure according to claim 24 wherein said layered structure is between 10-1000nm thick.

26. The layered graphene structure according to any one of claims 20 to 25 wherein said layered structure comprises at least 2 to 100 graphene layers.

27. A device comprising a graphene structure according to any one of claims 20 to 26.

28. The device according to claim 27 wherein said device is a drug delivery device wherein said device is further modified to include at least one biologically active agent.

29. The device according to claim 28 wherein said device is a medical device.

30. The device according to claim 28 wherein said biological agent is an anti-cancer agent.

31. A method of producing a layered graphene structure the method including the steps of:

mixing graphene and a solution of spacer units having a first end group and a second end group in a solution;

non-covalently bonding a first end group of the spacer unit to a first side of at least a first graphene sheet;

non-covalently bonding a second end group of the spacer unit to a first side of at least a second graphene sheet;

wherein the spacer units form a spacer layer, so as to provide a desired predetermined space between the at least first graphene sheet and the at least second graphene sheet.

32. The method according to claim 31 wherein the layered graphene structure is self-assembled.

33. The method according to claim 31 or 32 wherein the spacer units facilitates the self-assembly and stabilisation of the layered graphene structure.

34. The method according to any one of claims 31 to 33 wherein, the spacer unit is at least one amino acid.

35. The method according to any one of claims 31 to 34 wherein the spacer units at least one peptide.

36. The method according to any one of claims 31 to 35 wherein the first end group and the second end group of the spacer units are selected from the group of functional groups including aromatic and non-aromatic functional groups.

37. A process for the purification of one or more molecules comprising the steps:

- i) providing a mixture comprising a molecule to be purified;
- ii) contacting said mixture with a layered graphene structure according to any one of claims 20 to 26 and provide conditions to allow association of said one or more molecules with said layered graphene structure to provide a graphene structure comprising said molecule[s];
- iii) contacting the layered graphene comprising molecule[s] with a wash buffer to remove non-specifically associated molecules; optionally
- iv) repeating step ii) and/or iii);
- v) eluting associated molecule[s] from said layered graphene to provide a purified solution of said molecule[s]; and optionally
- vi) repeating step v).

38. The process according to claim 37 wherein said layered graphene is part of a column and said molecules are contacted with said layered graphene.

39. The process according to claim 37 wherein said layered graphene is contacted with a solution comprising a mixture of said molecules.

Abstract

The disclosure relates to spacer molecules and their use in forming layered graphene and related materials and structures and methods for producing through self-assembly layered graphene and related structures of controlled pore size.

Appendix B: Patent Figures

Figure 1

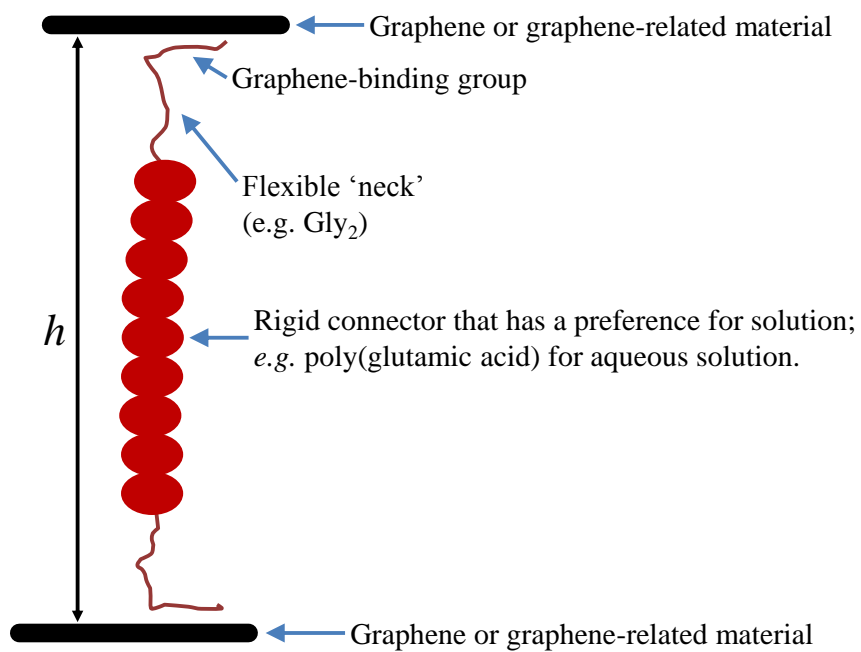


Figure 2



Figure 3



Figure 4

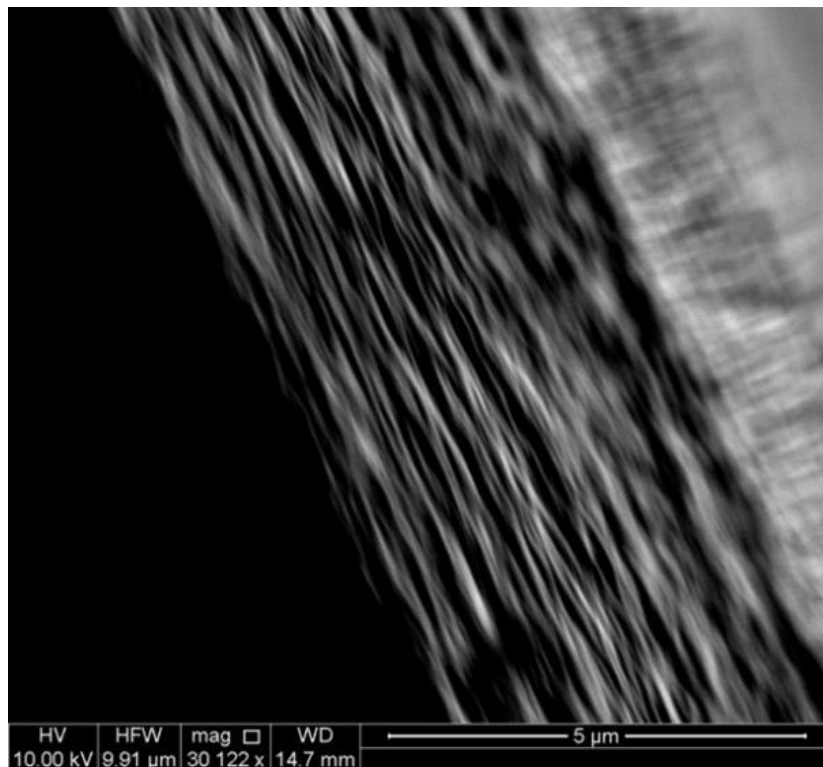


Figure 5

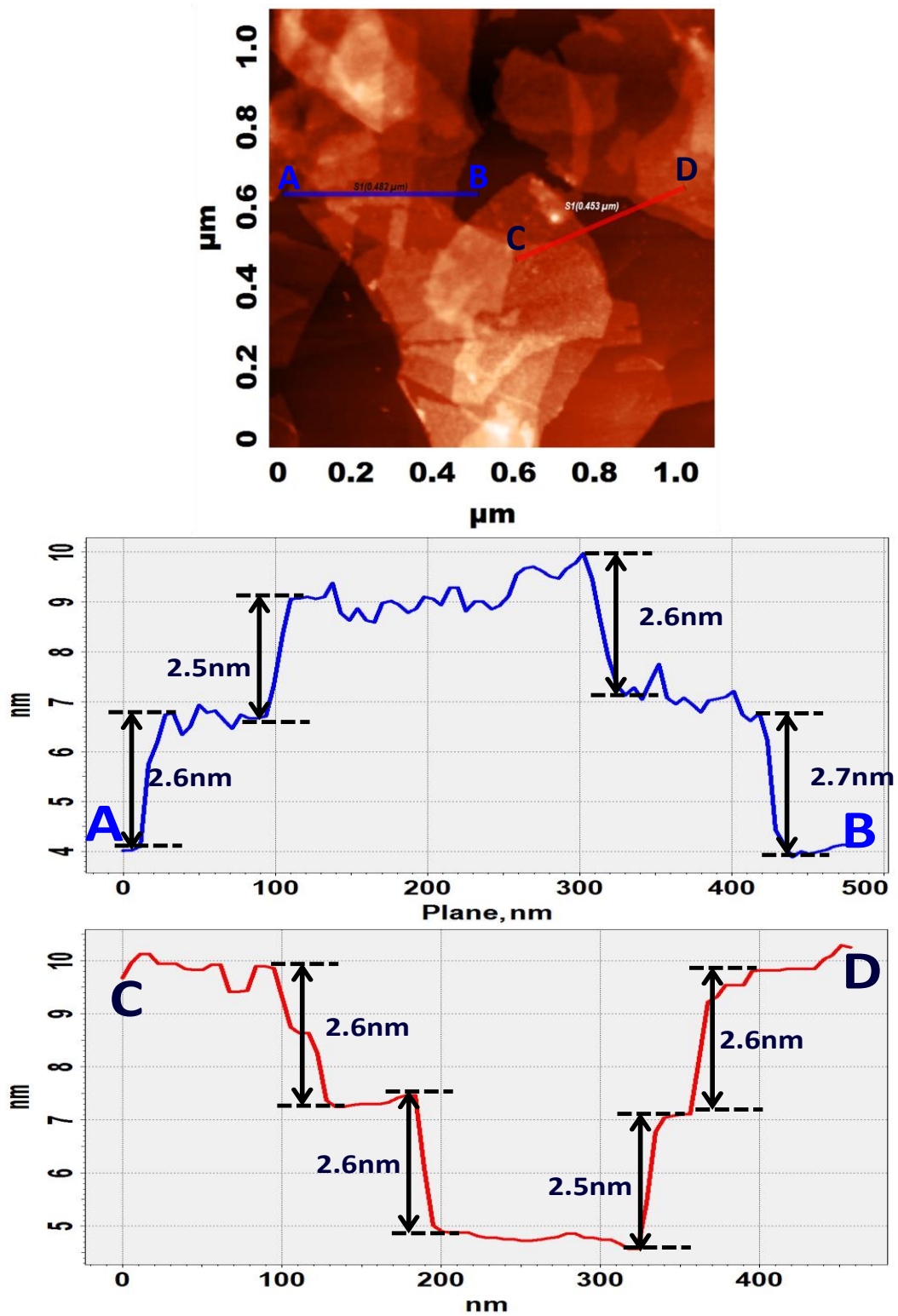


Figure 6

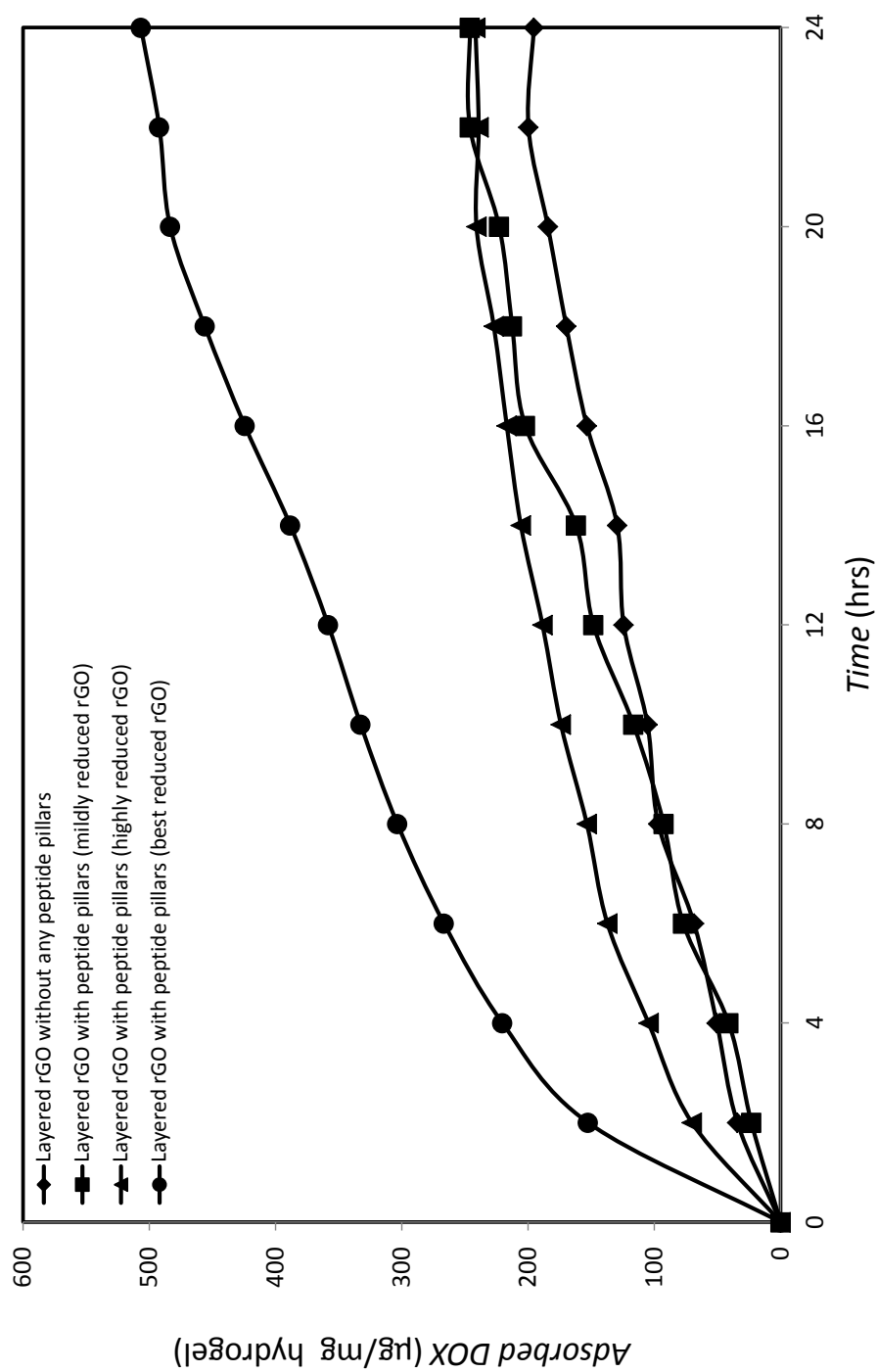


Figure 7

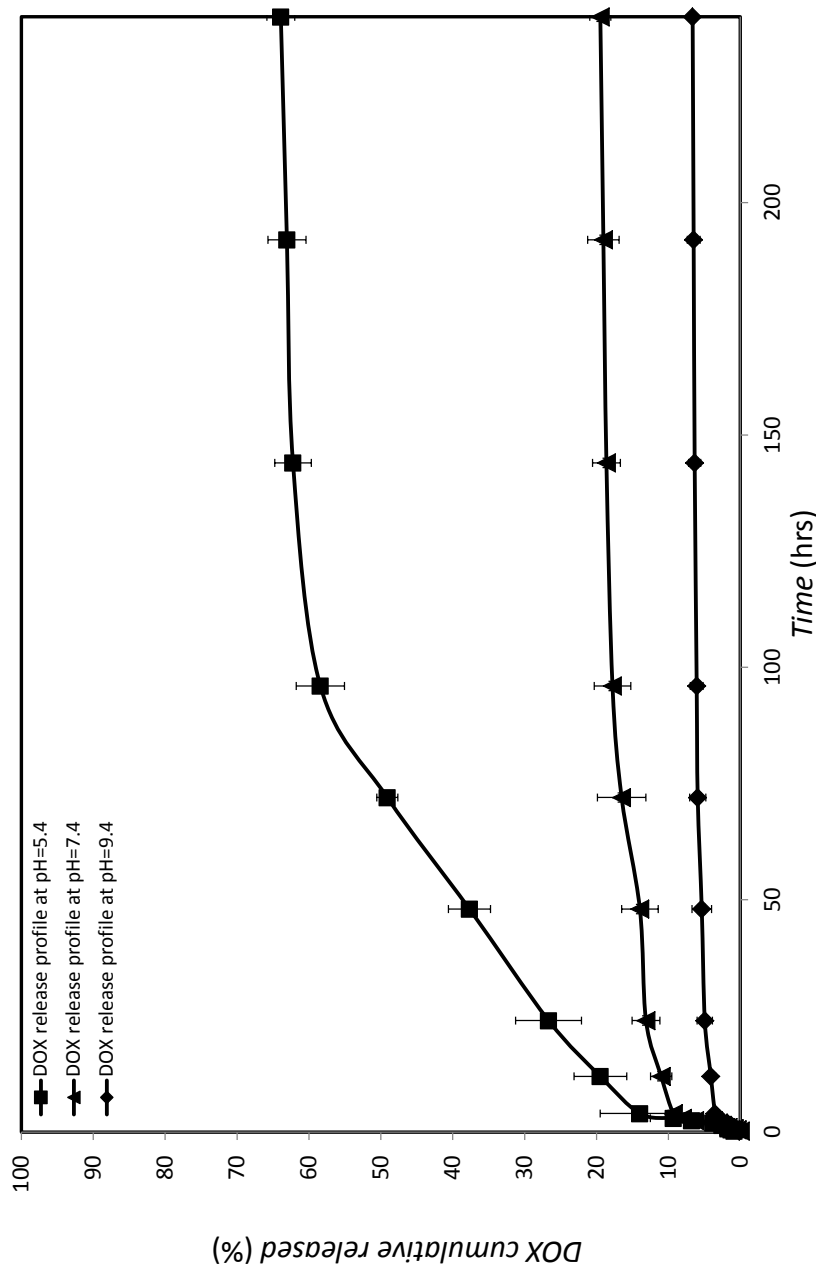


Figure 8

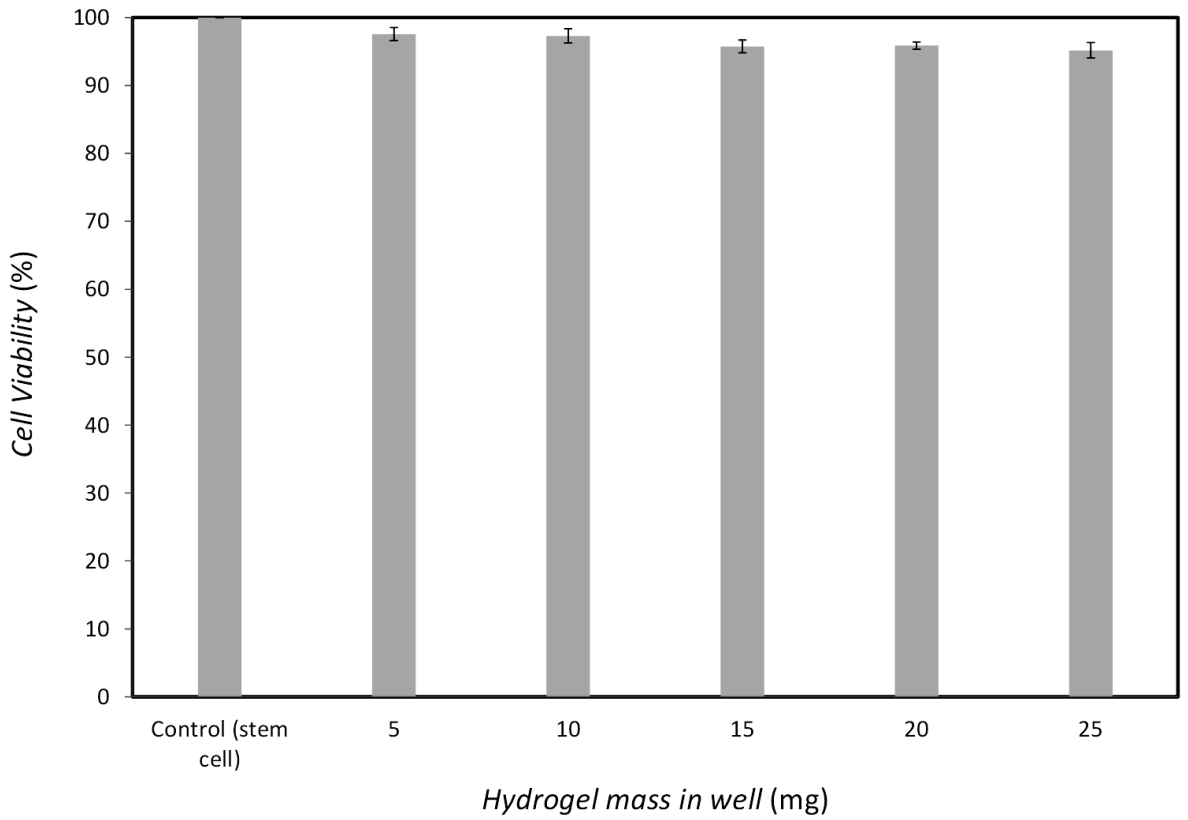


Figure 9

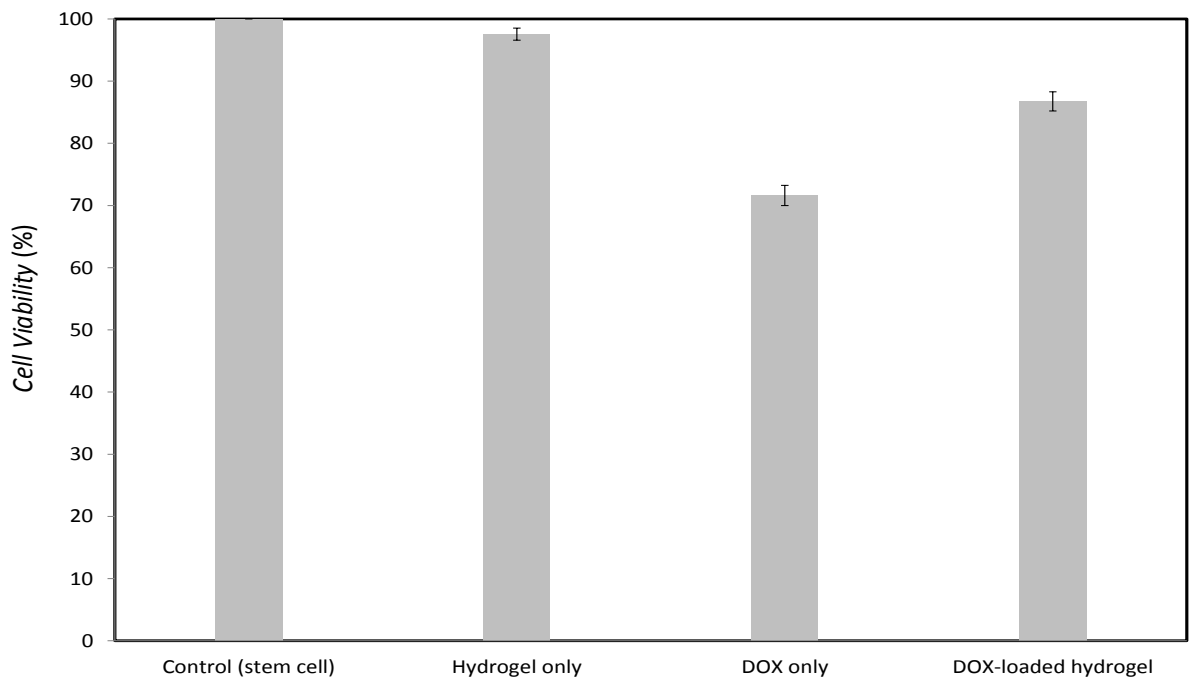


Figure 10

